University of Strathclyde

Department of Physics
Photophysics Research Group

Plasmonic Nanostructures for Metal-Enhanced Applications

A Thesis submitted to the University of Strathclyde
for the degree of

Doctor of Philosophy

By

Milan Adelt

Glasgow, 2022

Declaration

This thesis is the result of the author's original research. It has been composed by the author and has not been previously submitted for examination which has led to the award of a degree.

The copyright of this thesis belongs to the author under the terms of the United Kingdom Copyright Acts as qualified by University of Strathclyde Regulation 3.50. Due acknowledgement must always be made of the use of any material contained in, or derived from, this thesis.

Signed:

Date:

Acknowledgements

First of all, I would like to express my gratitude to my supervisor Dr. Yu Chen for giving me the invaluable opportunity to undertake a PhD as her student, for allowing me to learn from her, and for guiding me during my PhD. Also, many thanks to my second supervisor Professor David Birch for his guidance and advice in solving technical issues I have encountered during my research.

I would like to thank Engineering and Physical Sciences Research Council (EPSRC) for their financial support, without which I would not have been able to complete my PhD.

Thank you to everyone in the Photophysics group for becoming my second family. I feel very lucky to have met such a friendly and fun group to work in. To Lucas, Hazel, Chloe, Ben, Alastair, Yok, Rhona, Daniel, and Gillian, I will forever miss our Friday lunches and will never forget the friendships I have made.

I would like to thank my friends and collaborators who have played a role in my research. Thank you to Dr. P. R. Edwards for his assistance with electron microscopy and solving technical issues. I must give thanks to Dr. K. H. Aaron Lau for welcoming me to his lab and sharing his knowledge and expertise in anodizing. Many thanks to Dr. Gregory Wallace for sharing his knowledge in plasmonic substrates and for the assistance with numerical simulations. Thank you to Dr. Donald MacLaren from University of Glasgow for his expertise in electron microscopy and contributions to my first publication. Many thanks to Dr. Marwa Ben Yaala for her assistance with optical characterization of my samples. I would like to thank Dr. Monika Warzecha for her assistance with atomic force microscopy. I would also like to acknowledge Dr. Xianzhong Chen from Heriot Watt University and Dr. Jinglong Yin from Teer Coatings Ltd for thin film deposition.

Finally, to my family, words cannot express how grateful I am for the support and strength you have been giving me both in my personal life and during my studies, without which I would not have been able to get where I am now. Thank you for always believing in me and for guiding me through difficult times.

Abstract

Surface plasmon resonance is an optical phenomenon which has attracted a broad research interest due to the ability to harvest and localize incident light in the nanoscale and to enhance electromagnetic fields in the vicinity of certain metallic nanostructures. These enhanced electromagnetic fields have the ability to improve photophysical and molecular properties of molecular species of interest, giving rise to “metal-enhanced” techniques with improved performance. Techniques and processes involving fluorescence or chemical reactions are often hindered by low quantum yields and insufficient photostability or low reaction yields, respectively. By implementing metallic nanostructures with the structure and plasmonic properties adapted to characteristics of involved molecules and experimental conditions, these limitations can be overcome.

In this thesis, the fabrication, characterization, application of various plasmonic nanostructures and metallic substrates with characteristics suitable for metal-enhanced fluorescence (MEF) or plasmonic photocatalysis are described.

In the first part, an emphasis is placed on systematically investigating an anisotropic coating of the ends of gold nanorods (GNRs) with silica as well as the influence of growth conditions on the formation of silica shells through electron microscopy and absorption spectroscopy. Such modification could allow a selective positioning of molecules of interest near the ends of GNRs where their strong longitudinal plasmon resonance can be exploited. By exploiting unique surface characteristics of GNRs, three nanostructures with various coating morphologies were produced: fully encapsulated core-shell GNRs, GNRs with only one end coated with silica, and dumbbell-like GNRs (dGNRs) with both ends coated. The study was performed at conditions, where controlling the solubility and micellization of the surfactant cetyltrimethylammonium bromide (CTAB) is possible, which can be tuned to affect the morphology and stability of resulting silica shells. A combination with an appropriate aspect ratio of GNRs led to a significant improvement of the growth yield of dGNRs. Thus, a protocol for a high-yield synthesis of dGNRs was developed, with a maximum yield exceeding 90%. This study advanced the understanding of the anisotropic coating process on GNRs which is relevant for GNR-based nanostructures for fluorescence/scattering amplifiers or plasmon-enhanced catalysis.

In the second part, aluminium foil was tested as an affordable substrate for MEF in the UV-Vis region of spectrum using bovine serum albumin (BSA) and BSA-encapsulated gold nanoclusters (BSA-AuNCs). Fluorescence of BSA and BSA-AuNCs was evaluated by analysing fluorescence emissions of amino acid tryptophan and AuNCs. Steady-state and time-resolved fluorescence spectroscopy of BSA and BSA-AuNCs immobilized and dried on the two sides (shiny and matt) of the aluminium foil revealed that the matt side supported a moderate fluorescence enhancement of both tryptophan and AuNCs emissions, while the fluorescence emission intensity on the shiny side decreased, suggesting quenching of fluorescence. It is believed that the observed enhancement on the matt side originated due to the nanoscale corrugation which supported generation of locally enhanced electromagnetic fields responsible for an improved excitation efficiency of fluorophores, increased radiative decay rate of tryptophan in BSA as well as improved Förster resonance energy transfer (FRET) from tryptophan to AuNCs in BSA-AuNCs. The observed emission enhancement suggests the matt side could be used as a simple substrate for MEF in the UV and blue region of visible spectrum.

In the third part, plasmonic substrates with periodic arrays of three-dimensional gold nanobowls (AuNB) of various diameters and optical properties suitable for MEF in the UV and visible spectrum were fabricated. AuNBs were rigorously analysed both experimentally and numerically to determine their physical and optical properties. The substrates exhibited significant reflectance minima from UV to 500 nm, indicating strong absorption in this region, which is particularly valuable for MEF with the limited number of substrates active in the UV. Numerical simulations were employed to probe size- and excitation-dependent spatial distribution of electric fields of AuNBs in the UV and visible spectrum given by their specific geometry. The effect of fine structural features such the wall thickness between NBs and the thickness of Au coating on the electric field distribution was investigated as well. The results suggest that the wall thickness influences the electric field intensity at rims of NBs and the coating thickness influences the strength and the size of electric fields induced inside NBs. It is hoped that this work provides insight into designing and optimizing AuNB substrates for fluorescence applications with optical properties tailored to photophysical properties of incorporated fluorophores.

Finally, the performance of AuNBs for MEF in the UV and visible spectrum was investigated using BSA-AuNCs, which is believed to be the first MEF study on AuNBs performed in the UV with a protein and fluorescent AuNCs as emitters. Fluorescence emission was investigated on two groups of small- and large-diameter AuNBs under various excitation wavelengths and angles. It was found that the fluorescence emission of BSA-AuNCs exhibited a structure-specific angular dependence on both types of AuNB arrays. Large-diameter AuNB supported a consistent broadband enhancement of fluorescence emission BSA-AuNCs for excitation wavelengths in the UV and visible regions of spectrum, which was attributed to the broadband excitation rate enhancement mediated by the geometry of nanobowls and a structure-dependent coupling of BSA-AuNCs with AuNB arrays. This led to the highest observed fluorescence enhancement of 34.5-fold of the AuNC emission on large-diameter AuNBs. Small-diameter AuNB arrays induced less consistent angular dependence of the fluorescence emission of BSA-AuNCs. This was interpreted to arise from different angle-dependent optical properties of small-diameter AuNBs composed of arrays of nanocaps which do not support mechanisms typical for large-diameter bowl-like architectures. It is hoped that by combining findings gained by structural and fluorescence characterizations, implications for further use of AuNBs in fluorescence applications in UV and visible regions of spectrum could be better understood.

Publications and proceedings

Adelt, M.; MacLaren, D. A.; Birch, D. J. S.; Chen, Y. Morphological Changes of Silica Shells Deposited on Gold Nanorods: Implications for Nanoscale Photocatalysts. ACS Appl. Nano Mater. 2021, acsanm.1c00977. https://doi.org/10.1021/acsanm.1c00977.

Arivazhagan, V.; Gun, F.; Reddy, R. K. K.; Li, T.; Adelt, M.; Robertson, N.; Chen, Y.; Ivaturi, A. Indoor Light Harvesting Lead-Free 2-Aminothiazolium Bismuth Iodide Solar Cells. *Sustain. Energy Fuels* 2022, 2–9. https://doi.org/10.1039/d1se02017j.

Gandhi, M. B.; Arivazhagan, V.; Nicholson, S.; Adelt, M.; Martin, R.; Chen, Y.; Sridharan, M. B.; Ivaturi, A.; Investigation on Guanidinium Bromide Incorporation in Methylammonium Lead Iodide for Enhanced Efficiency and Stability of Perovskite Solar Cells. *Manuscript in submission process.*

Adelt, M.; Chen, Y.; Birch, D. J. S.; “Investigating morphological changes of silica coating on gold nanorods”, Poster Presentation, SUPA SUPA Annual Gathering 2019, Glasgow.

Adelt, M.; Chen, Y.; Birch, D. J. S.; “Investigating morphological changes of silica coating on gold nanorods”, Poster Presentation, Applied Nanotechnology and Nanoscience International Conference (5th edition) – ANNIC 2019 2019, Paris.

Adelt, M.; Chen, Y.; Birch, D. J. S.; “Investigating morphological changes of silica coating on gold nanorods”, Poster Presentation, SUPA Photonex conference 2019, Glasgow.

Abbreviations

ADC – Analogue-to-digital converter

AFM – Atomic force microscopy

AgNBs – Silver nanobowls

AlNB – Aluminium nanobowl

APTES – (3-aminopropyl)triethoxysilane

AuNB – Gold nanobowl

AuNC – Gold nanocluster

bCTAB – Bound cetyltrimethylammonium bromide

BDAC – Benzyldimethylhexadecylammonium chloride

BSA – Bovine serum albumin

BSA-AuNC – Bovine serum albumin-encapsulated gold nanoclusters

CFD – Constant fraction discriminator

CMC – Critical micelle concentration

CTAB – Cetyltrimethylammonium bromide

[CTAB] – Concentration of CTAB

CuNB – Copper nanobowl

DMSO – Dimethyl sulfoxide

DDA – Discreet dipole approximation

dGNRs – Dumbbell-like gold nanorods

EELS – Energy-electron loss spectroscopy

EEM – Excitation emission matrix

EF – Enhancement factor

EM - Electromagnetic

fCTAB – Free cetyltrimethylammonium bromide

FDTD – Finite-difference time-domain

FEG – Field emission gun

FRET – Förster resonant energy transfer

GNP – Gold nanoparticle

GNR – Gold nanorod

[GNR] – Concentration of gold nanorods

HAADF – High-angle annular dark-field

IR – Infrared

IRF – Instrument response function

LED – Light-emitting diode

LSPm – Longitudinal surface plasmon mode

LSPR – Localised surface plasmon resonance

mAl – Matt side of aluminium foil

MCA – Multi-channel analyser

MEF – Metal-enhanced fluorescence

MHA – Mercaptohexanoic acid

mRNA – messenger Ribonucleic acid

NIR – Near-infrared

NLLS – Non-linear least squares

NP – Nanoparticle

P3TT – Poly[3-(2,5,8-trioxanonyl) thiophene]

PBS – Phosphate buffered saline

PMT – Photomultiplier

PPP – Poly(2,5-dioctyloxy-p-phenylene)

PVD – Physical vapor deposition

sAl – Shiny side of aluminium foil

SEM – Scanning electron microscopy

SERS – Surface-enhanced Raman spectroscopy

SET – Surface energy transfer

SIF – Silver island film

SPR – Surface plasmon resonance

STEM – Scanning transmission electron microscopy

TAC – Time-to-amplitude converter

TBE – Tris/Borate/EDTA buffer

TCSPC – Time-correlated single-photon counting

TEM – Transmission electron microscopy

TEOS – Tetraethyl orthosilicate

TPL – Two-photon luminescence

TSPm – Transverse surface plasmon mode

UV-Vis – Ultraviolet-visible spectrum

Vis – Visible

Table of Contents

List of Tables

List of Figures

1. Introduction

The development of modern scientific methods has provided an interdisciplinary knowledge necessary for the application of materials where it had not been previously possible. New means in the material synthesis and nanofabrication has allowed to shrink these materials to the nanometre scale and produce nanostructures with size-related optical and mechanical properties previously hidden in their macroscopic form. This represents foundations of nanotechnology which has led to rapid advancements in research, biomedical as well as industrial fields.

Metallic nanostructures and metallic films, in particular, have proven to possess tremendous potential in this regard due to their ability to enhance surrounding electromagnetic fields through optically excited coherent oscillations of conduction band electrons known as surface plasmon resonance (SPR).[1] The implementation of metallic nanostructures has laid foundations of new branches of analytical and imaging techniques that rely on the enhancement of various photophysical phenomena in the presence of such nanodevices.[2] Among these, surface-enhanced spectroscopy involving metal-enhanced fluorescence (MEF) spectroscopy and surface-enhanced Raman spectroscopy (SERS) has evolved considerably over the past several decades.[2–4] The enhancement of fluorescence in MEF is an area of particular interest as fluorescence is arguably one of the most widely spread phenomena in optical techniques.[3,4] As a result, in order to optimize this enhancement, a need for nanostructures with optical and chemical properties tailored to satisfy requirements for specific applications has greatly increased.

1.1. Gold Nanorods

Gold nanoparticles (GNPs) have sparked a keen interest in the research community due to their excellent physiochemical properties which have made them one of the most explored groups of nanostructures. Compared to other metals, gold is highly biocompatible, chemically stable and supports strong SPR.[5] Due to their large surface-to-volume ratio, size- and shape-dependent optical properties which give rise to the ability to locally enhance electric fields in their vicinity via localized surface plasmon resonance (LSPR), GNPs have been employed in numerous biomedical applications.[6,7]

Among GNPs, gold nanorods (GNRs) attract extreme attention due to their specific LSPR arising from the elongated shape and size which are the source of their absorption and scattering properties in the visible (Vis) and infrared (IR) regions.[8] This shape anisotropy supports the excitation of two distinct plasmonic modes. These modes originate from electron oscillations in transverse and longitudinal directions, giving rise to two absorption bands in the absorption spectrum of GNRs (Figure 1).[8] The wavelength of the longitudinal plasmon mode is highly shape- and size-dependent and can be fine-tuned up to the IR by controlling nanorods' aspect ratio during their synthesis.[8] This ability has made GNRs useful platforms for MEF and other phenomena, where the position of the plasmon band with respect to absorption/emission properties of signalling reporters is critical.[3]

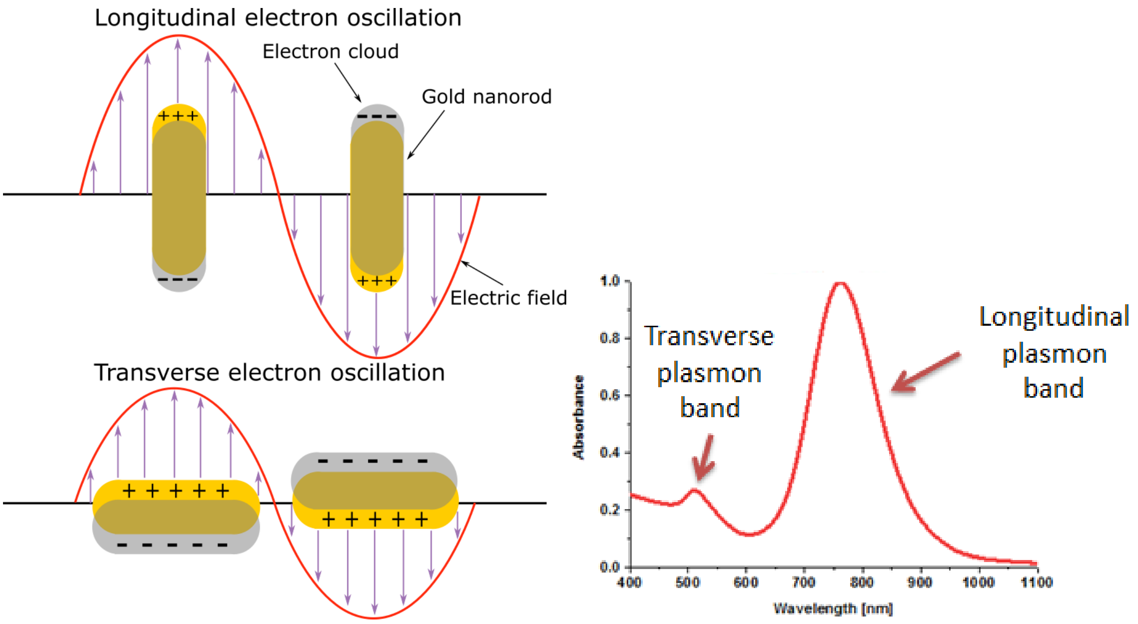

Figure 1: Schematic of GNRs with oscillating free conduction electrons in transverse and longitudinal directions (left) and a typical absorption spectrum of GNRs (right) with transverse and longitudinal plasmon bands generated as a result of electron oscillations in the two respective directions. Adapted from [9].

1.1.1. Surface Plasmon Resonance

The phenomenon of SPR is based on the interaction of metallic structures with electromagnetic (EM) radiation which excites collective oscillations of free conduction electrons (plasmons) of the metal.[10] For bulk plasmons, electron oscillations occur at the plasma frequency (ω_p) defined as[10]

$$\omega_p = \frac{1}{2\pi}\sqrt{\frac{n_e e^2}{m_e \varepsilon_0}}, \qquad \textit{Equation 1}$$

where ε_0 is the dielectric constant of free space, n_e is the electron density of the metal, e is the electron charge, and m_e is the effective mass of an electron.

At a metal-dielectric interface, plasmons are classified as surface plasmons or surface plasmon polaritons.[10] Surface plasmons are optically excited surface plasmon waves driven by the oscillating electric field of the incident light, which propagate at the interface between the metal surface and a dielectric material when the incident light's wave vector is parallel to the surface. When optically excited, the frequency of induced electron oscillations matches the frequency of incident light. The induced EM field of surface plasmons can greatly enhance optical near-fields near the metallic surface but its intensity decays exponentially away from the interface and thus, their practical application is limited by the distance relative to the metallic surface.[11]

1.1.2. Localized Surface Plasmon Resonance

Localized surface plasmon resonance occurs when a surface plasmon is confined to a nanostructure or a nanoparticle (NP) that are smaller than the wavelength of incident light.[3,12] Upon excitation, conduction electrons, confined in a small volume of NPs, are displaced from their equilibrium positions relative to the particle's core which generates uncompensated charges (Figure 1). Polarization of the metal surface represents the restoring force and causes NPs to behave as resonant oscillators with the LSPR.[5] The resonant frequency can be found in the absorption spectrum of such NPs, where its value corresponds to the wavelength of the absorption maximum of the corresponding plasmon band (Figure 1).[10]

The induced plasmonic field remains localized at the nanostructure's surface and enhances electromagnetic fields in its vicinity, providing enhanced absorption and scattering in Vis and IR spectral region.[12,13] This effect is particularly strong in metals such as gold or silver which exhibit exceptional absorption and is also responsible for strong vibrant colour of gold colloidal solutions.[14] The strength of the generated plasmon field decays rapidly with the size of nanostructures and with the increasing distance from the metal surface, which allows utilizing NPs for metal-enhanced techniques in only a nanoscale volume.[11,15] The phenomenon of the LSPR is rather complex but can be explained using the following scattering theory.

1.1.2.1. Mie Theory

The first description of optical properties of metallic NPs was given by Mie[13] for spherical gold NPs. Mie applied the general theory of light extinction to small nanoparticles by finding a solution to Maxwell's equations with boundary conditions in spherical coordinates and provided the description of the light-nanoparticle interaction as well as the extinction of spherical metallic NPs. Considered were NPs much smaller than the wavelength of incident light which allows to dismiss the effect of scattering that would otherwise become effective and used approximations would no longer apply.[16]

Mie's solution led to obtaining extinction (σ_{ext}) and scattering (σ_{sca}) cross-sections of a homogeneous conducting sphere by finding the scattered fields generated by an incident plane wave.[10,17] Ultimately, absorption cross-section (σ_{ext}) of a spherical nanoparticle can be calculated as[16]:

$$\sigma_{ext} = \frac{2}{x^2}\sum_{L=1}^{\infty}(2L+1)[Re(a_L + b_L)] \qquad \textit{Equation 2}$$

$$\sigma_{sca} = \frac{2}{x^2}\sum_{L=1}^{\infty}(2L+1)[Re(|a_L|^2 + |b_L|^2)] \qquad \textit{Equation 3}$$

$$\sigma_{abs} = \sigma_{ext} - \sigma_{sca} \qquad \textit{Equation 4}$$

The parameter x represents size and can be described as follows:

$$x = \frac{2\pi R n_m}{\lambda} \qquad \textit{Equation 5}$$

The integer L represents the dipole, R is the radius of the particle, n_m is the refractive index of the surrounding medium, λ is the wavelength of light in vacuum, and a_L and b_L are scattering coefficients which can be defined using Ricatti-Bessel expressions[16,18]:

$$a_L = \frac{m\psi_L(mx)\psi_L'(x) - \psi_L(y)\psi_L'(mx)}{m\psi_L(mx)\xi_L'(x) - \xi_L(x)\psi_L'(mx)} \qquad \textit{Equation 6}$$

$$b_L = \frac{\psi_L(mx)\psi_L'(x) - m\psi_L(y)\psi_L'(mx)}{\psi_L(mx)\xi_L'(x) - m\xi_L(x)\psi_L'(mx)} \qquad \textit{Equation 7}$$

Here, ψ_L and ξ_L are Ricatti-Bessel cylindrical functions ($m = \tilde{n}/n_m$) where $\tilde{n}$ is the complex refractive index ($\tilde{n} = n_r + in_i$) of the particle. This complex description can be simplified under the assumption that nanoparticles are much smaller than the wavelength of incident light (2R << λ), both nanoparticles and their environment are homogeneous and can be each described using their bulk dielectric functions.[10,16] For particles of this size, the Mie theory can be reduced to:

$$\sigma_{ext} = \frac{18\pi\varepsilon_m^{3/2}V}{\lambda}\frac{\varepsilon_2(\lambda)}{[\varepsilon_1(\lambda) + 2\varepsilon_m]^2 + [\varepsilon_2(\lambda)]^2} \qquad \textit{Equation 8}$$

The corresponding σ_{sca} can be described as[10]:

$$\sigma_{sca} = \frac{34\pi^4\varepsilon_m^{3/2}V^2}{\lambda^4}\frac{(\varepsilon_1 - \varepsilon_m)^2 + {\varepsilon_2}^2}{(\varepsilon_1 + 2\varepsilon_m)^2 + (\varepsilon_2)^2}, \qquad \textit{Equation 9}$$

where V is the volume of the spherical particle ($4\pi R^3/3$), λ is the wavelength of light in the medium, ε_m is the dielectric function of the medium and ε_1 and ε_2 are real and imaginary parts of the material's dielectric functions ($\varepsilon(\lambda) = \varepsilon_1(\lambda) + i\varepsilon_2(\lambda)$), respectively. The width and height of the resonance are determined by the imaginary part of the metal's dielectric function ε_2, which is related to plasmon damping,[16] whereas the position of the plasmon peak and the sensitivity of the LSPR on refractive index are determined by ε_1.[19] The different volume dependency in Equation 8 and Equation 9 suggests that in the case of small NPs the dominant effect is absorption whereas for larger NPs, the dominant component is scattering.[20] Therefore, smaller NPs would be preferred in areas such as thermotherapy where an effective photothermal conversion of incident EM radiation is critical, and larger NPs with greater scattering contribution should be more suitable for imaging techniques and MEF.[21]

Although the size approximation is valid only to small NPs (<20 nm), predictions of σ_{ext} and σ_{sca} provide accurate results even for larger NPs.[10,16] Their extinction coefficients will, however, depend explicitly on the size, which ultimately affects the position of the peak resonant wavelength and the bandwidth due to the existence of higher number of modes caused by the inhomogeneous polarization. Retardation effects of the EM field across the NP's surface will cause shifts and broadening of the SPR.[16,22]

From Equation 8, one can see a clear dependence of the extinction cross-section on ε_m and that the highest value of the extinction cross-section is achieved when the resonant condition $\varepsilon_1 = -2\varepsilon_m$ is fulfilled. For example, if the refractive index of the medium increases, the position of the plasmon band maximum will be shifted to longer wavelengths. This sensitivity of the SPR to the refractive index of the medium is the basis for designing analytical assays and plasmonic biosensors.[10,12,23] Such devices allow to measure intensity changes and shifts in the peak wavelength of the plasmon band in the presence of analytes of interest.

1.1.2.2. Gans Theory

The applicability of Mie theory on strictly spherical particles does not allow this model to be used for asymmetrical nanoparticles such as spheroids or nanorods. For this purpose, Mie theory was extended by Richard Gans to describe radiative properties of spheroids of any aspect ratio, using small particle approximation.[10,24] According to the Gans theory, the extinction cross-section σ_{exc} of a randomly oriented spheroid can be described using a formula analogous to that derived for spheres (Equation 8):

$$\sigma_{exc} = \frac{2\pi V}{3\lambda}\varepsilon_m^{3/2}\sum_j \frac{\left(1/P_j^2\right)\varepsilon_i}{[\varepsilon_r + (\frac{1-P_j}{P_j})\varepsilon_m]^2 + \varepsilon_i^2}, \qquad \textit{Equation 10}$$

where ε_m is the dielectric constant of the medium, ε_r and ε_i are relative and imaginary dielectric constants of the bulk metal ($\varepsilon = \varepsilon_r + i\varepsilon_i$), λ is the wavelength of the incident light, V is the volume of the particle, and P_j are depolarization factors for the three axes (a, b, c) of a spheroid (Figure 2).

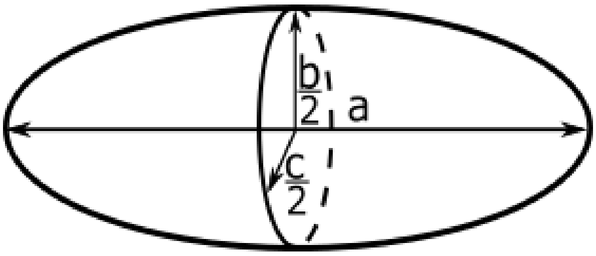

Figure 2: A simplified schematic of a nanorod with indicated major axis and minor axes b and c.

Axes b and c are perpendicular to the major axis and have the same length (b = c). Therefore, depolarization factors can be described using only axes a – length and b – width (Equation 11 and Equation 12):

$$P_a = \frac{1-e^2}{e^2}\left(\frac{1}{2e}\ln\frac{1+e}{1-e} - 1\right) \qquad \textit{Equation 11}$$

$$P_c = P_b = \left(\frac{1-P_a}{2}\right) \qquad \textit{Equation 12}$$

To account for the size asymmetry, depolarization factors include the geometrical factor e which can be defined using the aspect ratio of a rod:

$$e = \sqrt{1-\frac{b^2}{a^2}} = \sqrt{1-\left(\frac{length}{width}\right)^{-2}} \qquad \textit{Equation 13}$$

Because the extinction cross-section is a sum of contributions (depolarization factors) in all three dimensions, the extinction spectrum of GNRs exhibits the two aforementioned distinct peaks, a smaller transverse peak located at around 520 nm and a tunable longitudinal peak, which correspond to resonances in transverse and longitudinal directions (Figure 1). It is now clear that parameters ε_m and $\frac{1-P_j}{P_j}$ in Equation 10 explain the red shift of the longitudinal plasmon peak with increasing refractive index of the medium and with increasing aspect ratio of nanorods.[22] The factor $\frac{1-P_j}{P_j}$ is sometimes referred to as “shape factor” and its value for spherical particles is 2 and increases for higher aspect ratios.[2,10]

1.2. Fluorescence Photophysics

A popular way of studying living organisms at cellular and molecular levels is through luminescence. Luminescence is a spontaneous emission of light emitted by electronically excited molecules that is not associated with the heating of the energy source used for the excitation. One form of luminescence is photoluminescence, which utilizes photoexcitation through an absorption of electromagnetic (EM) radiation (UV-Vis-IR) by a fluorescent molecule. The excited molecule relaxes to its ground energy state and releases the excess of acquired energy in a form of a photon of light.

The mechanism of photoluminescence can be explained using the well-known Jablonski diagram (Figure 3). Jablonski diagram is a diagram of energy levels and illustrates various energy transitions between energy levels and processes associated with photoluminescence.

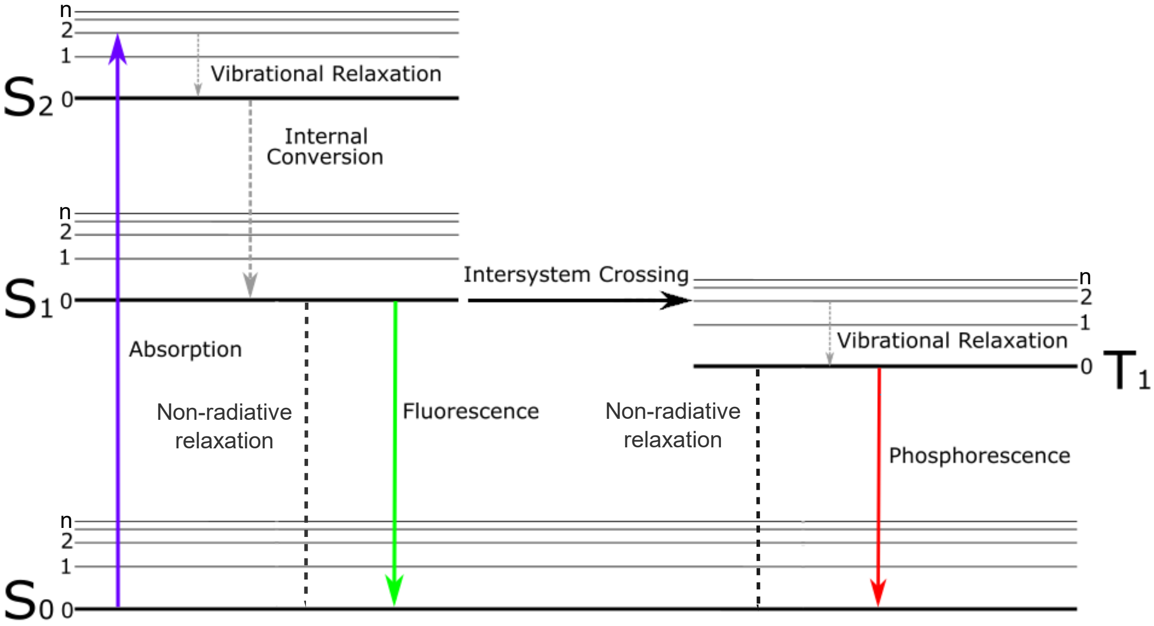

Figure 3: Jablonski diagram of energy levels of a fluorescent molecule. Solid vertical lines represent radiative transitions between energy states of a molecule. Horizontal lines represent electronic states (black) and vibrational levels (grey). Dashed lines illustrate non-radiative transitions. S_0 is a ground state and S_1 and S_2 are electronic excited states, T_1 is a triplet state.

When the energy of an incident photon of light matches the energy difference between ground and excited states of a molecule, an electron undergoes excitation from the ground state (S_0) to a higher electronic excited singlet state (S_1, S_2, …) from which it relaxes to the lowest vibrational level of the first electronic excited state (S_1) through processes termed vibrational relaxation (10^{-12} s) and internal conversion ($S_2 \rightarrow S_1$) (10^{-6} – 10^{-12} s). From the S_1 state, the molecule can take part in two processes: a radiative relaxation to the ground state (S_0) ($S_1 \rightarrow S_0$) or a non-radiative intersystem crossing (10^{-4} – 10^{-12} s) to the triplet state (T_1) ($S_1 \rightarrow T_1$) followed by a radiative relaxation to the ground state (S_0). The former process results in the fluorescence emission whereas the latter produces phosphorescence.[25,26]

Singlet states are quantum states where spins of electrons are paired and compensated. The total spin is 0 and the spin multiplicity of the singlet sate (given by $2S+1$) is equal to 1 ($2(1/2-1/2)+1 = 1$), where S represents the total spin angular momentum of electrons.[27] The transition between singlet states is referred to as “spin allowed’’ due to paired spins of electrons in orbitals and the coupling of vibrational and electronic energy levels. On the other hand, during the intersystem crossing, the spin of the electron is reversed into a parallel position and is not paired with the ground state electron anymore. The spin multiplicity of the excited triplet state T is given by $2(1/2+1/2)+1 = 3$.[27] Because of the spin change, this transition is often referred to as “spin forbidden” and is also the reason for much longer relaxation times of molecules in triplet states. The electron loses only a negligible amount of its energy during intersystem crossing because the transition occurs only when vibrational levels of involved S and T states overlap.[28] Therefore, singlet-to-triplet states have much lower probability of occurrence than singlet-to-singlet transitions.

Fluorescence is characterised by a very short duration ($\sim 10^{-9}$ s) compared to phosphorescence ($\sim 10^{-3}$ – 10^{0} s). Fluorescence photons also carry lower energy than excitation photons due to non-radiative losses of energy in the excited state.[25,29] This shift in energies is termed Stokes shift and is represented by a red-shifted fluorescence emission spectrum with respect to the absorption spectrum of a fluorophore (Figure 4). Both spectra may display a mirror image symmetry across their overlap due to the similar spacing between vibrational levels of electronic excited states and the ground state [25,29]

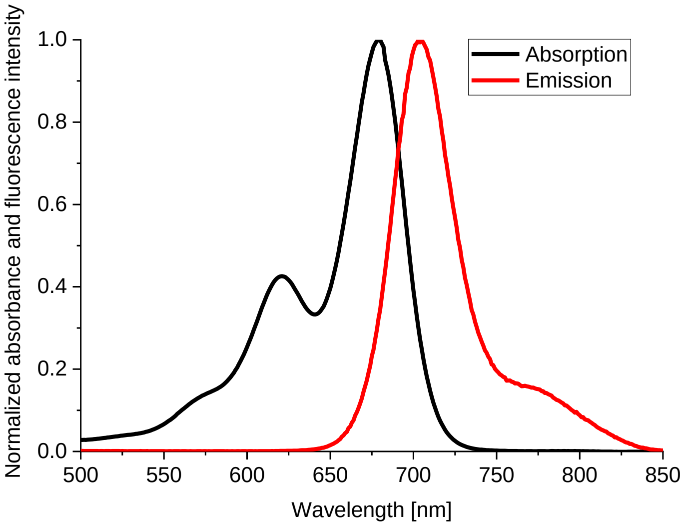

Figure 4: Normalized absorption and emission spectra of a fluorescent dye Rhodamine 800, demonstrating Stokes shift in peak wavelength positions that originates from energy losses of excited electrons experienced during their relaxation from higher electronic excited states.

1.2.1. Fluorescence Lifetime and Quantum Yield

Fluorescence is a complex multi-parameter phenomenon that allows us to study fluorescent molecules through various techniques and by combining their results, a comprehensive description of the studied problem can be gained. Two commonly investigated parameters are fluorescence lifetime and quantum yield. Fluorescent molecules can stay in the excited state only for a limited period of time. The average time which an excited fluorophore spends in the excited state before it relaxes to the ground state is termed fluorescence lifetime. Over this time period, typically on a nanosecond timescale, excited molecules can interact with their immediate environment. Such interactions may affect the lifetime and result into changes of its values that carry information about the state of the environment (polarity, concentration of quenchers, pH, energy transfers or molecular binding) or the internal state of molecules.[30,31] The main advantage of lifetime-based techniques is the relative independence of fluorescence lifetime on absorptivity and concentration of samples or the excitation intensity.

Fluorescence lifetime τ can be expressed as an inverse of the sum of all radiative (k_r) and non-radiative (k_{nr}) decay rates of radiative and non-radiative relaxation processes (Equation 14).

$$\tau = \frac{1}{k_r + k_{nr}} \qquad \textit{Equation 14}$$

In a system without non-radiative processes affecting the fluorescence lifetime, the lifetime can be described as the intrinsic lifetime (Equation 15):

$$\tau_0 = \frac{1}{k_r} \qquad \textit{Equation 15}$$

Fluorescence quantum yield is a ratio of photons generated through fluorescence to the number of photons absorbed during excitation. The mathematical definition in Equation 16 shows that quantum yield (Φ) can be defined as a ratio of the radiative decay rate and all radiative and non-radiative contributions to excited state relaxation processes.

$$\Phi = \frac{k_r}{k_r + k_{nr}} \qquad \textit{Equation 16}$$

Based on the definition of fluorescence lifetime in Equation 14 and Equation 15, the Equation 16 can be simplified to:

$$\Phi = \frac{\tau}{\tau_0} \qquad \textit{Equation 17}$$

Possible values of the quantum yield are within the interval of 0 – 1 (0 – 100%). However, in a real system, the quantum yield is always less than unity due to energy losses.

1.2.2. Fluorescence Quenching

Fluorescence quenching is a biomolecular process which causes a reduction of fluorescence intensity. Quenching occurs when an excited fluorophore is subjected to external effects such as collisions with other molecules (collisional quenching), formation of non-fluorescent complexes in the ground state (static quenching), self-quenching with its own molecules or to an energy transfer. Static quenching is a process when a fluorophore encounters a quencher and forms a non-fluorescent complex. Static quenching does not interfere with the excited state of the fluorescent molecule and so the fluorescence lifetime is unaffected.[25] Collisional (dynamic) quenching occurs when an excited fluorescent molecule experiences collisions with a quencher that can deactivate the excited state and cause a non-radiative relaxation to the ground state. The excess of energy carried by the excited fluorophore is transferred to the quencher and released as heat into its surroundings.[25] The simplest case of collisional quenching can be described by Stern-Volmer equation which shows the reduction of fluorescence intensity of a fluorophore in the presence of a quencher (Equation 18)[26].

$$\frac{I_0}{I} = 1 + K_{SV}[Q] = 1 + \tau_0 k_q [Q] \qquad \textit{Equation 18}$$

Parameters I_0 and I are fluorescence intensities measured in the absence and presence of the quencher (Q) described by its concentration [Q]. K_{SV} is the Stern-Volmer quenching constant that represents the sensitivity of the fluorophore to the quencher, τ_0 is the lifetime of the fluorophore in the absence of the quencher and k_q is the quenching rate constant.

Because the collisional quenching requires fluorophore-quencher pair to be in contact, it is a diffusion-dependent mechanism which in turn is dependent on the temperature and the viscosity of the environment.[26,32] For example, a higher temperature will increase the diffusion rate of molecules, leading to more collisions and a stronger collisional quenching. Increased temperature has an opposite effect on the static quenching because weakly bound non-fluorescent complexes may dissociate.[26] A typical example of collisional quenching is quenching by oxygen, which is a well-known and efficient quencher with diffusion-controlled behaviour.[32]

1.2.3. Förster Resonant Energy Transfer

A frequently occurring quenching process is Förster resonant energy transfer (FRET). FRET is a non-radiate contactless energy transfer from an excited fluorophore, a donor (D), to another fluorescent molecule, an acceptor (A), which is excited during the process through a dipole-dipole coupling and subsequently emits fluorescence. Because the direction of the energy transfer is from D to A, indicators of an ongoing FRET are a decrease in the fluorescence intensity and lifetime of D, accompanied by an increase in the fluorescence intensity of A.[33]

Molecular interactions such as FRET can occur only at very short distances (≤10 nm[25]) and changes in the separation distance between D and A will have a significant effect on the efficiency of FRET between the two partners.[25,33] The extent of FRET is also dependent on the mutual orientation of FRET partners and the spectral overlap between emission and absorption spectra of D and A, respectively (Figure 5).

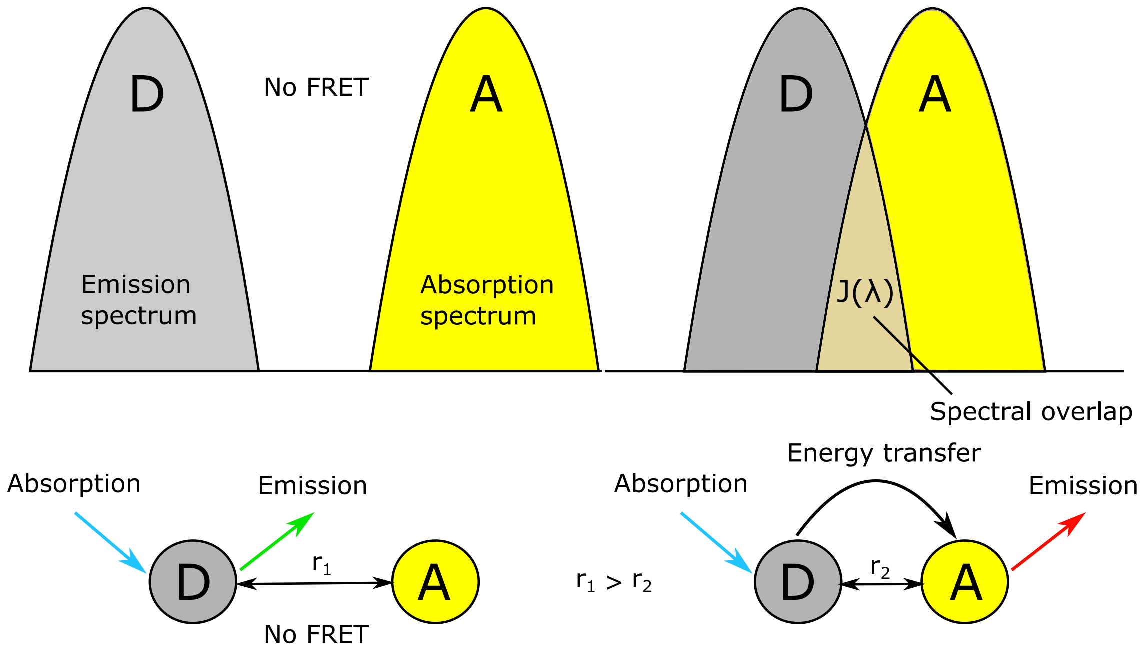

Figure 5: Schematic of FRET between the donor (D) and the acceptor (A) separated by the distance r. When r exceeds the critical distance or the absorption spectrum of A does not overlap with the emission spectrum of D, FRET does not occur (left). When the separation between D and A becomes shorter ($r_2 < r_1$) and their spectra overlap, excited D transfers its excessive energy to A which becomes excited and consequently emits fluorescence.

The FRET efficiency *E* is inversely proportional to the sixth power of the separation distance of the D-A pair (Equation 19).

$$E = \frac{1}{1 - \left(\frac{r}{R_0}\right)^6}, \qquad \textit{Equation 19}$$

Where r is the separation distance between D and A and R_0 [nm] is Förster distance. Förster distance is the distance at which the energy transfer has 50% efficiency and can be described as[33]:

$$R_0 = 0.211\{\kappa^2 n^{-4} \Phi_D J(\lambda)\}^{\frac{1}{6}}, \qquad \textit{Equation 20}$$

where κ is the orientation factor describing relative positions and orientation of transition dipole moments of D and A against the inter-fluorophore displacement vector, n is the refractive index of the medium, Φ_D is the quantum yield of the donor. $J(\lambda)$ is the degree of spectral overlap as illustrated in Figure 5 and can be described by Equation 21[33].

$$J(\lambda) = \int_0^{\propto} I_D(\lambda)\varepsilon_A(\lambda)\lambda^4 \, d\lambda, \qquad \textit{Equation 21}$$

where $I_D(\lambda)$ is the fluorescence intensity of D in the absence of A, $\varepsilon_A(\lambda)$ [$\mathrm{M}^{-1}\cdot\mathrm{cm}^{-1}$] is the extinction coefficient of A and λ [nm] is the wavelength of incident light.

The rate of the energy transfer can be described by Equation 22.

$$k_t(r) = \frac{1}{\tau_D}\left(\frac{R_0}{r}\right)^6 \qquad \textit{Equation 22}$$

Due to the high sensitivity of FRET to the distance between molecules given by the $1/r^6$ dependence, FRET has been referred to as “spectroscopic ruler“ and has become a popular tool for measuring nanoscopic distances between two fluorescent species.[25,33] It is also possible to enhance FRET if the D-A pair is in the vicinity of a metallic nanostructure that can generate SPR.[20,34,35] Ghenuche et al showed that Atto 550 (D) and Atto 647N (A) dyes, attached to a DNA strand at a fixed distance, exhibited enhanced FRET rate in the vicinity of a thin porous gold plate due to an intense EM field created within plate’s cavities.[34] Szmacinski et al demonstrated a 25-fold enhancement of FRET rate between Cy3 (D) and Cy5 (A) near silver island films and reported an exceptionally high FRET efficiency of 90 %.[35]

Resonant energy transfer is not restricted only to interactions between molecules but can also occur between fluorescent molecules and plasmonic nanostructures, causing quenching of fluorescence.[36–38] The energy transfer from fluorophores to metals is sometimes referred to as surface energy transfer (SET) and can be described through the corresponding SET model.[39] Contrary to FRET, SET is not based on resonant electronic transitions but rather on a coupling of the fluorophores’ (dipole) EM field generated upon excitation to free conduction electrons in the metal.[39] Due to the effect of the plasmon field, the distance dependence of the energy transfer rate changes to $1/r^4$.[39,40]

In this configuration, a metallic nanostructure separated from a fluorophore by the distance d acts as the acceptor (quencher), which changes the Equation 22 to:

$$k_{SET}(r) = \frac{1}{\tau_D}\left(\frac{d_0}{d}\right)^4 \qquad \textit{Equation 23}$$

Here, d_0 is the SET distance at which the SET efficiency is 50 %.

This change in the distance dependence greatly extends the effective energy transfer distance for SET measurements (up to 40 nm) compared with the conventional FRET.[41] The higher efficiency of SET at longer distances is ascribed to the dipolar coupling of the fluorophore with the cooperative effect of an array of dipoles which a metal surface can be “split” into.[39] Since the strength of the plasmon field is dependent on the size of plasmonic nanostructures, FRET and SET distances as well as the quenching efficiency will also be determined by their size and geometry.[41]

1.3. Principles of Metal-Enhanced Fluorescence

Fluorescence is an extraordinary source of information. However, even though improvements are being made, there is a need of numerous applications to overcome limitations stemming from imperfections of fluorescent dyes. A poor photostability, low quantum yield and the corresponding weak fluorescence emission are often responsible for a limited efficiency of fluorescence-based techniques. This is strongly felt, particularly in imaging and sensing fields where a high sensitivity and short detection times are of crucial importance. In order to improve these parameters, efficient means to enhance fluorescence properties of fluorophores are being sought.

The emission of fluorescent molecules is normally governed by changes in the non-radiative decay rate, arising from environmental effects, such as fluorescence quenching and energy transfers, viscosity, polarity of solvents etc. Under certain conditions, the molecular environment can be engineered to modify the radiative decay rate and enhanced fluorescence properties of fluorophores through amplification of the strength of surrounding EM fields by placing metallic nanostructures in their vicinity (Figure 6).[20,26] This process is referred to as metal-enhanced fluorescence (MEF) and has proven to be one of the key fluorescence enhancing tools in nanotechnology.

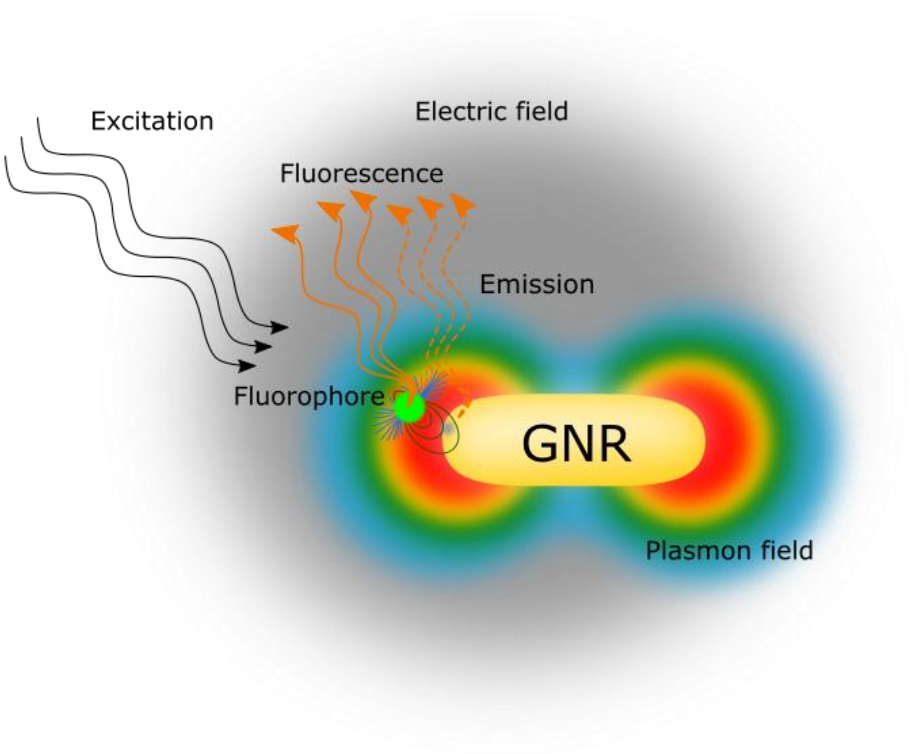

Figure 6: Schematic representation of the near-field metal-fluorophore interaction upon photoexcitation. The excited fluorophore emits fluorescence and may induce LSPR in the nearby GNR. The plasmon field enhances the local electric field which changes the fluorophore's excitation rate and emission properties and may lead to enhanced fluorescence emission or quenching.

The radiative plasmon model can be used to describe MEF.[26,42] It was mentioned before that extinction of noble metal NPs has absorption and scattering components. It has been proposed that this scattering component contributes to the observable far-field emission of metal nanostructures at the same wavelength as the incident light.[20] A fluorophore in its excited state behaves as an oscillating dipole and can induce plasmons in the nearby plasmonic nanostructure which rapidly radiate into free space with characteristics very similar to those of the fluorophore except for their very short lifetime (50 fs).[20] Because the metal's emission adopts characteristics of the excitation, it is difficult to discern which of the two species is emitting and therefore it is more convenient to consider the metal-fluorophore complex as one emitting species.[20] Fluorescence is a highly directional phenomenon which also applies to MEF. The magnitude of MEF depends on the orientation of the dipole moment and position of the fluorophore with respect to the plasmonic nanostructure. The resulting plasmon field interacts with the excited state fluorophore and influences its emission and spatial distribution of the radiated energy.[26]

Light-induced electron oscillations alter the local electric field intensity that is “felt” by the fluorophore and change its excitation rate by focusing the incident light into smaller volume near the metal surface (lightening-rod effect), which leads to a more effective excitation.[11,26,43] Thus, the metal-fluorophore relationship is reciprocal.

The effect of metal-fluorophore interactions can be further visualized using a modified Jablonski diagram for a fluorophore in the presence of a metal in Figure 7.

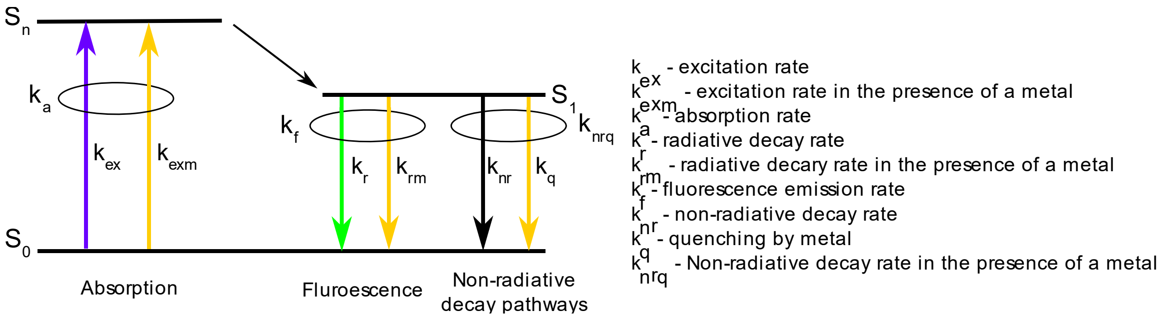

Figure 7: Simplified Jablonski diagram with indicated excitation and relaxation pathways in the presence of a plasmon field generated by the nearby metal nanostructures.

It is possible to mathematically express MEF by considering additional decay pathways that modify the fluorescence dynamics and expressing them as fluorescence lifetime (τ_m) and quantum yield (Φ_m) in the presence of a metal. Describing these changes can be done by introducing a plasmon-induced radiative rate (k_{rm}) enhancement and a non-radiative decay rate (k_q) enhancement driven by the energy transfer to the metal (Equation 24).[20]

$$\tau_m = \frac{1}{k_r + k_{rm} + k_{nr} + k_q} \qquad \textit{Equation 24}$$

If same changes are applied to the quantum yield (Equation 16), the modified expression for the fluorophore’s quantum yield in the presence of metal (Φ_m) is:

$$\Phi_m = \frac{k_r + k_{rm}}{k_r + k_{rm} + k_{nr} + k_q} \qquad \textit{Equation 25}$$

From Equation 24 and Equation 25, it is clear that in the presence of the metal, fluorescence lifetime decreases and the quantum yield increases. The decrease in fluorescence lifetime means that fluorophores can cycle through the excited state at faster rate and will emit more photons in a shorter period of time as well as be less prone to optical saturation and photobleaching.[20,44] Fluorescence lifetime is therefore a good indicator of metal-fluorophore interactions and energy transfers.[44] Additionally, the response of fluorophores is largely dependent on their intrinsic quantum yield, providing notable enhancements for fluorophores with low quantum yields but rapidly losing efficiency when the quantum yield larger than 20 %.[11,26,45]

Same as SET, MEF is highly dependent on the wavelength of the metal's plasmon band maximum and the metal-fluorophore distance. The overall fluorescence enhancement is directly proportional to the degree of spectral overlap of the plasmon band with absorption/emission spectra of the fluorophore.[46] The metal-fluorophore distance determines whether the fluorescence will be quenched or enhanced.[47] This parameter has been investigated in several studies of various plasmonic nanoparticles, and strong fluorescence enhancements were observed at distances between 5 to 25 nm.[47–51] Within this range, the emission is driven by plasmon fields, leading to the enhancement of the radiative decay rate through which the quantum yield also increases.[11] At distances <5 nm, quenching takes place due to the resonant energy transfer where the metal-enhanced non-radiative decay rate shortens the fluorophore's lifetime while the absorbed energy is dissipated as heat.[11] Fluorescence lifetime decreases in both cases, which may give the false impression that only quenching is taking place. Therefore, fluorescence intensity with respect to the blank sample should be taken into account.[50–53] At longer distances (>25 nm), this near-field effect is weak due to the limited reach of plasmons and fluorophores are decoupled from the plasmon field.[11]

Protecting fluorophores from quenching in MEF is often ensured by using biomolecular linkers such as DNA strands[38,43], polymeric spacers (typically silica)[49,50,54] or polyelectrolytes.[55]

It is clear that the metal-dye interaction is a complex process and while most models are based only on EM interactions of the fluorophore and neglect all chemical and surface interactions with metals, it is difficult to describe it with a complete electromagnetic theory.[20] The MEF includes many effects that need to be considered during the data analysis and combining the information from fluorescence lifetime analysis with fluorescence intensity measurements can provide more detailed insight into fluorophore's behaviour.

Many studies also support their experimental data with theoretical modelling and simulate situations which would otherwise be experimentally challenging.[10,51,52,56,57] There are currently three widely used numerical methods used for modelling of electrodynamics of complex systems such as metal-fluorophore and metal-metal complexes. The first method is Mie theory described earlier in this work.[20,54] The second method is the discrete-dipole approximation (DDA) which iteratively calculates the distribution of charges from a predefined initial charge distribution, allowing the charge at each point to interact with nearby charges.[20] DDA replaces solid objects of finite volumes by an array of dipoles that are separated at a fixed distance and defined by their polarizability and location, each in response to the incident field and the electric field by remaining dipoles. The result are optical cross-sections and polarizations of individual dipoles that contribute to the electric field induced by the incident field.[56,57] Near-field fluorophore-metal interactions can be calculated as well.[51] However, it is difficult to predict the relationship between far-field distribution of the radiated energy and the near-fields surrounding large NPs. The third alternative is the finite-difference time-domain (FDTD) method which provides an exact solution of Maxwell's equations and yields electric fields distribution in a direct way.[56] FDTD reduces structures of interest regardless of their size and shape to a grid, which means that it does not require reformulating integral equations for different shapes, and relies on propagation of the EM field through consecutive time steps. FDTD allows to calculate both near-field and far-field properties for metallic nanoparticles of any shape and size as well as the time-response of the structure to the incident field.[11,58] The response of the system is calculated through time steps that are shorter than the light frequency and a grid size smaller than the incident wavelength. The limitations of FDTD are the length of time steps and the grid size because the accuracy is determined by the grid-spacing and the grid must be updated after every time step. These increase the time consumption of FDTD and the computing power required for complex simulations.[20,56]

Theoretical models show that elongated nanoparticles or nanoparticles with sharp tips and edges generate stronger electromagnetic fields than smooth surfaces, which makes them potentially more effective for MEF.[10,11,20] By comparing plasmonic properties of spherical nanoparticles and GNRs, a greater effect can be achieved with GNRs if the fluorophore is aligned with their longitudinal axis and preferentially, its transition dipole moment is perpendicular to the gold surface (Figure 8).[26] The benefit of using the dominant longitudinal plasmon mode of GNRs for MEF has been demonstrated both theoretically and experimentally.[43,51] For example, GNRs have been used for enhancing the emission of Cy5-labeled single stranded DNA covalently linked to ends of GNRs through selective streptavidin-biotin linkage.[43] Up to 40-fold increase in fluorescence intensity of Cy5 was observed due to the effect of the longitudinal plasmon field of GNRs. Khatua et al. showed that fluorescence of a single molecule of fluorescent dye crystal violet, positioned near the end of an immobilized GNR, can be enhanced up to 1000-fold, including excitation rate and effective emission enhancements of ~130 and ~9, respectively.

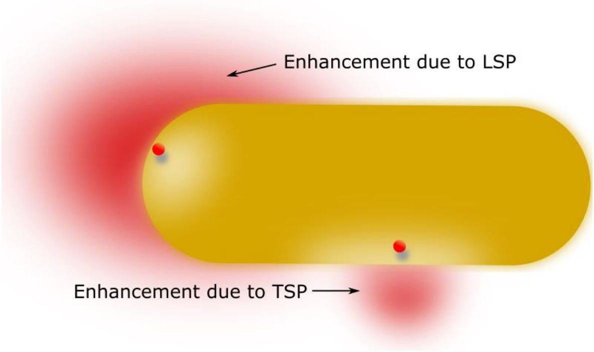

Figure 8: Schematic of the effect of longitudinal and transverse plasmon fields on the fluorescence of adjacent fluorophores.

1.4. Functionalization Strategies and Biomedical Applications of Gold Nanorods

In order to improve the performance of colloidal GNRs in various techniques or to develop new approaches, researchers have been exploring the surface chemistry of GNRs and have developed various functionalization strategies which allow to modify their surfaces with a still expanding range of ligands and biomolecules such as functional groups, nucleic acids, antibodies, enzymes or proteins.[12,59] Conjugated molecules can then serve directly as probes or imaging tools and contrast agents, linkers for the attachment of additional moieties or to overcome challenges associated with the stability and internalization of GNRs in cells.[59,60] Functionalization can be realized predominantly through two types of interactions, physical and chemical, between GNPs and ligands.[12,60] Physical (or electrostatic) interactions are simple and straightforward interactions that occur between negatively charged GNPs and positively charged molecules. Their limitation is the restriction from being able to conjugate only molecules with opposite charges and the sensitivity to environmental properties. Chemical (or covalent) interactions allow to produce robust functionalization but usually require modification of a molecule, are affected by chemical degradation and surface oxidation, or may be interfered with by other chemical groups.

A frequently used functionalization to improve the stability and biocompatibility of NPs utilizes silicon dioxide (silica, SiO_2) coating.[61] Silica is highly stable and creates pores which can be doped with therapeutic or imaging agents.[50,62] A high affinity of gold to sulphur allows covalent functionalization with thiolates and disulphides through the formation of Au-S bonds, which is useful for a direct linkage of thiolated DNA strands[38,63] or polymers such as polyethylene glycol thiol (PEG-SH).[59] PEG is popular coating agent that increases the circulation time by improving the stability of NPs in the blood stream and improves the facilitates internalization into cells by decreasing non-specific absorption of proteins.[64] Polymer coatings can be used further to conjugate biomolecules through electrostatic adsorption or hydrophobic interactions.[50,65] Similarly, charged proteins or proteins with thiol binding sites such as bovine serum albumin (BSA) can be conjugated to GNRs in order to enhance their biocompatibility.[59] In order to improve molecular or cell recognition and achieved specific targeting, binding of aptamers and antibodies to GNRs can be utilized.[59,64] Layer-by-layer polyelectrolyte overcoating of GNRs based on sequential deposition of anionic and cationic polyelectrolytes allows to tailor the surface charge to be accessible for various functional groups and functionalized biomolecules.[64] Apart from biomolecular functionalization, hard coatings of GNRs with metals[66–68], metal oxides[69] or semiconductors[70] is possible as well. A particular advantage of GNRs over other shapes stems from the asymmetrical shape which is suitable for a unique functionalization and allows site-selective deposition of ligands and polymer coatings on either their ends or sides.[43,69,71,72]

As was shown earlier, the size-dependence of optical properties of GNRs allows to control their absorption or scattering. By selecting larger GNRs with higher aspect ratios, scattering can be prioritized, making GNRs useful imaging agents as, contrary to conventional fluorophores, GNRs are not prone to photobleaching.[73] Such GNRs can be utilized as efficient scattering labels for improving contrast in dark-field microscopy of biological samples.[60] There have also been reports of GNRs in photoacoustic imaging where GNRs can serve as contrast agents for tumour imaging or image-guided therapy.[74] In general, due to their tunable LSPR which allows to tailor the absorption across Vis and near-infra red (NIR) spectrum, GNRs are good candidates for applications in cells and *in vivo* research which benefit from working in the optical window (650-1350 nm) where absorption and scattering by blood and tissues are reduced, increasing the penetration depth of incident light.[74,75] Appropriate functionalization then allows targeted imaging and even multiplexed visualization of various cancer cell types.[74] GNRs can undergo two-photon luminescence with fluorescence lifetimes shorter that those of most fluorophores, providing a high-contrast agents for fluorescence and fluorescence lifetime imaging microscopy of cells.[36,73,76]

In diagnostics and therapy, surface functionalization of NPs is essential in order to selectively target areas of interest and achieve specific interactions with cells or biomolecules.[59,64] In diagnostics, being based on visualization methods, the recognition of biological and chemical agents uses GNRs primarily as contrast agents[60] or fluorescence-enhancing carriers.[36,38] In therapy, GNRs have been used as versatile carriers for targeted therapy and drug delivery.[59,64,77] GNRs have also shown great promise as therapeutic agents in plasmonic photothermal therapy based on local heating of optically excited GNRs accumulated within tumours and inducing localized hyperthermia followed by a thermal destruction of cancer cells.[21,59,60] Another therapeutic technique in oncology where GNRs found their use as carriers is photodynamic therapy (PDT), where the LSPR of GNRs improves the generation of cytotoxic reactive oxygen species by nearby photosensitizers which disrupt cells in the area of interest.[62,78]

1.5. Plasmonic Substrates in Metal-enhanced Fluorescence

When determining the type of nanostructure and the method of fabrication, it should be done so by considering the desired outcome. The design of a nanostructure plays a critical role in determining its applicability in MEF, as it defines its optical as well as surface properties. The resulting EM field enhancement generated near metallic surfaces is then directly responsible for the scale at which photophysical properties of nearby molecules will be affected. Thus, the main goal when designing plasmonic substrates is to achieve high field intensity enhancements upon excitation of SPR in combination with suitable surface characteristics that will allow easy manipulation through a simple fabrication method.

Apart from gold and silver, which are the most frequently used metals for plasmonic platforms in Vis and NIR regions, in the UV plasmonics, aluminium is usually the metal of choice. Although silver supports a good quality SPR,[79] a major disadvantage of silver is its chemical instability and degradation through oxidation processes, which could presents a toxicologic problem when applied in cells as well as may damage the surface functionalization or cause an early release of carried molecules and drugs.[80] This is why gold is commonly preferred over silver for biological applications. Aluminium is a simple and a cost-effective solution with a broad SPR tunable across UV-Vis-NIR region of spectrum due to its high abundance, stability by forming a protective surface oxidation layer, and simplicity of processing.[79,81] The attractiveness of the UV SPR of aluminium for plasmonic applications stems primarily from the need to analyse biomolecules or biological systems which exhibit intrinsic photophysical characteristics in the UV.

It has been shown on the example of GNRs that plasmonic NPs are versatile nanostructures with a tremendous potential for improving the efficiency of a large number of existing biomedical and photophysical techniques. An unavoidable limitation of colloidal NPs is that they operate strictly as individual blocks with great separation distance between individual NPs. This restricts them from cooperating and combining their LSPRs to achieve greater EM field enhancements and consequently inducing stronger fluorescence emission. Various types of nanostructures and nanostructured substrates have been developed for this purpose.[11] The structurally simplest one could be considered an assembly of NPs into more complex assemblies such as dimers where plasmon fields of both nanostructures undergo near-field coupling in the gap between dimer partners, establishing a new plasmon mode and creating hot spots of localized high-intensity EM field.[52,82–85] This strong EM field can dramatically amplify the fluorescence emission of a fluorophore situated in the gap.[52,82,86] Some dimer and higher-order assemblies can still be produced in colloids through chemical routes,[82–84,87] but the functionalization process is often challenging due to the difficult linkage of the fluorophore into hot spots within the assembly. This is why most approaches rely on nanostructured planar substrates and periodical arrays of plasmonic nanostructures.

1.5.1. Metallic Films

Metallic films usually exhibit non-periodical roughness or particulate surfaces with topography dependent spatial distribution of EM fields.[11,20,88,89] Metallic islands made of randomly distributed NPs offer a simple solution for nanostructuring of continuous surfaces to obtain fluorescence-enhancing substrates in UV-Vis.[11,20,88,89] Silver island films (SIFs) and gold particulate films produced by a vapour deposition of metals on quartz substrates have been shown to cause fluorescence enhancements of fluorophores, quantum dots and proteins.[20,81,90] Hsu et al. recently showed that by utilizing a seed-mediated growth process and by varying the deposition time of silver, nanogaps between NPs of SIFs can be adjusted to increase the EM field intensity in nanogaps.[89] Through a regioselective modification of the substrate, an increased fluorescence enhancement of a NIR dye IR800 immobilized within nanogaps was observed.[89] Similar approaches to SIFs have be used to prepare particulate Al films for the fluorescence enhancement of proteins such as BSA, streptavidin, and immunoglobulin G[91] or a DNA base analogue 2-AP and a coumarin derivative 7-HC[88] in the UV-Vis. While studies involving roughened and particulate substrates are still being performed, the difficulty to predict EM fields and fluorescence enhancements due to the inhomogeneous distribution and varying geometry of surface features[89] has led to the transition to substrates with finely controlled optical properties produced by different nanofabrication processes.

1.5.2. Periodic Nanostructured Substrates

Modern nanofabrication techniques are powerful tools for producing an extensive range of nanostructured plasmonic substrates[4,92,93] with various shapes, sizes and organisation of surface features that can be tailored to specific MEF studies on individual molecules. Periodic arrays of metallic nanostructures allow tuning of the EM field intensity through the shape and the distance between individual surface features.[11] The ability to tailor optical properties of patterned plasmonic surfaces with large surface areas on demand has been demonstrated as crucial for the development of optical devices and sensors.[11,81]

Compared to the LSPR of individual colloidal NPs and surface plasmons on continuous surfaces, periodic arrays provide an additional pathway to achieve desired field enhancements by supporting diffractive coupling between neighbouring nanostructures that causes generation of collective (lattice) localized surface plasmons.[94] This interaction originates from phase matching of localized surface plasmons at wavelengths that coincide with the LSPR of individual nanostructures, being particularly strong for their symmetrical arrays.[11,95] For example, an alternative to nanoparticle dimers was reported by Kinkhabwala et al. who investigated the enhancement capability of a dimer nanostructure termed bow tie nanoantenna composed of two nanotriangles created by electron-beam lithography.[52] The array of bowties was coated with a thin layer of poly(methyl methacrylate) doped with an NIR fluorescent dye TPQDI. Fluorescence enhancement that was observed for a single molecule of TPQDI in the tunable gap was enhanced by a factor of ~1340, which remains to be one of the highest single-molecule fluorescence enhancements achieved to date. The high enhancement was attributed to the triangle geometry which allows to concentrate the plasmon field intensity more efficiently at tips. As was demonstrated by the above study, electron beam lithography is a powerful technique which allows to fabricate a structurally diverse nanostructures with high precision and flexibility. However, these are sometimes outweighed by the low throughput and high running cost, making them more suitable for research rather than for a large-scale fabrication. A different method which allows producing NP arrays over large-surface areas that are active in Vis-NIR spectral region is colloidal (or nanosphere) lithography.[96,97] The method utilizes self-assembled monolayers of spherical NPs (polystyrene or silica) on a flat substrate followed by a deposition of metallic layers. For example, this method have been used for the fabrication of an ordered array of copper nanostructures with a strong LSPR generation which induced fluorescence enhancement of a porphyrin dye and indocyanine green by tuning the LSPR via the diameter of the spherical template and spacer interlayers.[96] By depositing a thin layer of plasmonic metal onto the spherical template and a subsequent removal of the template, a bow-tie-like plasmonic array of circularly arranged nanotriangles capable of up 100-fold fluorescence enhancement of a red fluorescent dye’s IRIS-5 emission can be produced as well.[98] The LSPR and hot spots between triangles can be tuned though dimension of the template and thickness of the spacer layer. Arrays of Au nanodiscs with tunable plasmonic properties and fluorescence enhancements in Vis-NIR can be produced by templating via self-assembly of colloidal spheres on a metallic film followed by a reactive ion milling around the template.[99]

Periodically patterned metallic films with inverse architectures are an alternative mean for improving photophysical properties of fluorophores through diffraction.[11,100,101] Patterns such as gratings, nanoholes and nanovoids exhibit good coupling efficiency and can be produced controllably across large surface areas, which makes them suitable for a planar integration in conventional microscope setups or spectroscopic devices.[100,102,103] By manipulating the dimension of a pattern, a better coupling of surface plasmons and incident light can be achieved and consequently, a greater improvement of fluorescence emission.[100] The SPR of gratings and the corresponding fluorescence enhancement can be controlled by adjusting the grating profile and enhancement factors as high as ~13-100x in Vis have been observed.[11,100,102] However, gratings underperform in fluorescence imaging with cone-shaped non-polarized light, as SPR is excited only from a resonant angle and other angles are ineffective.[102] Nanoholes, exhibit a more efficient coupling to excitation light and provide increased fluorescence sensitivity, with optical properties and fluorescence enhancements controlled by adjusting the symmetry and dimensions of nanoholes.[100,104] Fluorescence enhancement factors up to ~110 have been achieved with nanohole arrays.[11] An exceptionally high fluorescence enhancement of up to ~1600-fold for Alexa Fluor 647 was observed by Zhang et al. on a gold nanohole array fabricated by nanoimprinting from a sandwich immunoassay for the detection of prostate-specific antigen.[105] While an enhancement of up to 10-fold was achieved from surface plasmons at the top surface, an enhancement of 100-fold was observed when only localized surface plasmons at rims were excited, which increased 16-fold upon simultaneous excitation of localized plasmons and surface plasmons. It was shown that the ability to control the co-excitation of various classes of surface plasmons has a tremendous potential for maximizing the MEF effect.

The last group of periodical patterned surface with inverse nanostructures are plasmonic 3D nanovoids. These can be prepared either on the surface of a substrate or embedded in the substrate, taking form of nanocups,[106] nanodishes,[107,108] nanocones,[109] or spherical bowl-like architectures[101,110–116]. The variety of shapes also reflects the range of respective nanofabrication methods capable of producing them with various dimensions (~100 nm – 3 μm) such as nanoimprint lithography (nanodishes),[107,108] molding with nanopillars (nanocups),[106] electrochemical templating via anodizing of aluminium (nanocones, spherical nanovoids)[109,117,118] and templating via colloidal lithography (spherical nanovoids),[119–123] some of which are followed by a deposition of plasmonic metals to create a plasmonic surface. Adding an extra dimension to surface features further extends the range of optical properties of nanovoid architectures and gives rise to intriguing size-dependent characteristics such as generation of localized and delocalized plasmons or light trapping,[101,113,124] all of which are particularly attractive for MEF and have mediated various fluorescence enhancements (2 – 170-fold) in Vis-NIR.[103,106,118–120,123,125] Furthermore, nanovoids can serve as reaction vessels and nanomolds for the templated manufacturing of nanostructures, where the distribution of surface features across large surface areas are critical. The applicability of NBs in this area has been demonstrated on the fabrication of quantum dots and semiconductor nanopillars,[126] gold nanoparticle arrays,[114,127] silver islands and nanocluster arrays,[93] silver nanostructures[115,116,128], and TiO_2 nanorods[112].

1.6. Thesis Summary

The overall aim of this project was to fabricate plasmonic nanostructures that exhibit characteristics suitable for metal-enhanced photophysical phenomena as well as to investigate the phenomenon of metal-enhanced fluorescence on various metallic substrates in the UV and visible spectral regions using fluorescent protein complexes and gold nanoclusters. Growth mechanisms and fabrication methodologies are presented for produced nanostructures and the information critical for their manufacturing and usage is highlighted.

Chapter 2 details main experimental techniques and related instrumentation employed to carry out the research presented in this work. The Chapter describes techniques used for the characterization of produced nanostructures as well as the theoretical and technical background behind spectroscopic and microscopic methods used for optical and structural measurements.

Chapter 3 investigates the mechanism of the anisotropic coating of GNRs with silica and provides a comprehensive description of the effect of reaction parameters on the coating's morphology, demonstrating a high-yield synthesis of end-coated, dumbbell-like GNRs with characteristics suitable for fluorescence/scattering amplifiers or plasmon-enhanced catalysis.

Chapter 4 investigates the use of a commercial aluminium foil as a low-cost substrate for MEF in UV and visible regions of spectrum by utilizing fluorescent protein bovine serum albumin (BSA) and bovine serum albumin-encapsulated gold nanoclusters (BSA-AuNCs) as probe molecules and reveals opposite effects of the two sides of the aluminium foil, where the matt side supported fluorescence enhancement in UV-blue spectral region whereas the shiny side induced a decrease of fluorescence emission. Underlying mechanisms are discussed.

Chapter 5 presents a fabrication and a complex analysis of optical properties of plasmonic arrays of Au nanobowls of various diameters, produced by the electrochemical templating via anodizing of aluminium and an Au deposition. Based on structural characteristics, size- and excitation-dependent optical properties as well as decreased reflectance in UV and visible spectrum, the study further discusses the applicability of Au nanobowl arrays as broadband plasmonic platforms in MEF within this spectral region.

Chapter 6 demonstrates the use of selected Au nanobowl arrays in a broadband MEF via fluorescence spectroscopy of BSA-AuNCs in the UV and visible spectrum under varying excitation conditions. Fluorescence enhancement was observed and the mechanism of MEF in relation to characteristics of employed Au nanobowls was discussed.

In the final chapter, major findings of the presented work are summarized, including a discussion of potential future areas of research based on projects in this thesis.

2. Experimental Methodology

2.1. UV-Vis Spectroscopy

UV-Vis spectroscopy (or absorption spectroscopy) is a quantitative technique used for determining the absorptivity of an illuminated sample at a given wavelength. Absorption measurements therefore precede fluorescence measurements to identify absorption band(s) of a specimen and the range of wavelengths for the most efficient excitation. This information is acquired by comparing the intensity of light which passed through a sample of interest $I(\lambda)$ to the intensity of incident light $I_0(\lambda)$. The ratio of the two intensities is referred to as transmission ($T(\lambda)$) (Equation 26) and can be used to calculate absorbance A at each wavelength λ ($A(\lambda)$) (Equation 27).

$$T(\lambda) = \frac{I(\lambda)}{I_0(\lambda)} \qquad \textit{Equation 26}$$

$$A(\lambda) = \log\frac{I_0(\lambda)}{I(\lambda)} = -\log T(\lambda) \qquad \textit{Equation 27}$$

From the known value of absorbance, the concentration of the measured substance can be calculated using following the Beer-Lambert law (Equation 28). This law states that the absorbance of a substance is dependent on three parameters that are responsible for the attenuation of light as it passes through the sample. These parameters are the optical path length l, the molar concentration of the measured substance c and the molar extinction coefficient $\varepsilon(\lambda)$ ($M^{-1}cm^{-1}$):

$$A(\lambda) = \varepsilon(\lambda) \cdot l \cdot c \qquad \textit{Equation 28}$$

Determining the molar concentration of GNRs from extinction spectra is more complicated because their molar extinction coefficients are shape- and size-dependent. Therefore, an extinction spectrum also reflects the size distribution of GNRs within the solution. Extinction coefficients as well as absorption spectra can be calculated through theoretical models and can be directly compared with the experimental data.[57,129] Then, the Beer-Lambert law can be applied and the molar concentration of GNRs calculated.

The device used for the acquisition of absorption spectra is an absorption spectrometer. Figure 9 shows a schematic diagram of a typical absorption spectrometer PerkinElmer

Lambda 2 UV-Vis with dual sample chamber.[130] The instrument contains deuterium (190 – 330 nm) and halogen (330 – 1100 nm) lamps which cover the working wavelength range of the spectrometer. The light is guided by a set of mirrors to the monochromator where wavelengths are gradually selected so that measured samples are exposed to one wavelength at the time until the absorbance from the selected wavelength range has been acquired. The beam of light is split into two separate beams by the beam splitter, and they are guided to the reference sample and the measured sample for the simultaneous acquisition of corresponding intensities. The reference signal is taken to compensate for the absorption by the solvent and the cuvette which contains the sample. The absorbance is then derived from the difference between signals produced on both detectors.

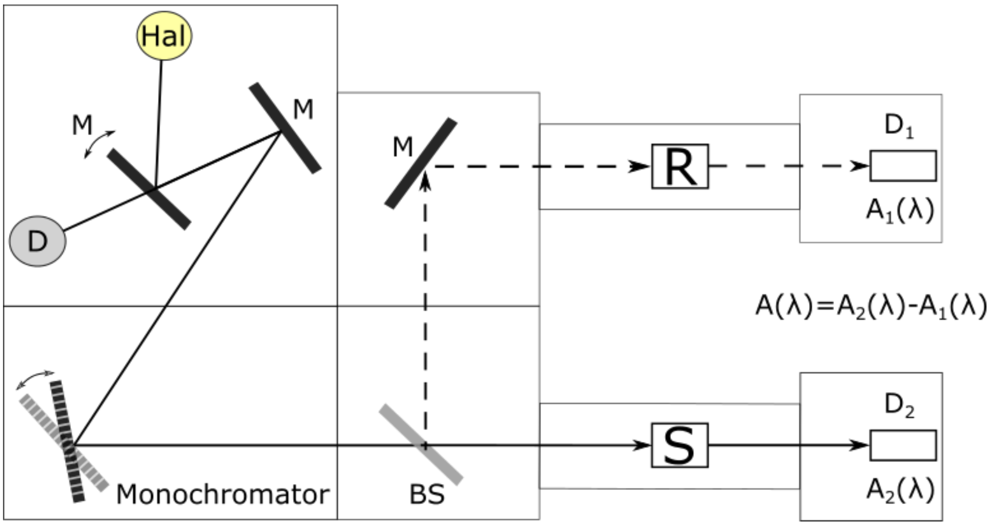

Figure 9: Schematic of a Perkin Elmer Lambda 2 absorption spectrometer. The radiation generated by deuterium (D) (190 – 330 nm) and halogen (Hal) (330 – 1100 nm) lamps is guided by mirrors (M) to the monochromator and then through the beam splitter (BS) to reference (R) and measured (S) samples and finally to corresponding detectors (D_1, D_2). Adapted from [130].

2.2. Steady-state Fluorescence Spectroscopy

Steady-state fluorescence measurements serve for the acquisition of fluorescence intensity and fluorescence emission spectra of a specimen under a continuous illumination. A fluorescence emission spectrum is a representation of the average fluorescence intensity measured over a range of emission wavelengths at a constant excitation wavelength.

Fluorescence emission spectra can be collected using a spectrofluorometer such as HORIBA Fluorolog-3 illustrated in Figure 10. Fluorolog-3 is a modular system that is composed of an excitation source housing, two single-grating monochromators, sample chamber and photomultiplier detector. The excitation source is a 450W xenon lamp that produces a continuum of light from UV to NIR. The lamp light passes through the excitation monochromator which houses a set of mirrors and a diffraction grating that isolates only the selected wavelength needed for the excitation and filters out the rest. Then, the excitation light enters the sample chamber and illuminates the sample. To monitor and compensate for variations in the xenon lamp output, a small fraction of the excitation light is diverted to the reference detector (silicon photodiode).[131] Fluorescence emission is collected at an angle of 90 ° to avoid detection of excitation and reflected light. Then, it enters the emission monochromator which allows only the selected range of emission wavelengths to pass onto the detector. The detector is a R928P photomultiplier tube (PMT) suitable for a sensitive spectral characterization in the UV-VIS-NIR.

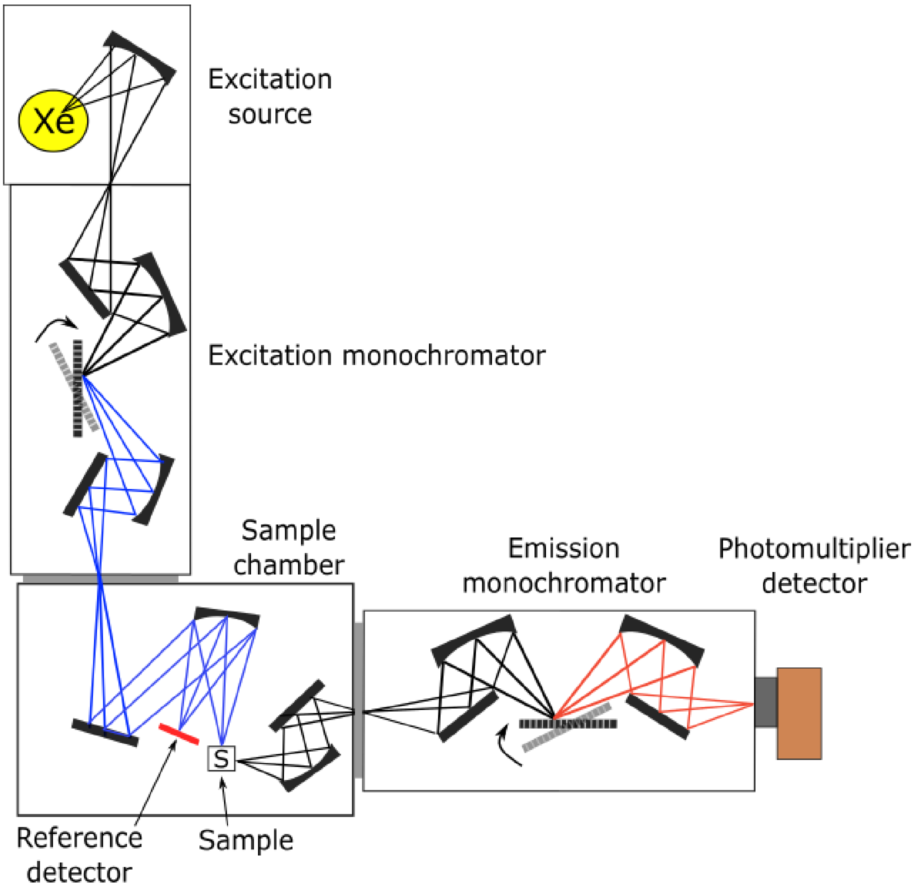

Figure 10: Schematic diagram of the HORIBA Fluorolog-3 spectrofluorometer. Adapted from [131].

2.3. Time-resolved Fluorescence Spectroscopy

Time-resolved fluorescence measurements are based on the acquisition of fluorescence lifetimes from measured specimens. Combined with steady-state measurements, this technique provides an additional information about the specimen and its molecular environment. Fluorescence lifetime spectroscopy can be divided into two techniques with different approaches of measuring fluorescence lifetimes depending on the mechanism of the signal generation –frequency-domain and time-domain measurements. Frequency-domain (phase-modulated) measurements are based on the harmonic modulation of the excitation light intensity at high frequency.[26] The resulting fluorescence emission has the same frequency as the excitation light but is phase-shifted (delayed) and demodulated due to the lifetime.[26] The lifetime is determined either from the phase shift or from the modulation depth (peak-to-peak height of the emission with respect to that of the excitation light) of the emission signal.[25] Frequency domain measurements are beyond the scope of this work and only the time-domain technique will be discussed further.

Time-correlated single photon counting (TCSPC) is the main technique that will be used for the acquisition of fluorescence lifetimes in this work. TCSPC is a high-precision technique with a single-photon sensitivity that allows to measure fluorescence lifetimes on a picosecond scale.[132] The method is based on measuring photon arrival times after a pulsed excitation of a fluorophore. The sample is excited by a sequence of very short laser pulses generated by a laser diode or an LED. As a response, the fluorophore emits a fluorescence photon of which the arrival time on the detector is registered and the time delay between the excitation and the photon arrival on the detector is registered. The precise detection is achieved by using sensitive detectors such as a PMT. Arrival times are sorted into a histogram of occurrences over arrival times after excitation (Figure 11).

The principle of TCSPC and the acquisition of fluorescence decays are illustrated in Figure 11. Each excitation cycle is triggered by a reference signal sent from the excitation source the moment each excitation pulse is released. The measurement cycle is terminated when a fluorescence photon arrives on the detector. Arrival times are accurately measured by constant fraction discriminators (CFD) which pass registered signals to a time-to-amplitude converter (TAC). TAC contains a capacitor that charges when the reference

(START) signal is registered and stops upon arrival of the fluorescence photon (STOP). The accumulated charge is converted to a voltage output that is proportional to the time delay in the given cycle. If a fluorescence photon is not generated in the given cycle, the voltage ramp will reach the pre-set threshold and the TAC voltage is reset to zero. The TAC signal is amplified and sent to an analogue-to-digital converter (ADC) which converts the analogue representation of the time delay to a digital form. A multi-channel analyser (MCA) stores the digital signal into the corresponding time channel of the histogram as an individual event. A complete histogram is formed after many repetitions of the described process until a pre-set number of counts has been collected (typically 10 000 counts in the peak[133,134]).

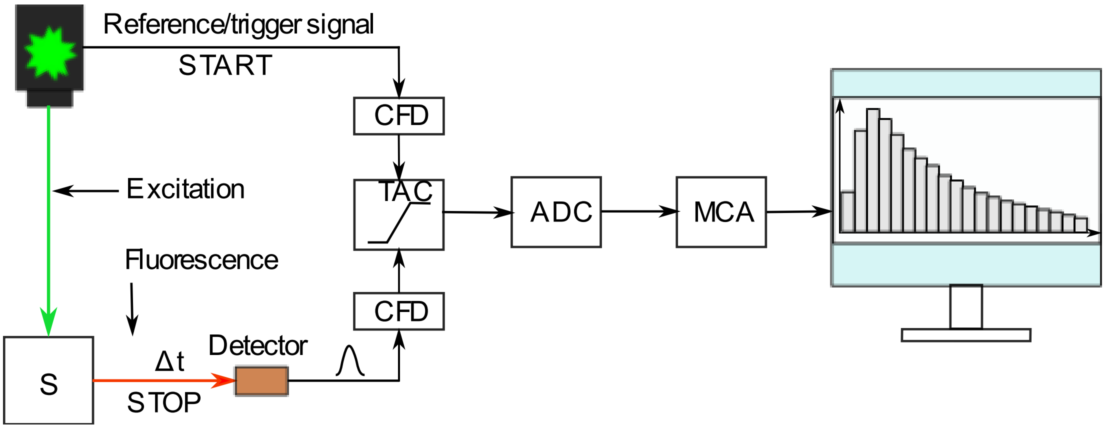

Figure 11: Principle of TCSPC and the acquisition of fluorescence decays. The light source generates a light pulse which is registered by the timing electronics as a START signal of the measurement. The STOP signal is represented by the registered (delayed) fluorescence photon. Timing electronics converts the delay time to voltage which is then converted to a digital information and stored as a photon count in a histogram of coincidences. S represents measured sample, CFD constant fraction discriminator, TAC time-to-amplitude converter, ADC analogue-to-digital converter, MCA multi-channel analyser.

Despite the fast single-photon performance, detectors are limited by their "dead time" (μs – ns)[132] for which they are recovering from the previously detected photon. During this period, any other photon arriving in the same cycle remains undetected and the information is lost.[135,136] The highest probability of detecting a photon is shortly after the excitation. Detecting several photons in one excitation cycle would cause distortion of the histogram and a shift of fluorescence decays to shorter times (pile-up effect). The pile-up effect can be prevented by exciting the sample with low-amplitude pulses, which individually may not lead to the excitation of the sample. This keeps the probability of photon detection in each cycle low; approximately 1 fluorescence photon per 100 excitation pulses. Experimentally, the detector count rate is kept below 2 %.[137] Modern systems currently operate with detectors that are capable of detecting multiple photons in one excitation cycle.[132] If the probability of the photon detection were above the threshold, the TAC could be constantly reset and the data would be lost. This drawback can be bypassed by measuring with the TAC in a reverse mode where the START and STOP signals are generated by the fluorescence photon and the following excitation pulse, respectively.

Figure 12 shows the architecture of a TCSPC instrument HORIBA DeltaFlex. The system consists of an excitation source, sample chamber, automated excitation and emission polarizers, emission monochromator and a detector connected to the timing electronics. The setup can be controlled through the software DAS6 (Horiba) installed on a control PC. The fluorescence emission is collected at an angle of 90 ° and is led through the vertically oriented emission polarizer that is set to the “magic angle” of 54.7 °[26]. Measuring under the magic angle when using polarised light sources eliminates the component from depolarisation effects (FRET, molecular rotation)[138] which could otherwise cause the decay to appear more complex.[133,139] The sample chamber also contains holders where optical filters can be mounted to filter excitation/emission wavelengths or to reduce scattered light. Neutral density filters can be also used to keep the detector count rate in the required range (<2 %). The emission monochromator is used to filter unwanted wavelengths from the collected emission and can be also used to control the intensity of the emission by changing the width of its entrance and exit slits.

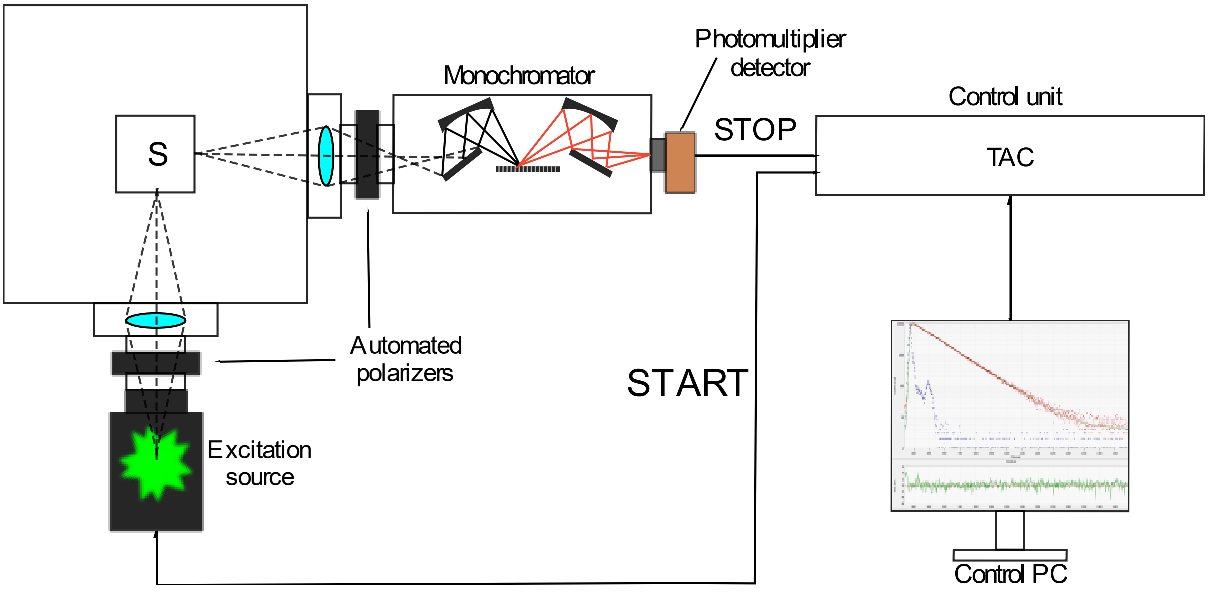

Figure 12: Schematic of HORIBA Delta Flex TCSPC device and the TCSPC process. A light pulse from the excitation source sends a START signal which starts the signal electronics and excites the sample (S). The detection of a fluorescence photon stops the timing electronics. Delay times are converted to a voltage and consequently to a digital signal, which is then stored in a histogram of count events.

Before each measurement, a response of the instrumentation to the excitation pulse (instrument response function – IRF) must be recorded in order to extract fluorescence lifetimes from the recorded decay curve. The IRF (blue curve in Figure 13) represents the timing resolution of a TCSPC system and is obtained by collecting scattered excitation light at the excitation wavelength from a scattering medium (typically LUDOX SM-AS solution of colloidal silica particles). In the ideal case, an IRF recorded as a response of the ideal TCSPC instrumentation to a δ function would be infinitely narrow.[26,132] In reality, excitation sources, the electronics and optical components are imperfect and affect the passing light, causing broadening of the IRF.[133]

2.3.1. Fluorescence Lifetime Analysis

When a population of molecules M is excited by absorption of incident photons, the excited state population M^* decays to the ground state accompanied by the emission of fluorescence via non-radiative and radiative processes per following rate equation[25]:

$$\frac{d[M^*]}{dt} = -(k_r + k_{nr})[M^*] \qquad \textit{Equation 29}$$

By integrating this equation and using the mathematical definition of fluorescence lifetime from Equation 14, the fluorescence impulse response to the excitation δ-pulse at t=0 can be gained:

$$I(t) = I_0 e^{-\frac{t}{\tau}} \qquad \textit{Equation 30}$$

where *I(t)* is the fluorescence intensity and I_0 is the fluorescence intensity at $t = 0$, *t* is the time after excitation and τ is the fluorescence lifetime. In terms of the intensity decay, τ is the time at which the intensity of the fluorophore decays to *1/e* (~37 %) of its peak value. Equation 30 applies to a simple mono-exponential decay. However, many fluorescent systems exhibit a complex multi-exponential behaviour, and the use of a multi-exponential fitting function may be required to describe them. For a multi-exponential system, the Equation 30 changes into a sum of exponentials:

$$I(t) = \sum_{i=1}^{n} \alpha_i e^{-\frac{t}{\tau_i}} \qquad \textit{Equation 31}$$

where *n* is the number of contributing components and α_i and τ_i are their amplitudes and lifetimes, respectively.

Due to imperfections of the instrumentation, measured fluorescence decay is a convolution of the exponential fluorescence decay with the IRF. Therefore, decay parameters cannot be obtained directly from measured data. The measured fluorescence decay *F(t)*is a convolution of the true fluorescence decay function *(I(t))* and the IRF (*P(t)*) (Equation 32)[25,26]

$$F(t) = I(t) \otimes P(t), \qquad \textit{Equation 32}$$

where ⊗ denotes the convolution.

If a fluorophore is excited by a series of excitation *δ* pulses, the intensity of the measured fluorescence function *F(t)* will increase proportionately to the height of *δ* pulses where each pulse generates an impulse response (*j(t)*) at different delay times.[26] The sum of individual responses to these *δ* pulses represents the measured fluorescence decay which can be expressed using the convolution integral:

$$F(t) = \oint_{t'=0}^{t} P(t')j(t-t')dt' \qquad \textit{Equation 33}$$

The parameter t' is the time of excitation, $t - t'$ is the timing interval in which fluorescence photons are generated after excitation.

Obtaining fluorescence lifetimes is possible if the reconvolution is applied to the measured fluorescence decay. The reconvolution is an iterative process, where the selected exponential model is convoluted with the pre-recorded IRF and then, the resulting function is compared with the experimental data. This process is repeated until a model that best fits the experimental data is found and the difference between measured and calculated parameters (lifetime and pre-exponential factors) is minimal.[26,133,138]

The model (F_D) that is fitted to the measured fluorescence decay data is described as[140]

$$F_D(t) = A + B_i e^{-\frac{t}{\tau_i}} \qquad \textit{Equation 34}$$

The integer "i" denotes individual exponential components and parameters A and B_i represent the background offset and the pre-exponential factor (the intensity contribution of the given lifetime component), respectively.

The quality of the fit, a degree of how well the selected model $F_D(k)$ matches with the measured data $Y(k)$ for each channel k, can be determined via the non-linear least squares analysis (NLLS). The goal is to find the best matching results by minimizing the indicator of the goodness of fit χ^2:

$$\chi^2 = \sum_{k=1}^{N} \frac{[Y(k) - F_D(k)\,]^2}{\sigma(k)^2} \qquad \textit{Equation 35}$$

The $\sigma(k)$ represents the expected standard deviation of $Y(k)$, $Y(k) - F_D(k)$ is the deviation of the model from the experimental data at each channel and N is the number of data channels used in the analysis. The value of the χ^2 parameter for a perfect fit should be close to 1.0,[26,133] but the interval $0.9 \leq \chi^2 \geq 1.25$ is generally accepted.[133] The advantage of the TCSPC is the known Poisson statistical distribution of the data. This allows to easily determine the standard deviation as $\sigma(k) = \sqrt{Y(k)}$. From $\sigma(k) = \sqrt{Y(k)}$, it is clear that σ becomes less significant and the precision increases with increasing number of collected counts.

The goodness-of-fit parameter χ^2 is not the only indicator of the quality of the fit. Weighted residuals (*R(k)*) shown as green curve in Figure 13 and described by Equation 36 are also obtained from the fit and graphically represent the deviation of the selected theoretical model from measured data as well as areas of mismatch.[140] This is particularly useful when dealing with multi-exponential decays as residuals will indicate whether the selected model is acceptable or a different one should be applied.[26,133] A good fit is indicated by weighted residuals that are randomly distributed around 0.[26]

$$R(k) = \frac{Y(k) - F_D(k)}{\sigma(k)} \qquad \textit{Equation 36}$$

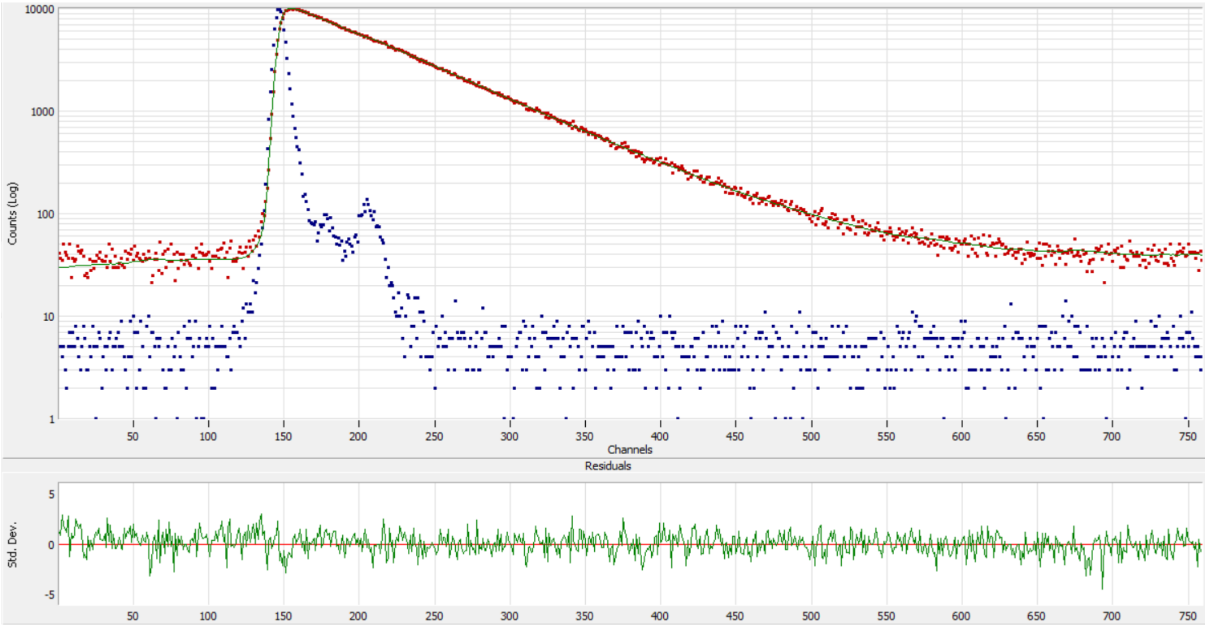

Figure 13: Typical fluorescent decay of a fluorescent dye Rhodamine 800 (red) with the IRF (blue) and the fitted model to the experimental data (green curve in top window). Bottom part shows randomly distributed weighted residuals indicating a good fit with χ^2~1.12.

2.4. Electron Microscopy

Electron microscopy is a high-resolution imaging technique used for characterizing structural details of biological and non-biological specimens. Instead of using EM radiation, a focused beam of accelerated electrons is used for illumination. The high resolution is achieved through the high acceleration voltage of electrons (~10× kV – ~100× kV) with much shorter wavelengths compared to the conventional light microscopy techniques.[141] The magnification that can be achieved with electron microscopy due to high-energy electrons can reach $10^6\times$.[142]

High-energy electrons produce a variety of signals generated from electron-specimen interactions which provide a broad scope of information. Based on the method of image acquisition and the character of interactions of the primary electron beam with the analysed object (Figure 14), the electron microscopy can be divided into three main types: transmission electron microscopy (TEM), scanning electron microscopy (SEM) and scanning transmission electron microscopy (STEM).

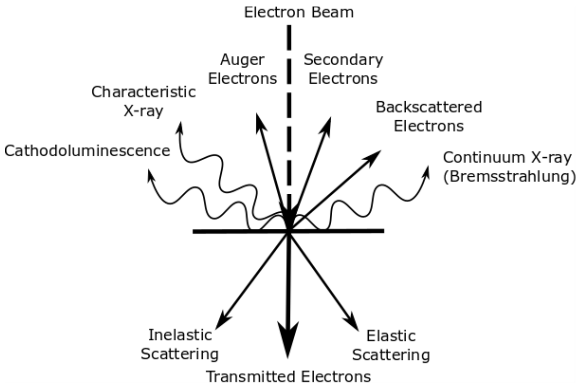

Figure 14: Schematic of signals produced by electron-sample interactions that may occur in electron microscopy. Adapted from [143].

Electron microscopy has been applied in this work for the structural characterization of silica-coated GNRs (SEM, TEM, STEM) and metallic Al and Au substrates (SEM) used for MEF experiments. Due to the conductive nature of these samples, the sample preparation consisted of only attaching either carbon TEM grids loaded with silica-coated GNRs or metal stubs with attached metallic substrates to the imaging stage.

2.4.1. Scanning Electron Microscopy (SEM)

SEM is a non-destructive imaging method employed for the characterization of surface topography and morphology, crystalline structure, and chemical composition of a specimen by detecting signals that originated from interactions of the electron beam with the specimen's surface. The image is generated by scanning the incident electron beam (typically 2 – 40 keV)[142] across the selected area in a raster and the information is assembled pixel-by-pixel which corresponds to individual scanned spots that are correlated with the position of the beam. A typical SEM utilizes secondary and backscattered electrons, but additional techniques may be used to expand the scope of registered information.[142,143] Secondary electrons are electrons that were knocked out of their orbits by incident electrons and escaped the sample with energies <50 eV.[142] These provide images with high spatial resolution and carry information about the topography because they emerge from shallow areas near the surface. Backscattered electrons are incident electrons that have been scattered near the nuclei at large angles and escaped the surface still carrying a large portion of their original energy. The analysis of backscattered electrons provides information about the composition and the crystalline structure.

Figure 15 shows a schematic of a field-emission environmental scanning electron microscope FEI Quanta 250 FEG-ESEM. The source of electrons is the field emission gun (FEG) with a tungsten needle. Electrons are extracted from the needle by the applied electric field and are accelerated by a potential gradient between the cathode and the anode with a circular aperture through which electrons enter the system of vertically stacked electromagnetic lenses.

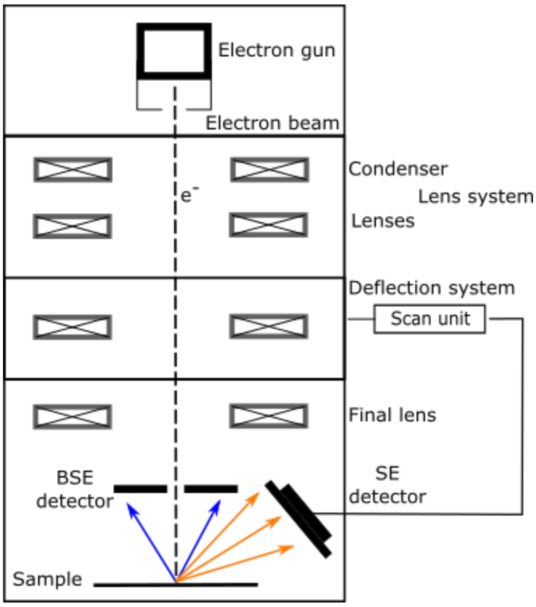

Figure 15: Schematic diagram of the scanning electron microscope FEI Quanta 250 FEG-ESEM with detectors of secondary (SE) and backscattered (BSE) electrons.

Lenses create electromagnetic fields that are responsible for focusing the electron beam on the specimen. The lens system starts with a condenser which focuses electrons into a beam that is further focused into a small spot. The deflection system is responsible for deflecting electrons and scanning in the raster pattern by applying electrostatic or magnetic fields to the electron beam at right angles. The sample chamber is equipped with a motorized stage surrounded by detectors. To avoid undesired losses of energy from collisions of electrons with molecules in air, the beam path is evacuated.

2.4.2. Transmission Electron Microscopy (TEM)

Conventional TEM is based on detecting electrons that have been transmitted through a thin specimen with a detector positioned in the path of the primary electron beam (Figure 16). Transmitted electrons may lose some of their primary energy depending on the density of the specimen and the character of electron-specimen interactions. The energy loss is specific to elements with which electrons interacted. Hence, transmitted electrons carry information about the density of the imaged area and the elemental composition of the specimen. The final image displays heavier elements as dark objects on a bright background (bright-field image). The second mode is the dark-field mode which is based on detecting electrons forescattered or diffracted into small angles, carrying crystallographic information. These electrons escaped the sample at certain angles and since points of their incidence are located outside of the primary beam, they are collected by a ring-shaped annular dark-field detector. The dark-field image displays dense materials as bright objects on a dark background (areas without scattering). The two modes are complementary and are usually displayed simultaneously, providing information about the mass and crystallinity. Due to the higher acceleration voltage of TEM systems (100 – 300 kV), the available resolution is higher than that of SEM. However, TEM is limited by the small penetration depth of electrons and can be used only for very thin samples.[143]

2.4.3. Scanning Transmission Electron Microscopy (STEM)

STEM is a type of TEM with a scanning function. STEM like SEM uses a focused electron beam that is scanned across the specimen and the synchronised detection of directly transmitted and forescattered electrons is done by detectors inserted below a thin specimen (Figure 16). The bright-field and dark-field modes are analogous to aforementioned TEM imaging modes. By using a larger, high-angle annular dark-field (HAADF) detector, electrons scattered into higher angles can be detected, improving the atomic number dependency of the image. The contrast of the reconstructed image is directly related to the atomic number of the scanned material (Z-contrast image).[143]

Additionally, detectors for secondary electrons and backscattered electrons can be installed above the sample which allows to obtain information about surface morphology and topography.[143]

STEM systems can also be equipped with an electron spectrometer for electron-energy loss spectroscopy (EELS), a technique that enables chemical characterization of the specimen by detecting inelastically scattered electrons.[143,144] The amount of lost kinetic energy of these electrons is attributed to certain inelastic interactions and what caused them. Some energy losses correlate with threshold energies necessary to promote an inner-shell ionization of elements. Since threshold energies are specific for each element, they can be used to identify which elements were struck by the detected electron. The collected data can be converted into a colour map to highlight individual elements in the imaged object.

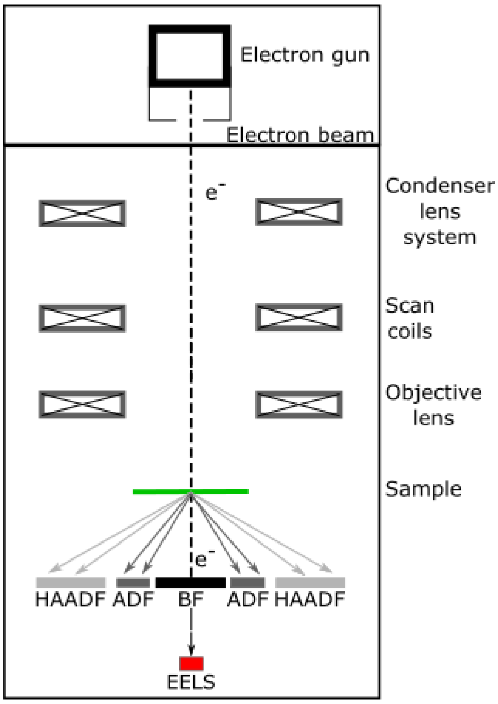

Figure 16: Schematic diagram of a scanning transmission electron microscope showing the beam path and the detector arrangement. Transmitted electrons are detected by the bright-field detector (BF), the annular dark-field detector (ADF) and the high-angle annular dark-field (HAADF) detector. Electron-energy loss spectroscopy (EELS) can be performed by analysing the energy losses of transmitted electrons.

3. Anisotropic Silica Coating of Gold Nanorods

3.1. Introduction

The use of GNPs in nanoscience has generally depended on their ability to support strong localized surface plasmon resonances (LSPRs)[11,12,145–148] and on the ease of modifications of their surfaces.[6,7,38,149,150] The LSPR of GNRs enhances electromagnetic fields in their vicinity,[5] which in turn, can be used to enhance fluorescence, light scattering, photocatalytic process and other properties of nearby molecules.[3,12,26,43,62,78,151] GNRs in particular have emerged as versatile nanoplatforms for numerous applications due to their tunable optical properties[8,36,37,63,83,152,153] mediated by the shape anisotropy.[85] In order for GNRs to be used as fluorescence or catalytic amplifiers, the molecules to be stimulated should ideally be located near the GNR ends, where the strong longitudinal field greatly enhances their molecular or photophysical properties.[20,44,51,154] However, anchoring molecules in this specific area requires to employ site-specific functionalization strategies of the GNR surface.

As was mentioned earlier in this work, silica is one of the most widely used coating agents for noble metal nanoparticles.[61] Due to its optical transparency, porosity and stability,[61,155,156] a silica shell can be modified with various functional molecules such as photosensitizers and chemotherapeutics[62,78,156] or fluorescent dyes.[50,58,65] Silica also exhibits low toxicity, driving a broad range of biomedical applications.[157] Furthermore, a silica layer can be used as a spacer between the GNR surface and adsorbates such as fluorescent dyes, which are otherwise prone to quenching in the proximity of metals. In comparison to the complete encapsulation by silica, coating just the ends of GNRs would facilitate a more anisotropic functionalization and a more selective excitation of adjacent molecules. Such anisotropic silica coating would be a promising step towards improving the performance of GNRs as fluorescence/catalytic amplifiers but is technically challenging.

GNRs produced via the seed-mediated growth method have their surfaces covered with a positively charged bilayer of the cationic surfactant cetyltrimethylammonium bromide (CTAB).[158,159] CTAB acts as an organic template for the deposition of alkoxysilanes such as tetraethyl orthosilicate (TEOS) to mediate the formation of silica shells.[160] The CTAB bilayer is not uniformly distributed over the surface of GNRs and is assumed to be less densely packed at the GNR ends due to their curvature (Figure 17).[66,67,159,161–164] This makes the end-functionalization of GNRs with various coating agents possible.[43,66–69,155,161,163–165] Resulting anisotropic structures are particularly suitable for photocatalysis, as they allow coating of the ends with materials such as Pd,[66] TiO_2[69] or semiconductors,[70] which can act as catalysts, while the bare sides of GNRs can directly participate in oxidation reactions. For example, the LSPR-induced hot electron generation from gold to catalysts enables more efficient electron transfer from the catalyst to molecules of the solvent, which may be used to enhance the hydrogen production under near-infrared illumination.[69,70] Alternatively, Yin et al. demonstrated the use of magnetically active gadolinium-coated dumbbell-like GNRs as tumour-targeted probes for photothermal therapy that are capable of two-photon luminescence as well as being suitable for MRI as contrast agents.[166] The spatial control over the end functionalization creates additional avenues for surface-enhanced spectroscopy techniques such as MEF spectroscopy which greatly benefit from the strong longitudinal plasmon field of GNRs.

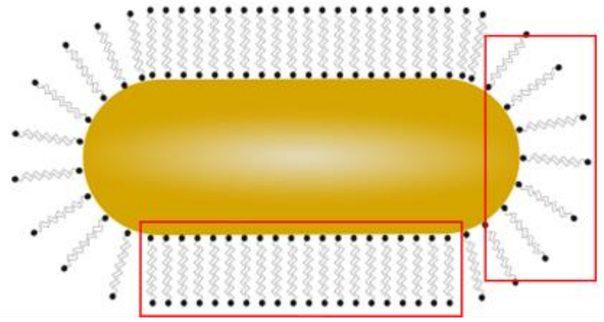

Figure 17: Distribution of CTAB on the surface of a gold nanorod. Molecules of CTAB assemble into pairs which ultimately form a bilayer with a positive external surface and hydrophobic region within. The packing density of CTAB is not uniform on the surface, being less compact on ends.

The deposition of silica on the ends of elongated nanoparticles has previously been achieved through fine control of CTAB and TEOS concentrations.[67,72,161,163] By limiting the concentration of GNRs, thus changing the amount of TEOS available per particle, the morphology of deposited silica shells can be varied between full encapsulation and a dumbbell-like coated GNRs (dGNRs) with a silica sphere attached to each end of the gold core.[161] Additionally, other factors such as the aspect ratio,[167] the width of GNRs or the CTAB chain length[69] have been shown to play important roles in the end-functionalization of GNRs as they all influence the density of the CTAB bilayer on the GNR ends. The growth temperature was found to affect the thickness of the mesoporous silica shells[168] due to the temperature-dependent solubility of CTAB.[168,169] However, it is believed that the influence of temperature on the anisotropic coating of GNRs with silica has not been reported. Understanding how temperature and other parameters affect the process of site-selective silica coating of GNRs should provide valuable insight into the mechanism of synthesizing bespoke dGNRs. So far, mechanistic studies have been limited to investigation of only a few parameters at a time and often do not include quantification of reaction yields of synthesized nanostructures.

In this chapter, a systematic study of the effect of GNR morphology and growth conditions such as temperature and the concentrations of GNRs and CTAB on the morphology of silica shells deposited on GNRs is presented.[71] Three morphologies are examined, from fully encapsulated GNRs (core-shell GNRs) to dumbbell-like, end-coated GNRs (dGNRs) and GNRs with only one end coated with silica (nanolollipops) (Figure 18). It was found that variations in morphology are determined by the interplay between all the reaction parameters and the roles of each parameter on the formation of dGNRs are elucidated. Presented findings demonstrate a high-yield synthesis of end-functionalized GNRs with silica at a rate exceeding 90 %, which is, to the best of our knowledge, the highest yield reported to date.

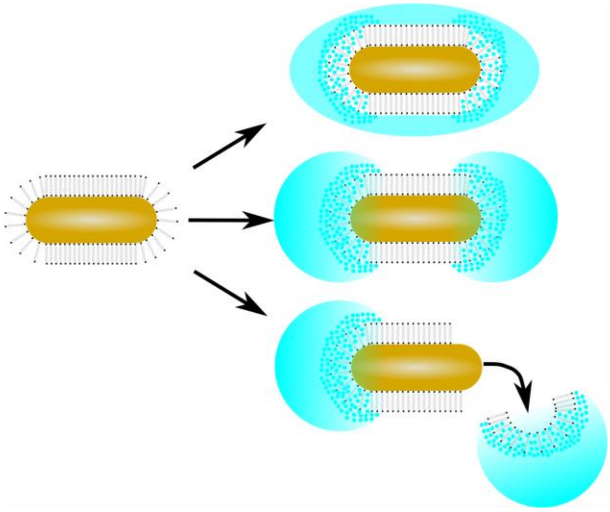

Figure 18: Schematic illustration of synthesized nanostructures – core-shell GNRs, dumbbell GNRs (dGNRs) and nanolollipops.

3.2. Tuning of the Aspect Ratio and Plasmon Resonance of Gold Nanorods

The seed-mediated synthesis of GNRs allows a reproducible tuning of aspect ratio and plasmon wavelengths of GNRs in the approximate spectral range of 600 – 850 nm (aspect ratio ~1.5 – 4.5).[158,170] Monodisperse GNRs with wavelengths of longitudinal plasmon modes above 850 nm can be also prepared using additives such as sodium oleate[171] or benzyldimethylhexadecylammonium chloride (BDAC) in binary surfactant mixtures.[158,172]

The seed-mediated growth method consists of two steps.[158,173] In the first step, spherical gold seeds (~1 – 5 nm) are formed from Au^{3+} by reducing a gold salt ($HAuCl_4$) in the presence of a stabilizing surfactant and a reducing agent (sodium borohydride, $NaBH_4$). The reducing agent creates building blocks by reducing Au^{3+} into Au^{+}. In the second step, seeds are mixed with the growth solution and grow into nanorods of a desired size (aspect ratio) under controlled conditions. The growth solution usually contains another reducing agent (ascorbic acid), higher concentration of gold ions, the surfactant, and a shape-directing agent (silver nitrite, $AgNO_3$).

A commonly used surfactant in the seed-mediated growth is cetyltrimethylammonium bromide (CTAB) which is responsible for the electrostatic stabilization of the colloid and assists in promoting the anisotropic growth of GNRs.[174] CTAB consists of a hydrophobic carbon chain and a polar head made of a quaternary ammonium group. CTAB has replaced previously used sodium citrate due to its ability to form single-crystalline seeds whereas citrate-capped seeds were found to be 'multiply twinned' and are suitable for producing more geometrically diverse nanoparticles than nanorods.[173,175] Gold seeds have several crystallographic facets with different surface energies ({110} > {100} > {111}[173,175]) which can be selectively grown and utilized for a directional shaping of NPs. The facet {110} exhibits the highest surface energy and is the preferential adsorption site for CTAB hydrophilic groups. The preferential binding to certain facets leads to the formation of a more tightly packed CTAB layer and assists in restricting the growth of nanoparticles in this direction. Both {100} and {111} facets exhibit lower surface energies and are located along the direction of the growth where the elongation progresses relatively unhindered once the random symmetry breaking occurs.[175] In an aqueous environment, polar heads adsorb onto the negatively charged gold surface and leave hydrophobic tails facing the exterior where an additional layer of CTAB monomers is established, forming a CTAB bilayer with the outer layer made of polar heads and a hydrophobic region made of carbon chains inside this bilayer.[176] Due to curved ends of prolate nanoparticles, the CTAB coating of tips is less compact.

An essential factor in the synthesis of GNRs is the appropriate amount of silver nitrite ($AgNO_3$) responsible for a well-defined shape and control over the aspect ratio.[173] Same as CTAB, silver has a higher binding affinity to the more open surfaces of facets {110} which leads to a significantly slower growth of nuclei in width and promotes the elongation.[173] Although GNRs have been a subject of a considerable research interest, the shape control mechanism is still not fully understood. Three different growth mechanisms have been proposed in order to explain the role of silver in the growth process. One possible mechanism was proposed by Jana et al,[177] that the growth restriction is not governed by the direct adsorption of Ag^+ ions onto GNRs but by silver bromide (AgBr) formed from Ag^+ ($AgNO_3$) and Br^- (CTAB). The reason is that ascorbic acid, used as the reducing agent in the growth solution, can effectively reduce gold but is weak for reducing silver to its atomic form (Ag(0)). Therefore, the formation of AgBr as capping agent at the gold surface is possible. Another explanation was provided by Liu et al.[175] who proposed that AgBr is an inert molecule of a relatively small fraction in the growth solution and therefore, is unlikely to provide sufficient blocking and promote the anisotropic growth. However, it is possible that the shape control is governed by the deposition of Ag(I), where silver ions serve as a surfactant and assemble into a monolayer of Ag(0) without being reduced to bulk metal.[175] The third opinion states that the anisotropic growth of GNRs could be promoted through a competitive facet-specific caping by CTA-Br-Ag complexes in the presence of CTAB as a cosurfactant.[178,179] The common factor in these mechanisms is the crucial importance of bromide counterions in CTAB which has been identified as essential for the preparation of a rod shaped nanoparticles with high yields.[159,178]

The effect of silver ions on the growth of GNRs and their plasmon resonance can be seen in Table 1. Small amounts of silver are insufficient for the elongation and produce only spherical particles with the wavelength of plasmon resonance around 530 nm.[8] As the concentration of silver in a growth solution increases, spherical particles assume more rod-like shapes and a second (longitudinal) plasmon mode can be detected. Figure 19 demonstrates these changes along with the fine-tuning of the longitudinal plasmon resonance of GNRs across the spectral range from 624 to 794 nm. Higher concentrations of silver nitrate lead to a gradual redshift of longitudinal plasmon band peak wavelengths, while those of transverse plasmon bands blueshift (Figure 19a,b).

Table 1: Tuning of plasmon resonance of GNRs by controlling the concentration of silver nitrate ([AgNO$_3$]) in 10 mL growth solutions.

[AgNO$_3$] [µL]	**12**	**15**	**17.5**	**20**	**25**	**35**	**45**	**50**	**55**	**60**	**65**	**75**	**100**
[AgNO$_3$] final [mM]	0.12	0.15	0.18	0.20	0.25	0.35	0.45	0.49	0.54	0.59	0.64	0.74	0.98
λ_{LSPm} [nm]^a	-	-	624	668	681	691	719	718	737	740	753	780	800
λ_{TSPm} [nm]^b	533	532	523	522	518	514	511	512	511	509	509	513	512

[a,b] Maximum wavelengths of longitudinal (LSPm) and transverse (TSPm) plasmon modes (absorption bands).

The process of plasmon tuning can be observed with the naked eye. Variations in the aspect ratio of GNRs alter absorption and scattering properties of colloids which subsequently affect the perceived coloration of solutions from purple/pink to brown as the aspect ratio increases (Figure 19c).[152]

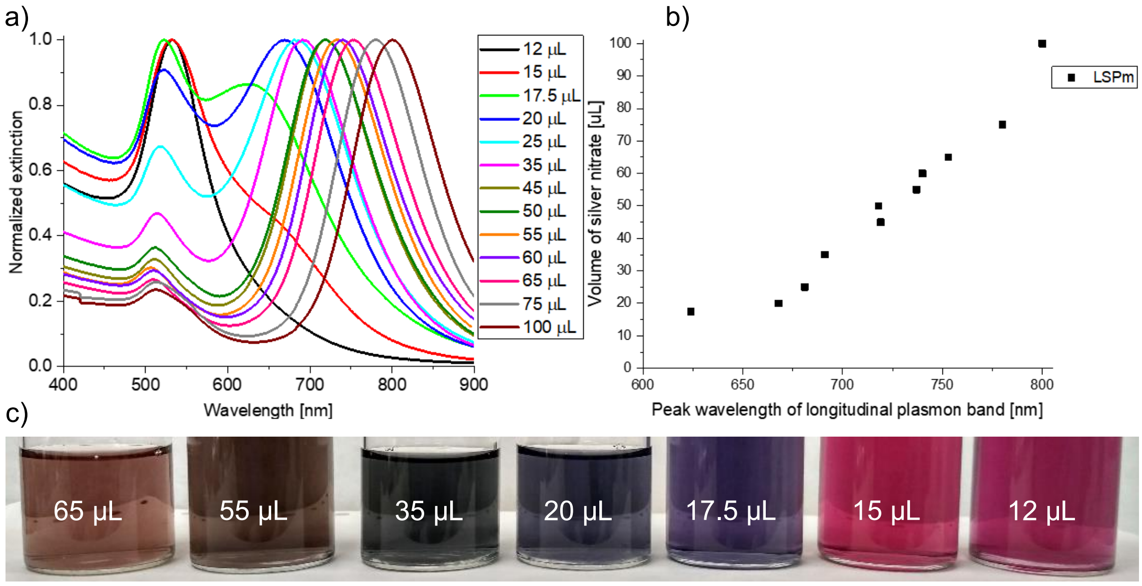

Figure 19: a) Extinction spectra of GNRs and b) changes in peak wavelengths of longitudinal plasmon modes (LSPm) controlled by various added volumes of silver nitrate (0.1M) in growth solutions (~10 mL), c) changes in colouration of GNR colloids related to different aspect ratios of GNRs.

3.3. Silica Coating of Gold Nanorods

The silica coating of NPs was derived from sol-gel techniques used for the preparation of silica NPs. These often utilize alkoxide precursors tetraethyl orthosilicate (TEOS) and tetramethyl orthosilicate (TMOS) which allow a precise control of the porosity, size of silica NPs, and branching of the polymer.[180]

Silica networks are made of SiO_4 tetrahedra with some tetrahedra containing hydroxyl groups and alkoxy groups. In silica precursors such as TEOS that is used in this work, central silicon atoms are covalently attached to organic groups via an ether linkage (Si–O–R′). When placed in an aqueous solution, alkoxy groups of TEOS are hydrolyzed to generate silanol groups (Si–OH) in the presence of a catalyst (Equation 37). TEOS hydrolyses gradually and newly formed hydroxyl groups (–OH) may already take part in the condensation with other partially hydrolyzed TEOS molecules before the second hydrolysis takes place (Equation 38).[181,182]

$$\mathrm{Si(OC_2H_5)_4 + 4H_2O \rightarrow Si(OH)_4 + 4C_2H_5OH} \qquad \textit{Equation 37}$$

$$\mathrm{Si(OC_2H_5)_4} + x\mathrm{H_2O} \rightarrow \mathrm{Si(OC_2H_5)_{4-x}(OH)_x} + x\mathrm{C_2H_5OH} \qquad \textit{Equation 38}$$

Further hydrolysis leads to crosslinking and more complex networks. Once silanol groups are created, TEOS condensates through a series of condensation reactions, forming siloxane bonds (≡Si–O–Si≡) between individual tetrahedra, and molecules of water (Equation 39) or alcohol (Equation 40) are produced as biproducts.[182] Depending on the catalyst and the pH induced by the catalyst, $Si(OH)_4$ (orthosilicic acid) assembles into linear (acidic pH) or highly branched (alkaline pH) structures.[180,181]

$$\equiv Si–OH + HO–Si\equiv \rightarrow \equiv Si–O–Si\equiv + H_2O \qquad \textit{Equation 39}$$

$$\equiv Si–OH + H_5C_2O–Si\equiv \rightarrow \equiv Si–O–Si\equiv + C_2H_5OH \qquad \textit{Equation 40}$$

Stöber et al. introduced a process of synthesizing silica nanoparticles with a controllable uniform size distribution (up to 2 μm) using TEOS in an aqueous solution of ethanol and ammonia.[183] This method was later improved by adding cationic surfactants as structural directing agents into the mixture to gain a better control over the particle size.[180,184,185] The cationic surfactant-based synthesis takes advantage of electrostatic interactions between silicate species and surfactant templates, which, due to their chemical structure, possess hydrophobic and hydrophilic parts such as those of CTAB. In conditions where surfactant reaches the critical micelle concentration, its molecules can form micelles, aggregates with polar parts oriented outward and hydrophobic parts "protected" inside.[180] These micelles bind with negatively charged alkoxy silanes and contribute to the formation of mesoporous silica polymers directly as CTAB/silica clusters or as reservoirs of CTAB molecules.[184]

In general, the synthesis of mesoporous silica is a three-stage process[185]:

- The first stage proceeds as a base-catalysed hydrolysis of alkoxysilanes followed by the condensation of silica. Blocks of orthosilicic acid assemble into oligomers immediately upon addition to water prior formation of CTAB/silica particles.
- The second stage is the formation of CTAB/silica particles. These particles consist of silica oligomers/polymers which electrostatically bind monomers of CTAB and are further supplied with additional surfactant ions from free CTAB micelles.
- Third step is the aggregation of CTAB/silica particles and the continuous deposition of CTAB and silica.

Controlling the reaction kinetics to achieve desired silica structures is crucial. Charge states of silica species that interact with cationic surfactants are of special importance due to their dependency on the pH and their effect on reaction rates of hydrolysis and condensation.[186] The pH of the reaction mixture is set by adding acidic/basic catalysts. In acidic conditions (pH ~2 – 7) above the isoelectric point (pH = 2), silica is negatively charged and can interact with both neutral polymers and cationic surfactants. The highest negative charge density is reached at pH > 7 where only electrostatic interactions between silica species and cationic surfactants can occur. At pH above ~10.5, silica is unstable and dissolves. However, the strong electrostatic interaction between negatively charged silicates and positively charged surfactants stabilizes the system even at this high pH. The condensation rate reaches maximum at pH ~7 and then decreases due to the aforementioned instability of silicates at high pH. Most synthesis methods are performed at higher pH range which allows a better reaction control due to the relatively fast condensation rate and enables a rapid and simultaneous growth of initial nuclei.[186]

Silica coating of CTAB-coated GNRs is a process similar to the templated synthesis of silica particles which takes advantage of the CTAB bilayer. A single-step silica coating method of CTAB-coated GNRs was first demonstrated by Gorelikov and Matsuura in 2008.[160] In this method, the surface-bound CTAB acts as a soft organic template for the deposition of negatively charged, hydrolyzed TEOS. By selecting appropriate range of reagent concentrations in the reaction mixture so that the majority of CTAB is present on GNR surfaces, one can achieve a preferential binding of silica and aggregation of silica/CTAB species onto the CTAB bilayer as well as control the shell size by adjusting concentrations of TEOS or CTAB.[50,158,159] The process of anisotropic silica coating of GNRs and its dependence on reaction conditions as well as on individual reagents will be discussed below in more detail.

3.4.Experimental

3.4.1.1. Materials

Silver nitrate ($AgNO_3$, S6506-5G), gold (III) chloride trihydrate ($HAuCl_4$, G4022-1G), sodium borohydride ($NaBH_4$, 452882-25G), cetyl trimethylammonium bromide (CTAB, H6269-500G), ascorbic acid (A5960-25G), tetraethyl orthosilicate (TEOS, 86578-

250ML), sodium hydroxide (NaOH, S5881-500G-M), methanol (≤ 99.8%, 32213-M) and ethanol (≥99.8%) were purchased from Sigma-Aldrich. Distilled water was used as a solvent in the synthesis of GNRs.

3.4.1.2. Synthesis of Gold Nanorods

CTAB-coated GNRs were prepared using an adapted standard seed-mediated growth method,[158] consisting of two steps: (1) the preparation of the seed solution; and (2) the subsequent growth of seeds in the growth solution.

10 mL of the seed solution was prepared by mixing 9.75 mL of 0.1M aqueous CTAB solution with 0.25 mL of 0.01M $HAuCl_4 \cdot 3H_2O$. The solution was then stirred for 10 min, then 0.6 mL of 0.01M $NaBH_4$ (prepared in ice-cold water) was added under vigorous stirring for 5 min. After that, the seed solution was left to stand in the dark for 3 hours to allow the growth of the seeds.

10 mL of growth solution was prepared by mixing 9.5 mL of 0.1M aqueous CTAB solution with 0.5 mL of 0.01M $HAuCl_4 \cdot 3H_2O$. The solution was stirred for 10 min before adding 15, 45, 50 or 60 μL of 0.1M $AgNO_3$ to tune the wavelength maxima of longitudinal plasmon resonances of GNRs to ~628, 726, 742 or 748 nm (Figure 20).[8] After an additional 5 min of stirring, 55 μL of 0.1M ascorbic acid was added. The final step was the addition of 12 μL of seeds under gentle stirring. The solution was then stored in the dark to age overnight at room temperature. The following day, GNRs were purified via centrifugation (Sigma 1-4 Microfuge) at 12 000 g for 20 min. The supernatant was then extracted, and the pellet re-suspended in distilled water to achieve the desired concentration.

After the purification, extinction spectra of the newly prepared GNR solution were measured using a Lambda 2 UV/VIS spectrometer (PerkinElmer) to determine the maximum wavelength of the longitudinal plasmon band. The concentration of the GNR solution was calculated using Equation 28 from the extinction at the longitudinal plasmon band maximum and corresponding molar extinction coefficients at the longitudinal plasmon band maxima (2.6, 3.9 and $4.1 \cdot 10^9$ $M^{-1}.cm^{-1}$ for GNRs with plasmon resonances at 628, 726 and 742, 748 nm). The GNR dimensions and hence aspect ratios (the ratio of length to diameter) and errors (as sample standard deviations) were measured manually for more than one hundred nanoparticles from STEM images using image processing software ImageJ.

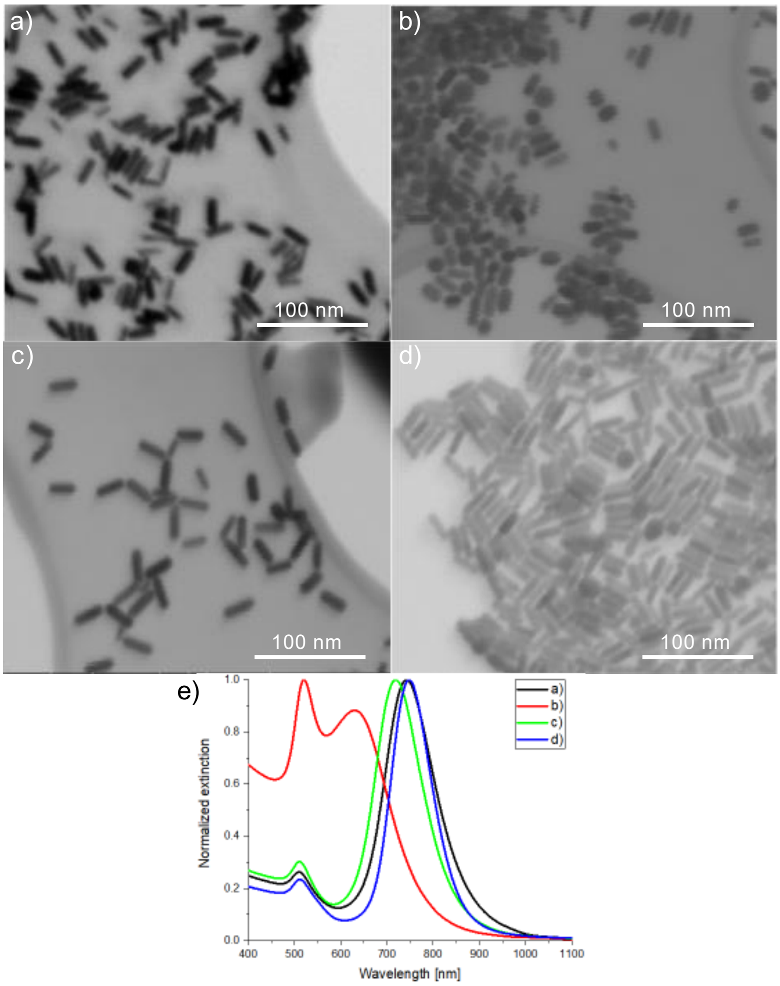

Figure 20: STEM images of gold nanorods with longitudinal plasmon resonances tailored to a) 742 nm, b) 628 nm, c) 726 nm, d) 748 nm and extinction spectra of above gold nanorods e).

3.4.1.3. End-selective Silica Coating of GNRs

Silica coating was carried out via the modified single-step silica coating method developed by Gorelikov.[50,160] CTAB-capped GNRs, synthesized in the previous step, were centrifuged for a second time at 11 200 g for 20 min to remove excess CTAB from the solution and bring the CTAB concentration to approximately <0.01 mM.[50] Further on in the process, a close control of the CTAB concentration is essential, which is achieved after centrifugation by removing the supernatant and re-suspending the pellet in 1.2, 1.4 and 1.6mM aqueous CTAB solutions (3 mL) so that final concentrations of GNRs were ~0.6 nM and ~1 nM. Adding CTAB solutions to pellets ensures more accurate control over the reaction conditions. Suspensions were mixed overnight to allow CTAB to equilibrate on the nanorod surface prior to silica coating. The next day, 12 µL of 0.1M NaOH was added to each 3mL sample to set the pH to approximately 10.5, and the solutions were mixed for 30 min. Then, 27 μL of 20vol% TEOS in methanol was added and mixed for 5 min to homogenize TEOS in the reaction mixture. After 5 min, each sample was transferred to three 1.5 mL centrifuge tubes (1 mL in each tube) and placed in a shaker (ThermoMixer, Eppendorf) for shaking at 19, 21 or 23 °C and at 700 rpm overnight. At lower speed, a certain degree of sedimentation could occur. The GNRs were then centrifuged at 8 000 g for 20 min. Supernatant was removed and the pellet was re-suspended in a mixture of ethanol and water (3:2). The yields of synthesized nanoparticles were calculated from STEM images as fractions of more than one hundred nanoparticles in each sample.

3.4.2. Characterization

High-angle annular dark-field scanning transmission electron microscopy (HAADF-STEM) and transmission electron microscopy (TEM) data were recorded on a probe-corrected JEOL ARM200cF instrument with a cold field emission source operating at an acceleration voltage of 200 kV. Elemental mapping was performed by electron energy-loss spectroscopy (EELS) using a Gatan 965 Quantum ER post-column spectrometer. Scanning electron microscopy (SEM) images were acquired using a field-emission environmental scanning electron microscope (FEI Quanta 250 FEG-ESEM) with a modular STEM detector at an acceleration voltage of 30 kV. Samples were prepared by drop-casting 5 μL of a sample solution onto a carbon-coated 300-mesh holey Cu grid (Agar Scientific) which was left to dry at room temperature.

3.5. Results and Discussion

3.5.1. Influence of Temperature and CTAB Concentration on the Anisotropic Silica Coating of GNRs

For the synthesis of end-coated nanoparticles and to identify the effect of individual reaction conditions, CTAB-capped GNRs with an aspect ratio of ~3.3 (42.8 ± 4.3/13.0 ± 1.8 nm) and GNR concentration ([GNR]) of ~1 nM were coated with silica via the modified single-step silica coating method[160] (Figure 20a). The concentration of CTAB ([CTAB]) was varied to be ~1.2, 1.4, 1.6 mM at selected temperatures: 19, 21, 23 °C Table 2). To ensure accurate [CTAB] for comparison, GNRs were purified twice via centrifugation to reduce the residual [CTAB] (<0.01 mM) well below working concentrations.[159,165] Purified GNRs were then dispersed in CTAB solutions of defined [CTAB]. Resulting samples were characterized via scanning transmission electron microscopy (STEM) (Figure 21) that revealed 3 populations of nanostructures: dGNRs, core-shell GNRs and nanolollipops, with various reaction yields. Table 1 lists the experimental conditions and corresponding yields (%) of the three populations of GNR structures.

The process of end-selective coating of GNRs is based on a similar principle as the synthesis of mesoporous silica in the presence of CTAB.[185] The CTAB bilayer on the ends of GNRs is known to be less compact than that on the sides of GNRs (Figure 21a).[67,159,161–163] This presents less steric hindrance for the deposition of silica, allowing hydrolyzed TEOS species to access GNR ends and condense.[67,161,163,165] To achieve the delicate non-uniform distribution of the CTAB bilayer, two populations of CTAB must be considered – free CTAB (fCTAB) and CTAB bound to GNRs (bCTAB). High concentration of fCTAB may cause saturation of the GNR surface with a dense CTAB bilayer,[69] which consequently raises the concentration of positively charged CTAB micelles in the solution.[165] As a result, free silica nanoparticles can be generated or GNRs will grow full shells.[165] Thus, bCTAB and components of fCTAB compete in the attraction of negatively charged, hydrolyzed TEOS species.[165] The reaction dynamics of CTAB are dependent on the reaction temperature. The Krafft temperature represents the temperature below which micelles do not form as the maximum solubility of the surfactant does not reach the critical micelle concentration (CMC,~1 mM[159]).[169] No silica shells form bellow the Krafft temperature. For CTAB in an aqueous solution, this temperature has been reported to be between 20 and 25 °C.[168,169]

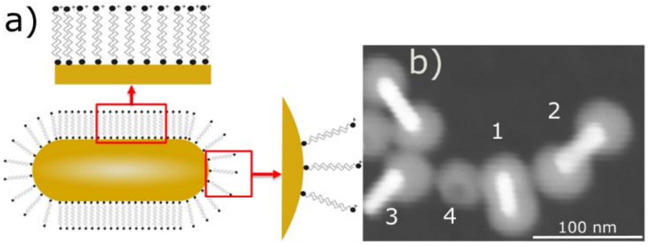

Figure 21: a) Schematic representation of the distribution of CTAB on the surface of GNR and b) a STEM image of a sample containing a representative mixture of (1) core-shell, fully encapsulated GNRs, (2) dGNRs and (3) nanolollipops with a (4) separated silica sphere.

Table 2: Synthesis parameters and % yields[a] of silica-coated GNRs 1.2, 1.4, 1.6a-c produced at various molar concentrations of CTAB and at increasing reaction temperatures of 19 (a), 21 (b) and 23 (c) °C.

Sample	**1.2a**	**1.2b**	**1.2c**	**1.4a**	**1.4b**	**1.4c**	**1.6a**	**1.6b**	**1.6c**
CTAB [mM]	1.2	1.2	1.2	1.4	1.4	1.4	1.6	1.6	1.6
GNR [nM]	1	1	1	1	1	1	1	1	1
T [°C]	19	21	23	19	21	23	19	21	23
Dumbbell [%]	-	*a*	24.5	-	34.1	24.6	-	51.4	27.7
Core-shell [%]	-	*a*	36	-	21.2	73.9	-	28.4	71.4
Nanololl. [%]	-	*a*	39.5	-	44.7	1.5	-	20.2	0.9

[a] Yields of nanoparticles in sample 1.2b (Figure 22a) were not quantified due to non-uniform coating.

It is apparent that temperature and [CTAB] do indeed influence the morphology of silica shells. The yield of dGNRs and nanolollipops decreased while that of core-shell GNRs increased with increasing temperature. Silica coating was not observed at 19 °C and was not uniform at low [CTAB] at 21 °C. The absence of coating for all samples at 19 °C can be explained by the low solubility of CTAB, which is likely to remain crystallized below the Krafft point.[168] At 21 °C, sample 1.2b contained non-uniformly coated GNRs and GNRs aggregated mostly in a side-by-side orientation (Figure 22a). This type of aggregation is typical for uncoated GNRs and was most likely induced by capillary forces during drying.[187,188] The incomplete coating with 1.2 mM of [CTAB] indicates that at 21 °C, CTAB dissolved enough to exceed the CMC, facilitating the formation of CTAB/silica species and their subsequent aggregation on GNRs. However, the amount of CTAB was presumably insufficient to form a uniform coating, which appeared only after a further increase in temperature to 23 °C (sample 1.2c). As [CTAB] was increased to 1.4 and 1.6 mM, the CMC was exceeded even at lower temperature of 21 °C, and more CTAB monomers were available for coating, facilitating the formation of silica shells at 21 °C. At 21 °C and [CTAB] ~1.4 mM, sample 1.4b contained about four times as many end-coated GNRs as core-shell nanoparticles (78.8 %:21.2 %). When [CTAB] was increased to 1.6 mM at the same temperature, the numbers of end-coated GNRs and core-shell GNRs changed only slightly (71.6 %:28.4 %), with a higher ratio of dGNRs in sample 1.6b. The reaction yields of end-coated GNRs changed dramatically at 23 °C compared with results observed at lower temperatures and reached 64 % at [CTAB] ~1.2 mM, while at [CTAB] ~1.4 and 1.6 mM, the ratio reversed and over 70 % of particles were core-shell GNRs. At 23 °C and [CTAB] ~1.6 mM, sample 1.6c also contained a large number of silica nanoparticles (Figure 22b), indicating an abundance of CTAB. Under these conditions, CTAB crystals completely dissolved, which led to an increased concentration of fCTAB, exceeding that of bCTAB, as well as causing the saturation of bCTAB on GNR surfaces.

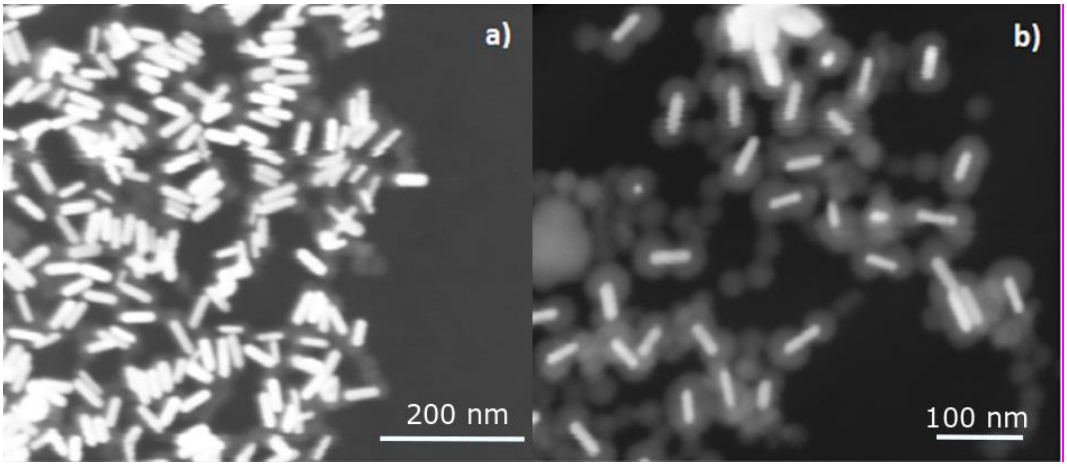

Figure 22: Representative STEM images of non-uniformly silica-coated GNRs in sample 1.2b a) and STEM image of sample 1.6c b).

The analysis of STEM images revealed that some GNRs retained only one silica sphere, likely due to the other being torn off by mechanical forces during centrifugation and drying (Figure 23). Several isolated silica spheres in Figure 23 show hollow, round-shaped areas which indicate that they originally grew on GNRs. This separation is likely to be due to weak interaction between the silica coating and the GNR, perhaps enhanced by the less compact surfactant bilayer that was exploited for the anisotropic coating.

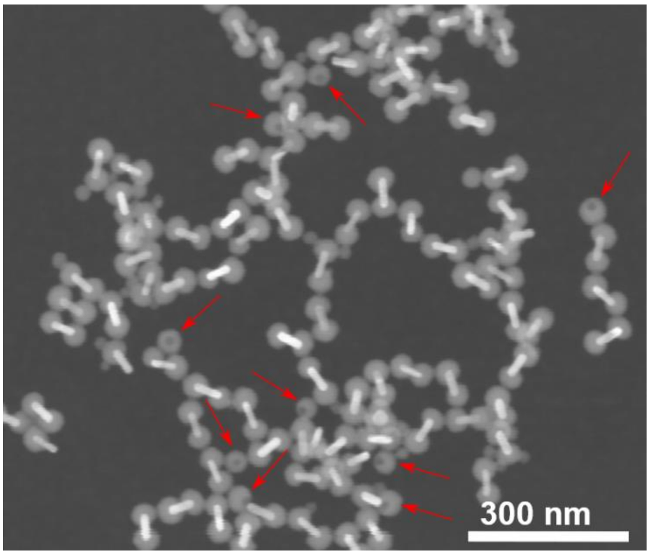

Figure 23: STEM image of end-coated GNRs indicating isolated hollow silica spheres that have been detached from gold cores.

It is noted that, at the same [CTAB], the ratio of nanolollipops to dGNRs decreases as temperature increases, suggesting a less porous, thus more robust silica structure, at higher temperature, possibly related to a faster shell assembly rate resulting from the abundance of fCTAB. At low temperatures, when the density of terminal silica spheres is low, the porous coating is likely to be more fragile at the interface between the gold surface and terminal spheres, making separation from gold cores easier.

STEM images have shown dGNRs with separated terminal spheres as well as some dGNRs with overlapping silica that extends from spheres to sides (Figure 24a). Figure 24b shows a TEM image of a dGNR with a thin layer of silica on the side that connects both terminal spheres. The thickness of the side coating can vary from a few nanometres (Figure 24b) to a thicker and more significant overlap (Figure 24a). This side coating could affect further functionalization and result in molecules assembling on both the silica spheres and the silica-coated sides of the GNRs. Side layers could also hinder the oxidation efficiency of bare gold in GNRs when combined with catalysts on their ends. As discussed below, the radius of attached spheres remains approximately 20 nm and is insensitive to growth conditions. This suggests that the growth of dGNRs is self-limiting so that once a maximum end-cap size is achieved growth stops and side layers grow from remaining TEOS and CTAB. This is in agreement with a model that has been used elsewhere to explain the end-functionalization of rod-like NPs and other NPs with tips and edges, in which the functionalization occurs preferentially at curved surfaces due to their unevenly distributed CTAB bilayer and a lesser steric hindrance, as depicted in Figure 24c.[67,69,159,162,163,165,182] There, the condensation may proceed deeper inside the bilayer than it would be possible on sides where the density of the bilayer is higher (Figure 24d), which allows silica spheres to form (Figure 25). The thickness of a CTAB bilayer is only 0.8 – 2.2 nm, which is difficult to visualize when GNRs are encapsulated in silica shells of higher density and CTAB chains within the bilayer are compressed or bent.[189,190]

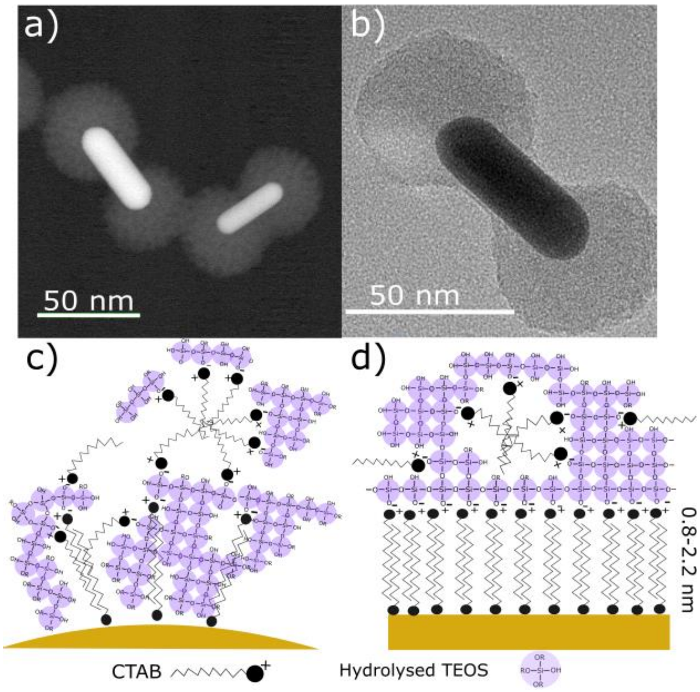

Figure 24: STEM image of dGNRs and porous silica coating a) and TEM image of dGNR with a thin, porous silica layer on the sides of GNRs b). Schematics of the growth of silica (purple) with CTAB chains (black zig zag lines) on ends c) and sides d) of GNRs.

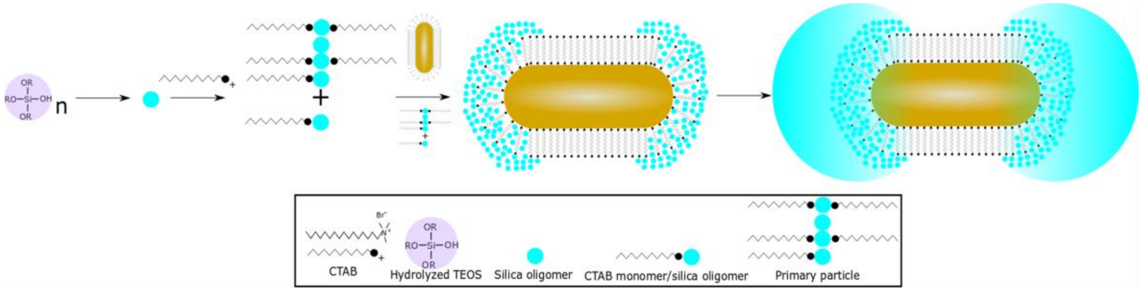

Figure 25: Schematic of the growth mechanism of dumbbell-like nanorods.

Figure 26 shows elemental mapping of two dGNRs of different aspect ratios, collected using electron energy loss spectroscopy (EELS) in STEM. The shell material is indicated by the strong presence of Si, O and C, which together are indicative of the incorporation of CTAB and TEOS reaction products inside the silica structure. The top panels are for a relatively long dGNR, for which the growth of the silica spheres has terminated before the spheres overlap. Only a thin silica coating is expected around the middle of the GNR. The bottom panels relate to a shorter GNR, where the silica spheres have grown sufficiently close that the silica coating on the intervening has thickened to produce a 'hybrid' structure that is intermediate between a dGNR and a core-shell GNR. Note that the stronger signal intensities in the lower panels indicate denser silica for the shorter GNR.

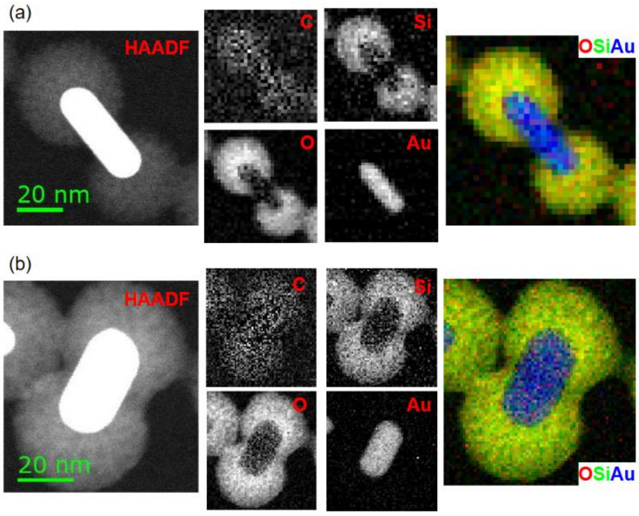

Figure 26:STEM-EELS elemental mapping of two dGNRs with (a) a high and (b) a lower aspect ratio. (Left) A HAADF-STEM image of the spectrum image area, with contrast boosted to reveal the relatively weak signal from the silica shell, which saturates the GNR signal. (Middle) Elemental maps, measured using the K-edges of C, O and Si and the M4,5 edge of Au and following background subtraction. The carbon signal is weak due to the spectrometer acquisition timing. (Right) False-coloured map showing the distribution of (red) oxygen, (green) silicon and (blue) gold, with silica appearing as yellow. The same area is imaged in the HAADF as in the subsequent panels for each GNR, with the scalebar in the HAADF image indicating the GNR size.

CTAB clearly plays a critical role in the synthesis of end-functionalized GNRs by determining the aggregation sites for silica. As will be discussed below, the increased stability of the coating/dumbbell morphology, higher yield of core-shell GNRs and lower yields of nanolollipops observed at higher temperatures all rely on the abundance of CTAB incorporated in shells. The high sensitivity to CTAB and temperature shows the importance of carefully selecting the range of reaction conditions, as small deviations in either the reaction temperature or the amount of CTAB may lead to an irregular coating, generation of core-shell GNRs or unwanted secondary products such as free silica particles.

3.5.2. The Effect of the GNR Concentration on the Formation of dGNRs

The surface area available for adsorption on precursor GNRs and their aspect ratio are expected to affect the growth mechanism of dGNRs. To investigate the effect of [GNR] on the synthesis of dGNRs, [GNR] was reduced to ~0.6 nM while maintaining other parameters. The [CTAB] was set at ~1.6 mM as the highest yield of dGNRs was produced at this condition. The data were then compared with samples 1.6a-c in Table 3. In contrast to the absence of silica coating observed from previous samples prepared at 19 °C with [GNR] 1nM, sample 1.6d contained over 85 % of end-coated nanostructures. However, the morphology of product nanoparticles shifted to core-shell GNRs when the temperature was increased to 21 and 23 °C. Despite the high yield of end-coated GNRs, it should be noted that synthesis at 19 °C is very sensitive to experimental uncertainty that impairs the reproducibility of the method.

The decrease of [GNR] at 19 °C probably resulted in an increased amount of CTAB and TEOS per GNR, which established a bilayer and allowed silica shells to be formed. This also contributed to higher yields of core-shell GNRs formed at temperatures above 21 °C (1.6e,f) compared with [GNRs]~1 nM. This confirms that [GNR] can be used to control the synthesis/yield of the synthesis.[161]

Table 3: Comparison of final growth % yields of silica-coated GNRs prepared at 1.6 mM concentration of CTAB, 1 and 0.6nM GNR solutions (1.6a-c and 1.6d-f) and at increasing reaction temperatures of 19 (a,d), 21 (b,e) and 23 (c,f) °C.

Samples	**1.6a**	**1.6b**	**1.6c**	**1.6d**	**1.6e**	**1.6f**
CTAB [mM]	1.6	1.6	1.6	1.6	1.6	1.6
GNR [nM]	1	1	1	0.6	0.6	0.6
T [°C]	19	21	23	19	21	23
Dumbbell [%]	-	51.4	27.7	40.5	27.4	27.7
Core-shell [%]	-	28.4	71.4	14.5	61	65.7
Nanololl. [%]	-	20.2	0.9	45.0	11.6	6.6

Because [GNR] ~0.6 nM enabled the production of end-functionalized GNRs at all the investigated temperatures, this concentration was investigated further to determine the effect of aspect ratio on the shell morphology.

3.5.3. The Effect of Aspect Ratio on the Formation of dGNRs

Apart from reagent concentrations, another crucial factor in the silica coating of GNRs that has received little attention is the aspect ratio of gold cores. Wu and co-workers showed that the right combination of the CTAB chain length and diameter of GNRs is important for the end-coating of GNRs with TiO_2, as both parameters influence the density of the CTAB bilayer.[69] The diameter of GNRs was shown to determine the compactness of the CTAB bilayer by limiting the number of CTAB chains that can cover the gold surface on curved ends. CTAB chains of different lengths on GNRs exhibit different hydrophobic interactions between molecules as well as different hindrance to approaching coating agents. Terminal curvatures, the width of GNRs and steric hindrance between CTAB chains all change with aspect ratio. Therefore, GNRs with various aspect ratios may yield different numbers of end-coated GNRs and an optimal combination of aspect ratio and [CTAB] is needed to achieve high yield synthesis.

In order to investigate the effect of aspect ratio on the growth of dGNRs, the presented method of anisotropic silica coating was applied to GNRs with aspect ratios ~2.1 (34.8 ± 6.8/16.5 ± 4.2 nm) (GNR1) and ~3 (50.6 ± 5.3/16.6 ± 2) (GNR2) (Figure 20b,c). Two temperatures, 21 and 23 °C, were compared. The temperature 19 °C was excluded because of the low surfactant solubility. The amount of TEOS remained unchanged, 27 µL in 3mL solutions. Experimental conditions and corresponding results are summarized in Table 4.

Table 4: Summary of experimental conditions used for the anisotropic silica coating of GNRs of various aspect ratios and the resulting reaction yields of synthesized nanostructures.

Samples	GNR1_21	GNR1_23	GNR2_21	GNR2_23
CTAB [mM]	1.6	1.6	1.6	1.6
GNR [nM]	0.6	0.6	0.6	0.6
LSPR [nm]	635	635	726	726
T [°C]	21	23	21	23
Dumbbell [%]	18.8	11.6	48.9	76.0
Core-shell [%]	80.5	86.6	34.4	22.9
Nanololl. [%]	0.7	1.8	16.7	1.0

GNRs with low aspect ratio (~2.1) (GNR1_21 – 23) (Figure 27a) formed predominantly core-shell GNRs and notably less dGNRs, whereas the yield of dGNRs containing GNRs with high aspect ratio (~3) (GNR2_21 – 23) increased up to 76.0 % at 23 °C. The significant difference in yields of dGNRs implies a clear dependence of the site-selective coating on aspect ratio. The uniform shape of dGNRs in GNR2_23 (Figure 27b) also suggests that an aspect ratio of ~3 and CTAB are a suitable combination for the synthesis of dGNRs.[69]

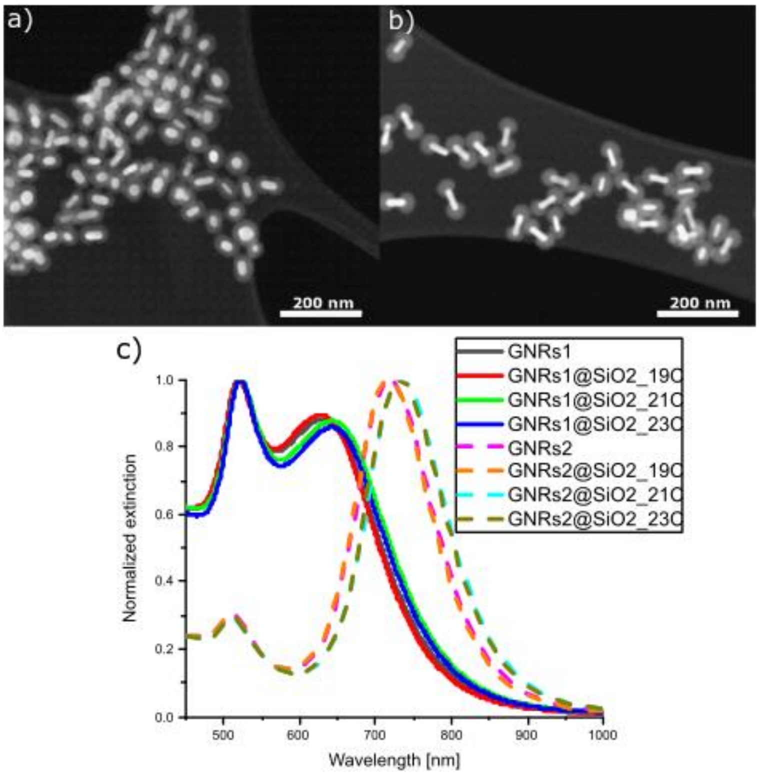

Figure 27: STEM images of a) GNR1_23 and b) GNR2_23 and c) comparison of extinction spectra of gold cores and silica-coated GNRs.

A comparison of extinction spectra (Figure 27c) shows that wavelengths of longitudinal surface plasmon bands of GNRs prepared at 19 °C did not shift with respect to the original GNRs as the coating was not successful at this temperature. At reaction temperatures 21 and 23 °C, extinction spectra were red-shifted by approximately 15 nm upon silica coating compared to uncoated GNRs. The change in the extinction is attributed to the higher refractive index of the silica layer compared with water, which influences the longitudinal plasmon mode due to its sensitivity to changes of refractive index at the surface.[161,163]

The results suggest that the full coating is the dominant shell morphology on short GNRs. This is probably due to the fact that the length of rods defines the distance between two terminal silica spheres. In the case of short rods, their terminal spheres could be in contact before reaching their self-limiting size. When the two spheres are not energetically favourable anymore, resulting surface diffusion and growth in the neck could lead to a core-shell structure.[146] In contrast, a greater length sets the ends of GNRs farther apart, which facilitates the growth of isolated silica at the endcaps. Silica spheres on long GNRs will remain separate for longer,[167] until the continuous deposition of CTAB/silica particles increases the surface area of silica to the point where attached spheres begin to merge into full shells. This, again, is consistent with the growth model described above

3.5.4. Tuning of the Optimal Growth Yield

To further optimize the shape and yields of end-coated GNRs and to reduce the number of core-shell GNRs, the aspect ratio of gold cores was increased to ~3.6 (44.3 ± 4.2/12.3 ± 1.9 nm) (Figure 20d) and the amount of TEOS was varied in the range 27, 25, 23 and 21 μL. The reaction temperature was maintained at 23 °C because in the previous step, the highest yields of end-coated GNRs were achieved at this temperature. The decreasing amount of TEOS in combination with the higher aspect ratio of gold cores improved growth yields of dGNRs to >87 %, reaching 91 % when the added volume of TEOS was 23 μL, while yields of core-shell GNRs were reduced to less than 10 % for all three samples (27, 25 and 23 μL) (Figure 28). It is believed that the above yields of dGNRs are the highest values reported in studies of anisotropic silica coating of GNRs.[163,164] When 21 uL of TEOS was added, the total yield of end-coated GNRs was over 90 % but with a relatively large fraction of nanolollipops. As discussed, nanolollipops originated from dGNRs with silica spheres detached from GNRs. It was reported that TEOS at low volumes may not fully surmount the energy barrier of the CTAB bilayer on ends.[164] In these conditions, silica does not reach the gold surface and penetrates the CTAB bilayer only partially. The resulting silica spheres could have lower density foundations and be mechanically less robust, generating more nanolollipops. Even though detached silica spheres were present in all samples, considerably higher yields of dGNRs (>87%) were achieved with most TEOS volumes used in this study (i.e., 27, 25, 23 μL), indicating an improved efficiency and stability of the dGNR morphology. Furthermore, the thickness of silica coatings was investigated to determine whether varying the amount of TEOS also produces different sizes of end caps. It was found that the radius of attached silica did not vary significantly between the four samples and remained approximately 20 nm. Varying volumes of TEOS in this region to optimize the dGNR yield therefore did not cause significant changes in proportions of terminal silica spheres.

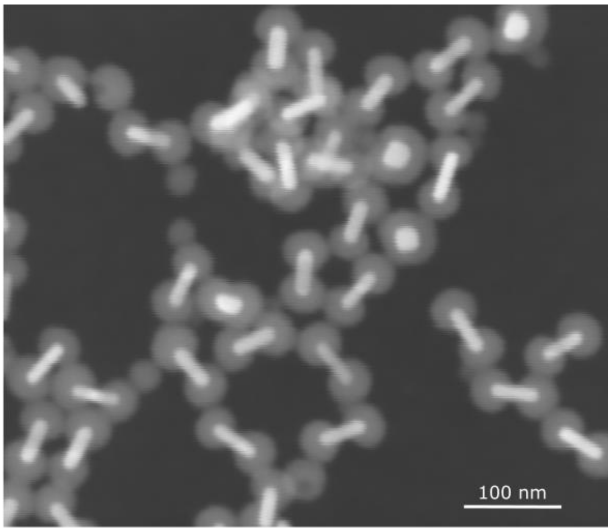

Figure 28: STEM image of silica-coated GNRs with a high count of dGNRs. The aspect ratio of gold cores was ~3.6.

3.6. Conclusions

This chapter has systemically investigated the effect of various reaction parameters on the morphology of silica coating on GNRs. The key factor in end-functionalization of GNRs was indicated to be the irregular CTAB layer on nanorod ends, which allows the hydrolyzed TEOS species to directly access the gold surface and form silica shells. It was observed that temperature significantly influences the shell morphology and the final yield of dGNRs by affecting the solubility of CTAB. The growth of silica is hampered at 19 °C due to the low solubility of CTAB that can be, to some degree, compensated by increasing the concentration of free surfactant in the solution. This hindrance seems to be eliminated at 21 and 23 °C, when sufficient amounts of CTAB are dissolved and are available for the formation of CTAB/silica building blocks that assemble into shells.

Both the temperature and variations in CTAB concentration cause a transition between the three types of nanostructures, yielding more end-functionalized GNRs than core-shell GNRs at lower temperatures and lower CTAB concentrations. The stability of coating improves with increasing temperature and concentration of CTAB, gradually decreasing the number of nanolollipops with separated terminal silica spheres. In some cases, silica can extend to the sides and create a porous layer of varying thickness that links two terminal silica spheres and may represent a potential complication for further site-selective functionalization. The presence of a silica side layer suggests that silica spheres grow first directly on ends of GNRs and then merge as a result of an ongoing deposition of remaining CTAB with TEOS.

The results further suggest that the aspect ratio of GNRs determines the stability of the dumbbell shape by establishing the inter-sphere distance as well as the compactness of the CTAB bilayer. Therefore, GNRs with higher aspect ratio seem to be better suited for end-functionalization. The full coating was found to be the dominant shell morphology for GNRs with low aspect ratios. Furthermore, it has been demonstrated that with the right combination of aspect ratio and reaction parameters, the dumbbell shape as well as the yield of dGNRs may exceed even 90 %, which is the highest yield reported so far.

The dumbbell-like morphology is an interesting platform with two binding sites on its ends that are available for additional surface modification. A direct loading of porous coating with various reporter molecules is also possible, so that these nanostructures may find application in metal-enhanced fluorescence and SERS. Fluorophores and other probes that could benefit from the spatially restricted localization and interaction with strong longitudinal plasmon fields are an obvious choice for investigating the enhancing potential of this nanostructure on their performance. Moreover, due to the bare sides of gold cores, gold can directly participate in oxidation reactions when paired with catalysts, which makes them particularly suitable for photocatalytic systems.

4. Fluorescent Spectroscopy of Bovine Serum Albumin (BSA) and BSA-Au Nanoclusters on Aluminium foil

4.1. Introduction

4.1.1. Considerations for Metal-enhanced Fluorescence on Aluminium foil

Metal-enhanced fluorescence (MEF) has been performed in Vis and NIR spectrum mainly by using Au and Ag nanostructures, benefiting from their well-established methods of synthesis, wide selection of shapes and accurate tuneability of their plasmon resonance within this spectral region.[11,191] Moving to the UV region greatly limits the selection of suitable plasmonic materials and nanostructures, as Au and Ag do not support good SPR in UV due to inter-band transitions that cause dissipative channels for plasmon resonances shorter than approximately 500 and 310 nm, respectively.[79] A large number of important biomolecules such as DNA, amino acids and proteins,[88,191] exhibit an intrinsic UV and blue fluorescence with low quantum efficiency, which drives the need to extend plasmonics into this part of EM spectrum. Taking advantage of the enhancing plasmonic effect in the UV region would be highly beneficial especially for biosensing and label-free detection. For this reason, exploring plasmonic capabilities of Al nanostructures has become increasingly popular due to its intrinsic ability to support tunable SPR in a broad frequency range across the UV-Vis-NIR spectrum.[79,91,192] The additional advantages of Al are undoubtedly its affordable cost and stability due to the self-limiting native surface oxide layer which provides binding sites for a number of functional groups (silanes, carbonyls, phosphates), allowing different surface-molecule interactions and binding pathways compared with Au and Ag.[7,193] Exploiting the applicability of the Al SPR in the UV region is relevant particularly for the development of efficient and inexpensive devices capable of refractive index sensing, surface-enhanced phenomena (SERS, MEF) and photocatalysis.[79,88,191–195] One such substrate that is universally available and can be readily used without extensive preparation is a commercial aluminium foil. Several studies have shown that using the Al foil as a stand-alone substrate in Vis spectral window can lead to fluorescence enhancements of quantum dots that are comparable to those induced by some conventional Al, Au and Ag plasmonic films.[196,197] For example, Sultangaziyev et al. utilized an untreated Al foil for MEF of CdSeS/ZnS quantum dots *and E. coli* bacterial cells labelled with CdSeS/ZnS quantum dots and observed an enhanced fluorescence emission that was comparable with the emission on Au and Al films as well as an improved contrast of the emission from labelled cells.[196] Bukasov et al. observed a high contrast MEF from *E. coli* cells labelled with carbon nanodots on the Al foil and also achieved enhancements similar to those from Au and Al films.[197] Fluorescence emission of cells labelled with graphene quantum dots was also enhanced on the Al foil, albeit with lower enhancement factors than from other substrates. These initial reports indicate that the Al foil is a cost-effective substrate suitable for surface-enhanced techniques which can compete with other metallic films. It is believed that, to this date, the commercial Al foil has been utilized primarily for MEF in the Vis region and has not been applied in the UV where the range of available efficient UV-active substrates is limited.

4.1.2. Bovine Serum Albumin-encapsulated Gold Nanoclusters (BSA-AuNC)

Bovine serum albumin (BSA) is a suitable candidate for exploring enhancing capabilities of metallic substrates in the UV due to its excitation and emission characteristics being within this spectral region. Serum albumin is the most abundant protein in mammalian plasma and is responsible for transporting various endogenous and exogenous compounds such as hormones and fatty acids in the blood stream.[198] Due to its high affinity to many different types of molecules, including drug molecules, amino acids, steroids as well as close similarity to human serum albumin, BSA is often used as a model system for studying interactions of albumins with pharmaceuticals.[198–200]

BSA is a heart-shaped globular protein that consists of 583 amino acids arranged into a single polypeptide chain with molecular weight of 66.5 kDa (84 x 84 x 31.5 Å).[201] The molecule of BSA molecule can be divided into 3 domains (I, II and III) and each domain can be further divided into 2 subdomains (A, B) (Figure 29).[202] Of the fluorescent amino acids in the BSA (tyrosine, tryptophan, phenylalanine), tryptophan (Trp 134 and Trp 212) located in subdomains IB and IIA has the highest quantum yield (~0.20) and is the main contributor to the intrinsic fluorescence of BSA.[26] Tryptophan exhibits fluorescence emission in the UV region with the emission maximum at around 340 nm that can be excited from 240 to 300 nm. However, the absorption spectrum of tryptophan overlaps with the other two amino acids below 290 nm and its selective excitation is possible only in a narrow ~10 nm band from 290 to 300 nm.[26] BSA is also prone to conformational changes at alkaline and acidic pH.[203] Such changes alter the local environment of tryptophan residues which directly affects their fluorescence emission. For this reason, the fluorescence of tryptophan is often used as an indicator of conformation changes.[26] Considering the pH sensitivity of BSA, the data presented in this work were collected at pH ~7 where the BSA is known to assume a stable form.

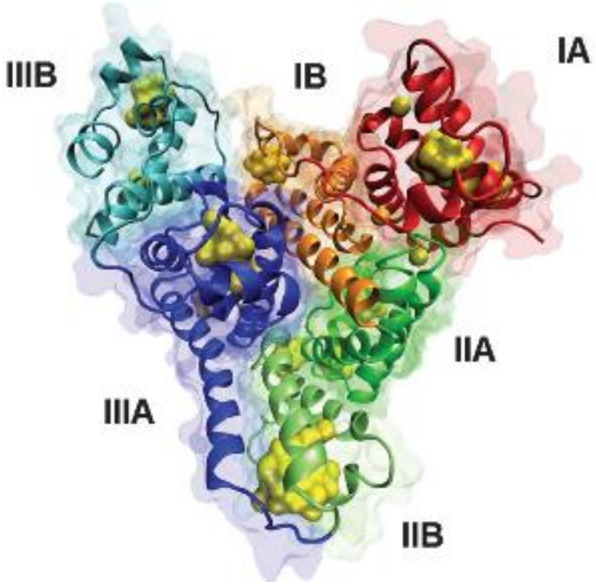

Figure 29: 3D Structure of BSA with encapsulated AuNCs obtained by molecular dynamic simulations. Two large fluorescent clusters (yellow globules) are located within domains IA and IIB with additional smaller clusters dispersed through the protein. Tryptophan residues are located in domains IIA and IB. Reproduced from Ref. [202] with permission from the Royal Society of Chemistry.

Another property of the BSA is the ability to reduce and encapsulate gold atoms, producing stable red fluorescent AuNCs.[202,204,205] This technique was developed by Xie et al. who used a commercially available BSA for a one-pot synthesis of AuNCs.[206] The process takes advantage of the reducing ability of tyrosine residues in the BSA at alkaline pH and the high affinity of gold to sulphur in thiol groups of cysteine residues. Tyrosine is able to reduce Au^{3+} through its phenolic groups and cysteine residues, located in hydrophobic pockets of the BSA, stabilize Au atoms through the stable thiol linkage and facilitate the nucleation of AuNCs that consist of 25 atoms (Au_{25})[206] in the subdomain IIB.[202]

In general, unlike GNPs, smaller AuNCs (< 2 nm) do not support LSPR because of the quantization of the continuous conduction band into discrete energy levels.[207] Instead, AuNCs emit fluorescence in Vis-NIR. Compared to conventional fluorophores, fluorescent AuNCs exhibit many superior properties such as excellent stability, low toxicity and large Stokes shift.[205,208] On the other hand, a major limiting factor in the application of AuNCs in fluorescence-based techniques is the low quantum yield (typically below 20 %).[206,209] Another property that sets AuNCs apart from fluorophores is their long μs fluorescence lifetime. Due to the quantum confinement effect, optical and electronic properties of AuNCs are highly dependent on the number of Au atoms[207] that is determined by stabilizing surface ligands.[205] Therefore, selecting the appropriate ligand is particularly important when designing AuNC-based fluorescent probes. Not only ligands provide protection of AuNCs from being quenched by oxygen in air and from collisional quenching, but fluorescence properties of AuNCs are also determined by the ligand-directed charge transfer from S to AuNCs.[210,211] It has been shown that thiolate-protected Au_{25}NCs exhibit a core-shell structure where 13 Au(0) atoms form an icosahedral Au core (Au_{13}) surrounded by the outer shell that is made of six dimeric [-S-Au(I)-S-Au(I)-S-] staples.[211,212] The ability of ligands to donate electrons to AuNCs can lead to a significant enhancement of quantum yield, particularly in systems where ligands contain electron-rich atoms, such as O and N, which can donate delocalized electrons to the Au core.[211]

To utilize BSA-AuNCs as fluorescent probes, their fluorescence properties must be considered. The absorption is very broad, ranging from 280 nm to 600 nm.[213,214] The UV and blue part of this absorption heavily overlaps the emission band of tryptophan which facilitates FRET to AuNCs and provides an additional excitation pathway.[202,213] The red fluorescence emission of BSA-AuNCs is centred at around ~670 nm.[206] BSA-AuNCs also exhibit the characteristic long multi-exponential fluorescence lifetime with one lifetime component of 1 μs and a longer component of 2 μs.[212] The quantum yield of as-prepared BSA-AuNCs is around 6 %,[206] which is rather low and makes BSA-AuNCs relevant for MEF and the evaluation of fluorescence-enhancing metallic substrates, such as the Al foil, as MEF is known to have stronger effect on fluorescent species with low quantum yields.[26]

The origin of the red BSA-AuNC emission is still debated. Wen et al.[214,215] investigated the red fluorescence using the aforementioned core-shell structure of thiolate-stabilized AuNCs. Their hypothesis was based on AuNCs being stabilized in BSA via thiol linkage between Au atoms and surrounding cysteine residues. It was revealed that the red fluorescence of BSA-AuNCs is composed of two emission bands; a major band at 710 nm and a minor band at 640 nm.[214] The major band was proposed to originate from the icosahedral Au core (Au_{13}) and the minor band was assigned to the outer Au(I)-S shell.[212,214] The relevance of the model is supported by the fact that small BSA-AuNCs such as BSA-Au_8NCs do not exhibit the long lifetime component due to the absence of the shell.[215] The mechanism of the red fluorescence was attributed to a thermally activated delayed fluorescence associated with the formation of ligand-localized triplet states and ligand-to-metal charge transfer triplet states in the Au(I)-S shell.[215,216] A very small energy gap (30.6 meV) between the triplet and singlet states of AuNCs reduces the spin-forbidden character of the transition and allows for an efficient intersystem crossing to the triplet state and a reverse intersystem crossing to the singlet state that leads to the delayed fluorescence. The core-shell model was considered also by Xie et al. who developed the aforementioned one-pot synthesis of BSA-AuNCs used in this thesis.[206]

To date, fluorescent BSA-AuNCs have been utilized in a wide range of sensing and imaging applications as signal molecules.[208,217,218] The detection mechanism is generally based on an analyte-induced quenching of the AuNC fluorescence through interactions with either the BSA or AuNCs.[217] BSA-AuNCs have shown a particularly high sensitivity to the presence of some heavy metal ions which are known to be highly toxic to humans as well as to the environment. Xie et al. used BSA-AuNCs for a selective label-free detection of Hg^{2+} ions.[219] The sensing mechanism was based on a strong metal-metal interactions between Hg^{2+} and the AuNC surface, which caused quenching of the AuNC fluorescence. The technique was further used for the development of nitrocellulose test strips loaded with BSA-AuNCs which could be used for a rapid visual estimation of Hg^{2+} levels in water. BSA-AuNCs can be also used for the detection of Cu^{2+} ions which are known to bind to prion proteins and cause their misfolding and fibrilization, leading to abnormal functioning of the protein and various neurodegenerative diseases.[220] The binding of Cu^{2+} also causes quenching of the BSA-AuNC fluorescence but the mechanism is driven by a direct binding of Cu^{2+} to the BSA rather than through interactions with AuNCs. The binding of Cu^{2+} promotes an intersystem crossing of excited-state electrons of AuNCs and reduces the fluorescence emission intensity through energy losses. Durgadas et al. employed BSA-AuNCs for the imaging of Cu^{2+} ions in live

HeLa cells and demonstrated a selective quenching and recovery of the AuNC fluorescence by adding an appropriate chelator, glycine.[220] In addition to the detection of heavy metal ions, BSA-AuNCs can be used to detect harmful anions, such as cyanide (CN^-), nitrite (NO^{2-}) and sulfide (S^{2-}), through the quenching of AuNC fluorescence caused by an aggregation of BSA (NO^{2-}) or a degradation of the BSA-AuNC structure and formation of complexes with Au (CN^-, S^{2-}).[217,218]

The detection of biomolecules with BSA-AuNCs as a fluorescent probe has been successfully realized for dopamine, a vital neurotransmitter in human nervous system.[205] Tao et al. developed a highly sensitive and selective fluorometric technique of dopamine detection using BSA-AuNCs in various complex environments.[221] The presence of dopamine caused quenching of the AuNC fluorescence through a dynamic photo-induced electron transfer from the electrostatically attached dopamine to AuNCs. Changes in the BSA-AuNC emission at various levels of dopamine were visible by the naked eye under UV illumination and the detection limit of 10 nM, achieved with as-prepared BSA-AuNCs, suggests a promising potential for diagnostic purposes. Benefits of using BSA-AuNCs as drug carriers and contrast agents in diagnostics and therapy have been explored as well, taking advantage of the biocompatibility and affinity of BSA to bind various biomolecules.[217] Wu et al. reported on the first use of unmodified BSA-AuNCs as contrast agents for an *in vivo* tumour fluorescence imaging.[222] In this application, the NIR wavelength of BSA-AuNC emission offered a deeper tissue penetration and visualization of labelled tissues with good contrast. Since then, various functionalization strategies have been employed to improve the performance of BSA-AuNCs. For example, BSA-AuNCs functionalized with tumour target molecules, such as herceptin and folic acid, exhibit an enhanced cellular uptake and can be used for highly specific drug delivery and imaging of tumours with high expression of corresponding receptors.[205,217]

In this chapter, the applicability of a commercial Al foil as an affordable fluorescence-enhancing substrate was, for the first time, investigated using BSA and BSA-AuNCs as probe molecules. Fluorescence characteristics of both complexes were examined through steady-state and time-resolved fluorescence spectroscopy of amino acid tryptophan and AuNCs. Protein complexes were immobilized on both sides (shiny and matt) of the Al foil via passive adsorption and air-dried. It was found that immobilization on planar substrates induced only minor changes in the BSA’s structure and that the protein most likely solidified in a folded form which preserved the fluorescence emission upon drying. The two sides of the Al foil induced opposite effects on fluorescence emissions of tryptophan and AuNCs. The matt side supported more than a 2-fold fluorescence enhancement of tryptophan and AuNC emission intensities compared to those on quartz. The enhancement was associated with the nanoscale corrugation of the matt side which supported the excitation of locally enhanced electromagnetic fields and was most likely responsible for an improved FRET from tryptophan to AuNCs as well as a more efficient excitation of tryptophan and AuNCs. The shiny side caused a decrease in fluorescence emissions of tryptophan and AuNCs which was attributed to the surface energy transfer (SET) and reduced FRET efficiency on the shiny Al surface. The enhancement of the AuNC fluorescence emission indicates that the matt side of the Al foil can be used for MEF beyond UV as far as the blue region of visible spectrum.

4.2. Experimental

4.2.1. Materials

All chemicals were purchased from Sigma-Aldrich. Bovine serum albumin (lyophilized powder, > 99 %), gold(III) chloride trihydrate (HAuCl4), Sodium hydroxide (NaOH), phosphate buffered saline (PBS), distilled water. Wrapping aluminium foil was purchased from Sainsbury’s.

4.2.2. Sample Preparation

Synthesis of BSA-AuNCs

Synthesis of fluorescent bovine serum albumin protected gold nanocluster (BSA-AuNC) was carried out using a one pot-method reported by Xie et al..[206] First, 17 mg of $HAuCl_4$ is dissolved in 5 mL of distilled water (10 mM) and mixed at 37 °C. Then, the solution was mixed with an aqueous solution of BSA (750 μM) made by dissolving 250 mg of BSA in 5 mL of distilled water at 37 °C. The mixture was vigorously stirred for 2 minutes. After that, 0.5 mL of 1M NaOH was added into the mixture to set the pH to >10 while stirred for 6 hours at 37 °C in a water bath. The mixture was then transferred to a brown bottle, wrapped in a non-transparent foil, and was stored in an oven for 48 hours at 37 °C. The BSA-AuNC solution was then purified via dialysis using PBS buffer solution (pH

~7.4) and dialysis cassettes with a molecular weight cut-off 10,000 Da. After that, the solution was stored in dark. Due to the high concentrations of the as synthesized BSA-AuNC solution, the solution should be diluted at least to 10 % of its original concentration before taking any measurements.

Deposition of BSA and BSA-AuNC on the Al foil

BSA and BSA-AuNC solutions made in the first step and diluted to 10 % of their original concentration were pipetted (100 uL) on strips of a standard aluminium foil (thickness ~0.016 mm) (matt and shiny sides) attached to a microscope slide. All substrates were cleaned with distilled water prior BSA and BSA-AuNC deposition. Same procedure was carried out for the preparation of reference samples on a quartz microscope slide and same concentrations were also used for measurements in a solution phase. Protein solutions on substrates were then air dried at room temperature for several hours before fluorescence measurements. An example of images of dried BSA solutions on the three substrates is shown in Figure 30.

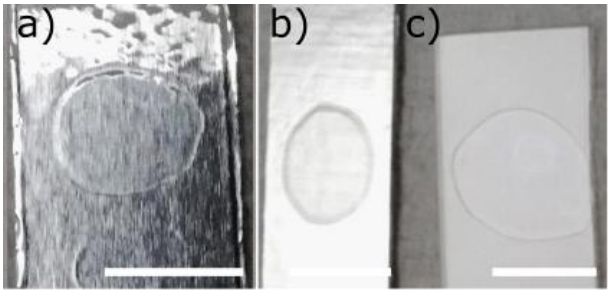

Figure 30: Photographic images of BSA on a) matt, b) shiny side of Al foil and c) quartz slide. The scale bar represents1 cm.

4.2.3. Surface Characterization

SEM imaging

The surface of the aluminium foil was characterized via SEM using a FEI Quanta 250 FEG-ESEM scanning electron microscope at an acceleration voltage of 5 kV.

Reflectivity measurements

Reflectivity measurements were carried out using PHOTON RT UV-VIS-MWIR Spectrophotometer for coaters in the range of wavelength from 250 to 1000 nm at angles of 8 °, 30 °, 45 ° (with respect to a substrates' normal). The reflected light was collected at angles of 16 °, 60 °, 90 °.

4.2.4. Fluorescence Measurements and Data Analysis

Fluorescence steady-state measurements

Fluorescence measurements were performed using fluorescence spectrometer Fluorolog-3 (HORIBA) at excitation wavelengths 295 and 463 nm and the fluorescence emission was collected from 310 nm – 800 nm with a 1 nm increment and an integration time 0.1 s. All samples were excited at an angle of 30 °. Excitation and emission slit bandwidths were set to 5 nm. All collected fluorescence emission spectra were treated with excitation and emission wavelength correction factors.

Fluorescence time-resolved measurements

Time-resolved fluorescence data were obtained using the TCSPC kit HORIBA DeltaFlex described earlier. Excitation sources were pulsed NanoLED (HORIBA) with a peak emission wavelength of 295 nm and a 463 nm DeltaDiode (HORIBA). All samples were excited vertically at an angle of 30 °. Fluorescence emission was detected at 340 nm (BSA and BSA-AuNC) and 670 nm (AuNC) with time ranges of 100 ns (BSA) and 13 μs (AuNCs) until 10 000 counts in the peak were collected. The AuNCs emission was collected using 645 nm long-pass filter to reduce the contribution of scattered light, and a 335 nm long-pass filter was used to collect the tryptophan emission. The polarizer remained fixed at the magic angle. The TCSPC data analysis for tryptophan emission was performed in the software DAS6 (HORIBA) via the nonlinear least squares (NLLS) reconvolution analysis described earlier in this work. Tail fitting of decay curves was employed to extract fluorescence lifetimes of AuNCs.[223] The intensity weighted average lifetime (τ_{avg}) for n lifetime components (τ_i) with corresponding fluorescence lifetime amplitudes (B_i) was calculated using Equation 41[26,212].

$$\tau_{avg} = \frac{\sum_{i=1}^{n} B_i \tau_i^2}{\sum_{i=1}^{n} B_i \tau_i} \qquad \textit{Equation 41}$$

4.3. Results and Discussion

4.3.1. Characterization of BSA and BSA-AuNCs

Initially, fluorescence properties of both BSA and BSA-AuNCs were characterized via steady-state and time-resolved fluorescence techniques. To maintain the stability of both systems, measurements were carried out at a neutral pH.[202] Molar concentrations of protein solutions were also kept constant at 37.6 µM. Figure 31 shows absorption/emission spectra and a fluorescence decay of BSA. The absorption band reaches maximum at ~278 nm and the emission maximum is located at around 340 nm. The wavelength of 295 nm was selected for the selective excitation of tryptophan residues and to avoid the excitation of other intrinsic fluorescent amino acids (tyrosine and phenylalanine) present in the BSA. The fluorescent decay of BSA was collected via TCSPC and was best fit to a 2-exponential decay, producing two lifetime components $\tau_1 = 2.99 \pm 0.08$ ns and $\tau_2 = 6.75 \pm 0.01$ ns with relative contributions 13.41 % and 86.59 %, respectively. These are in agreement with lifetimes of the BSA reported in the literature.[199,213]

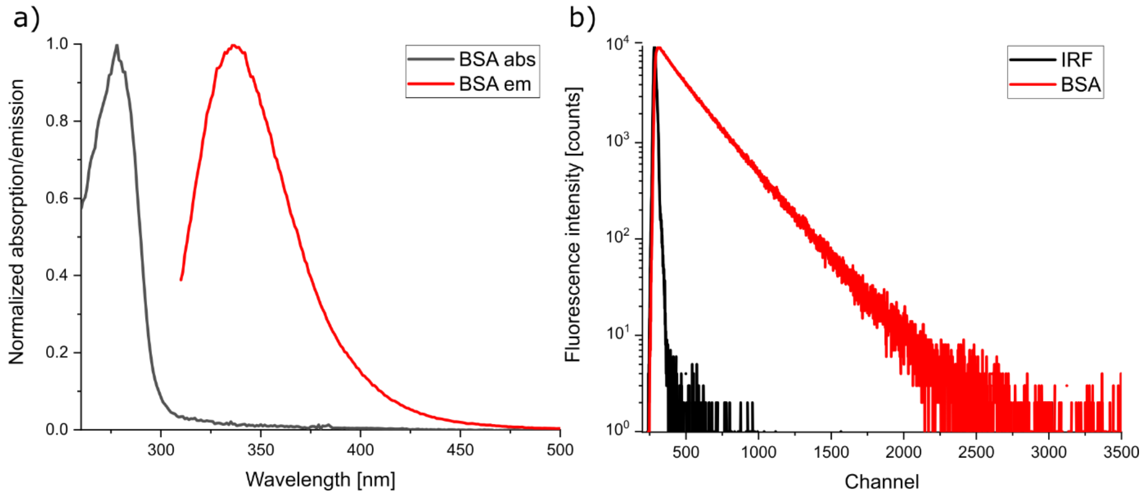

Figure 31: Absorption and fluorescence spectra (left) and a fluorescence decay curve (right) of BSA. The sample was excited at 295 nm and the emission collected over a 310 – 500 nm range. The same excitation wavelength was used to collect the fluorescence decay at 340 nm.

Fluorescent properties of the BSA-AuNC complex were characterized using a similar approach (Figure 32). A notable feature of the BSA-AuNCs' absorption spectrum compared to that of BSA is the broad absorption band with a descending shoulder from

300 to 600 nm. This allows the excitation of AuNC fluorescence within a wide range of wavelengths including UV. When the complex is excited at 295 nm, the tryptophan emission is quenched due to the FRET to AuNCs which becomes the main excitation mechanism.[202,213] The emission maximum of tryptophan is also blue-shifted to 327 nm due to the conformational change that BSA undergoes to incorporate AuNCs (Figure 32b), which draws tryptophan residues deeper into the more hydrophobic core where they are better shieled from the solvent.[224] The second excitation of AuNCs was done at 463 nm near the absorption maximum at around 470 nm.[206,213] The fluorescence emission of AuNCs exhibited maxima at 680 nm for the 295 nm excitation and 675 nm for the 463 nm excitation. It is clear from Figure 32b that the UV excitation is a more efficient excitation pathway compared to the direct excitation at 463 nm.

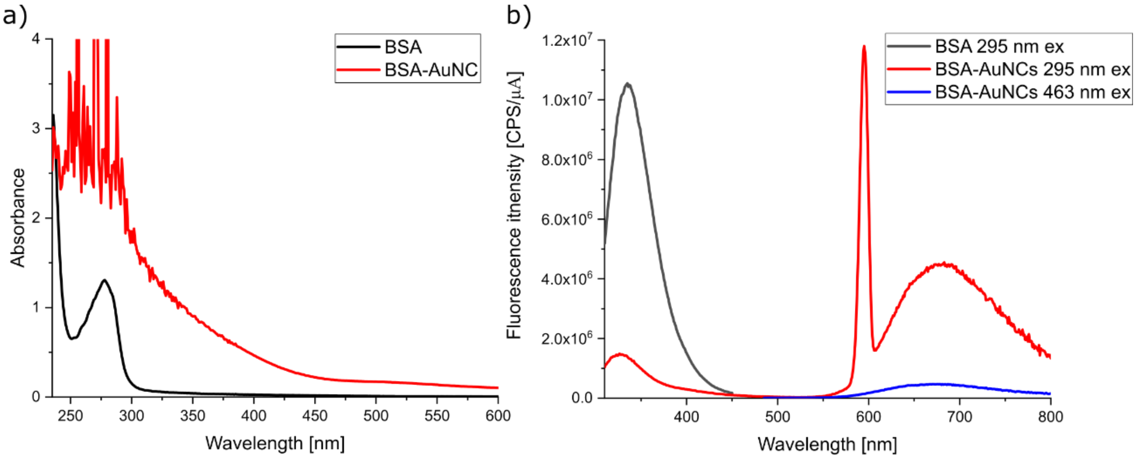

Figure 32: Absorption (left) and fluorescence emission (right) spectra of BSA and BSA-AuNC (37.5 µM). The absorption spectrum of BSA-AuNC reaches saturation levels of the spectrometer below 300 nm due to strong scattering with a broad absorption band from 300 to 600 nm. Fluorescence emission of tryptophan in BSA-AuNCs is quenched in the presence of AuNCs due to FRET which causes the increase in the fluorescence intensity of AuNCs compared to the selective excitation of AuNCs at 463 nm.

Next were analysed fluorescence lifetimes of tryptophan and AuNCs using TCSPC (Figure 33). The lifetime analysis of AuNCs was carried out at both excitation wavelengths of 295 nm and 463 nm (Table 5). The fluorescence decay of tryptophan was fitted with a 3-exponential function, producing lifetimes of $\tau_1 = 0.67 \pm 0.01$ ns, $\tau_2 = 2.37 \pm 0.08$ ns and $\tau_3 = 5.64 \pm 0.04$ ns. The decrease in fluorescence lifetime of tryptophan compared to that of native BSA is a result of the aforementioned FRET to nearby AuNCs.[213] Fluorescence decays of AuNCs were found to be best fit to a 3-exponential model which revealed long (μs) lifetimes characteristic to AuNCs.[212] The shortest lifetime component was assigned to scattering. When excited at 295 nm, resulting lifetimes were τ_1 = 119 ± 8 ns, τ_2 = 1001 ± 28 ns and τ_3 = 2272 ± 7 ns, with the average lifetime being τ_{avg} = 2101 ns. The 463 nm excitation produced similar lifetimes of τ_1 = 98 ± 6 ns, τ_2 = 935 ± 27 ns and τ_3 = 2247 ± 75 ns with the average lifetime being τ_{avg} = 2081 ns. The origin of the two long lifetime components is related to the aforementioned core-shell structure of AuNCs[212,215] where the longest τ_3 component arises from the AuNC shell and the shorter τ_2 component is associated with the Au core.[225]

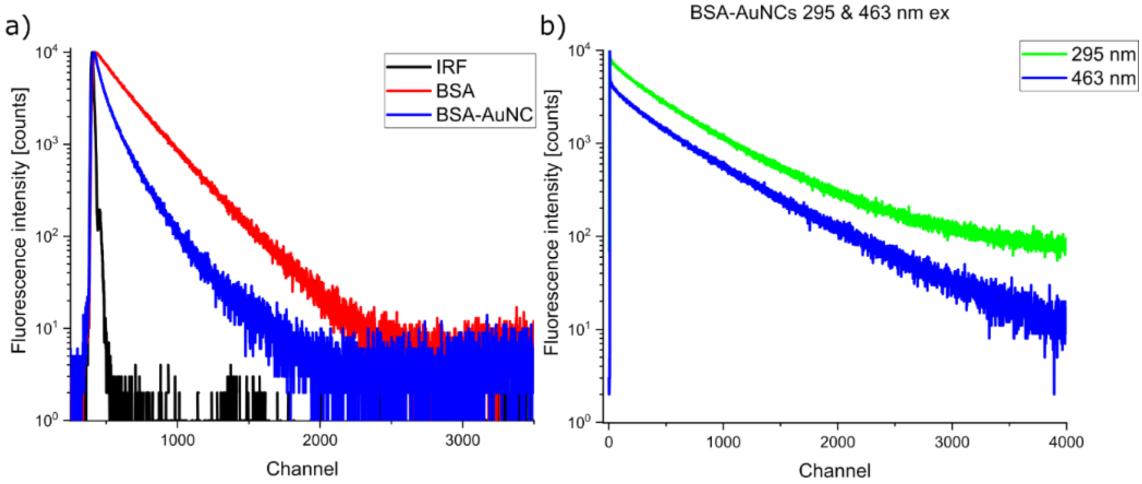

Figure 33: Fluorescence decays of BSA and BSA-AuNC collected at a) 340 nm after excitation at 295 nm and b) AuNC decays collected at 670 nm after excitation at 295 and 463 nm.

Table 5: Fluorescence lifetime parameters associated with fluorescence decay measurements of BSA-AuNC and BSA from Figure 33.

Sample	τ_1 [ns]	B_1 [%]	τ_2 [ns]	B_2 [%]	τ_3 [ns]	B_3[%]	χ^2	τ_{avg} [ns]
BSA			2.99 ± 0.08	13.41	6.75 ± 0.01	86.59	1.02	6.25
BSA-AuNCs 295x340 nm	0.67±0.01	20.38	2.37±0.08	47.73	5.64±0.04	31.89	1.18	4.21
BSA-AuNCs 295x670 nm	119 ± 8	0.86	1001 ± 28	25.69	2272 ± 7	73.45	1.11	2101
BSA-AuNCs 463x670 nm	98 ± 6	1.08	935 ± 27	25.46	2247 ± 75	73.46	1.10	2081

4.3.2. Fluorescence Spectroscopy of BSA on Aluminium Foil

Further work with BSA was performed on the Al foil. A BSA solution (2.5 mg/mL) was immobilized and dried on stripes of Al foil and a quartz microscope slide which was selected as a reference substrate. The effect of immobilization on the Al foil on fluorescence properties of BSA was investigated through same steady-state and time-resolved techniques used to characterize its native form.

First, the surface of the Al foil was characterized using SEM. Surface characteristics of metallic substrates are an important parameter as surface irregularities and pattering affect optical as well as wetting properties and ultimately the distribution of analytes on the surface.[226] The Al foil has two sides with different surface morphologies (Figure 34) and visual appearances – shiny and matt. Their characteristic appearances are a result of the manufacturing process where the foil is rolled with two layers pressed together that become matt sides, while sides that are milled without being in contact with other Al layers become shiny. SEM analysis of the shiny side of the Al foil (sAl foil) revealed protruding rolling stripes of varying (μm scale) width (Figure 34a) as well as a smooth surface on top of rolling stripes and in the interstitial space (Figure 34b). The surface of the matt side of the Al foil (mAl foil) does not possess such pattering (Figure 34c) but exhibits a nanoscale corrugation (Figure 34d).

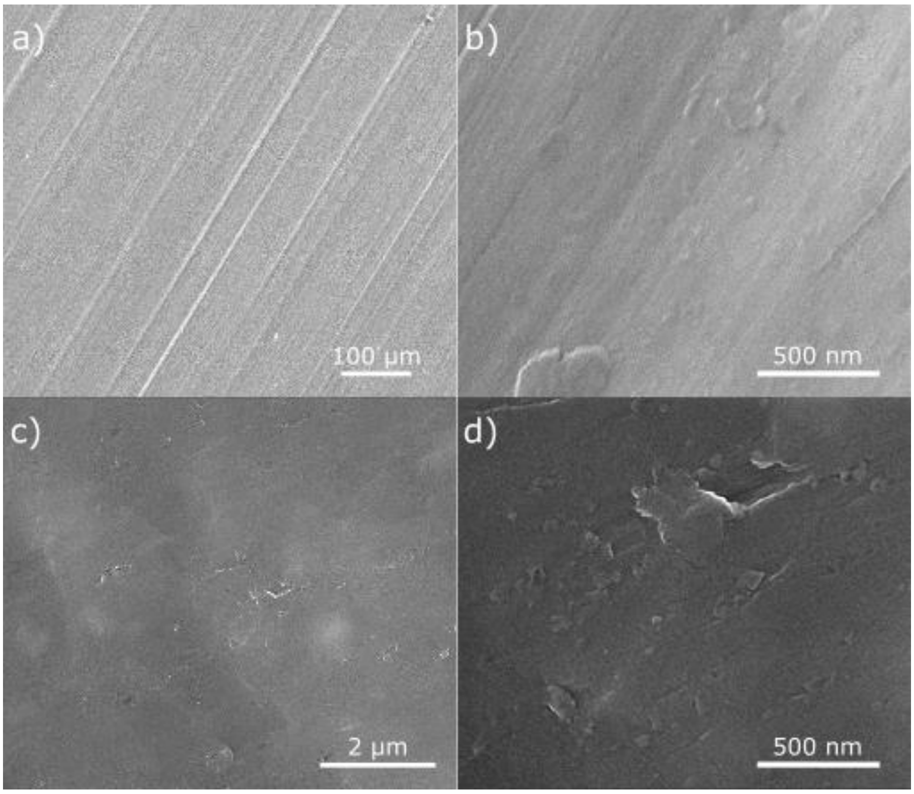

Figure 34: SEM images of the a-b) shiny side and c-d) the matt side of the Al foil.

Despite obvious differences in the surface morphology (Figure 34) as well as the appearance, reflectivity measurements revealed almost identical reflectance spectra for both sides of the Al foil (Figure 35). Small-scale surface features are generally the reason for a low contribution of specular reflectance as can be seen in the reflectivity of the mAl foil, whereas the smooth surface of sAl foil could be expected to increase the specular reflectivity of the surface. Pozzobon et al. performed reflectivity measurements on the Al foil using an integration sphere and their results showed similar shapes of specular reflectivity spectra but a higher specular reflectance of the shiny side by approximately 20 %.[227] This discrepancy could be ascribed to surface features on the two sides of the Al foil.[227] Rolling stripes, determined by the number of roll passings, can increase the macroscopic roughness of the shiny surface which may reduce specular reflectivity, making the reflection more anisotropic.

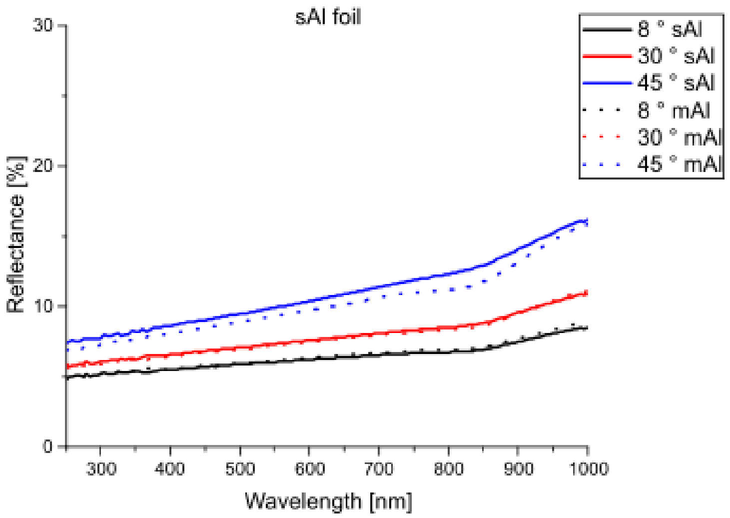

Figure 35: Reflectance spectra of shiny and matt side of Al foil collected at various angles of illumination.

Substrates coated with BSA were analysed first in order to investigate the less complex tryptophan emission in the native BSA. Fluorescence emission spectra of BSA on substrates were compared in Figure 36a,b. The fluorescence emission of BSA was found to be strongest on the mAl foil while fluorescence intensities collected from other substrates were lower by approximately 50 %. Changes in the fluorescence intensity of BSA on metallic substrates can be expressed as fluorescent enhancement factors (EF) using the following equation[228,229]:

$$EF = \frac{F}{F_0}, \qquad \textit{Equation 42}$$

where F and F_0 are fluorescence intensities of BSA on Al substrates and quartz, respectively. Calculated EFs are plotted in Figure 36c, showing the highest EF being 2.1 for BSA on the mAl foil. Emission maxima of the BSA on quartz and sAl foil blue shifted by 16 nm to 321 nm compared to the BSA solution (337 nm). The emission maximum of BSA on mAl foil was slightly red-shifted by 5 nm to 342 nm.

The effect of immobilization on the structure and fluorescence of BSA is usually investigated (theoretically and experimentally) in the solution phase where BSA is adsorbed on nanoparticles[230–232] and continuous surfaces[233–239] with little information being available about fluorescence properties of the “dry-state” BSA. Changes of the environment (pH, presence of nanoparticles and surfaces, aggregation, molecular crowding, …)[26,230–232] have been known to induce conformational changes of BSA. The adaptability of BSA stems from its relatively weak internal stability and different locations of hydrophobic and hydrophilic regions due to which the protein can change the structure based on the nature of its surroundings.[212,230,237] Consequently, every such change can potentially alter the local environment of tryptophan residues and influence the intrinsic tryptophan fluorescence.

When the solvent is evaporated and the final arrangement of the protein is established, the protein is expected to solidify[226] in the folded form. Its ability to emit fluorescence was clearly preserved. Even though the protein was not denatured by the solvent evaporation, the tryptophan emission was influenced by the adsorption. Determining the structure of the dry-state BSA is beyond the scope of this work as the protein was intended to be used as a signal molecule. Therefore, the information about the exact final geometry and the conformation of immobilized BSA in this work is limited. However, it is hoped that fluorescence lifetime analysis of the tryptophan emission could be used to determine the mechanism of fluorescence enhancement on the Al foil and gain a better understanding of differences in the BSA emission on substrates.

Fluorescence decays of tryptophan on substrates are displayed in Figure 36d. Looking at the shape of fluorescence decays of tryptophan in BSA suggests that the decay analysis would not be straightforward. The close resemblance of short fluorescence decays collected from the Al foil with the IRF caused the fitting process to be problematic and a good fit was not possible to achieve for the sAl foil by considering the whole decay curve. To work around this, the reconvolution analysis was applied on the tailof the decay.[223] The same method of fitting was applied also to other decays in order to maintain a consistent methodology. Collected decay curves were best fit to a 3-exponential model. The data showed reduced fluorescence lifetimes on all substrates (τ_{avg} = 4.08 ns (quartz) > 3.34 ns (mAl foil) > 2.90 ns (sAl foil)) (Table 6). The reduction of tryptophan lifetime on quartz is surprising as the protein immobilization and the solvent evaporation were expected to reduce the effect of collisional quenching and related non-radiative decay pathways which should lead to the increase in fluorescence lifetime and quantum yield. Thus, the decrease in lifetimes is indicative of only small contribution of the collisional quenching factor. Therefore, the change in fluorescence emission on quartz could be attributed to effects such as the influence of the surface and neighbouring molecules as well as induced modifications of the global structure of BSA and local microenvironments of tryptophan residues. Further decreased fluorescence lifetimes on the Al foil were expected as such change is often the result of interactions with metallic surfaces.

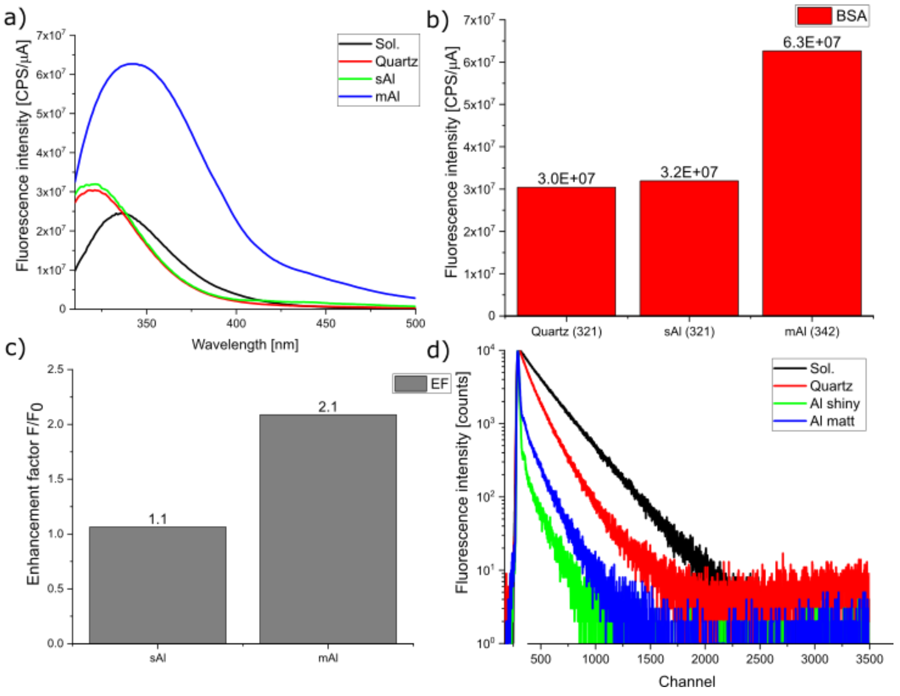

Figure 36: Fluorescence emission spectra of BSA on various substrates (295 nm ex) a), peak fluorescence intensities of BSA on each substrate b), enhancement factors calculated for BSA on the Al foil c), and fluorescence decays of BSA collected at 340 nm d).

Table 6: Fluorescence lifetimes of BSA on selected substrates. Excitation 295 nm, emission 340 nm.

Sample	τ_1 [ns]	B_1 [%]	τ_2 [ns]	B_2 [%]	τ_3 [ns]	B_3 [%]	χ^2	τ_{avg} [ns]
Sol.			2.99 ± 0.08	13.41	6.75 ± 0.01	86.59	1.02	6.25
Quartz	1.47 ± 0.24	19.27	3.43 ± 0.11	67.68	6.67 ± 0.17	13.05	1.24	4.08
sAl foil	0.11 ± 0.12	66.81	0.68 ± 0.36	7.5	3.27 ± 0.54	25.69	1.13	2.90
mAl foil	0.28 ± 0.07	54.46	2.41 ± 0.15	24.29	4.41 ± 0.07	21.25	0.91	3.34

The similarity of tryptophan lifetimes on quartz and in the native BSA suggests that the BSA on quartz was affected by a different mechanism than on the Al foil. The distribution of lifetimes on quartz is also indicative of two populations of BSA being present on the substrate;[240] a relatively unhindered near-native BSA near the surface of the protein layer and a BSA that is located closer to the substrate and is more affected by surrounding molecules and the substrate's surface. The increase in the relative contribution of the short τ_1 component can be attributed to a formation of larger aggregates induced by immobilization.[241] To explain the fluorescence behaviour of BSA on quartz, interactions that BSA can undergo with the substrate and surrounding BSA molecules must be considered as these can be expected to apply also to the BSA on Al foil.

In an aqueous solution at neutral pH, BSA remains folded and exposes polar amino acid residues to the solvent, keeping hydrophobic residues protected inside the hydrophobic core.[230] In the presence of hydrophobic/hydrophilic surfaces, BSA molecules can undergo various structural changes and consequently have their function altered.[230,231,242] Roach et al. demonstrated higher affinity of BSA towards a hydrophobic (–CH_3) compared to a hydrophilic (–OH) functionalized quartz surface and observed surface-specific deformations and adsorption mechanisms of the protein.[233] The adsorption on the hydrophobic surface was accompanied by a less ordered secondary structure due to the larger exclusion of water and the adjustment of hydrophobic regions with respect to the surface. As such, the protein can become distorted (hydrophobic surface) or retain its spherical form (hydrophilic surface). Thus, hydrophobic surfaces can cause partial unfolding of the protein to expose inner hydrophobic regions which may lead to aggregation through hydrophobic patches.[230–232] In this case, the exposure of internal structure to a hydrophobic environment can induce a blue shift of the emission maximum of tryptophan due to the higher hydrophobicity at the protein-surface interface.[231] On the other hand, hydrophilic surfaces can induce a different type of global structural changes during which tryptophan should remain in the non-polar pocket of BSA.[230,239] Rainbow et al. investigated adsorption behaviour of BSA on a quartz surface of a flow cell and observed two populations of BSA with two sets of mean lifetimes.[240] One lifetime (~6.3 ns) was similar to that of the native BSA, while the second lifetime was found to be shorter (~4.1 ns). By comparing their results with lifetimes of pH- and heat-denatured BSA, similar lifetimes values were found, and the longer lifetime was attributed to a weakly bound, partially unfolded near-native BSA. The shorter lifetime was associated with strongly bound molecules at the quartz surface with possibly further unfolded conformation. Tokarczyk et al. and Kubiak-Ossowska et al. investigated the adsorption of BSA on hydrophilic silica surfaces experimentally as well as through molecular dynamics simulations and found that the BSA remained largely intact during adsorption.[235,236] Their results indicated that the BSA was primarily anchored through a water layer (H-bonds) located on the silica surface with hydrophilic regions oriented towards the hydrophilic surface, exposing more hydrophobic parts to the solvent and consequently increasing the surface coverage. This structural rearrangement could be responsible for the decreased lifetime of BSA observed by Rainbow et al., as the exposure of hydrophobic parts to the solvent could also bring tryptophan residues closer to the protein's solvated surface.

The surface effect is limited in a system with multiple layers only to layers that are closest to the substrate.[243] In this case, the protein-protein interactions become more significant and the main factor affecting BSA would be the degree of the aforementioned molecular crowding governed by drying and induced changes of the BSA structure.[240,244–246] Ota et al. investigated the effect of macromolecular crowding on the BSA structure through Raman spectroscopy of tyrosine and phenylalanine residues which are indicators of hydration and nature of the protein's local environment.[246] It was found that an increase in the concentration of protein does not affect the secondary structure of BSA but alters the local environment of hydrophobic residues. These changes were proposed to stabilize the inner hydrophobicity primarily in areas associated with hydrophobic residues where BSA forms additional intramolecular hydrogen bonds. It is unclear whether these conditions apply also to the microenvironment of tryptophan which was not probed in this study. However, tryptophan has been proposed by various authors to be sensitive to quenching interactions with surrounding functional groups induced by similar conditions.[240,244] For example, one quenching mechanism was proposed by Singh et al. who reported on the effect of molecular crowding on local changes in the immediate vicinity of tryptophan residues.[244] Authors observed dramatic conformational changes in the BSA molecule as well as quenching of tryptophan emission but without a significant decrease in fluorescence lifetime which was attributed to a static quenching mechanism by non-polar side chains of surrounding amino acids. These can, due to the congestion imposed by crowders, diffuse near tryptophan, and introduce instantaneous quenching through a weak ground-state complex formation. The close proximity of neighbouring molecules can extend the duration of quenching by keeping amino acids near tryptophan, preventing them from pulling away from the active volume.[244]

Solution-based studies suggest that a similar BSA system can consist of multiple populations with different lifetimes and demonstrate that molecular crowding is a powerful mechanism that has a considerable effect on the internal structure and fluorescence of BSA. Drying is expected to contribute to the closer stacking of protein molecules, enhancing the physical effect of crowding. The steric hindrance is reduced due to the removal of the interfacial water layer[246] which makes the direct contact between BSA molecules possible. Consequently, additional quenching mechanisms of the sensitive tryptophan fluorescence responsible for the decrease in fluorescence lifetimes on quartz may have been induced in the compressed microenvironment.[240,247]

On the Al foil, the more significant decrease in fluorescence lifetimes compared to the BSA on quartz (τ_{avg} = 4.08 ns) can be attributed to properties of the two Al surfaces,[44,50] as indicated by different sets of lifetimes. The shortest lifetime was calculated for BSA on the sAl foil (τ_{avg} = 2.90 ns) where the metal-induced effect could be associated with a non-radiative quenching of tryptophan residues near the metallic surface caused by the surface energy transfer (SET).[35,47,50] It has been established that Al surfaces and nanostructures support SPR in the UV and exhibit absorption at wavelengths below 400 nm (films usually with a maximum at around ~340 nm[79,248]).[91,192] A non-radiative energy transfer from adjacent fluorescent molecules to the metal is accompanied by the decrease in fluorescence lifetime and quantum yield of donor molecules. Therefore, SET from tryptophan residues near the Al surface to the sAl foil is plausible. As was discussed earlier in this work, SET exhibits a longer effective energy transfer distance (compared to conventional FRET) which extends the number of immobilized BSA molecules that can be affected by the sAl surface.

BSA on the mAl foil exhibited a less significant lifetime reduction (τ_{avg} = 3.34) and an emission enhancement of EF = 2.1. A locally increased concentration of BSA caused by immobilization on the hydrophobic substrate could account for the higher fluorescence emission intensity of tryptophan. However, the fluorescence lifetime would not be affected if the BSA concentration was the main contributor. Furthermore, based on similar surface areas covered on both sides of the Al foil, the influence of increased concentration is expected to be minimal. This means that the enhancement mechanism must be linked to the metallic substrate. Observed emission characteristics are indicative of the MEF phenomenon.[20] As noted in the theory of MEF, the mechanism is a complex interplay of multiple factors that could be responsible for the emission enhancement near metallic surfaces. The key difference between the two sides of the Al foil is the surface topography where nanoscale surface corrugation on the mAl foil (Figure 34) may support generation of locally enhanced EM fields and promote the fluorescence enhancement. An enhancement of excitation field intensity and excitation rate near surface irregularities could lead to the increase in the observed fluorescence intensity of tryptophan, but this effect may not cause obvious changes in radiative and non-radiative rates of the fluorophore. The reduction in tryptophan lifetimes suggests that a contribution to the fluorescence enhancement was induced through a radiative rate enhancement and an improved quantum yield in the vicinity of the roughened mAl surface.[50] It is interesting to note that reflectance spectra of the Al foil (Figure 35) did not show reflectance dips which would indicate the SPR absorption near protein's absorption/emission wavelengths. Therefore, it would be difficult to estimate the efficiency of MEF and the possible contribution of radiative and non-radiative changes without analysing the spectral overlap with absorption/emission spectra of the BSA.

4.3.3. Fluorescence Spectroscopy of BSA-AuNCs on Aluminium Foil

To explore whether the Al foil can be employed for a broadband enhancement of fluorescence outside of the UV range, fluorescence measurements of tryptophan and red-emitting BSA-AuNCs on the Al foil were carried out. Utilizing BSA-AuNCs also allows to explore the effect of Al foil on FRET between tryptophan and AuNCs, which is crucial for exciting the red emission of AuNCs in the UV. Figure 37a-c shows fluorescence emission spectra of tryptophan excited at 295 nm and AuNCs excited at 295 nm and 463 nm. The highest fluorescence intensity of tryptophan was observed on quartz and decreased intensities were found on both sides of the Al foil together with a 10 nm blue shift of emission maxima from 327 nm to 317 nm. The red emission of AuNCs showed a different trend. A 2.5x fluorescence enhancement was achieved on the mAl foil compared to quartz when AuNCs were excited at 295 nm (Figure 37e). Fluorescence enhancement of nearly 2x was observed also for directly excited AuNCs at 463 nm with approximately 10x lower fluorescence intensities compared to the 295 nm excitation (Figure 37d), showing that the UV excitation remained the more efficient excitation pathway after immobilization. The larger enhancement observed at 295 nm excitation implies an increased tryptophan excitation and FRET efficiency. On the other hand, fluorescence intensities of AuNCs collected from the sAl foil were the lowest for both excitation wavelengths. Emission maxima of AuNCs blue-shifted on all substrates after the solvent evaporation by 20 nm for the 295 nm excitation and by 15 nm for the direct excitation at 463 nm. Previously, a blue shift of 20 nm was reported for BSA-AuNCs doped in silica nanoparticles,[249] which was attributed to the entrapment of the BSA-AuNC complex in silica and to the stiffness of the protein's surroundings. Therefore, the blue shift of the AuNC emission observed here could be attributed to the immobilization of the protein complex in the congested environment created upon drying.

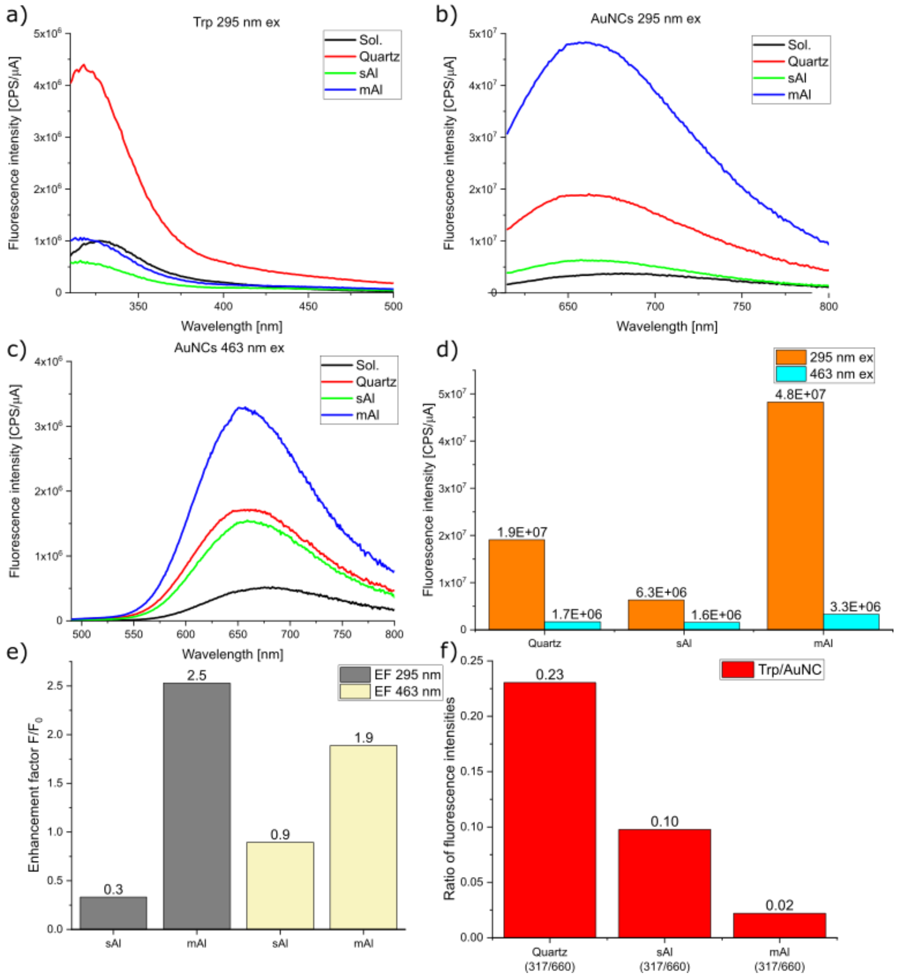

Figure 37: Fluorescence emission spectra of a,b) BSA, BSA-AuNCs after 295 nm and c) 463 nm excitations, d) fluorescence emission intensities of AuNCs after 295 nm and 463 nm excitations, e) enhancement factors calculated for the fluorescence of AuNCs on the Al foil, f) ratios of fluorescence intensities collected at emission maxima of tryptophan (Trp) (a) and AuNCs (b) after 295 nm excitation with indicated peak absorption and emission wavelengths on each substrate.

To better understand changes in the fluorescence emission on substrates, results of steady-state fluorescence measurements in conjunction with fluorescence decay analysis must be considered. Fluorescence decay analysis of tryptophan (Figure 38a) required using the same fitting method that was applied on BSA decays due to the problematic fitting of the short decay collected from the mAl foil. The decay curves were best fit to a 3-exponential model. The immobilization caused a rather uniform decrease in lifetimes with relatively small differences between substrates (Table 7). Despite similar tryptophan lifetimes, the difference in fluorescence intensities of tryptophan and AuNCs are indicative of different mechanisms affecting the fluorescence emissions.

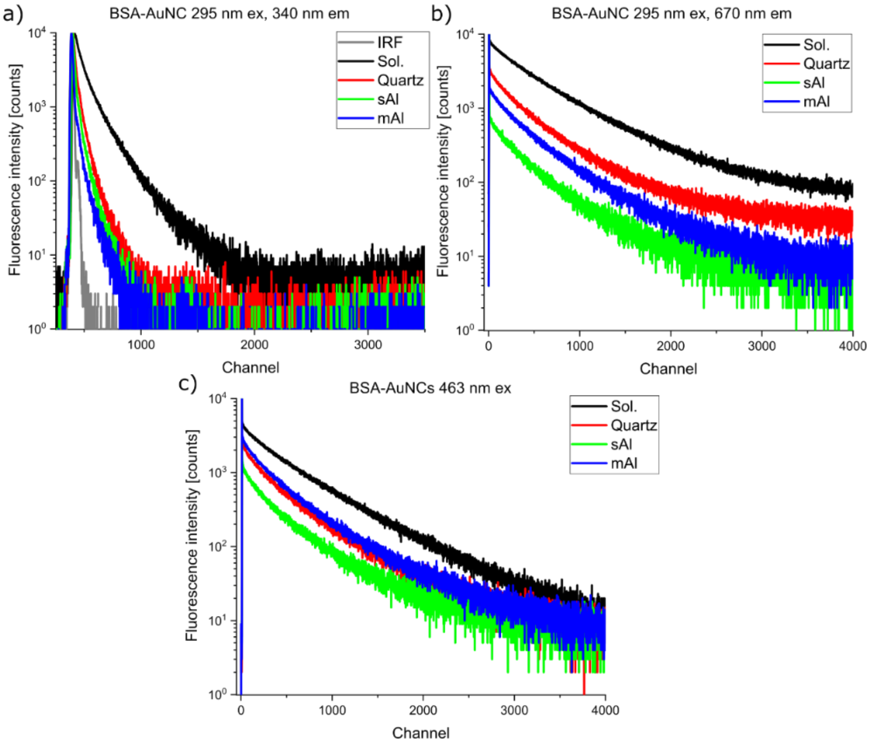

Figure 38: Fluorescence decay curves of BSA-AuNCs collected at a) 340nm (295 nm ex), b) 670 nm (295 nm ex) and c) 670 nm (463 nm ex).

Table 7: Fluorescence lifetimes of tryptophan in BSA-AuNCs on substrates. Concentration 37.6 µM, excitation 295 nm, emission 340 nm.

Sample	τ_1 [ns]	B_1 [%]	τ_2 [ns]	B_2 [%]	τ_3 [ns]	B_3 [%]	χ^2	τ_{avg} [ns]
Sol	0.67 ± 0.01	20.38	2.37 ± 0.08	47.73	5.64 ± 0.04	31.89	1.18	3.1
Quartz	0.07 ± 0.03	79.19	1.23 ± 0.15	14.03	2.57 ± 0.13	6.78	1.08	1.65
sAl foil	0.08 ± 0.04	76.13	1.21 ± 0.15	16.07	2.57 ± 0.12	7.81	1.07	1.66
mAl foil	0.33 ± 0.18	53.61	0.92 ± 0.20	26.09	2.40 ± 0.09	20.30	1.01	1.60

The effect of the Al foil on the BSA-AuNC fluorescence emission was further investigated by analysing fluorescence decays of BSA-AuNCs measured for excitation wavelengths 295 nm and 463 nm on substrates (Figure 38b,c). The extraction of fluorescence lifetimes from AuNCs required using a 3-exponential model[250] (Table 8, Table 9) where the shortest component was attributed to scattering. Both sets of lifetimes show changes in relative contributions of components τ_2 and τ_3 on substrates, with the shorter τ_2, associated with the Au core, contributing more to the overall fluorescence. An increase in τ_3, associated with the Au(I)-S shell, is indicative of an alteration of the AuNC microenvironment that was possibly induced by molecular crowding and drying. Alkudaisi et al. carried out protein unfolding and aggregation studies of lysozyme-encapsulated Au_{25}NCs[250,251] and observed higher sensitivity of the long (µs) component τ_3 (Au(I)-S shell) due to changes in the microenvironment of AuNCs, while the shorter component τ_2 (Au core) was found to be less sensitive and relatively stable throughout induced structural modulations. Changes in the long lifetime were linked to physical interactions of AuNCs with their immediate environment as a result of conformational changes induced during early stages of aggregation. This is in good agreement with results obtained for the 463 nm excited AuNCs where τ_3 increased, suggesting that the Au(I)-S shell was indeed affected. Xu et al. associated a blue-shifted AuNC emission of BSA-AuNC molecules covalently conjugated to iron oxide nanoparticles with conformational changes within the BSA and resulting alteration of the local environment of AuNCs as well as reduced dynamic conformation of BSA.[212] Pyo et al. recently demonstrated that rigidification of Au(I)-S shells of glutathione-encapsulated Au_{22}NCs and of the AuNC environment by freezing or chemically with tetraoctylammonium (TOA) cations leads to an increase in fluorescence lifetimes as well as enhancement of the AuNC emission.[252] Upon freezing, the AuNC emission exhibited a blue shift which was attributed to the reduction of non-radiate relaxation processes. Authors proposed that freezing causes a destabilization of a lower energy, solvent-stabilized luminescent triplet state with a charge-transfer affinity to surrounding ligands due to reduced solvent interactions. Instead, the relaxation from the gold core is followed by an intersystem crossing to a higher energy, highly luminescent intrinsic triplet state which is not influenced by non-radiative solvent relaxation pathways or ligand fluctuations. TOA-paired Au_{25}NCs also exhibited a fluorescence enhancement and an increased lifetime, demonstrating that the rigidifying effect applies also to this type of AuNCs. These findings are closely related to the two-band red fluorescence emission of BSA-Au_{25}NCs[214] and could explain the blue-shifted AuNC spectra as well as the increased τ_3 in solidified BSA-AuNC samples.

Table 8: Fluorescence lifetimes of AuNCs in BSA-AuNCs on substrates. Concentration 37.6 µM, excitation 295 nm, emission 670 nm.

Sample	τ_1 [ns]	B_1 [%]	τ_2 [ns]	B_2 [%]	τ_3 [ns]	B_3 [%]	χ^2	τ_{avg} [ns]
Sol	119 ± 8	0.86	1001 ± 28	25.69	2272 ± 7	73.45	1.11	1927
Quartz	186 ± 12	3.00	912 ± 37	45.78	2201 ± 17	51.22	1.22	1853
sAl foil	115 ± 17	1.96	814 ± 50	45.22	2071 ± 30	52.82	1.20	1755
mAl foil	298 ± 14	5.80	1080 ± 72	54.44	2428 ± 42	39.76	1.11	1918

Table 9: Fluorescence lifetimes of AuNCs in BSA-AuNCs on substrates. Concentration 37.6 µM, excitation 463 nm, emission 670 nm.

Sample	τ_1 [ns]	B_1 [%]	τ_2 [ns]	B_2 [%]	τ_3 [ns]	B_3 [%]	χ^2	τ_{avg} [ns]
Sol	98 ± 6	1.08	935 ± 27	25.46	2247 ± 75	73.46	1.10	2080
Quartz	192 ± 8	4.63	943 ± 39	49.21	2390 ± 23	46.16	1.10	1962
sAl foil.	141 ± 9	4.14	878 ± 68	49.69	2393 ± 33	46.17	1.16	1964
mAl foil	164 ± 8	3.53	934 ± 24	50.98	2371 ± 17	45.49	1.13	1931

So far, it is believed that the effect of immobilization on the AuNC fluorescence has been identified. However, it cannot explain different emission intensities of tryptophan and AuNCs on the Al foil which were again most likely governed by the metallic surface. As discussed, metal-induced effects that influenced the fluorescence emission of tryptophan in the BSA should be applicable also to the BSA-AuNC complex. On the mAl foil, the enhancement of radiative decay rate or the enhancement of excitation rate of tryptophan could account for the increased fluorescence intensity of AuNCs. Although FRET is the main excitation mechanism in the UV, the wavelength 295 nm also excites AuNCs directly and could contribute to the increased fluorescence intensity through the increased excitation field intensity/excitation rate as well. An increase of the fluorescence intensity due to a radiative rate enhancement and an increase in quantum yield of AuNCs would be accompanied by a decrease in lifetime as opposed to the observed increase. Ratios of peak fluorescence intensities of tryptophan and AuNCs in Figure 37f suggest that the mAl foil influenced the FRET process. An increased local electric field arising from locally enhanced EM fields can also enhance the dipole-dipole interaction between a donor and an acceptor.[253] One of the reported effects of MEF is the enhancement of FRET efficiency that is governed by the increase in quantum yield of the donor due to modifications of the radiative decay rate in the close proximity of plasmonic metals.[20,34,35] The intensity ratio of 0.02 calculated for the emission from the mAl foil, compared to 0.23 on quartz, points to an improved FRET, which would explain the observed simultaneous decrease of tryptophan emission intensity and the increase of the emission intensity of AuNCs, although the enhanced rate of direct excitation of AuNCs at 295 nm could also be responsible.

Lifetimes of 463 nm excited AuNCs on the mAl foil were only marginally affected compared to quartz. Therefore, the intensity increase should arise primarily from processes that do not affect the quantum yield. The mAl foil is assumed to promote the fluorescence enhancement through increased local excitation fields near surface irregularities and the resulting higher excitation rate, which would drive the increase in the observed fluorescence intensity without affecting the lifetime. The fluorescence enhancement observed for the excitation wavelength 463 nm therefore implies that the mAl foil is active also in the blue region of Vis spectrum, which may be due to a non-uniform size of said surface irregularities that extend the sensitivity of the surface even beyond the UV region.

Contrary to the fluorescence emission of AuNCs on the mAl foil, the 295 nm excited emission intensity of AuNCs on the sAl foil decreased compared to the intensity on quartz (Figure 37b). This could be linked to a decreased efficiency of FRET to AuNCs caused by the quenching of tryptophan fluorescence indicated in Figure 37a, as was also observed for the BSA on the sAl foil. A competitive SET between tryptophan and the sAl surface could indeed negatively affect the ability of tryptophan to transfer energy to AuNCs.[35] Furthermore, it cannot be ruled out that the observed decrease in fluorescence intensity and fluorescence lifetime of 295 nm excited AuNCs on the sAl foil was caused by quenching of the AuNC fluorescence through SET with the Al surface. For the excitation at 463 nm, the fluorescence spectrum of AuNCs on the sAl foil showed a smaller decrease of intensity with little change in lifetime compared to the AuNC emission on quartz. This suggests a weak energy transfer from excited AuNC to the sAl surface.

4.4. Conclusions

For the first time, a commercially available Al foil has been tested as a fluorescence-enhancing substrate by utilizing fluorescence emissions of the amino acid tryptophan and AuNCs in passively immobilized and dried BSA and BSA-AuNC protein complexes. In addition, implications of immobilization on the proteins' conformation-sensitive fluorescence properties have been discussed as well. Both proteins are assumed to have solidified in a folded form upon solvent evaporation which preserved their ability to produce fluorescence. While some changes in the fluorescence of tryptophan and AuNCs were associated with the state of the environment created by the immobilization, the structural modulation of BSA was not significant and seems to have had only minor effect on the overall fluorescence emission. The two sides (matt, shiny) of the Al foil were found to induce opposite effects on the emission of both fluorescing species. While the fluorescence of both protein complexes decreased on the shiny side, the matt side supported more than 2-fold fluorescence enhancements of tryptophan (BSA) and AuNC emissions. The main factor responsible for the fluorescence enhancement was most likely the different topography of both surfaces where the nanoscale corrugation of the matt side supported the excitation of locally enhanced electromagnetic fields. It is believed that the increase in fluorescence intensity of BSA accompanied by the decreased lifetime on the matt side was due to the combination of an increased radiative rate of tryptophan and an increased excitation rate in the vicinity of the roughened Al surface. The decrease of the BSA emission intensity on the shiny side was attributed to quenching by SET. Results of the fluorescence analysis of BSA-AuNCs suggest that the increase in the AuNC emission on the matt side at 295 nm excitation was a result of an improved FRET and an enhanced excitation rate of tryptophan and AuNCs. On the other hand, the enhancement of 463 nm excited fluorescence emission of AuNCs was attributed to an enhanced excitation rate of AuNCs. This enhancement of the AuNC emission intensity implies that the matt side of the Al foil can be used for MEF in the UV and visible region. The weak fluorescence emission of AuNCs on the shiny side was attributed to the reduced FRET efficiency caused by quenching of the tryptophan fluorescence through SET on the smoother shiny Al surface and a possible SET from AuNCs to the Al surface.

Presented results demonstrate the first use of the Al foil for MEF of BSA and BSA-AuNCs as well as provide an insight into the fluorescence behaviour of proteins and AuNCs under rarely investigated conditions. The methodology and observation reported in this study highlighted key factors that can influence fluorescence properties of both species and could be relevant to further protein research on planar metallic substrates.

5. Fabrication of Plasmonic Gold Nanobowls

5.1. Introduction

There is intense global interest in research and development of novel plasmonic nanostructures with optical properties that can boost the field enhancement of nanomaterials, light harvesting, or photocatalytic performance. With current manufacturing techniques and well-understood chemistry, producing tailored nanostructures with strong enhancing capabilities is possible both in colloids and on planar substrates. Compared with continuous metallic substrates which exhibit high reflectivity and lack hot spots, roughened and patterned surfaces with controllable sub-wavelength features can couple with incident light and generate tunable surface plasmon resonance as well as localized EM field enhancements. The improvement of efficiency of optically active sites and hot spots has been a major target in MEF, where boosting the performance of selected fluorophores is highly desirable. Such endeavour requires a consideration of the physical design with respect to desired surface and optical characteristics which determine the overall signal enhancement.[11,20,49,52,93,112,193,254]

A high degree of EM field localization can be achieved with hollow plasmonic 3D nanovoids.[110] As was mentioned earlier, the particular advantage of these nanostructures is their size- and shape-dependent optical properties mediated by the hollow architecture which supports increased absorption of light via efficient light trapping. The strong coupling to incident light gives rise to a complex plasmonic behaviour which leads to the excitation of cavity plasmon modes confined in the hollow space.[111] Of special interest to this work are truncated spherical nanovoids or nanobowls (NBs) which exhibit a broadband EM field enhancement due to the refractive index gradient induced by the curved surface.[128] Moreover, the concave interior of NBs allows to control the reflectivity and scattering properties of the surface by manipulating their dimensions and periodicity.[255] The specular reflection from NB arrays can be largely supressed so that diffraction and scattering of light into oblique-angle directions dominate the optical response, increasing the optical path length of light and improving the light trapping by the surface.[255] This is a particularly attractive property for metal-enhanced analytical techniques[123,128], label-free detection and photocatalysis,[112,115,256] which benefit from the resulting efficient excitation and enhancement of analytes' photophysical properties.

Several cost-effective and versatile techniques can nowadays produce ordered arrays of NBs with controlled geometry across large surface areas. The first technique combines nanosphere lithography[257] with electrochemical deposition of metals to manufacture uniform hexagonal NB arrays with tunable dimensions.[113] An array of silica or polystyrene nanospheres is assembled onto a pre-treated substrate and serves as a mask through which the substrate is selectively patterned by electrochemical reduction of metal complex ions in the interstitial space around nanospheres. The template is then selectively dissolved, producing hollow spherical cavities on the substrate. The thickness of the deposited metal can be accurately controlled by monitoring the charge passed through an electrochemical plating bath to deposit the film. Although electrochemical plating removes drawbacks of chemical conversion routes such as volume shrinkage and cracking,[113] the technique usually requires long periods of pre-treatment of the substrate and of a carefully controlled evaporation of the bead solution to form a closely packed monolayer, both of which prolong the manufacturing process. Another approach combines colloidal lithography with nanoimprinting where the pattern is transferred through a mechanical deformation of a template layer or by coating the template with an elastomer to produce flexible spherical patterns.[115,258,259] The liquid elastomer is used to coat the array of nanospheres and cured to preserve the transferred pattern. The elastomer can be peeled off and the spherical template is removed in an appropriate solvent, leaving the polymer to be used as mold for additional surface modification. To produce plasmonic NBs, a desired metal is coated onto the patterned polymer. A common feature of such techniques is their relatively high complexity.

A different, non-lithographic, approach which can produce robust metallic NBs relies on templates produced by anodizing of Al.[260] Anodizing of Al, which is also the method of choice in this work, is an electrochemical method which rapidly produces self-assembled porous oxide layers on metallic surfaces in an electrolyte bath with a high degree of reproducibility.[114,126,261] The technique allows simple fabrication, scalable templating and a facile control of pore periodicity and diameters. The aluminium oxide extends down to the Al substrate where pores are terminated with round cavities. The porous oxide layer can be selectively etched to expose a robust Al NB array that forms at round bases of pores.[261] Al nanobowls (AlNBs) adopt the same periodicity as pores with dimensions likewise tunable by manipulating anodizing conditions during the manufacturing process.[262] Although only certain metals and alloys are suitable for anodizing, optical properties can be further optimized by depositing thin metallic films onto AlNBs, using AlNBs as ordered templates to produce arrays of plasmonic NBs.[126,261]

Several of the aforementioned studies have investigated properties of various plasmonic nanovoids and demonstrated their applications in SERS or fluorescence[103,106,118–121,123,125]. These NBs were produced predominantly by colloidal lithography and reports on the application of NBs produced by anodizing have been limited. There is also lack of an in-depth analysis of the effect of fine structural features, such as the thickness of plasmonic metal coatings on nanovoid templates and the wall thickness between neighbouring nanovoids, on induced EM fields.

This chapter demonstrates the fabrication of plasmonic AuNB substrates with characteristics suitable for MEF spectroscopy in the UV-Vis and provides a complex analysis of the surface morphology as well as the dependence of substrates' optical properties on various illumination conditions and structural features. AuNBs were produced by anodizing of Al and coating AlNB templates with diameters of ~100 nm and ~500 nm with Au films of various thicknesses. Optical properties of AuNB patterns were investigated through reflectance measurements and finite-difference time-domain (FDTD) calculations. The reflectance of AuNBs was found to be a combination of properties of both the Au and the geometry of AlNBs, exhibiting a promising broad reflectance minimum from UV to 500 nm. Since the tuning and the position of EM fields is critical for the application of plasmonic nanostructures in MEF, FDTD calculations were also employed to establish excitation-dependent spatial distribution of electric fields over the nanostructure for varying excitation conditions. Effects of structural features such as the thickness of walls between neighbouring AuNBs and that of deposited Au films on electric fields were also investigated. It was found that the wall thickness primarily affects the field intensity at rims of AuNBs and the surface coverage of the upper Au surface near rims. The strength and the size of confined electric fields can be increased by decreasing the thickness of the Au coating. It is hoped that this work provides insight into designing and optimizing AuNB substrates for fluorescence applications with optical properties tailored to photophysical properties of incorporated fluorophores.

5.2. Anodizing of Aluminium

Anodizing is an electrochemical process that transforms surfaces of metals into oxides with various chemical, mechanical, and optical properties. Anodizing of Al can be performed in acidic electrolytes (typically sulphuric, phosphoric, chromic, oxalic acids) that, in combination with applied voltage, produce porous oxides layers with various pore diameters, inter-pore distance and thicknesses.[262,263] The process is usually performed in an electrochemical cell that is filled with an electrolyte. Immersed electrodes are connected to a direct-current power supply and a positive electric charge is applied to the Al substrate which acts as the anode ("anodizing"), while a negative charge is applied to another metal plate suspended in the electrolyte, making it the cathode. Charged plates attract ions of opposite charges and drive their diffusion at the metal-electrolyte interface, which enables conversion of the Al substrate into the aluminium oxide (Figure 39). Depending on the electrolyte and anodizing conditions, pore diameters can be tuned from ~20 nm up to ~880 nm.[263–265] The depth of nanopores can be controlled from tens of nanometres up to hundreds of micrometres through the anodizing time.[263] The ability to produce oxide films is further determined by the applied voltage (or current density), the alloy being anodized, and the concentration and nature of the electrolyte.[262] Electrolytes of choice in this work are oxalic and phosphoric acids. Oxalic acid is the simplest carboxylic acid ($C_2H_2O_4$) that is used for anodizing performed typically in the range of 20 – 60 V, producing pores with diameters 50 – 150 nm.[261,262] Phosphoric acid can be used for growing pores with diameters up to 500 nm at around 195 V.[266]

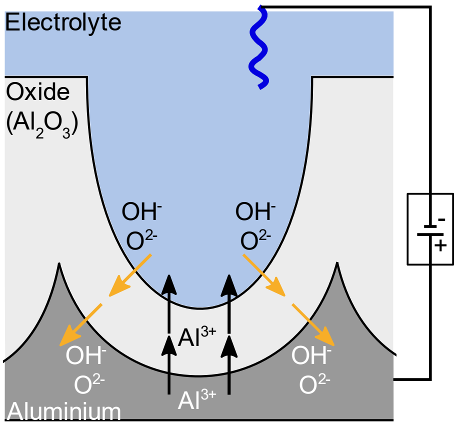

Figure 39: Illustration of the ion transport at the Al-electrolyte interface. Electric current passes through the medium and drives the release of oxygen ions from the electrolyte towards the Al surface where they recombine with Al atoms and produce aluminium oxide.

Equation 43 demonstrates the reaction mechanism of the aluminium oxide assembly.[262] Hydroxyl and oxygen anions are driven to the barrier oxide where Al and oxygen ions recombine into the aluminium oxide (Al_2O_3) and hydrogen is released in the solution.

$$2Al + 3H_2O \rightarrow Al_2O_3 + 6H^+ + 6e^- \qquad \textit{Equation 43}$$

Initially a thin, dense layer of a barrier oxide is formed at the Al surface (Figure 40). At the same time, the barrier layer is etched by the acidic electrolyte. The simultaneous etching and growth of the oxide are selective processes that are dependent on the presence of roughness and defects which influence the electric field distribution at the surface.[263,264] Electric current is focused at these regions where growth of the porous oxide initially occurs, proceeds through the barrier layer and erodes down to the Al substrate. The porous oxide is composed of self-organised hexagonal cells, perpendicular to the Al surface, with nanopores situated in their centre. Nanopores are initially formed in a random fashion, but the ordering and the distribution of pores improve over time. Pores propagate through the oxide layer and along the surface due to the mechanical stress induced by repulsive forces between neighbouring cells.[263] In the final step, the porous oxide is selectively etched in the mixture of phosphoric (H_2PO_4) and chromic acids (CrO_3) at high temperature to uncover NBs at hemispherical bases of pores. The aluminium substrate can be also selectively etched in a copper chloride ($CuCl_2$) solution to produce a porous alumina membrane.[93] Further improvement of the pore ordering is also possible by a multi-step anodizing which is based on repeated etching and anodizing of the newly formed porous oxide.[262]

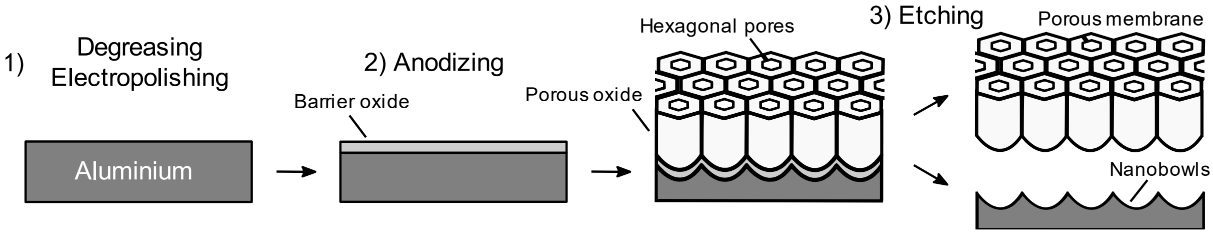

Figure 40: Schematic diagram of anodizing of Al. 1) Degreasing and electropolishing remove surface irregularities and flatten the aluminium surface. 2) Anodizing produces the porous aluminium oxide with hexagonal cells. 3) The resulting oxide layer can be selectively etched to expose an ordered array of NBs. Selective dissolution of the aluminium substrate is also possible to obtain porous alumina membranes.

5.3. Experimental

5.3.1. Materials

Phosphoric acid (H_3PO_4, Sigma-Aldrich, UK), oxalic acid ($C_2H_2O_4$, VWR, UK), Chromium trioxide (CrO_3, Sigma-Aldrich, UK), ethanol (Sigma-Aldrich, UK), distilled water, aluminium sheets (99.999 %, Advent Materials, UK)

5.3.2. Preparation of Gold Nanobowls

AuNBs were prepared by a multi-step process which includes fabrication of the porous aluminium oxide, selective etching of the newly formed oxide layer and a subsequent ion-beam deposition of thin Au films of various thicknesses.

Fabrication of the porous aluminium oxide

Porous aluminium oxide was prepared via a single-step anodizing method adapted from works of Fan et al. and Masuda et al..[261,266] The fabrication was carried out on 1.5 × 1.5 cm high-purity (99.999 %) aluminium sheets using oxalic and phosphoric acids (Figure 41). Al sheets were first degreased in acetone and distilled water via sonication. A wire with the current rate 3A was attached and soldered to one corner of each Al sheet to improve the connection. The contact was sealed with an epoxy resin to restrict anodizing only to Al and to prevent anodization of the attached copper wire. Al sheets were connected to a TDK Lambda GEN1500W DC power supply and became working electrodes. A wire of pure platinum was used as the counter electrode. Then, electro-polishing was performed in a mixture of 40 % v/v H_3PO_4, 38 v/v % ethanol and 22 % v/v deionized water, at 45 °C for 5 minutes before anodizing. The current was set to 1.4 A which was calculated from the samples' surface area (~2 cm^2/side) and the optimum current density of 0.35 A/cm^2 (0.35 A/cm^2 x 4 cm^2). The polishing solution was vigorously stirred to remove bubbles from Al surfaces. After rinsing polished Al sheets in distilled water, samples were anodized in 0.3M oxalic acid (40 V) at 30 °C for 2 hours to produce small-diameter AlNBs or 0.1M phosphoric acid (195 V) at -2 °C for 1 hour to produce large-diameter NBs. The voltage was slowly increased from 0 V to the appropriate value to prevent the growth of surface deformations and poor pore ordering.[267] Anodizing was performed in a jacketed glass electrolytic cell coupled with a refrigerated/heating circulator (Julabo F12). Anodized samples were then washed several times with distilled water and the attached wire with the epoxy cap were removed.

Anodizing in phosphoric acid requires vigorous stirring of the electrolyte to remove generated heat and prevent burning of the aluminium oxide. The particular advantage of the sample configuration (Figure 41b) was found to be a double-sided cooling in the low temperature electrolyte which improves the heat dissipation. The risk of oxide breakdown was further reduced by decreasing the temperature of the electrolyte below 0 °C (recommended for phosphoric acid anodizing[266]). The appropriate temperature range was found to be between 0 °C and -2 °C due to the ice formation that occurred below -3 °C inside the electrochemical cell, which can interfere with the anodization process. More information about the impact of anodizing at high voltage on the quality of prepared AlNB patterns can be found in Appendix A.

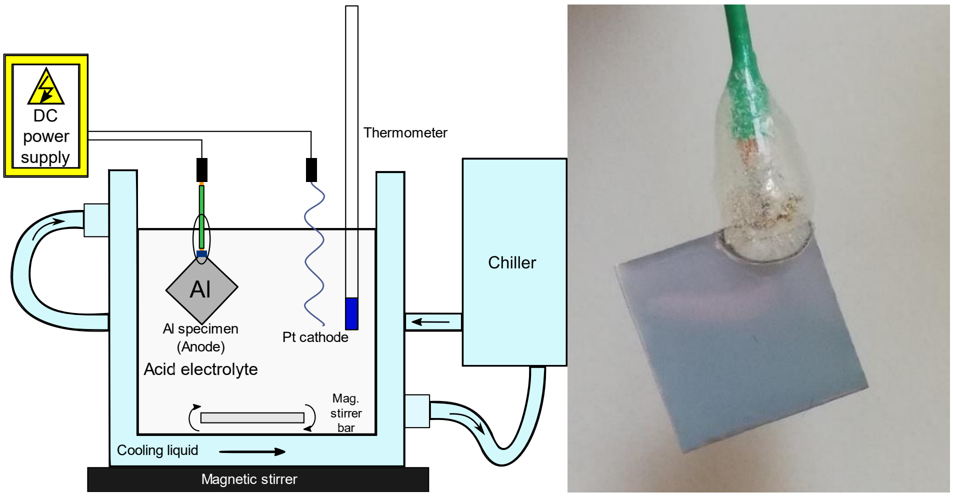

Figure 41: Diagram of the electrochemical apparatus (left) and a photograph of the anodized Al sheet (right). During anodizing, the Al sample and the Pt counter electrode are connected to the DC power supply and are submerged inside the jacketed electrochemical cell filled with the acid electrolyte. The chiller maintains stable temperature of the electrolyte. Magnetic stirrer bar homogenizes the temperature of the solution and removes bubbles from the specimen's surface. The thermometer serves as a secondary temperature control.

Fabrication of AlNBs

AlNBs were produced by selective etching of the newly formed aluminium oxide in the mixture of 1.8 wt% CrO_3 and 6 wt% H_3PO_4 (1:1) at 70 °C for 3 hours and under gentle stirring. Etched Al sheets with NB arrays were washed several times with distilled water and used further as prepared.

Thin film deposition to produce AuNBs

AuNBs were prepared by Teer Coatings Ltd and School of Engineering & Physical Sciences at Heriot Watt University via ion-beam deposition by sputter coating gold films (30, 40, 58 nm) onto AlNBs and a microscope slide which served as templates and a reference, respectively.

5.3.3. Characterization of Nanobowls

Topographic characterization

The growth of aluminium oxide and the morphology of Al and AuNBs were analysed using a FEI Quanta 250 FEG-ESEM scanning electron microscope at an acceleration voltage of 5 kV. Tilted SEM scanning was carried out at an angle of 45 °. Collected SEM images were used for the size analysis of AuNB substrates in the image analysis software ImageJ.

Reflectivity measurements

Reflectivity measurements were carried out using PHOTON RT UV-VIS-MWIR Spectrophotometer for coaters in the range of wavelength from 250 to 1000 nm and at various angles of illumination (8, 30, 45, 60 °) and observation (16, 60, 90, 120 °) with respect to a substrates' normal.

5.3.4. Electromagnetic Field Modelling

Finite-difference time-domain calculations were performed using commercial software FDTD solution (Lumerical) to simulate reflectance spectra and electromagnetic fields of various nanobowl geometries. Dimensions and metal thicknesses were based on four experimentally fabricated AuNB substrates. The geometry was approximated to hollow spherical NBs with diameters of 75 nm, 83 nm, 420 nm, 475 nm. The depth of AuNBs was set to correspond to respective radii.[255] The thickness of the Au layer on Al substrates was set to 30 nm and 50 nm. CRC[268] and Johnson and Christy[269] dielectric values were used for aluminium and gold, respectively. Illumination conditions included incident wavelengths 295, 470, 533, 650, 780 nm and angles of incidence 0, 30, 45, 60 °. The design of simulated AuNBs is summarized in Figure 42.

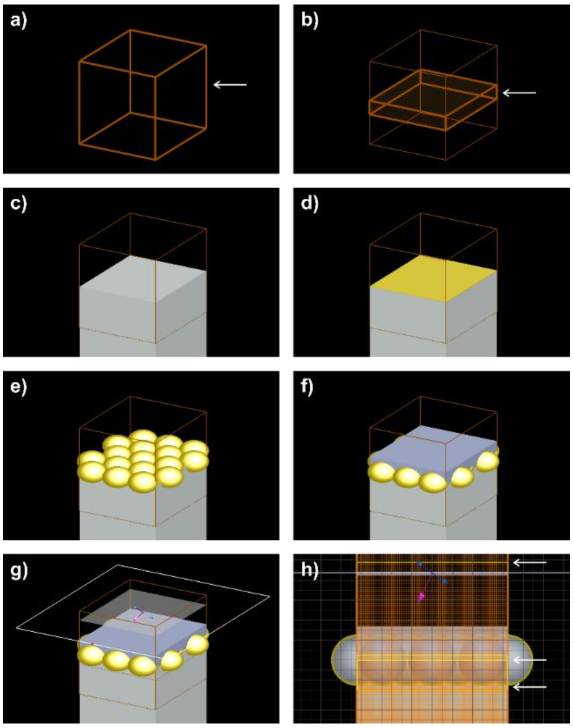

Figure 42: General design for FDTD calculations of AuNB arrays. a) The FDTD simulation window indicated by the arrow. b) A meshing region indicated by an arrow defined within the simulation window. c) An Al substrate extending through the simulation window. d) A thin Au film added to the surface of the Al substrate. e) A hexagonal close packed arrangement of gold and etch material nanospheres. The difference in diameters is 2× the metal thickness. f) A block of etch material is added to the top of the gold film. The thickness of the block is greater than the radius of the gold spheres to ensure that no excess gold is incorporated to the simulation. g) A plane wave source is placed above the nanostructures with a backward injection axis. The blue arrows indicate the polarization direction (along the *x*-axis for all calculations) and the purple arrow indicates the angle of incidence. h) Frequency domain power monitors (indicated by arrows) are added into the simulation. The monitor above the source is used to determine the reflectance spectra. A 2D monitor in the *z*-axis placed at the surface of the thin gold film is used to determine the E-field distribution at the surface of the NB sample (height = 0 µm). A second monitor in the *y*-axis is used to visualize the E-field at the cross-section of NBs.

As an example, 475 nm AuNBs with Au thickness of 30 nm and a bowl edge-to-edge barrier 10 nm were designed as follows: An Al substrate was extended through the bottom of the FDTD window, and a 30 nm thin Au film was added to the Al surface. Au nanospheres with a diameter of 535 nm were arranged in a hexagonal pattern with centre-to-centre spacing 485 nm between adjacent nanospheres in the *x*-axis and an offset of 420 nm in the *y*-axis. Spheres with a diameter of 475 nm made with the etch material were placed in the centre of each gold nanosphere. A final etch block was added with the minimum matching the top of the thin gold film, yielding the final idealized geometry AuNBs. Calculations involving the complete reflectance spectra at 0 ° of incidence for the plane wave source, periodic boundary conditions were used in the *x*- and *y*-axes, and a perfectly matched layer in the *z*-axis. For non-zero values of the angle of incidence or cases where reflectance spectra for single incident wavelengths were calculated, Bloch boundary conditions in the *x*- and *y*-axes were used, along with perfectly matched layer in the *z*-axis. Simulations of multiple cells of large-diameter AuNBs were performed with mesh conditions of 10 nm in all axes. Single cell calculations for large-diameter AuNBs were performed with mesh sizes of 2.5, 2.5 and 5 nm (x, y, z). Multiple cell calculations for small-diameter AuNBs used mesh size of 5 nm in all axes.

5.4. Results and Discussion

5.4.1. Fabrication and Characterization of Aluminium Nanobowls

The assembly of AlNBs and the fabrication of AuNBs are schematically shown in Figure 43. After the electropolishing, Al substrates were anodized in oxalic and phosphoric acids to grow ordered porous aluminium oxide with various pore diameters. The porous oxide was then etched to produce AlNBs. AlNB arrays were used as templates for the fabrication of AuNBs.

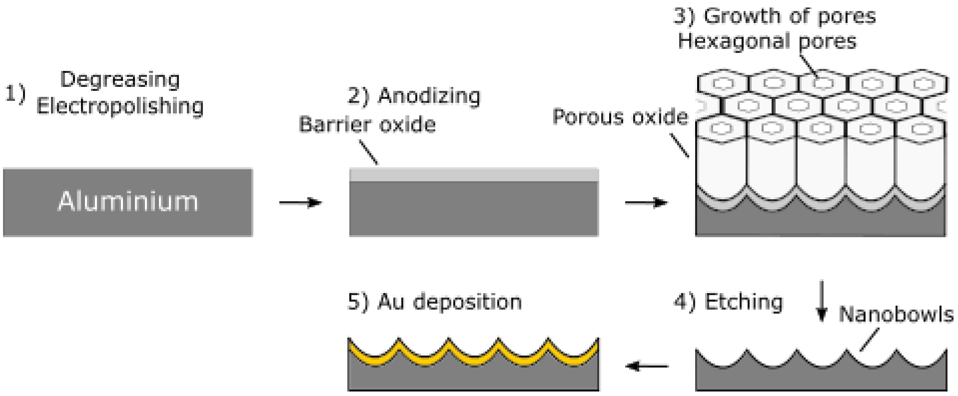

Figure 43: Schematic diagram of the anodizing process producing Al nanobowls.

The optimal pore ordering of aluminium oxide was achieved by applying anodizing voltage of 40 V (oxalic acid) and 195 V (phosphoric acid) (Figure 44).[261,266,270] The size analysis revealed that anodizing in oxalic acid produced NBs (AlNB@1) with smaller diameters of 99.2 ± 4 nm nm (Figure 44a,b) than phosphoric acid which produced NBs (AlNB@2) with slightly less uniform size distribution and diameters of ~488.3 ± 48.8 nm nm (Figure 44c,d). This feature can be attributed to the shorter anodizing time that was selected due to the heating of samples at 195 V which brings anodized Al to near-burning conditions and could cause an oxide breakdown.[262,271] The depth of NBs after etching is approximately the half length of centre-to-centre distances.[255] A concave cavity in the centre of each NB is surrounded by six other neighbouring NBs which exhibit protrusions in each corner of their polygonal shape (Figure 44c,f).

The optical characterization was done by measuring the reflectance of AlNBs and non/polished Al sheets (reference) at various angles of illumination (8, 30, 45, 60 °) and observation (16, 60, 90, 120 °) (Figure 44g). As could be expected, the electropolishing increases the reflectivity of Al substrates. Reflectance spectra of the polished sample (Al P) exhibit a small local minimum at ~825 nm which corresponds to the inter-band transition of aluminium at around 1.5 eV.[255,272] Reflectance spectra of AlNB@1 were found to be similar to spectra of the polished Al sheet but the presence of NBs on the surface resulted in a new dip located at around 270 nm, related to the SPR and absorption due to light trapping by AlNBs.[255,273] A significant decrease in reflectance was observed for AlNB@2 with a notable broadening and a red-shift of the 270 nm dip to 330 nm. The lowest reflectance was achieved under 8 ° (<5 %) and 30 ° (<10 %) illumination, highlighting angles at which the absorption should be particularly effective. The overall reflectivity increased at higher angles of incidence and both dips became less distinct. The wide UV dip also becomes progressively narrower and blue-shifted when the angle of incidence is increased, demonstrating the sensitivity of optical properties of AlNBs to the angle of illumination. Furthermore, the red shift and the broadening of the UV dip with increasing size of NBs show that absorption properties are dependent on the diameter of NBs.[110,255] This is particularly attractive for light harvesting and MEF which take advantage of the suppressed specular reflection from the surface and concentrated electromagnetic fields in the area of incidence.

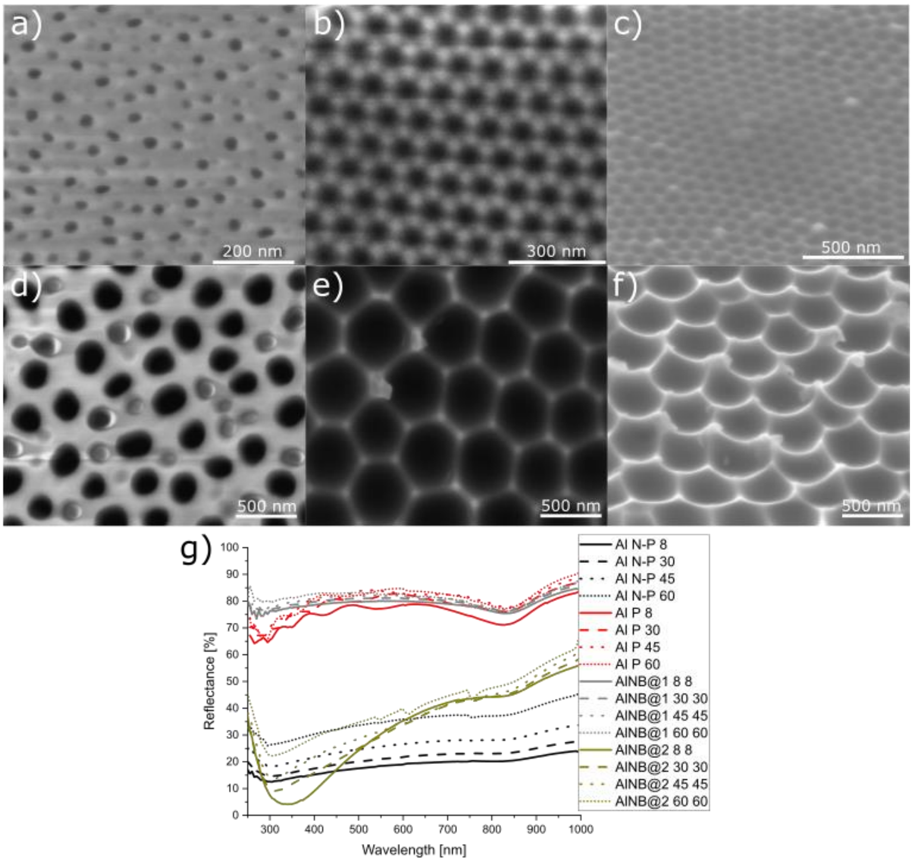

Figure 44: SEM images of the porous oxide synthesized in oxalic acid at a) 40 V, b) AlNB@1 after the oxide removal, c) SEM image of a tilted (45 °) AlNB@1 array, d) porous oxide synthesized in phosphoric acid at 195 V, e) AlNB@2 after the oxide removal, f) SEM image of a tilted (45 °) AlNB@2 array, and g) reflectance spectra of AlNB@1,2 and non/polished Al sheets (Al N-P, Al P) taken at various angles of illumination (8, 30, 45, 60 °).

An intriguing property of the aluminium oxide is its intrinsic fluorescence. The oxide exhibits a broad wavelength-dependent emission from UV to 650 nm when excited between 290 – 470 nm (Figure 45). The origin of this fluorescence remains to be a subject of discussions but two explanations for the presence of fluorescence centres in the porous aluminium oxide formed in organic electrolytes have been proposed. The first suggestion is that the intrinsic fluorescence originates from point defects that are related to F^+ and F oxygen vacancies.[274] The other explanation associates the fluorescence with oxalic impurities incorporated in the oxide during oxalic acid anodizing that transformed into photoluminescent centres.[275] The same mechanism is also generally accepted for oxide films produced in inorganic electrolytes such as phosphoric acid.[276] The barrier oxide likewise exhibits fluorescent behaviour, albeit much weaker than that of porous oxide films due to the limited nanometre thickness.[276] Thus, the emission intensity is proportional to the number of vacancies in the aluminium oxide and can be used for monitoring the growth as well as the etching of oxide layers through steady-state fluorescence measurements (Figure 45). The fluorescence cannot be completely removed due to the presence of the dense barrier oxide but can be significantly reduced by etching. In addition, further oxidation can be prevented by coating the surface with a thin layer of more stable material, such as gold or graphene.[248]

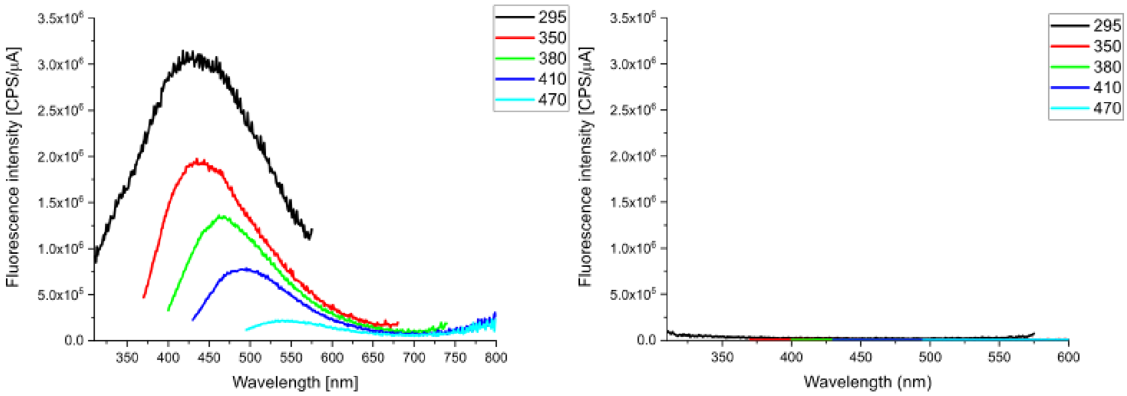

Figure 45: Fluorescence emission spectra of aluminium oxide for various excitation wavelengths before (left) and after (right) etching.

3.6.1. Fabrication and Characterization of Gold Nanobowls

In the next step, gold films with thicknesses of 30, 40 and 58 nm were deposited onto AlNB@1 and AlNB@2 substrates (AlNB@1 → AuNB@1, AlNB@2 → AuNB@2) (Figure 46). Thicknesses of Au coatings and dimension of AuNBs were summarized in Table 10, where AuNB@1 were designated as S1, S2, S3 (“Small”) with respect to the increasing thickness of the Au layers; 30, 40, 58 nm (Figure 47a-c). Same description was used for AuNB@2 where samples were designated as L1, L2, L3 (“Large”) with respect to AlNB@2 with 30, 40 and 58 nm Au layers (Figure 47d-f). An Au-coated glass slide was used as a reference substrate for the optical characterization and fluorescence measurements. Au coating thicknesses are values measured on a flat substrate and may slightly vary on NBs with respect to the geometry of AuNB@1 and AuNB@2. Furthermore, determining diameters and wall thicknesses of AuNB@2 was particularly challenging due to the small width and sharp edges of barriers between NBs (Figure 47d) as well as due to the concave geometry of NBs where upper sections of descending walls could be misinterpreted as parts of the upper edge of the barrier.

Table 10: Summary of dimensions of AuNBs.

	Glass	S1	S2	S3	L1	L2	L3
Au thick. [nm]	58	30	40	58	30	40	58
Diameter [nm]	-	83 ± 8	84 ± 6	75 ± 8	475 ± 49	482 ± 37	420 ± 33
Wall thick. [nm]	-	25 ± 4	22 ± 3	48 ± 5	23 ± 5	33 ± 7	71 ± 10

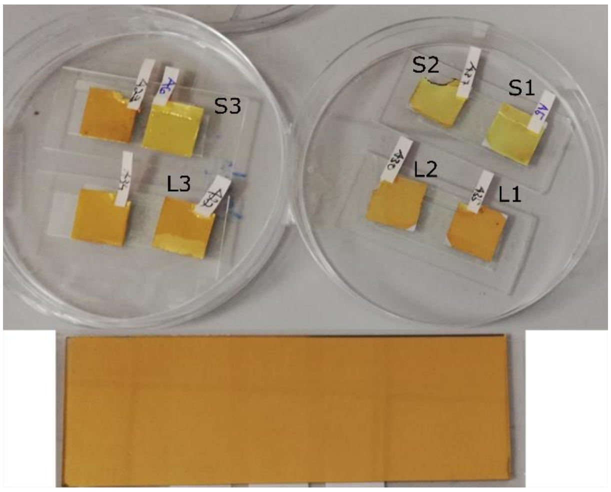

Figure 46: Photographs of Au-coated AlNB@1, 2 (upper row) and an Au-coated glass side (bottom row). Samples S1-S3 and L1-L3 correspond to small-diameter and large-diameter AuNBs, respectively.

The increase in sizes of rims after the coating with Au correspondingly reduced diameters of AuNB@1. The change was most prominent on S3 where the six the protrusions in each corner of NBs nearly fused, forming nanocaps separated by concave nanogaps (Figure 47c). AuNB@2 likewise showed a decrease in diameters with increasing thickness of the Au coating. By comparing upper sections of AlNB@2 and L1, it can be observed that sharp rims and protruding tips formed by etching became more rounded after the Au deposition, indicating the presence of Au on the surface. These sharp features were not observed on AuNB@2 when the Au thickness was increased further (Figure 47e,f).

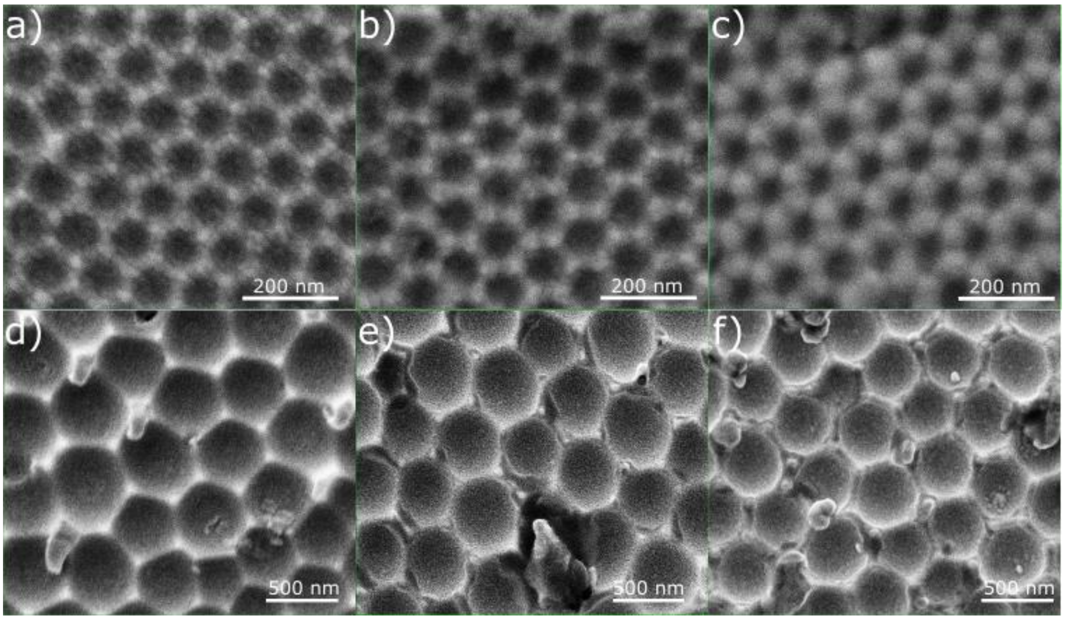

Figure 47: SEM images of AuNBs showing the structural evolution of NBs after the Au coating. Morphology of a-c) AuNB@1 with 30, 40, 58 nm Au coating, d-f) AuNB@2 with 30, 40, 58 nm Au coating.

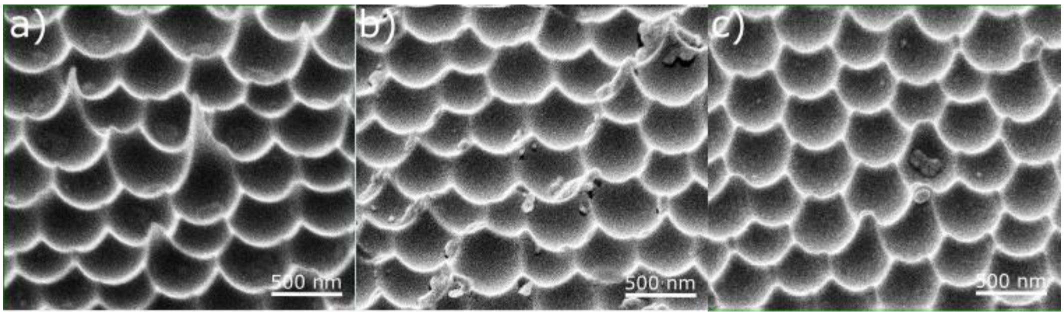

Figure 48: SEM images of tilted (45 °) AuNB samples a) L1, b) L2, c) L3.

Figure 46 shows that AuNB@1 and AuNB@2 exhibited slightly different coloration due to the scattering of light from closely packed NBs with different diameters.[277] Reflectance spectra of AuNBs were collected under same conditions as those of AlNBs (Figure 49). A feature that is common to all spectra is the absence of the 825 nm reflectivity dip associated with Al that disappeared after coating. The reflectance spectrum of the planar Au-coated glass slide (Au-Glass) shows a broad dip in reflectance between 300 nm and 500 nm (Figure 49a), with local minima at 350 nm and 480 nm related to absorptions by the substrate and Au, respectively.[113,278] Figure 49b shows reflectance spectra of AuNB@1 S1 – S3. The reflectance spectrum of S1decreased but still resembles that of the Au-coated slide. The two reflectance dips become visible only at higher angles of incidence. The reflectance spectrum of S2 exhibited a similar shape and the lowest reflectance out of the three samples. This is probably due to slightly deeper NBs which possess a better light trapping ability and a lower reflectance typical for porous metallic films.[126] Low reflectance due to insufficient etching (i.e. presence of deep pores) is unlikely because SEM images collected from various areas on S2 clearly showed the internal surface and bases of AuNBs (Figure 47b), which would otherwise be hidden in deep pores. This is further supported by the reflectance spectrum of S2 collected under 60 ° illumination which has almost identical shape as that of S1, as indicated by their similar surface characteristics. Reflectance of S3 was the highest with a close resemblance to the Au-coated glass slide. This can be attributed to smaller diameters of AuNBs that reduce the discontinuity of the Au surface.[113] Different shapes of AuNB@1 spectra demonstrate the effect of substrates' morphology (Figure 47a-c), such as the particulate structure of the top surface and the corresponding presence nanogaps of varying sizes between Au nanocaps,[117,118] on absorption properties of NBs. When the depth of NBs is reduced, light trapping in shallow NBs is less significant and specular reflection becomes the dominant effect.[255]

In contrast, reflectance spectra of AuNB@2 are more consistent for all angles of incidence (Figure 49c). The position of the major dip did not shift after increasing the diameter of NBs, but the reflectance was significantly reduced in this range, indicating strong absorption.[113,255] This can be attributed to the combined effect of absorption by the Au coating and the NB geometry due to the spatially variable refractive index gradient[128,255] induced by the curvature over the vertical axis of NBs. Also, at higher angles of illumination, the reflectance dip becomes narrower, approaching the shape of AlNB@2 reflectance spectrum. This suggests that at higher angles of incidence, the absorption could be dominated by light trapping in NBs. The interaction of light with fabricated AuNBs and resulting substrates' plasmonic behaviour are in greater detail explained through numerical simulations in the following section 5.4.2.

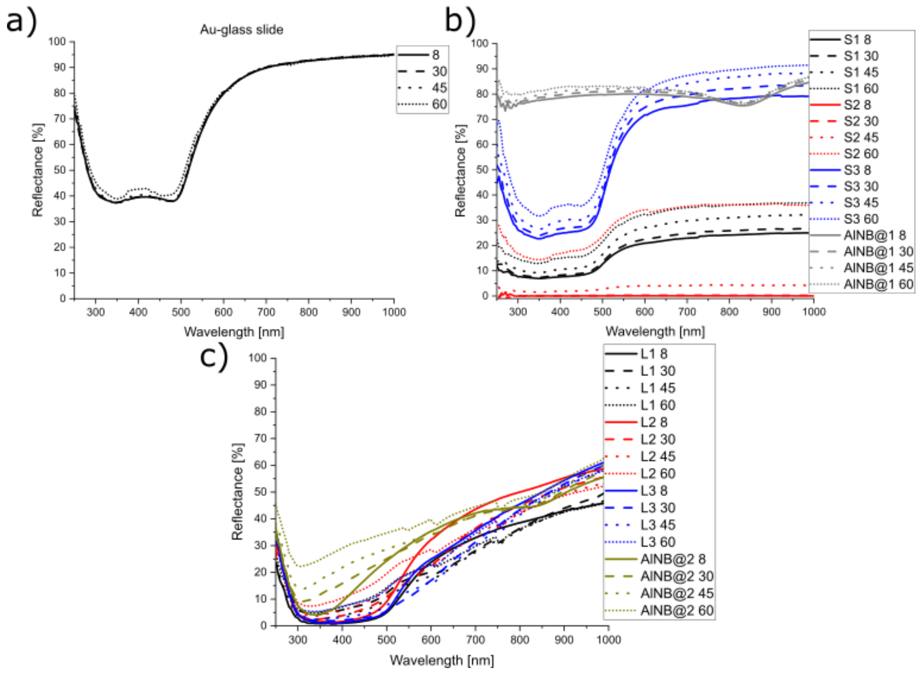

Figure 49: Reflectance spectra of a) Au-coated glass slide, b) AuNB@1 (S_i) and c) AuNB@2 (L_i) with various thicknesses of Au coating taken at 8, 30, 45, 60 ° of incidence. S1 – S3 and L1 – L3 correspond AuNBs with 30, 40, 58 nm Au coatings.

After the coating with Au, background emission spectra of AuNBs were also recorded to check for residual fluorescence originating from the aluminium oxide (Figure 45). Figure 50 shows background emission spectra of all substrates excited at various excitation wavelengths that were selected due to the wavelength dependent nature of the aluminium oxide's emission and to match excitation wavelengths of BSA-AuNCs. The oxide's emission was absent in background spectra and should not interfere with fluorescence of immobilized molecules. Some spectra exhibit relatively high background signal including periodically repeating sharp peaks which are assumed to be a result of scattered and reflected light from patterned surfaces.

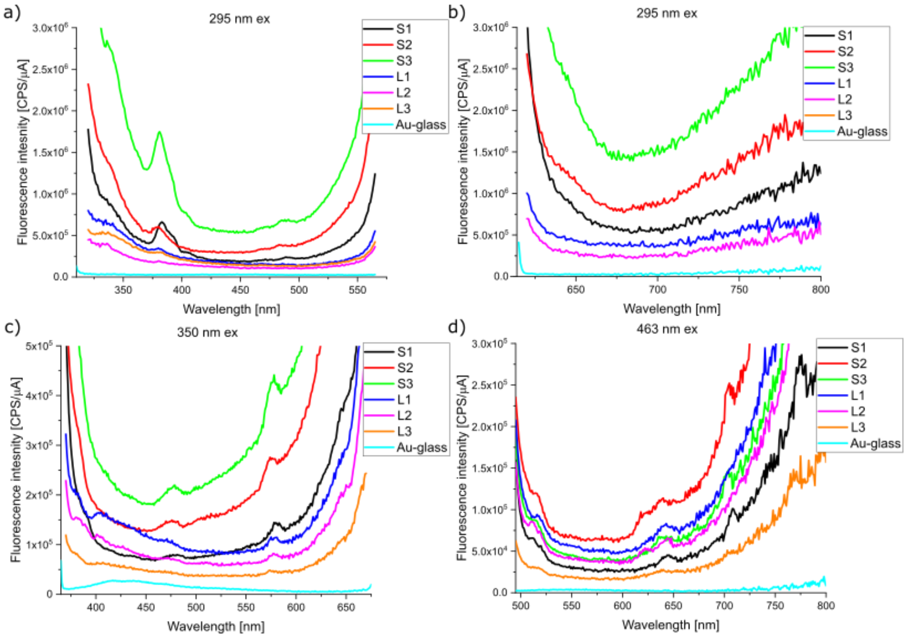

Figure 50: Background emission spectra of AuNBs collected for excitation wavelengths that correspond to those previously used for BSA, BSA-AuNCs (295 nm, 463 nm) and the aluminium oxide (350 nm).

5.4.2. Numerical Simulations of Optical Properties of Gold Nanobowls

As the purpose of AuNBs is to be used as substrates for MEF, three-dimensional FDTD simulations were carried out to probe reflectance and electromagnetic fields generated by AuNBs under various excitation conditions. Comparing theoretical and experimental results will allow to gain a better understanding of the functioning of the AuNB pattern and extend the knowledge of its optical properties which will help guide further experimental studies.

Reflectance spectra and electric field maps were calculated for spherical cavities using dimensions of AuNB@1 and AuNB@2 as starting parameters, specifically for AuNBs with lowest (S1, L1) and highest (S3, L3) sizes of Au films. A detailed description of performed FDTD calculations and of the simulated AuNB pattern can be found in the experimental section (5.3.4) of this chapter. The optical activity of AuNBs was probed for incident wavelengths 290 nm, 470 nm, 533 nm, 650 nm, 780 nm. The wavelength 290 nm was included as it is a commonly used excitation wavelength in the UV-vis region, suitable also, for example, for the excitation of tryptophan residues in proteins.

5.4.2.1. Modelling Reflectance of Gold Nanobowls

Theoretical reflectance spectra were simulated for a hexagonal array of AuNB@1 with diameters 75, 83 nm (S3, S1) and AuNB@2 with diameters 420, 475 nm (L3, L1) at 0 ° of incidence (Figure 51). The spectrum of L1 uses 10 nm upper walls to investigate the effect of thin barriers on the electric field distribution of large-diameter NBs. The effect of larger walls will be discussed later in the text. Both groups of AuNB spectra are in agreement with experimental spectra summarized in Figure 49, exhibiting the low reflectance below 500 nm. The slightly higher theoretical reflectance of AuNB@2 spectra compared to experimental spectra can be attributed to the perfectly spherical geometry of simulated NBs as the model does not take the more complex surface, which contributes to the reduced reflectivity, into account. Nevertheless, these results show that the reflectivity of AuNBs of can be predicted through theoretical modelling with reasonable accuracy.

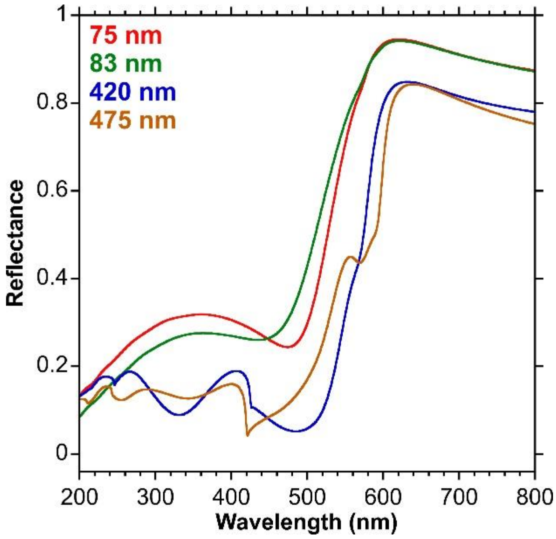

Figure 51: Theoretical reflectance spectra calculated for AuNBs with various diameters and wall thicknesses. Used diameters are highlighted in colours (S3 – 75 nm, S1 – 83 nm, L3 – 420 nm, L1 – 475 nm) and corresponding wall thicknesses are 48 nm (S3), 25 nm (S1), 71 nm (L3) and 10 nm (L1). The radius of NBs at surface was used as the depth.

Next was probed the reflectivity of AuNB@1 and AuNB@2 for varying incident angles and wavelengths in order to identify optimal excitation conditions (Figure 52). The results generated for AuNB@1 with a spherical geometry showed reflectance spectra without dips that would suggest angle-dependent absorption (Figure 52a,b). On the other hand, AuNB@2 exhibited a size- and an angle-dependent reflectivity of wavelengths 470 nm – 650 nm that seem to be determined by their different larger diameters. The reflectance of L3 reaches minima at 6 ° (470 nm), 16 ° (533 nm) and 35 ° (650 nm) of incidence (Figure 52c), and shift to 8 ° (470 nm), 18 ° (533 nm) and 38 ° (650 nm) for L1 (Figure 52d). While the shift in angles is relatively small, the difference in reflectance is more substantial, indicating angles for the preferential excitation of strongly absorbing plasmon modes. L3 exhibits improved absorption at 533 nm (6 ° – 20 °) but increasing the diameter enhances the absorption at 650 nm (10 ° – 46 °).

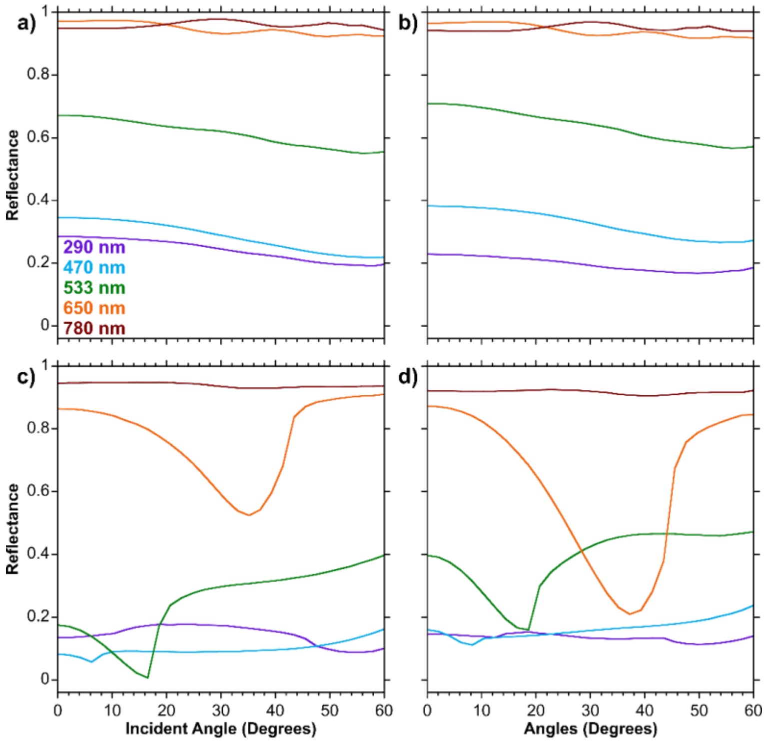

Figure 52: Theoretical reflectance spectra of AuNBs calculated for selected excitation wavelengths at varying angles of incidence. Diameters of AuNBs were a) 75 nm (S3), b) 83 nm (S1), c) 420 nm (L3), d) 475 nm (L1).

5.4.2.2. Modelling Electromagnetic Fields of Small-diameter Gold Nanobowls

To visualize the spatial distribution of electromagnetic fields across AuNBs, FDTD calculations were performed for AuNB@1 and AuNB@2 using the aforementioned selection of incident wavelengths and various angles of incidence (0 °, 30 °, 45 °, 60 °)[101,111,279] suitable for spectroscopic techniques. After examining electric field maps of AuNB@1, it appears that only small field enhancement can be gained for both diameters of the spherical geometry regardless of the Au film thickness or excitation conditions (Figure 53, Figure 54). A weak electric field can be seen only near edges of rims (best seen for 533 nm excitation) which may be attributed to a weak coupling between Au rims and the incident light.[111,279] Also, decreasing diameters causes AuNBs to appear more as a flat surface for longer wavelengths (smaller relative size of NBs with respect to the wavelength).[255]

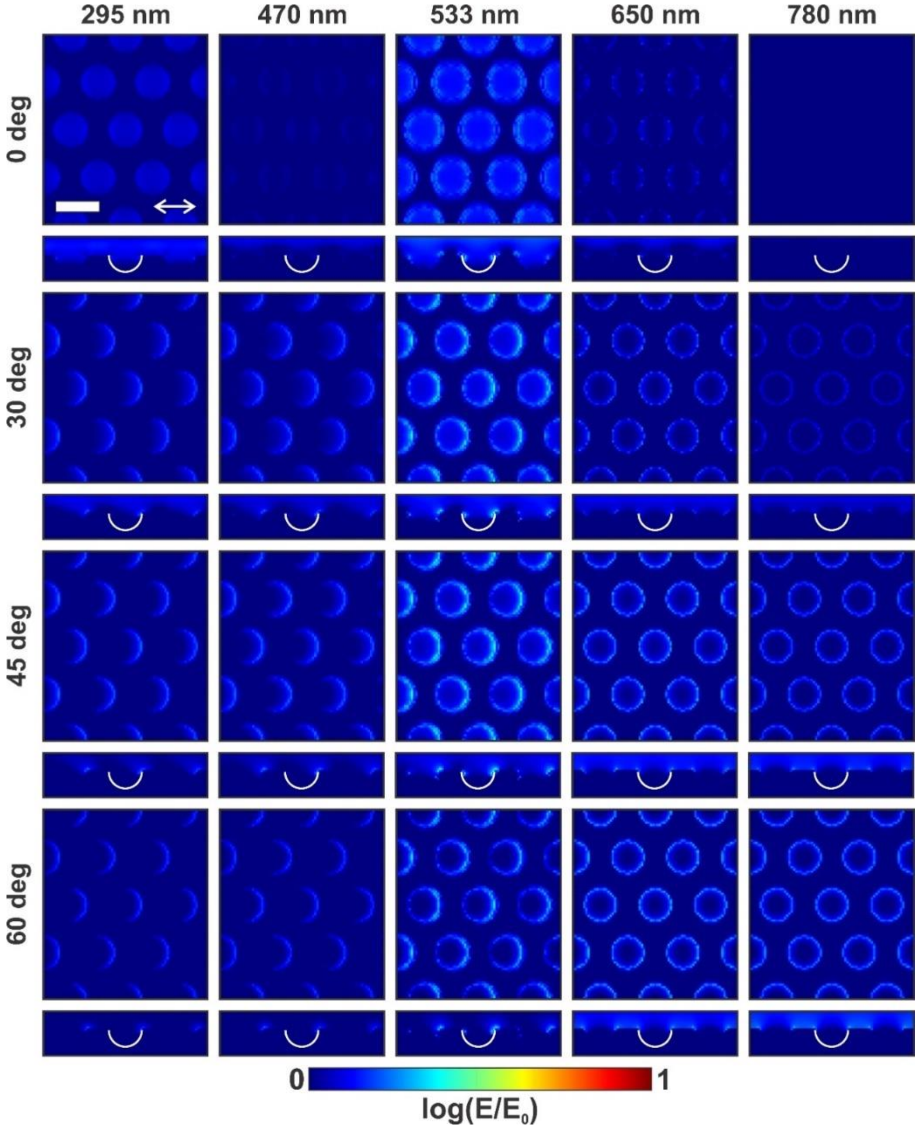

Figure 53: Electric field maps (top and side views) for AuNB@1 S3 with the 75 nm diameter. The arrow indicates the polarization angle, and the scale bar corresponds to 100 nm. E/E$_0$ corresponds to the ratio of incident (E$_0$) and induced (E) electric field intensities.

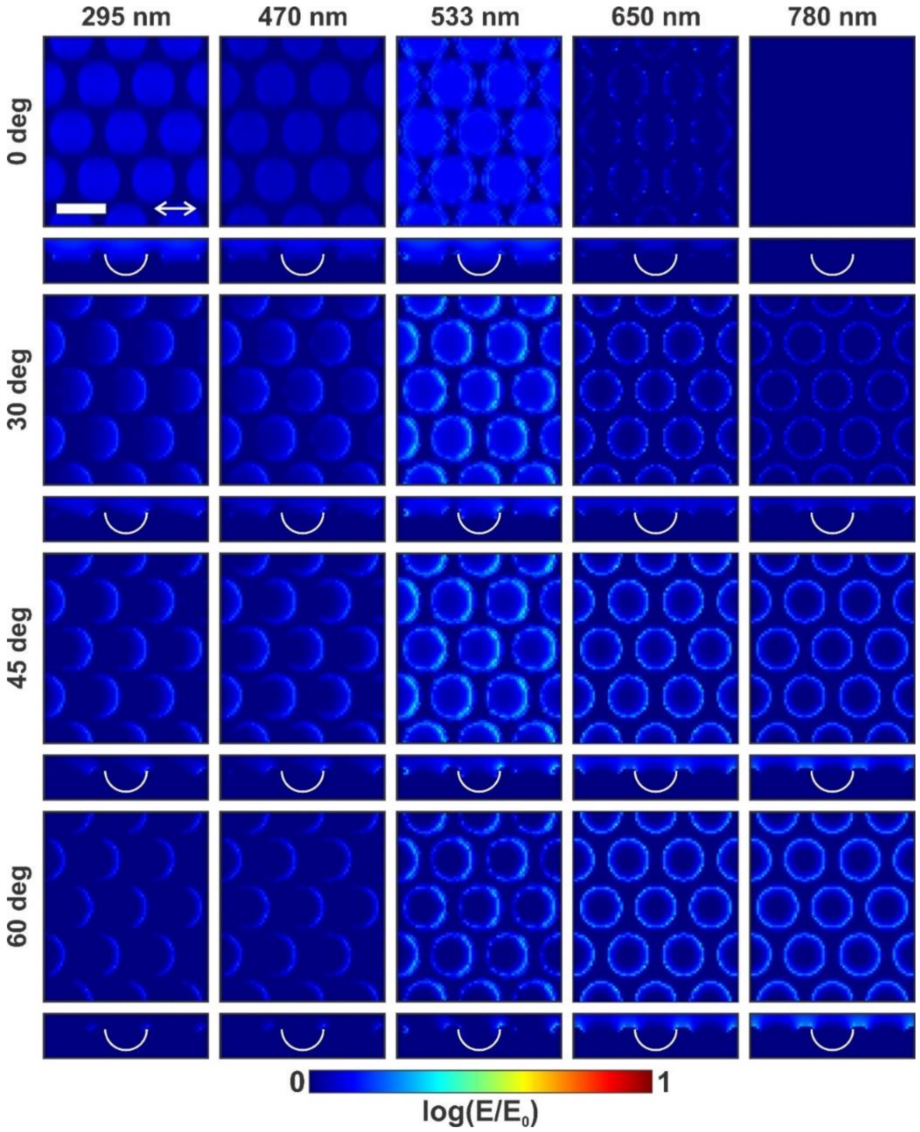

Figure 54: Electric field maps (top and side views) for AuNB@1 S1 with the 83 nm diameter. The arrow indicates the polarization angle, and the scale bar corresponds to 100 nm. E/E_0 corresponds to the ratio of incident (E_0) and induced (E) electric field intensities.

5.4.2.3. Modelling Electromagnetic Fields of Large-diameter Gold Nanobowls

Increasing the diameter of NBs leads to a major change in the electric field intensity and distribution (Figure 55, Figure 56). The most obvious features are highlighted plasmon modes of NBs. These are confined inside NBs for wavelengths shorter than 650 nm. For the 295 nm excitation (0 °), a well-resolved symmetrical lobed plasmon mode at the bottom surface can be observed. In general, plasmon modes localized at the AuNB surface are critical for the enhancement of signals from surface-bound molecules and EM fields of nanoparticles.[107,114,116] This is particularly useful for fluorescence microscopy which utilizes normal illumination. As the excitation wavelength approaches the diameter of NBs, the confinement of modes is disrupted, and the field enhancement moves from the bottom of NBs above the surface.

The angle-dependence of the electric field distribution and absorption of AuNBs becomes apparent at higher angles of incidence where plasmon modes with vertically oriented field distribution can be excited. These modes cannot couple to normally incident light[111] and could be of interest for fluorescence spectroscopy which utilizes illumination at higher angles. One can also see that the electric field of vertical modes overlaps the top surface between NBs. This suggests that the plasmon field can be extended beyond the interior of NBs even when excited at shorter wavelengths, increasing the active surface area on the substrate. For the 295 nm excitation, the electric field mode extends over a large surface area on the inner surface of NBs. For 470 nm and 533 nm excitations, these modes become focused closer to the centre of NBs and couple to rims at 650 nm. The strong coupling of confined modes with rim dipoles and the incident light results in the highest field enhancements for both diameters. This occurs because excitation wavelengths larger than the diameter of NBs cannot reach the bottom surface but can excite surface plasmons at rims and the flat upper surface.[101,111] The increase in electric field intensity for 650 nm observed for incident angles of 30 ° – 45 °, corresponds to the decreased reflectance (increased absorption) of AuNB@2 in Figure 52c,d. For the 780 nm excitation, all EM field modes are located above the structure, exhibiting a decreasing efficiency of coupling to AuNBs. In addition, the electric field distribution in Figure 55 and Figure 56 is not influenced by electric fields of neighbouring NBs which indicates that coupling between NBs is weak.[111,280] The results suggest that even higher enhancements could be generated with excitation conditions matching angle-dependent reflectance minima in Figure 52. Based on simulations, AuNB@2 substrates exhibit useful EM behaviour, particularly due to high electric field enhancements at rims as well as controllable electric field distribution within NBs.

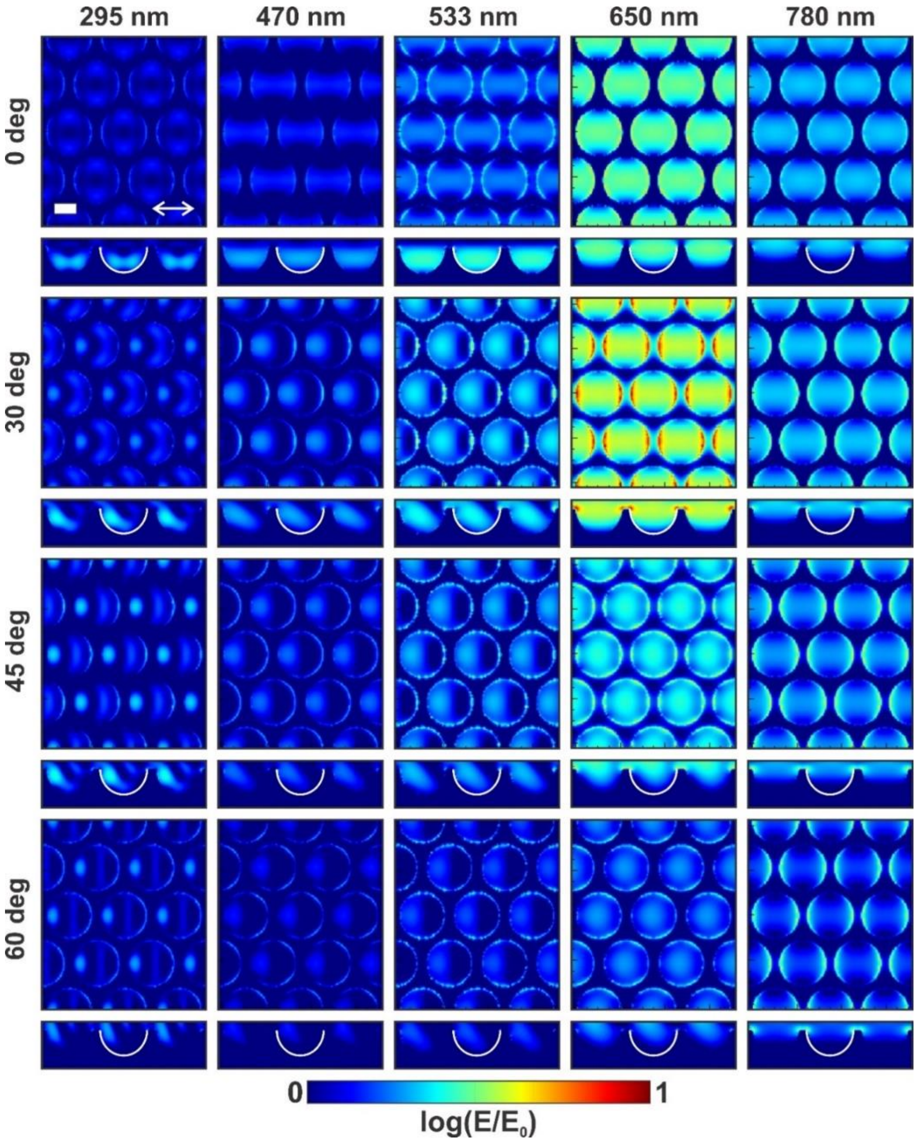

Figure 55: Electric field maps (top and side views) for AuNB@2 L3 with the 420 nm diameter. The arrow indicates the polarization angle, and the scale bar corresponds to 200 nm. E/E$_0$ corresponds to the ratio of incident (E$_0$) and induced (E) electric field intensities.

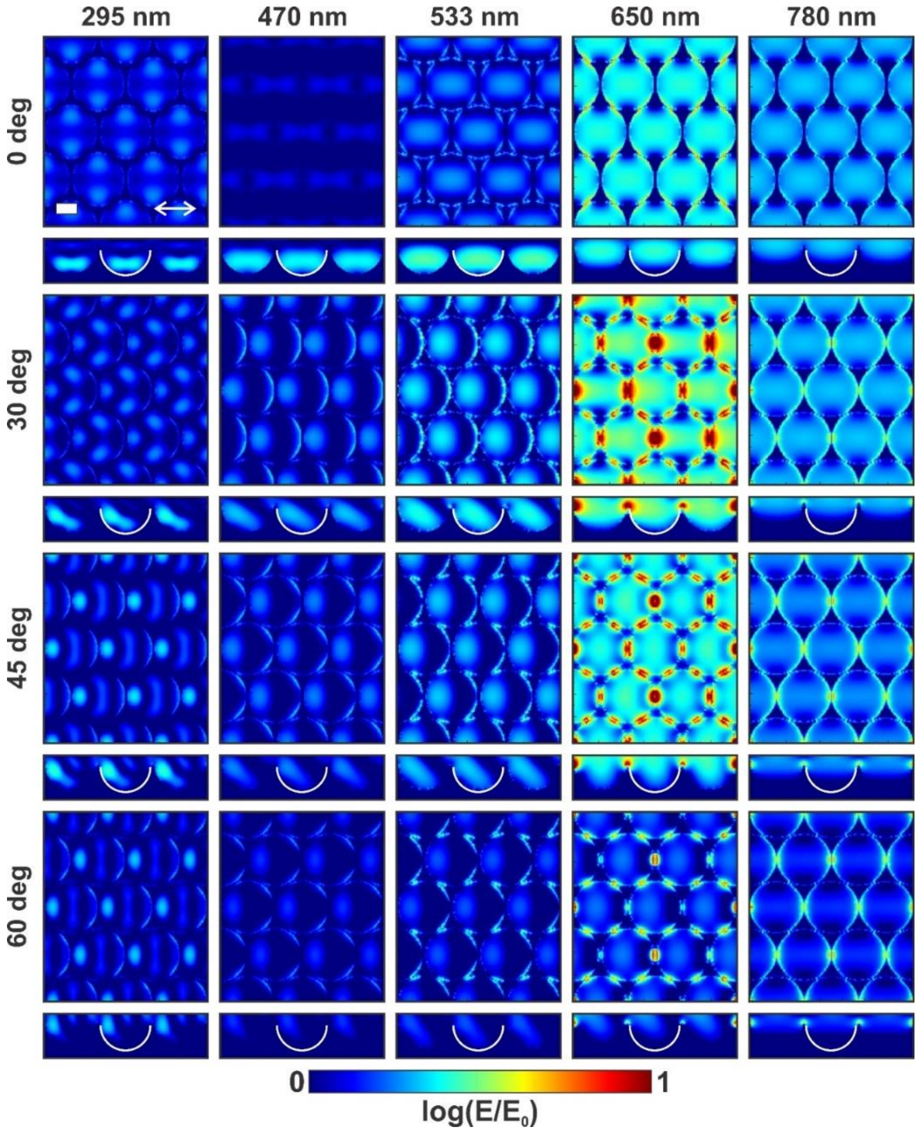

Figure 56: Electric field maps (top and side views) for AuNB@2 L1 with the 475 nm diameter. The arrow indicates the polarization angle, and the scale bar corresponds to 200 nm. E/E_0 corresponds to the ratio of incident (E_0) and induced (E) electric field intensities.

Electric field maps calculated for 650 nm excited L1 (Figure 56) show multiple hot spots localized at rims. This feature is the result of small nanogaps between walls created by the small wall thickness (10 nm) with respect to the FDTD grid size (10 nm). Sections of walls of two neighbouring NBs with a fixed size of the Au film (≥30 nm) overlap when the separation distance is set to create the 10 nm barrier. Sections that do not overlap extend inside neighbouring NBs and are treated as air. Due to the 10 nm mesh, the model does not resolve the 10 nm metal wall between two NBs as a solid Au surface but is treated as air because the majority of the said pixel is air. This area is then displayed as small gaps between Au nanostructures. The corresponding considerable enhancement (hot spots) in electric field maps can be expected when nano gaps are introduced between two plasmonic Au nanostructures. As will be shown later by employing finer mesh parameters, changing the wall size does not have any major effect on the electric field enhancement inside NBs.

A different approach was selected to assess preferential excitation wavelengths for each of the four substrates with respect to the localization of the electric field enhancement. Iso-wavelength maps allow to display the wavelength-dependent spatial distribution of electric field (enhancement) across different areas of a given structure (Figure 57).[281] By comparing electric field maps (calculated at different wavelengths), only pixels with maximum electric-field intensities can be visualized and are then assigned values of respective wavelengths that yielded these intensities. Calculations were performed for orthogonally polarized light and 0 ° of incidence which showed the clear mode confinement at the bottom surface of AuNB@2.

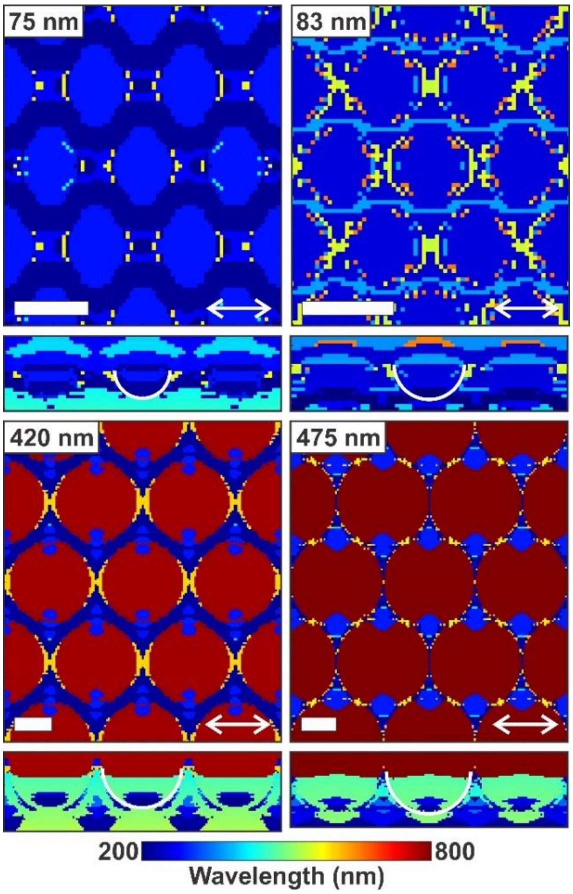

Figure 57: Iso-wavelength maps (top and side views) calculated for various diameters of AuNBs. The arrows indicate the polarization axis, and the scale bars are 100 nm for AuNB@1 (75, 83 nm diameters), and 200 nm for AuNB@2 (420, 475 nm diameters).

The iso-wavelength maps corroborate electric field maps. While simulated spherical AuNB@1 exhibit little electric field enhancement for probed conditions, iso-wavelength maps of AuNB@2 show a distinct wavelength-dependent variation of the electric field distribution. Rims respond to an excitation with incident wavelengths that are longer than the diameter. Wavelengths lower than the diameter induce plasmon modes within NBs and the enhanced field moves above the surface and between rims for wavelengths approaching the diameter of NBs. This could be exploited in processes where light harvesting[112,255] or selective excitation of reporter molecules located inside NBs are desired.

5.4.2.4. Effect of the Wall Thickness and the Thickness of the Gold Coating on Electromagnetic Fields of Gold Nanobowls

There is currently lack of information about the effect of finer structural features, such as the Au film thickness and the wall thickness, on the enhancement of EM fields induced in AuNBs. These parameters can be controlled through the deposition of Au in the final step of the fabrication process. Understanding how these factors influence optical properties of AuNBs is useful for identifying potential areas that could be optimized in order to improve their performance in MEF.

The effect of wall thickness on the electric field distribution was investigated for L1 (Figure 58) by first simulating reflectance spectra for -10 nm (air gap), 0 nm (fused rims), and 5 nm, 10 nm, and 15 nm (physical separation with Au) walls. Calculations were performed on a single lattice with finer mesh parameters of 2.5 × 2.5 × 5 nm (x, y, z) as opposed to previously used 10 × 10 × 10 nm (Figure 59). All reflectance spectra showed identical reflectance below 550 nm, but separations of -10 nm, 0 nm and 5 nm created noticeable dips in the region above 550 nm. These are the results of a staircasing error due to the limited capability of the software to precisely simulate shapes of objects that are smaller than the mesh size (“limit of resolution”). Reflectance spectra calculated for wall thicknesses above 10 nm do not show these features. Therefore, the 10 nm wall size is valid and only requires adjustment of the model’s mesh. More importantly, reflectance spectra in Figure 58 show that gaps in the model did not have any effect on the predicted reflectance in the spectral range of interest below 500 nm.

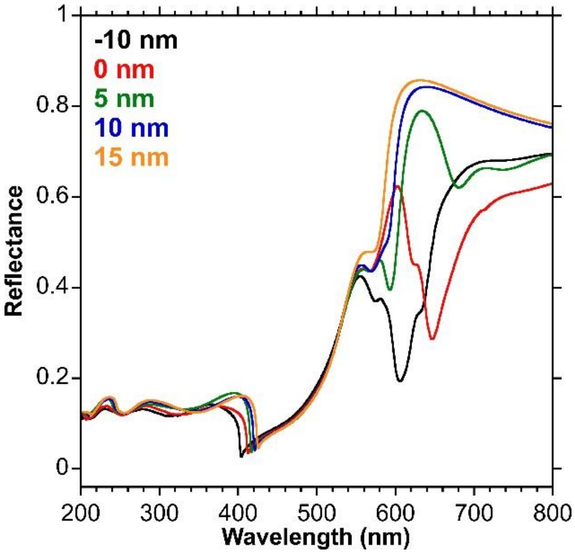

Figure 58: Reflectance spectra of AuNB@2 L1 (diameter of 475 nm) with various wall thicknesses.

A set of electric field maps was generated to evaluate the effect of selected sizes of walls on the electric field distribution of L1. Electric fields were probed for the angle of 45 ° and excitation wavelengths 470 nm and 650 nm which induced the weakest and the strongest field enhancements, respectively. Figure 59 shows that changing the wall thickness from -10 nm to 50 nm did not have any major effect on the intensity of the electric field at 470 nm but decreased its size. A shift of the electric field towards the wall is also visible, increasing the surface coverage along the rim. When the incident wavelength is increased to 650 nm, dramatic differences are noted. The electric field enhancement remains localized at rims and increases the coverage of the upper flat surface but gradually loses strength for wall thicknesses greater than 10 nm. For walls larger than 30 nm, the surface coverage of the electric field enhancement diminishes and is localized primarily at rims. By maintaining the wall thickness below 30 nm, higher localized electric field enhancement up to ~10^2 near rims can be achieved. Thinner walls may also be more suitable for generating larger confined EM fields along the AuNB surface with shorter excitation wavelengths.

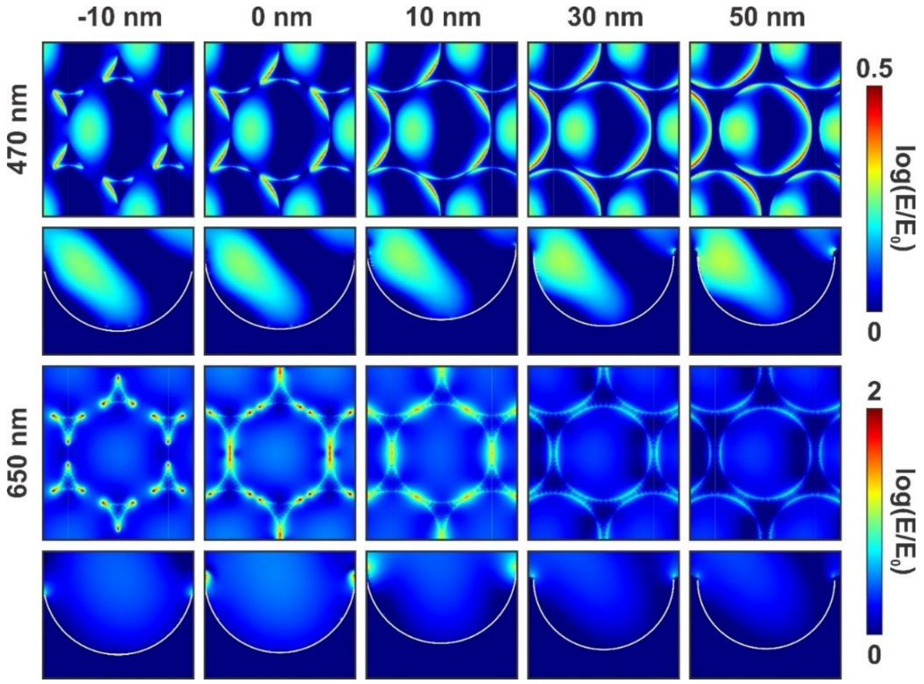

Figure 59: Electric field maps (top and side views) calculated under horizontal illumination for AuNB@2 (475 nm diameter), gold thickness of 30 nm and various sizes of walls. E/E$_0$ corresponds to the ratio of incident (E$_0$) and induced (E) electric field intensities.

The effect of Au film thickness on the electric field enhancement of L1 was also investigated (Figure 60). Electric field maps were calculated for 10 nm, 30 nm and 50 nm Au films using same conditions that were used in Figure 59. The electric field enhancement of AuNBs for 650 nm excitation appears to be unchanged by the altered Au thickness, and rims remain to be the only optically active areas of high electric field enhancement for longer wavelengths. In contrast, decreasing the film thickness enhances the strength and the range of confined fields inside NBs for the 470 nm excitation. A similar effect can be expected to occur for other wavelengths below 470 nm that can interact with the NB surface.

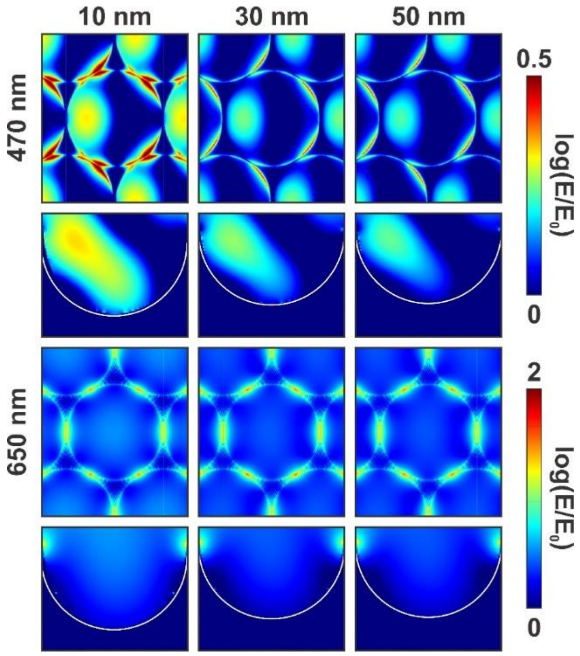

Figure 60: Dependence of the electric field distribution inside AuNBs (top and side views) on the Au film thickness. Electric field maps were calculated for L1 (diameter of 475 nm) under 470 nm, 650 nm illumination, 45 ° of incidence and Au film thicknesses of 10 nm, 30 nm, 50 nm. E/E$_0$ corresponds to the ratio of incident (E$_0$) and induced (E) electric field intensities.

5.5. Conclusions

This chapter has demonstrated the fabrication and the in-depth characterization of plasmonic AuNBs based on Au-coated AlNB arrays with optical properties suitable for MEF in the UV-Vis. AuNBs of various diameters and thicknesses of the Au coating were subjected to a complex analysis of optical properties in dependence on illumination conditions and structural features. Optical measurements indicated that the reflectance of AuNBs is a combination of effects determined by the thin Au coating, the geometry of the AlNB template, and the topography of Au-coated surfaces. Reflectance spectra of AuNBs exhibited a broad minimum ranging from 500 nm to the UV that is indicative of a strong absorption. This absorption range is highly desirable as it could support an improved excitation of incorporated fluorophores even in the UV.

By performing FDTD calculations under various illumination conditions, angle- and wavelength- dependent optical properties as well as the distribution of EM fields in AuNBs were determined. Simulations suggest that AuNB@1 exhibit a weak response to incident wavelengths which can be attributed to their small diameters. In contrast, large-diameter AuNBs exhibited size-, angle- and wavelength-dependent optical properties which may be controlled by manipulating excitation conditions. The diameter of AuNBs determines the spectral range of incident wavelengths which can interact with the interior surface or rims. As a result, various classes of plasmon modes of AuNB@2 have been identified which can directly participate in interactions with fluorophores or nanoparticles. Highest electric field enhancements were calculated near rims and the top surface for incident wavelengths that are similar to or longer than diameters of NBs. Wavelengths shorter that the diameter can interact with the interior of NBs and generate confined electromagnetic fields. The wall thickness was shown to have a minor effect on the intensity of confined fields but is the determining factor for achieving high-intensity rim hot spots and a larger coverage at the top surface. On the other hand, the strength and the size of confined electromagnetic fields was found to increase with the decreasing thickness of the Au coating.

The broadband response of large-diameter AuNBs to wavelengths below 650 nm and incident angles of 0 – 45 ° suggest that the application of AuNB substrates could be extended to fluorescence techniques where the fluorescence emission is detected at higher angles. In the current configuration, AuNBs generate electric field enhancements that are comparable to those of similar nanovoid architectures. However, simulations indicate that Au films with thickness $\leq$30 nm could improve the efficiency of AuNBs and that even higher enhancements could be achieved for specific wavelengths with excitation conditions matching angle-dependent reflectance minima of AuNBs in Figure 52.

The results presented here could serve as guidelines for designing plasmonic AuNB substrates for specific fluorescence as well as other spectroscopic techniques based on available excitation conditions and characteristics of photoactive molecules.

6. Fluorescence Spectroscopy of BSA-AuNCs on Gold Nanobowls

6.1. Introduction

In the previous chapter, it was shown that AuNBs exhibit optical properties and surface characteristics suitable for MEF in UV-Vis. As indicated by FDTD simulations, the wavelength selectivity as well as the absorption of light in the UV region exhibited by AuNBs are particularly intriguing as only a limited number of nanostructures can achieve this. Using anodized Al as a template for the fabrication of AuNBs is especially promising, considering the relatively simple fabrication, tunable dimensions of nanostructures and low cost, all of which are desired requirements for plasmonic substrates.

To date, applications of NBs have been focused mainly on SERS,[109,115,258,270,282,283] while MEF has been experimentally less widely studied on this type of ordered architecture despite exhibiting unique features that could be beneficial to various fluorescence applications. Several studies have looked into the parallel detection of SERS and MEF of a fluorescent ruthenium complex $[Ru(bpy)_2(Qbpy)]^{2+}$ on AuNBs.[103,121,123,284] The emphasis was mainly on inducing a signal enhancement and on exploring the angular dependence of both phenomena in combination with the angle-dependent plasmonics of the NB pattern. The results have shown a correlation between signal enhancements and localization of plasmon resonances as functions of incident angle on arrays with various dimensions and rim structures of NBs. Jose et al. analysed fluorescence emission of the $[Ru(bpy)_2(Qbpy)]^{2+}$ and fullerene immobilized inside AuNBs using conventional fluorescence microscopy and fluorescence lifetime microscopy.[103] Highly localized enhancements near the bottom surface of NBs were observed. Due to the dependence of the fluorescence emission enhancement on excitation wavelengths and only small changes in fluorescence lifetimes, it was suggested that the emission was governed by plasmonics through an improved excitation of both dyes. Following on this study, Lordan et al.[121] and Jose et al.[123] investigated the dependence of the emission intensity on the location of the dye by selectively functionalizing the inner or the top surface of AuNBs. Both studies showed variations of emission intensities depending on the location of the dye as well as dimensions of NBs and of the top surface. This was attributed to the presence of confined void plasmons and surface plasmons propagating at the top surface excited according to structures' dimensions with respect to incident wavelengths. The studies suggested that by using excitation wavelengths longer or similar to diameters of NBs, localized excitation of surface plasmons between neighbouring NBs can be achieved,[101,111,121,123,285] which may induce fluorescence enhancements greater than inside NBs. Recently, Gimenez et al.[122] and Lordan et al.[286] reported on the excitation-dependent MEF of ruthenium complexes on various sub-micrometre and micrometre AuNBs, including AuNBs modified with GNPs and AgNPs, respectively.[122] A trend of increased emission intensities from NBs combined with NPs was observed due to the higher structural complexity which modified void plasmons and led to the excitation of high-intensity hotspots near NPs. It was again shown that both MEF depends on NB dimensions with respect to excitation wavelengths and an additional nano-structuring of NBs.

Qiu et al. utilized small-diameter (~50 nm) AgNBs for a fluorescence imaging of P-FITC labelled cytoskeleton of Chinese Hamster Ovary cells and observed both enhanced fluorescence emission and increased photostability of the dye.[118] At this diameter, the array is formed of six protruding nanocaps, separated by concave nanogaps, in each corner of NBs, which may behave as an array of plasmonic nanoantennae upon resonant illumination. The emission enhancement was explained by an improved excitation of P-FITC and a far-field emission of nanocaps induced by the P-FITC fluorescence due to a coupling of LSPR of nanocaps with the dye, mediated by a spectral overlap between absorption/emission spectra of P-FITC and the LSPR. In another study of Qiu et al., an enhancement of fluorescence emission of a dye poly[2-methoxy-5-(2'-ethyl-hexyloxy)-p-phenylene vinylene] (MEH-PPV) was tailored by coupling to hexagonally arranged Ag nanocaps of NBs with various diameters (≤100 nm) and rim structures.[117] The proposed mechanism was based on the matching of LSPR of nanocaps with the absorption profile of a dye, which was critical for achieving a dipole-dipole interaction and, similarly to FRET, a plasmon resonance energy transfer from silver nanocaps to the dye. It was shown that the increase in the fluorescence emission can be partially controlled through the fabrication process by manipulating nanogaps between nanocaps during anodizing (diameter) and metal deposition (thickness of the metal). Promising results were observed for densely packed nanocaps and a smaller gap size where an EM field enhancement is localized. The same group investigated the band-gap-dependence of fluorescence emission of conjugated fluorescent polymer films poly(2,5-dioctyloxy-p-phenylene) (PPP) and poly[3-(2,5,8-trioxanonyl) thiophene] (P3TT) coupled to silver nanocaps of small-diameter (≤50 nm) AgNBs produced on the anodized aluminium oxide.[287] The absorption spectrum of P3TT and the emission spectrum of PPP overlapped with the absorption band of Ag nanocaps. Fluorescence emission of P3TT was enhanced and that of PPP was quenched. The emission enhancement was attributed primarily to the aforementioned plasmon resonance energy transfer from Ag nanocaps to P3TT which was proposed to be the key contributor compared to the enhancement due to an increased absorption of the dye and by the substrate. In addition, the contribution of surface plasmons localized in the Ag nanocap array and plasmons at the Ag-polymer interface was considered as well. Based on a red-shifted emission of PPP, the quenching of PPP fluorescence was associated with a radiative energy transfer to Ag nanocaps through the excitation of surface plasmons at the metal-polymer interface.

The application of copper NBs in MEF has been also reported.[119,120] Copper nanobowls (CuNBs) can be produced through the same colloidal lithography and electrochemical deposition approaches as Au patterns. Spada et al. modified the surface of shallow large-diameter (476, 756 nm) CuNBs with a blue fluorescent polymer polyfluorene (PFO) and observed stronger emission from NBs compared to the emission from the top surface.[120] This effect was ascribed to plasmonic effects and improved light absorption due to the geometry of CuNBs.

The above discussed studies utilized mainly colloidal templating to produce arrays of well-defined NBs with controllable dimensions of sub-micrometre and micrometre diameters, demonstrating benefits of the nanobowl geometry for fluorescence techniques. Investigations of the excitation dependence of dyes’ emissions from NB patterns outlined underlying mechanisms involved in the MEF but also pointed out the importance of considering the structural complexity of NBs. Nevertheless, an important gap regarding the probed spectral window can be found in these studies. It is believed that, to date, AuNBs have been utilized only in the visible and NIR regions of spectrum, but the application of properties of the nanobowl architecture for MEF in the UV has not been previously attempted. Furthermore, Chapter 5 demonstrated that anodizing of aluminium is a promising alternative to colloidal lithography, removing the necessity to rely on colloidal lithography for templating to produce plasmonic AuNB arrays with suitable characteristics for MEF. Therefore, utilizing AuNBs produced in Chapter 5 in fluorescence spectroscopy, will allow to determine whether this alternative methodology produces plasmonic AuNBs capable of inducing fluorescence enhancement that can be extended to the UV region.

This chapter aims to investigate the application and performance of AuNBs produced on an anodized aluminium template in MEF in the UV and visible regions of spectrum using previously introduced BSA-AuNCs. The complex was selected as a signal molecule due to its low quantum yield (~6 %) and excitation wavelengths of 295 nm and 463 nm being in both UV and Vis. Two groups of large- and small-diameter AuNBs with different Au film dimensions were tested under varying excitation conditions via steady-state fluorescence spectroscopy. In order to explain the fluorescence behaviour of BSA-AuNCs on AuNB substrates, results obtained from the fluorescence analysis were correlated with theoretically and experimentally obtained characteristics of AuNB substrates in Chapter 5. A structure-specific angular dependence of the BSA-AuNC fluorescence emission on both types of AuNBs was observed and a broadband enhancement of fluorescence emission from BSA-AuNCs on large-diameter AuNBs, with a maximum enhancement factor of ~34.5-fold, was demonstrated. This investigation of fabricated plasmonic AuNBs highlights their potential as fluorescence-enhancing platforms and demonstrates the applicability of AuNB substrate for fluorescence techniques in both UV and visible regions of spectrum.

6.2. Experimental

6.2.1. Materials

Mercaptohexanoic acid (MHA, 99.8%), toluene (99.8 %), isopropanol (99.5 %), dodecanethiol (98 %), acetone (99.9 %), methanol, and chemicals ($AgNO_3$, $HAuCl_4$, CTAB, $NaBH_4$, ascorbic acid) necessary for the synthesis of GNRs were purchased from Sigma-Aldrich. Hydrochloric acid (HCl) was purchased from Fluka.

6.2.2. Surface Modification of AuNBs

Surfaces of AuNB substrates AuNB@1 (S1, S3 with diameters of 83 nm and 75 nm) and AuNB@2 (L1, L3 with diameters of 475 nm and 420 nm) characterized in the previous chapter were initially coated with a dense SiO_2 spacer layer of ~10 nm. An Au-coated microscope slide was also coated with SiO_2 to produce a reference substrate. The SiO_2 deposition was done using a multiple-beam sputtering system[288] for physical vapor deposition (PVD). Samples were mounted on a rotation stage to produce uniform coatings. The source were Si targets (5N purity 99.999%) and the deposition was carried out at the base pressure of 3.4×10^{-6} mbar, deposition pressure 4.6×10^{-4} mbar and voltage 10 kV (ion energy = 10 keV). The deposition time of several minutes was set to correspond to the film thickness of ~10 nm on the quartz microbalance. The thickness of the spacer was also verified through atomic force microscopy (AFM) on the coated microscope slide by measuring cross-sections across scratches made at several areas on the surface (Figure 61). The data were collected by a Dimension Icon® AFM (Bruker, Santa Barbara, CA) using the PeakForce Tapping® scanning mode at 20 °C with a ScanAsyst-Air® probe (Bruker, Santa Barbara, CA) with a nominal spring constant $k = 0.4\ \mathrm{Nm}^{-1}$ and nominal tip radius of 2 nm.

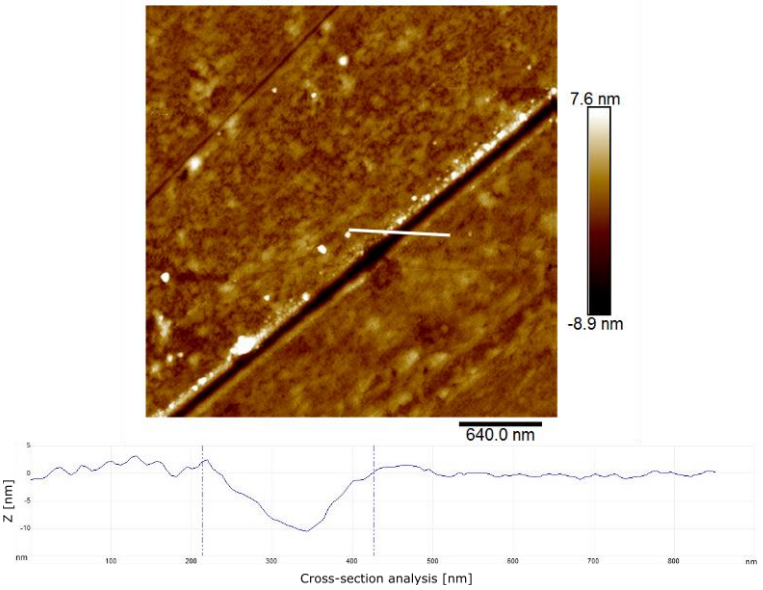

Figure 61: AFM image of a SiO_2-coated glass slide showing a scratch mark in the SiO2 spacer. The cross-section analysis (bottom row) was done along the white line indicated in the AFM image.

6.2.3. Deposition of BSA-AuNCs

An aqueous solution of fluorescent BSA-AuNCs with the concentration of 0.025 mg/mL (100 μL) was evenly applied across the Au-coated area on AuNB surfaces and was left to dry at room temperature before carrying out any fluorescence measurements.

6.2.4. Fluorescence Measurements

Fluorescence analysis of BSA-AuNCs on AuNBs was carried out under 8 °, 30 °, 45 ° and 60 ° of illumination (Figure 62) in the Fluorolog-3 spectrofluorometer with the standard 90 ° collection geometry that was used for fluorescence measurements of BSA-AuNCs on the Al foil in Chapter 4. Angles of incidence were controlled using an attached protractor. Excitation wavelengths were set to 295 and 463 nm, and the emission was collected without additional optical elements in the range from 310 nm to 800 nm with a 1 nm increment and an integration time 0.1 s. Excitation and emission slits were set to 5 nm. All fluorescence emission spectra were corrected to monochromator-response characteristics and dark counts.

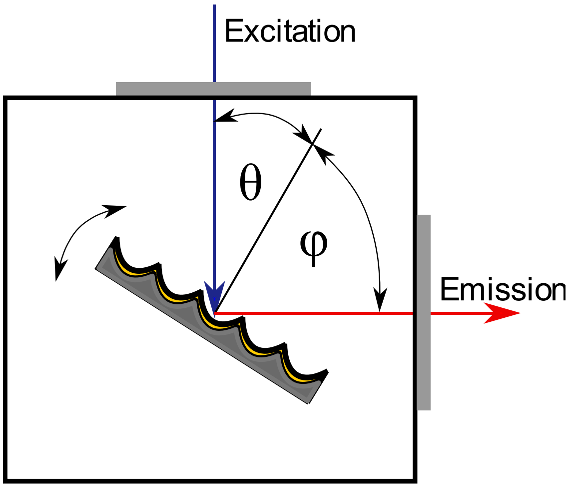

Figure 62: Schematic diagram of the excitation/detection geometry inside the sample compartment. Excitation and detection are arranged in the standard 90 ° geometry. Angles of excitation (θ) and emission (φ) are measured with respect to the sample's normal and are controlled by rotating the sample.

6.3. Results and Discussion

The first step towards application of AuNBs in fluorescence measurements was the deposition of a 10 nm silica spacer to achieve a sufficient metal-fluorophore distance in order to prevent a non-radiative quenching of the BSA-AuNC fluorescence by the metallic surface. An Au-coated glass slide with a 58 nm Au layer served as a reference substrate for all fluorescence measurements. AuNBs used in this experiment were AuNB@1 and AuNB@2 with 30 nm (S1, L1) and 58 nm (S3, L3) Au films and diameters of 83 nm (L1), 75 nm (L3), 475 nm (L1) and 420 nm (L3). BSA-AuNCs (~0.38 µM) were applied directly onto AuNBs without further modification. Fluorescence measurements were carried out using a conventional spectrofluorometer at various angles of illumination (8 °, 30 °, 45 °, 60 °) with respect to samples' normal, which is capable of excitation and detection in the UV. The fluorescence emission of BSA-AuNCs on AuNBs was collected over an unrestricted range of angles for set excitation angles.

6.3.1. Fluorescence Spectroscopy of BSA-AuNCs on Large-diameter AuNBs

Fluorescence spectra of BSA-AuNCs on AuNB@2 substrates L1 and L3 are shown in Figure 63. Both substrates exhibited a similar trend of increasing fluorescence intensities of tryptophan and AuNCs with an increasing angle of illumination. Both 295 nm and 463 nm excited AuNCs on L1 exhibited highest fluorescence intensities for the 45 ° illumination followed by a small decrease when excited at 60 ° (Figure 63a,c). Fluorescence spectra collected from L3 showed similar intensities for the excitation below 30 ° and an increase of emission when excited at 45 ° and 60 °. The difference between emissions collected from L1 and L3 was more significant for the UV excitation compared to the 463 nm excitation. For the 463 nm excitation, one can see that, except for the 60 ° excitation, the AuNC fluorescence emission exhibited similar intensities on both substrates, which suggests that for the blue excitation wavelength, AuNB@2 substrates have similar efficiency. For the 295 nm excitation, fluorescence spectra of tryptophan and AuNCs showed a corresponding increase in the intensity. This could indicate that both emitters responded to the change in the excitation angle similarly and that the FRET mechanism probably was not significantly affected, as the ratio of the tryptophan emission to the AuNC emission remained the same.

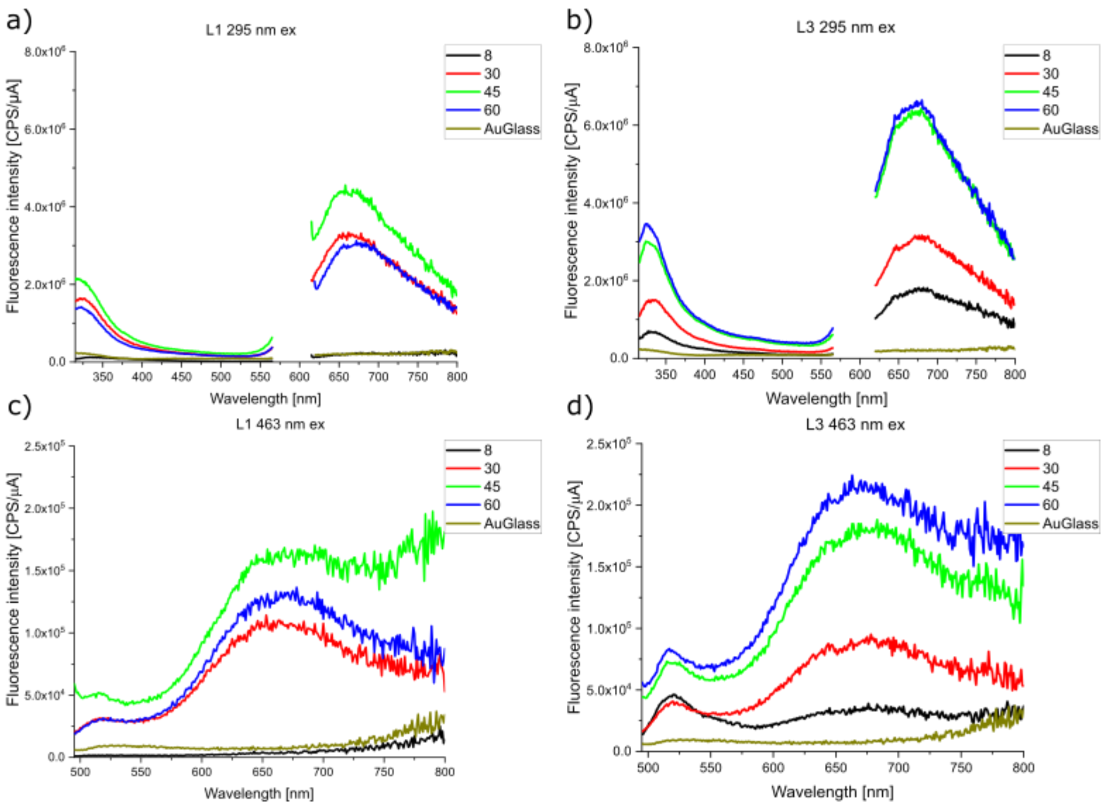

Figure 63: Fluorescence spectra of BSA-AuNC on AuNBs L1 (a, c) and L3 (b, d) excited at 295 nm, 463 nm, and various angles of incidence.

To evaluate the efficiency of AuNB@2, fluorescence intensities of BSA-AuNCs were used for calculating fluorescence EFs (Figure 64) as F/F_0, where F and F_0 are fluorescence intensities collected from AuNBs and the Au-coated glass, respectively. EFs again followed the same trend as fluorescence emission intensities. The highest enhancement on L1 was achieved for the 45 ° excitation where the EF exceeded 22.0 for 295 nm and 25.0 for 463 nm. EFs calculated for BSA-AuNCs on L3 showed that highest fluorescence enhancements were achieved with 45 ° and 60 ° excitations, reaching values from 29.0 to 34.5. The overall highest EF was 34.5, calculated for AuNCs emission collected from L3 when excited at 463 nm and 60 °. Because the UV excitation allows to measure the full BSA-AuNC spectrum, EFs were also calculated by subtracting background contributions (Figure 65) from fluorescence spectra of AuNCs on the reference substrate and AuNBs (EF_B) as $(F - F_B)/(F_0 - F_{0B})$, where F_B and F_{0B} are background intensities collected from AuNBs and the reference, respectively. Background values were selected from the range of wavelengths with the lowest intensity (500 nm – 525 nm) which was then averaged and subtracted from peak emission intensities of AuNCs. EF_{BS}s then increased to 37.4 for the 45 ° excitation on L1 and 54 – 55.5 for 45 and 60 ° excitations on L3, respectively (Figure 63a,b).

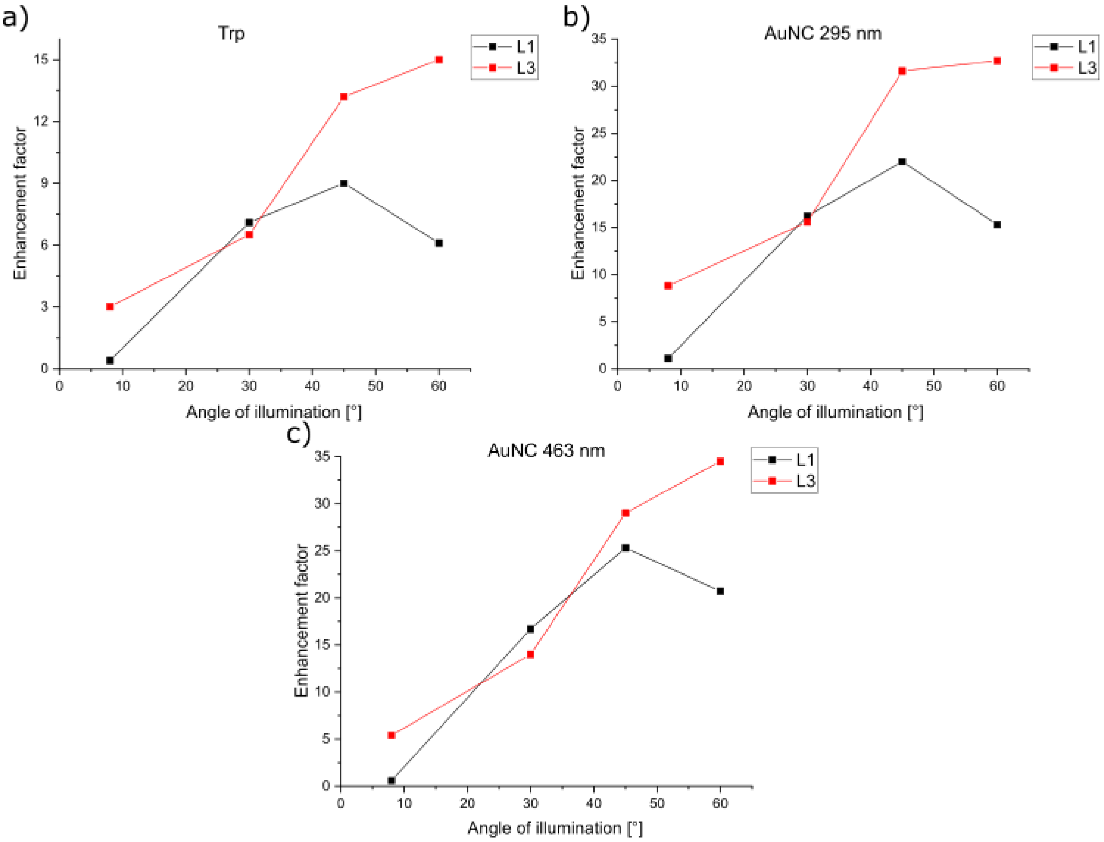

Figure 64: Enhancement factors calculated for the fluorescence emission of BSA-AuNCs on AuNBs L1 and L3.

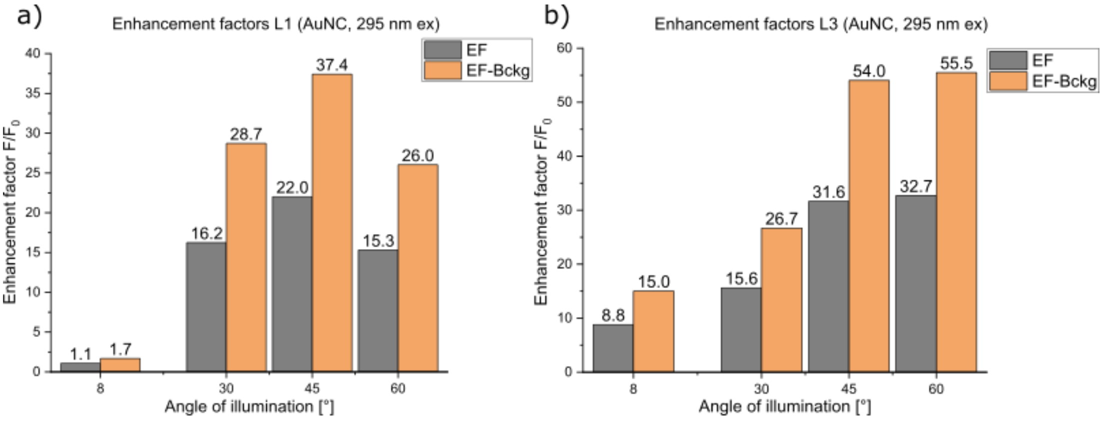

Figure 65: Comparison of enhancement factors calculated for the fluorescence emission of BSA-AuNCs excited at 295 nm on AuNBs L1 and L3 with a subtracted background signal (orange bars).

The observed emission enhancement demonstrates the advantage of patterned AuNB substrates over less corrugated gold surfaces which cannot benefit from the light-trapping and the EM field enhancement on AuNBs. At higher angles of illumination, the incident light can undergo various interactions within nanovoids[124] which enhance the local EM field intensity, light trapping and can lead to the improved excitation and emission of fluorophores.[103,120–122] FDTD simulations of AuNB@2 (Figure 55, Figure 56) showed that the diameter of NBs serves as cut-off for incident wavelengths and that both 295 nm and 463 nm excitation wavelengths can interact with the interior of NBs, exciting void plasmons. This was corroborated by the broad reflectance minimum below 500 nm in reflectance profiles of AuNBs, indicating a strong absorption of light by the NB pattern (Figure 49) at both excitation wavelengths. A slightly stronger electric field enhancement was predicted for the 295 nm excitation throughout the probed range of excitation angles due to larger diameters which may allow better light trapping of the shorter wavelength. Similar values of EFs for 295 nm and 463 nm excited AuNCs (≤45 °) as well as similar electric field intensities for AuNB@2 suggest that there may not be an obvious preference for either of the two wavelengths. The rather uniform emission enhancement observed for AuNCs when excited in the region of low reflectance could be due to combined effects of the geometry of AuNBs[120] and the overlap of absorption spectra of tryptophan and AuNCs with the reflectance minimum of AuNBs,[103,287] giving rise to a broadband excitation rate enhancement at shorter wavelengths. The contribution of the EM field enhancement inside AuNBs to the enhanced emission due to different Au film thickness on L1 and L3 was most likely not significant. As was shown in Figure 60 of electric field maps calculated for AuNB@2 with various thicknesses of the Au layer, the change from a 30 nm to a 50 nm Au film should have little effect on the intensity of void modes. Electric field maps of AuNB@2 also showed that higher excitation angles induce vertically oriented electric field modes confined in AuNBs which can extend to the top surface and therefore, the increased electric field intensity is not restricted only to the confined space of NBs and can increase the emission of BSA-AuNCs at the top surface by increasing the electric field intensity in the region between NBs.

Another mechanism that could govern the enhancement on AuNB@2 relies on a dipole-dipole interaction between an excited-state fluorophore and a plasmonic nanostructure where the excited fluorophore’s near-field emission is converted by excited plasmons into the far-field emission with almost identical spectrum.[20] An important requirement is a spectral overlap between the emission band of the fluorophore and the plasmonic band of the substrate. FDTD calculations predicted a strong coupling of wavelengths around 650 nm to rims. Thus, it can be assumed that the red emission of AuNCs at ~670 nm could couple to rims as well and generate radiating plasmons.[20,118,125] In addition, the effect of structure of the top AuNB surface on the fluorescence enhancement should not be excluded, as the top surface may support fluorescence enhancements due to the excitation of surface plasmons between NBs.[101,111,121,123] The deposition of an increasing amount of gold further nanostructures the top surface of AuNBs by highlighting surface irregularities localized between AuNBs, increasing the number of sites for interactions with the excitation light and for coupling of the AuNC emission to the surface of L3 (Figure 47d,f), which could be also responsible for the increased fluorescence enhancement of the AuNC emission on L3 compared to L1.

The increase of emission intensity with increasing angle of illumination could be indicative of a directionality of the fluorescence emission due to larger diameters and depths of AuNBs. Both substrates exhibited different emission spectra for 8 ° excitations; a low intensity AuNC emission from L1 and a well-defined AuNC spectrum from L3, followed by an equal increase in emission intensity when excited at 30 °. This feature probably occurred due to excitation/detection geometry (Figure 62) where the detection of fluorescence is done under a large angle when excited at 8 °. The size of the surface area between NBs increases with the Au thickness (L3 > L1) and can accommodate larger amount of the analyte that produces detectable fluorescence at near normal illumination.

Furthermore, several fluorescence spectra of 463 nm excited BSA-AuNCs showed additional weak excitation-dependent emission bands ranging from 400 to 550 nm (Figure 63). This emission range as well as the excitation-dependent behaviour corresponds to that of the aluminium oxide discussed in the previous Chapter 5 (Figure 45). Considering the small thickness and optical transparency of the Au coating, a residual oxide could be a possible source of an unwanted emission. The aluminium oxide produces fluorescence emission at around 430 nm when excited at 350 nm with both the band width and the position of the emission maximum similar to the blue emission band observed in several fluorescence spectra of BSA-AuNCs. It should be noted that no residual fluorescence emission bands were observed in background spectra of as-prepared AuNBs (Figure 50), indicating that the oxide's fluorescence was removed and further oxidation of the Al surface should not occur.[248]

To determine the origin of the blue emission band, the same BSA-AuNC solution was further measured with other excitation wavelengths in the range from 295 nm to 380 nm so that the emission profile can be compared with the oxides' fluorescence emission shown in Figure 45. Collected spectra showed only weak emission in the region of interest (Figure 66a, inset A). The emission became more distinct when the concentration of BSA-AuNCs was increased 10x to 3.8 μM, showing a red shift of the emission maximum with an increasing excitation wavelength (Figure 66a, inset B). When compared with a BSA solution of equal concentration, the blue emission was observed as well. Both results indicate that the source of the blue emission band is BSA and not the aluminium oxide or AuNCs.

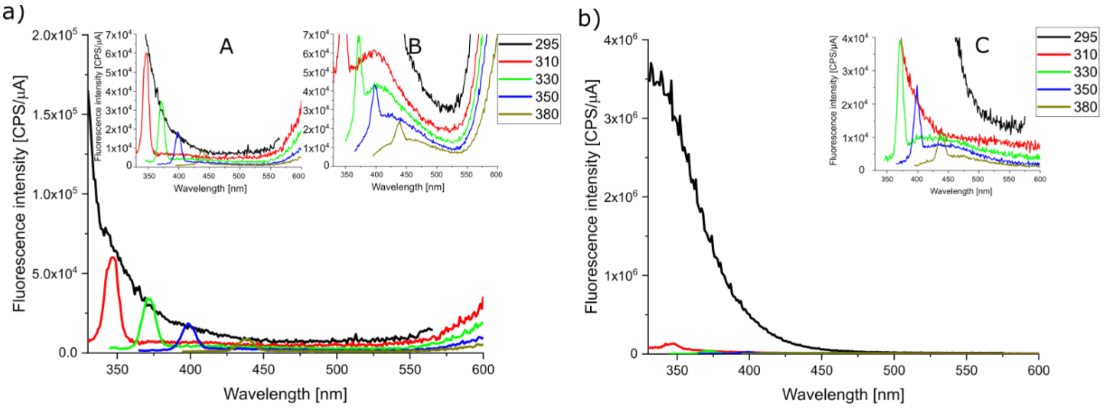

Figure 66: Fluorescence spectra of a) BSA-AuNCs and b) BSA (measured using various excitation wavelengths (295 – 380 nm). Inset A: Detail of low-intensity spectra collected from BSA-AuNCs concentration (~0.38 μM) at excitation wavelengths 310 – 380 nm. Inset B: Detail of spectra collected from ~3.8 μM BSA-AuNC solution. Inset C: Detail of low-intensity spectra collected from ~3.8 μM BSA at excitation wavelengths 310 – 380 nm. Narrow, gradually red-shifting peaks are Raman peaks of water which was used as a solvent.

It has been proposed that the source of the emission could be either oxidized tryptophan or other aromatic residues according to their local environment.[26,289] The same emission has been observed in micelle-encapsulated monomeric BSA as well as after a complete heat denaturation of the protein.[290] This suggests that the source of the blue fluorescence emission is not related to tryptophan, secondary and tertiary structures of the protein or aggregation, and is most likely an intrinsic property of the protein. Fluorescence spectra of monomeric and aggregated forms of lysozyme and other proteins likewise exhibit a blue emission band where it has been associated with the formation of intermolecular hydrogen bonds in the secondary structure which become sources of electron delocalization.[206,214,289–292] A blue emission has also been detected in various amino acids (charged, hydrophobic and aromatic).[292] The most likely source are carbonyl double bonds present in all amino acids as even simple organic compounds with carbonyls (formaldehyde, acetone, acrylamide) exhibit a blue autofluorescence that shifts to that observed in amino acids and proteins upon addition of an amid group near the carbonyl in acrylamide.[292]

6.3.2. Fluorescence Spectroscopy of BSA-AuNC on Small-diameter AuNBs

The effect of small-diameter AuNBs on the fluorescence of BSA-AuNCs is explored by measuring the AuNC emission on AuNB@1 substrates S1 and S3. The fluorescence analysis was carried out with same excitation parameters that were used also for AuNB@2. The results showed a less consistent evolution of fluorescence intensity compared to the BSA-AuNC emission from AuNB@2. The trend of variations in fluorescence emission intensity of tryptophan with respect to that of AuNCs differs from the one observed on AuNB@2, which indicates a different angular and wavelength dependence of the fluroescence emission as well as a possible modification of the FRET mechanism.

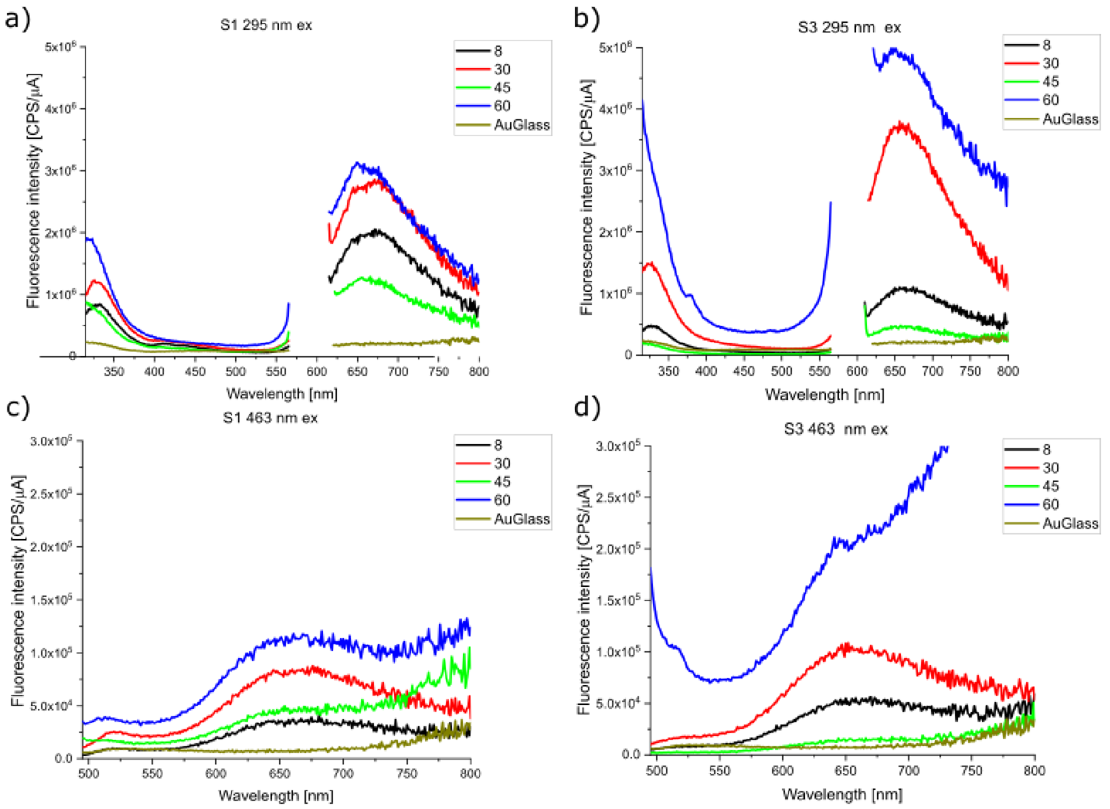

Figure 67: Fluorescence spectra of BSA-AuNC on AuNBs S1 (a, c) and S3 (b, d) excited at 295 nm, 463 nm, and various angles of incidence.

For AuNCs, highest fluorescence intensities were obtained under 30 ° and 60 ° of illumination on both substrates, while excitations at 8° and 45 ° were less effective (Figure 67). Fluorescence spectrum of 463 nm (60 °) excited AuNCs varies from other spectra. The distorted shape as well as the high background signal are probably the result of reflection and scattering of the excitation beam from the S3 substrate.

Measured fluorescence intensities were again used for calculating EFs (Figure 68). Highest fluorescence enhancements were achieved for 30 ° and 60 ° illumination on both substrates where the strong emission was observed. Corresponding EFs on S1 were 14.0 and 15.3 for 295 nm excited AuNCs and 12.6 and 18.1 for 463 nm excited AuNCs. EFs on S3 were 19.0 and 24.4 for 295 nm excited AuNCs and 16.0 and 33.4 for 463 nm excited AuNCs.

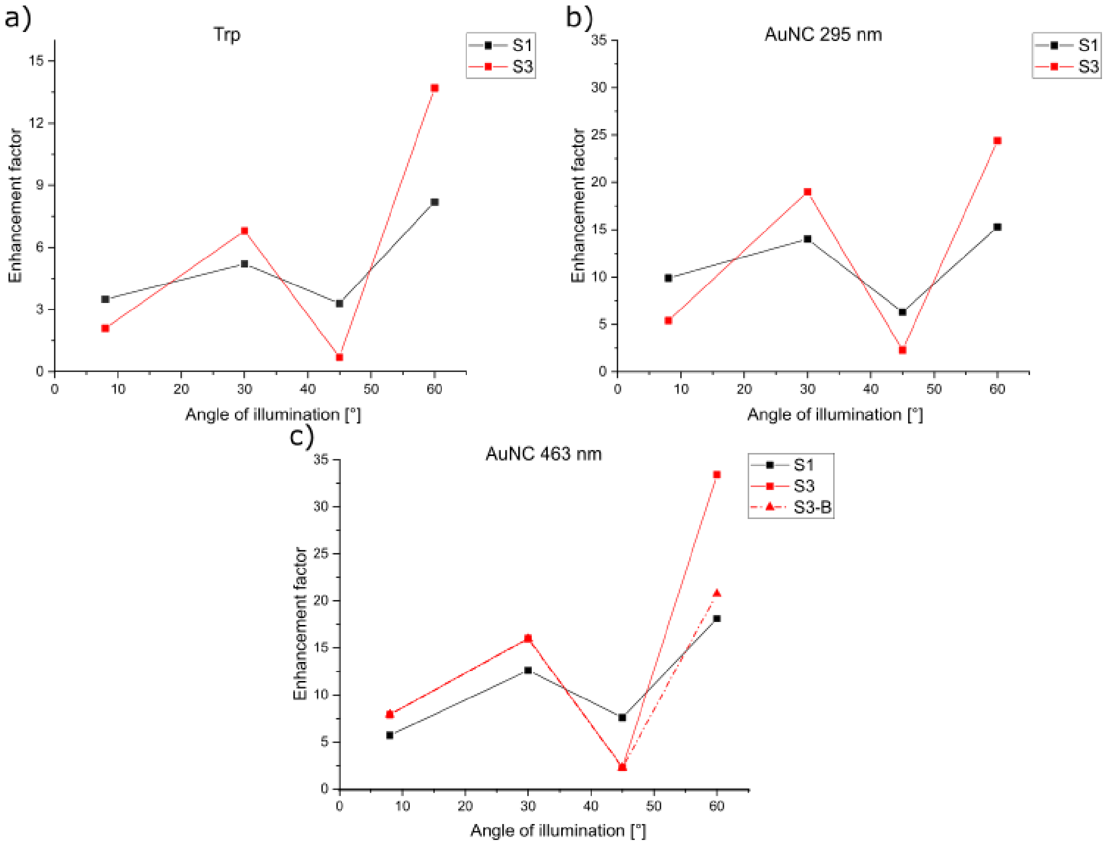

Figure 68: Enhancement factors calculated for the fluorescence emission of BSA-AuNCs on AuNBs S1 and S3. Enhancement factor of the AuNC emission from S3 (463 nm ex) is also displayed with subtracted background (S3-B) due to the high background signal in the corresponding fluorescence spectrum.

If the high background contribution is removed by subtracting the baseline from the 463 nm excited AuNC spectrum (60 °) (Figure 68c, blue curve), the intensity correspondingly decreases to a similar level as that of the AuNC emission excited at 30 °. The reduction in emission intensity is reflected in the EF which then decreases from 33.4 to approximately 20. EF$_{BS}$ calculated for the 295 nm excited AuNC emissions at 30 ° and 60 ° on S1 were 24.3 and 26.1, and 33 and 41 on S3 (Figure 69).

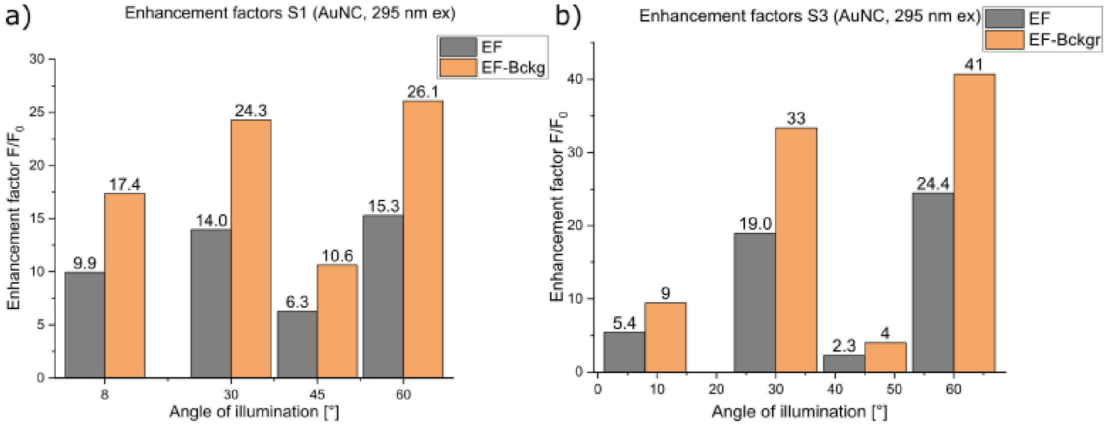

Figure 69: Comparison of enhancement factors calculated for the fluorescence emission of BSA-AuNCs on S1 and S3 with a subtracted background signal (orange bars).

In order to explain the evolution of fluorescence emission of BSA-AuNCs, first, properties of the AuNB@1 pattern should be considered. Contrary to simulations of AuNB@2, FDTD calculations of AuNB@1 suggested weak coupling to light and EM field enhancements on S1 and S3 regardless of excitation conditions, which was attributed to smaller diameters with respect to incident wavelengths (Figure 53, Figure 54). It has been shown that, due to reduced diameters of the AuNB@1, incident wavelengths of 295 nm and 463 nm should not interact with the interior of NBs, and the interaction of AuNBs with the incident light should thus be limited to the upper Au surface. At high angles of incidence, the incident light is expected to treat the patterned Au surface progressively as a flat surface.[255] This was partially visible in reflectance profiles of S3 (Figure 49b) which were approaching that of a continuous Au film at high excitation angles. It is noted that electric field maps of AuNB@1 (Figure 53, Figure 54) did not show excited electric fields that could be easily linked to the observed emission enhancement. On the other hand, reflectance spectra of AuNB@1 (Figure 49) showed a decreased reflectance at all angles, suggesting an absorption of light by the patterned substrate, particularly for S1 with more open and structured NBs. As it was pointed out, simulated model of AuNB@1 pattern is based on an ideal spherical geometry and does not consider the complex structure of small-diameter NBs within the array which do not exhibit the typical bow-like structure as AuNB@2, but a major feature are nanocaps surrounding a central cavity (Figure 47).

With the decreasing size of voids, the packing density of AuNBs increases which leads to the formation of a more nanostructured surface with nanosized areas of Au confined between NBs, thereby increasing the possibility of localization of surface plasmons.[121,123] Several studies have shown that plasmonic arrays of small-diameter AgNBs with a very similar organization as that of AuNB@1 support MEF.[117,118,125,287] A key factor was shown to be the matching between the absorption bands of metallic nanocaps and spectra of the fluorophore. A resonant excitation then allows to generate surface plasmons at nanocaps as well as localized high-intensity hot spots inside concave nanogaps between nanocaps and can lead to an improved absorption of light near nanocaps as well as improved excitation of nearby BSA-AuNCs. A possible mechanism governing the enhancement on small-diameter NBs, composed of nanocaps such as AuNB@1, is the dipole-dipole interaction between excited-state BSA-AuNCs and the nanocap array.[118,125] Here, the nanocaps can act as a plasmonic array of nanoantennae which convert the excited BSA-AuNCs' near-field emission into the far-field emission.[118,125]

An enhancement of the BSA-AuNC fluorescence could also originate from a plasmon resonance energy transfer from the nanocap array to a fluorophore.[117,118,125,287] The process is allowed when the absorption band of the array matches with that of the fluorophore, which likely promotes a dipole-dipole interaction between the resonating plasmon dipole in nanocaps and the fluorophore's dipole.[118] Considering the surface structure and dimensions of AuNB@1, the array can accumulate a large fraction of BSA-AuNCs with the broad absorption spectrum (Figure 32) near nanocaps were where the energy transfer occurs and photophysical properties of the complex can be affected by locally enhanced EM fields. This may account for the enhanced fluorescence emission from AuNB@1, where the surface is primarily made of Au nanocaps, suggesting that the small-diameter AuNB pattern is indeed optically active.

The comparison of EFs in Figure 70 shows that the fluorescence emission on all four substrates exhibited a trend of increasing fluorescence emission intensities of tryptophan and AuNCs when excited at angle of ≤ 30 °, which may not be directly related to optical properties of AuNBs substrates but rather to the geometry of the measurement. The previously mentioned directionality of emission could be the reason why main differences in fluorescence emission between substrates become more obvious at higher detection angles, indicating the influence of the combination of NB dimensions and structure of the top surface. This comparison further showed a clear difference between fluorescence emissions when excited at 45 ° where the fluorescence intensity collected from AuNB@1 was reduced. When excited at 60 °, fluorescence emissions exhibited similar fluorescence enhancements on substrates, except for L3 where the emission intensity increased further.

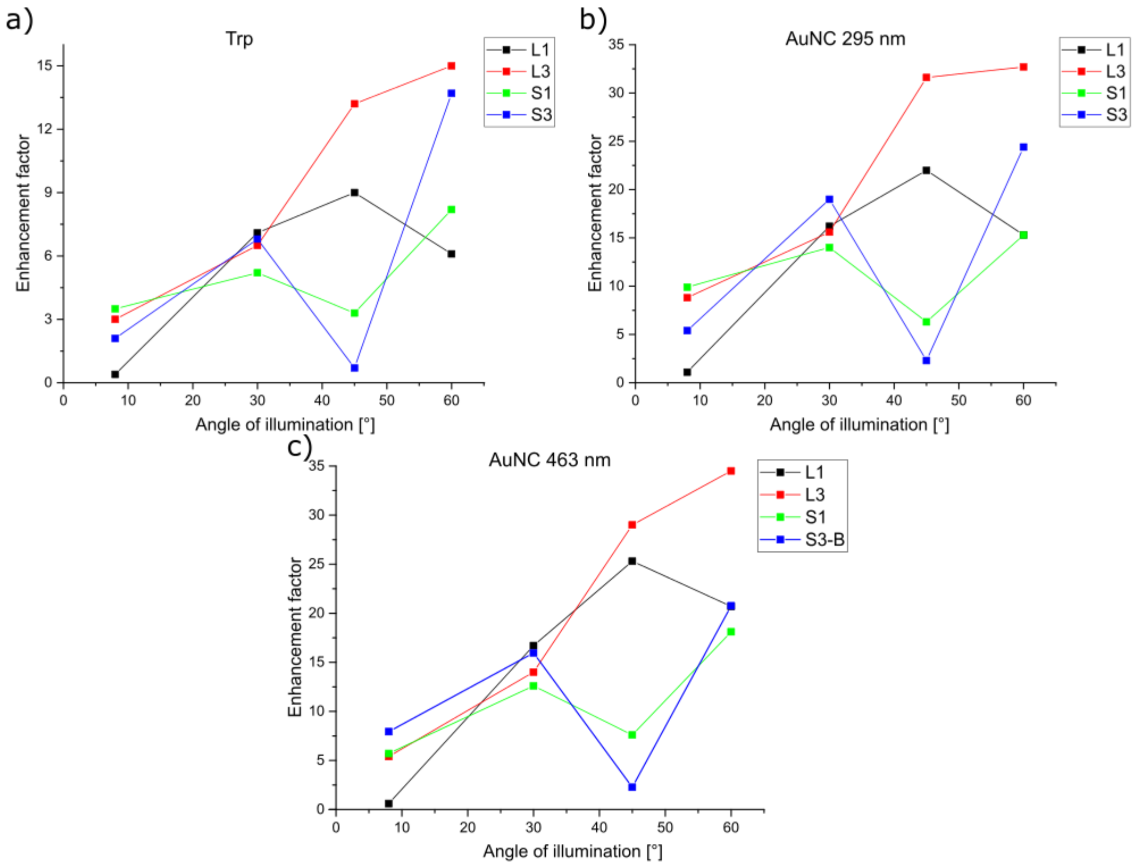

Figure 70: Comparison of enhancement factors calculated for the fluorescence emission of BSA-AuNCs on tested AuNB substrates. Enhancement factor of the AuNC emission from S3 (463 nm ex) is displayed with subtracted background (S3-B) due to the high background signal in the corresponding fluorescence spectrum.

Figure 70 further shows that large-diameter AuNBs provide a broadband fluorescence enhancement at various excitation angles, related to the particular nanobowl geometry, whereas small-diameter NBs, despite providing fluorescence enhancement, exhibit limitations in these aspects. It can be assumed that the different angular dependence of fluorescence emissions on AuNB@1 from that on AuNB@2 stems from the different organisation of AuNB@1 surfaces, given by nanocaps and additional nanofeatures of the array, which cannot benefit from the controllable geometry effect of the bowl-like architecture, giving rise to the different angular dependence of optical properties as well as interactions with the immobilized fluorophore. The nanocap architecture was not explored due to simplified simulations which investigated the geometry effect of the bowl-like architecture. Nevertheless, further study of optical properties of small-diameter AuNB arrays would be beneficial to better understand the effect of nanocaps. Particularly for S1 which, compared to other explored NB patterns, exhibits a distinct architecture. Such NBs with a more open structure and smaller separated nanocaps have not been characterized in combination with fluorescence in any of the known studies.

6.4. Conclusions

For the first time, it has been demonstrated through the steady-state fluorescence spectroscopy of fluorescent protein complex BSA-AuNCs that AuNBs produced by anodizing of Al and Au deposition can be utilized as fluorescence-enhancing substrates in the UV and visible spectrum. Two groups of small- and large-diameter AuNBs with different surface patterning have been tested and obtained results were correlated with results of reflectance measurements and FDTD calculations performed for the substrates.

A study of the angular and wavelength dependence of fluorescence emission of BSA-AuNCs immobilized on AuNBs revealed a structure-dependent evolution of fluorescence intensity of BSA-AuNCs. The highest fluorescence enhancement was achieved on large-diameter AuNB substrates where the emission intensity increased by a factor of 34.5. Similar enhancement factors were calculated for 295 nm and 463 nm excited AuNC emissions on large-diameter AuNBs, suggesting a consistent broadband enhancing effect. This was attributed to the broadband excitation rate enhancement supported by combined effects of the nanobowl geometry and matching of excitation wavelengths with overlapping absorption bands of BSA-AuNCs and the spectral region of low reflectance of AuNBs. Additionally, it is believed that the emission enhancement was also mediated by the angle-dependent orientation of electromagnetic fields in AuNBs and by the structure-dependent coupling of the BSA-AuNC emission to the surface of AuNB arrays.

Fluorescence emission of AuNCs on small-diameters AuNBs also exhibited an enhancement but with less consistent angular dependence of the fluorescence emission compared to large-diameter AuNBs. This difference was attributed to a different angular dependence of optical properties of small-diameter AuNB arrays determined by their specific structure composed primarily of hexagonally arranged nanocaps as opposed to the well-defined bowl-like architecture of large-diameter AuNBs. The fluorescence enhancement of BSA-AuNC emissions most likely originated from locally enhanced electromagnetic fields at nanocaps and interstitial nanogaps as well as dipole-dipole interactions of BSA-AuNCs with nanocap arrays.

This study highlights the possibility and benefits of utilizing AuNBs produced by anodizing of aluminium in fluorescence applications as fluorescence enhancing substrates. Based on the planar architecture of the AuNB pattern, it is believed that the substrate could find its use in fluorescence microscopy or flow systems where the evaporation of liquids can be prevented by sealing analyte solutions with cover slips or enclosing the whole substrate in flow cells. When moving forward with further use of AuNBs, such applications would be beneficial for testing of the long-term stability of the Au surface when exposed to liquids. This could also provide valuable information on the possibility of chemical functionalization of AuNBs and for selecting appropriate techniques.

7. Final Conclusions and Future Work

7.1. Conclusions

The work carried out in this thesis has added to the knowledge of fabrication, characterization, and application of various plasmonic nanostructures and metallic substrates that exhibit surface as well as optical characteristics suitable for plasmon-mediated phenomena such as MEF or plasmonic photocatalysis.

In Chapter 3, the effect of growth conditions on the process of anisotropic coating of GNRs with silica was elucidated. By conducting a systematic study of reaction conditions during the silica coating process, a protocol that produced a high-yield synthesis of end-modified dumbbell-like GNRs with silica spheres attached to their ends was developed. End-modified GNRs are of interest as these could be exploited for the enhancement of properties of plasmon-sensitive molecules and materials located near the ends where the strong longitudinal plasmon field of GNRs is generated. The study showed that the formation of various silica shell morphologies is determined by a complex interplay between all the reaction parameters and dimensions as well as the concentration of GNRs. By controlling these parameters various silica shell morphologies can be produced. The key factor is the inhomogeneous distribution of the surfactant CTAB on the GNR surface which allows the hydrolysis of silica precursor to take place within the surfactant layer and initiate the end-selective growth of silica. The temperature study revealed that the reaction temperature is crucial for controlling the solubility of CTAB which, in combination with tuning of CTAB concentration, allows transitions between various types of silica shell morphologies. The examination of the stability of the dumbbell-like morphology indicated that the stability increases with increasing temperature and CTAB concentration which reduced the risk of silica spheres being separated from the gold core. The stability can be further improved through an appropriate aspect ratio of GNRs which adjusts the inter-particles distance between silica spheres and density of CTAB at the ends. A structural characterization of some dGNRs revealed silica layers of various thicknesses overlapping sides of GNRs, which suggest that the growth of silica spheres originates at the ends, where the surface conditions are more favourable and overgrow when a critical size is reached.

Chapter 4 investigated the application of a commercial Al foil as a substrate for MEF of proteins (BSA) and gold nanoclusters (BSA-AuNCs) in the UV and visible spectral region, as the selection of simple and low-cost UV active metallic platforms suitable for fluorescence techniques compared to Vis-NIR spectral region is limited. Fluorescence spectroscopy of BSA and BSA-AuNCs allowed to probe fluorescent properties of both protein complexes in their dried state upon immobilization as well as investigate the effect of the metallic substrate. Steady-state and time-resolved analyses showed that by immobilizing both complexes on the matt side of the foil, a moderate fluorescence enhancement was achieved. By correlating increased fluorescence intensity of tryptophan in BSA with the reduced fluorescence lifetime, the intensity enhancement of the BSA emission was attributed to the increased excitation rate of tryptophan in combination with an increased radiative rate near the matt Al surface. Consequently, fluorescence enhancement of BSA-AuNCs was associated with the enhanced FRET between tryptophan and AuNCs as well as improved excitation of tryptophan and AuNCs. This was most likely due to the nanoscale corrugation of the matt surface which supported the excitation of locally enhanced electromagnetic fields upon illumination. On the other hand, fluorescence emission detected from the shiny side of Al foil decreased. The reduced emission intensity was associated with quenching of tryptophan fluorescence through SET, which also reduced the efficiency of FRET to AuNCs. The fluorescence lifetime analysis and reduced emission intensity of AuNCs were also indicative of a possible quenching through SET on the sAl foil.

To prepare a plasmonic substrate that exhibits a multispectral compatibility for MEF, particularly in the UV-Vis, Chapter 5 presents a simple fabrication and characterization plasmonic platform composed of an array of sub-micrometre three-dimensional Au nanobowls (AuNBs). Motivated by the concept of MEF and underlying requirement on such platforms, arrays with various diameters (~100 nm, ~500 nm) of NBs were produced by combining anodizing of aluminium and a subsequent deposition of thin Au films of various thicknesses. The small-diameter pattern composed of Au nanocaps exhibited optical properties similar to those of a continuous Au film, albeit with a decreased reflectance attributed to the surface morphology and absorption due to plasmon resonance of nanocaps. Large-diameter NBs exhibited a promising broadband optical activity in the UV-Vis. By performing finite-difference time-domain calculations, the spatial distribution of the electromagnetic fields over the surface of the pattern was determined and size-, angle-, wavelength-, and structure-dependent optical properties of the substrates were determined. The AuNB platform exhibits characteristics compatible with requirements for MEF in the UV-Vis region of spectrum.

The AuNB pattern presented in Chapter 5 was evaluated for MEF in the UV and visible regions of spectrum in Chapter 6 using immobilized fluorescent BSA-AuNCs as a probe. Through steady-state fluorescence spectroscopy, fluorescence emission of BSA-AuNCs on small- and large-diameter AuNBs was probed by manipulating the excitation/detection geometry at excitation wavelengths in both UV and visible regions. A structure-specific angular dependence of the fluorescence enhancement of BSA-AuNCs was observed. Fluorescence emission on large-diameter AuNB exhibited a consistent enhancement for both the UV and the visible excitation wavelengths which demonstrates the broadband effect of the nanobowl architecture attributed to the combination of broadband excitation rate enhancement due to the geometry of nanobowls and a structure-dependent coupling of BSA-AuNCs with the AuNB surface. The highest fluorescence enhancement factor of 34.5-fold was achieved for BSA-AuNCs on large-diameter AuNBs in comparison with a thin Au film coated on a glass slide. Fluorescence emission of BSA-AuNCs on small-diameter AuNBs exhibited a less consistent angular dependence which was attributed to the specific structure of small-diameter AuNBs and resulting different angular dependence of their optical properties. This investigation has shown that the bowl-like architecture of large-diameter AuNBs can be utilized for MEF in fluorescence spectroscopy in UV and visible regions of spectrum.

7.2. Future Work

There are several possible extensions to the work related to AuNBs. The potential of AuNBs as a suitable substrate for MEF has been recognized. It has been shown that the dimensions of nanobowls determine their optical properties. Exploring optical properties of AuNBs with different diameters could be beneficial for further implementing these substrates in fluorescence-based techniques. Moreover, this would allow the comparison with AuNBs produced by colloidal lithography which is currently the dominant method for producing NBs used in MEF.[123] Practically, diameters of AuNBs can be increased further via anodizing of Al in citric acid up to ~884 nm with a high degree of pore ordering.[255,265] This process combines approaches of mild and hard anodizing which include slow pore nucleation followed by a nonequilibrium self-organization of pores. The required anodizing voltage is in the range of 350 – 400 V which would normally cause the oxide breakdown. The unwanted oxide breakdown is prevented by implementing more powerful cooling systems for the citric acid solution. The resulting oxide can be selectively etched using the same method that was applied on AlNBs. Therefore, the citric acid anodizing could present an appropriate alternative for producing larger NBs compared to colloidal lithography.

Following on fluorescence measurements of BSA-AuNCs on small- and large-diameter AuNB substrates, a study was carried in order to further boost the fluorescence emission intensity of the fluorophore (Appendix B). It has been shown that the presence of NPs on a plasmonic substrate can modify optical properties of the substrate by coupling with its SPR.[109,115,128] Furthermore, the effect can be improved by an inter-particle coupling,[11,187] producing large field enhancement within inter-particle junctions.[109,115,128] Inspired by this approach, small GNRs[63,293] (~26 nm) were added to immobilized BSA-AuNCs on AuNBs and the effect of the LSPR of GNRs in combination with AuNBs was investigated. The length of GNRs was highly convenient as the small size allows GNRs to be incorporated inside AuNBs. Experimental details and corresponding results have been summarized in Appendix B. Fluorescence emission spectra of tryptophan and AuNCs showed inconsistent changes of the emission in the presence of GNRs. While in some cases, the fluorescence emission of tryptophan showed a moderate increase in the presence of GNRs, the emission intensity of AuNCs exhibited mostly decrease or negligible changes compared to BSA-AuNCs alone. This could have been caused by the protein-directed distribution of GNRs due to the prior immobilization of BSA-AuNCs, causing an inhomogeneous coverage on the substrate. It is possible that some decrease in the fluorescence emission was a result of quenching by GNRs due to the overlap of the LSPR with the emission spectrum of AuNCs. However, an interesting feature was observed when 3D excitation-emission matrices (EEMs) (Figure 76, Figure 79) were recorded, showing an enhancement of the blue protein emission in the presence of GNRs, which was probably caused by the modified electric field of AuNBs in the presence of GNRs. Although the results did not show the desired emission enhancement, the combination of NPs with AuNBs is relevant, as mentioned earlier. In order to improve the control over experimental conditions, a controlled deposition of NPs prior to application of probe molecules could be carried out. In addition, it should be noted that a repeated application of liquid samples and their subsequent drying may present a limitation for the mechanical stability of the Au surface, as shown in Appendix C.

Application of AuNBs may not be restricted to spectroscopic techniques but the specific geometry of the pattern could potentially find its use in biointerfaces. Recently, Huang et al. introduced an intriguing novel design of Petri dishes with a honeycomb NB pattern produced by utilizing a template of colloidal spheres to create a three-dimensional biological environment for cell cultures.[294] The surface of the NB pattern was functionalized with a PEG derivative to increase biocompatibility of the surface and a chitosan derivative to achieve a selective anti-bacterial activity, while maintaining biocompatibility with mammalian cells. In the case that the surface of AuNBs proves to be stable in a liquid environment in the long-term, such property could open new possibilities also for fluorescence investigations of cells and live samples in general, as the physical adaptability of cells to the surrounding environment should allow them to hug the convex surface on NB and nanocaps, respectively.[125] Here, the biocompatibility of gold surfaces as well as the affinity of gold to variety of linkers and functional groups could be exploited for designing a platform capable of enhancing the cellular fluorescence in a sealed environment, which could be beneficial for fluorescence imaging and sensor applications.

References

1. Link, S. & El-Sayed, M. A. Shape and size dependence of radiative, non-radiative and photothermal properties of gold nanocrystals. *Int. Rev. Phys. Chem.* **19**, 409–453 (2000).
2. Petryayeva, E. & Krull, U. J. Localized surface plasmon resonance: Nanostructures, bioassays and biosensing-A review. *Anal. Chim. Acta* **706**, 8–24 (2011).
3. Ranjan, R., Esimbekova, E. N., Kirillova, M. A. & Kratasyuk, V. A. Metal-enhanced luminescence: Current trend and future perspectives- A review. *Anal. Chim. Acta* **971**, 1–13 (2017).
4. Badshah, M. A. *et al.* Recent developments in plasmonic nanostructures for metal enhanced fluorescence-based biosensing. *Nanomaterials* **10**, 1–22 (2020).
5. Chen, H., Shao, L., Li, Q. & Wang, J. Gold nanorods and their plasmonic properties. *Chem. Soc. Rev.* **42**, 2679–2724 (2013).
6. Dykman, L. & Khlebtsov, N. Gold nanoparticles in biomedical applications: recent advances and perspectives. *Chem. Soc. Rev.* **41**, 2256–2282 (2012).
7. Biju, V. Chemical modifications and bioconjugate reactions of nanomaterials for sensing, imaging, drug delivery and therapy. *Chem. Soc. Rev.* **43**, 744–764 (2014).
8. Zhang, L. *et al.* Efficient and facile synthesis of gold nanorods with finely tunable plasmonic peaks from visible to near-IR range. *Chem. Mater.* **26**, 1794–1798 (2014).
9. Cao, J., Sun, T. & Grattan, K. T. V. Gold nanorod-based localized surface plasmon resonance biosensors: A review. *Sensors Actuators B Chem.* **195**, 332–351 (2014).
10. Mayer, K. M. & Hafner, J. H. Localized surface plasmon resonance sensors. *Chem. Rev.* **111**, 3828–3857 (2011).
11. Bauch, M., Toma, K., Toma, M., Zhang, Q. & Dostalek, J. Plasmon-Enhanced Fluorescence Biosensors: a Review. *Plasmonics* **9**, 781–799 (2014).

12. Doria, G. *et al.* Noble Metal Nanoparticles for Biosensing Applications. *Sensors* **12**, 1657–1687 (2012).

13. Mie, G. Beiträge zur Optik trüber Medien, speziell kolloidaler Metallösungen. *Ann. Phys.* **330**, 377–445 (1908).

14. Zeng, S. *et al.* A Review on Functionalized Gold Nanoparticles for Biosensing Applications. *Plasmonics* **6**, 491–506 (2011).

15. Sarid, D. & Challener, W. *Modern Introduction to Surface Plasmons. Theory, Mathematica Modeling and Applications* (Cambridge University Press, 2010).

16. Ghosh, S. K. & Pal, T. Interparticle coupling effect on the surface plasmon resonance of gold nanoparticles: From theory to applications. *Chem. Rev.* **107**, 4797–4862 (2007).

17. Bohren, C. F. & Huffman, D. R. *Absorption and Scattering of Light by Small Particles*. (Wiley-VCH, 1998).

18. Kreibig, U. & Vollmer, M. *Optical Properties of Metal Clusters*. **25**, (Springer Berlin Heidelberg, 1995).

19. Miller, M. M. & Lazarides, A. A. Sensitivity of metal nanoparticle surface plasmon resonance to the dielectric environment. *J. Phys. Chem. B* **109**, 21556–21565 (2005).

20. Lakowicz, J. R. *et al.* Plasmon-controlled fluorescence: a new paradigm in fluorescence spectroscopy. *Analyst* **133**, 1308 (2008).

21. Abadeer, N. S. & Murphy, C. J. Recent Progress in Cancer Thermal Therapy Using Gold Nanoparticles. *J. Phys. Chem. C* **120**, 4691–4716 (2016).

22. Link, S. & El-Sayed, M. A. Spectral Properties and Relaxation Dynamics of Surface Plasmon Electronic Oscillations in Gold and Silver Nanodots and Nanorods. *J. Phys. Chem. B* **103**, 8410–8426 (1999).

23. Homola, J. Surface plasmon resonance sensors for detection of chemical and biological species. *Chem. Rev.* **108**, 462–493 (2008).

24. Gans, R. Über die Form ultramikroskopischer Goldteilchen. *Ann. Phys.* **342**, 881–900 (1912).

25. Birch, D. J. S., Chen, Y. & Rolinski, O. J. Fluorescence. in *Photonics: Biomedical Photonics, Spectroscopy, and Microscopy, IV* (ed. Andrews, D. L.) **IV**, 1–58 (Wiley, 2015).

26. Lakowicz, J. R. *Principles of Fluorescence Spectroscopy*. (Springer US, 2006).

27. Schaller, C. P. Fluorescence and Phosphorescence, Chemistry - LibreTexts. (2020). Available at: https://chem.libretexts.org/Bookshelves/Physical_and_Theoretical_Chemistry_Textbook_Maps/Map%3A_Physical_Chemistry_for_the_Biosciences_(Chang)/14%3A_Spectroscopy/14.7%3A_Fluorescence_and_Phosphorescence.

28. Usai, C. & Diaspro, A. *Encyclopedia of Biophysics*. (Springer Berlin Heidelberg, 2013).

29. Berlman, I. B. *Handbook of Fluorescence Spectra of Aromatic Molecules*. *Handbook of Fluorescence Spectra of Aromatic Molecules* (Elsevier, 1971).

30. Becker, W. & Bergmann, A. Lifetime imaging techniques for optical microscopy. *Becker & Hickl GmbH,. Berlin* 1–41 (2002).

31. Trautmann, S., Buschmann, V., Orthaus, S., Koberling, F. & Ortmann, U. *Fluorescence Lifetime Imaging (FLIM) in Confocal Microscopy Applications: An Overview*. (2014).

32. Lakowicz, J. R. & Weber, G. Quenching of fluorescence by oxygen. Probe for structural fluctuations in macromolecules. *Biochemistry* **12**, 4161–4170 (1973).

33. Hussain, S. A. *et al.* Fluorescence Resonance Energy Transfer (FRET) sensor. arXiv preprint arXiv:1408.6559. (2014).

34. Ghenuche, P., De Torres, J., Moparthi, S. B., Grigoriev, V. & Wenger, J. Nanophotonic enhancement of the förster resonance energy-transfer rate with single nanoapertures. *Nano Lett.* **14**, 4707–4714 (2014).

35. Szmacinski, H., Ray, K. & Lakowicz, J. R. Effect of plasmonic nanostructures and nanofilms on fluorescence resonance energy transfer. *J. Biophotonics* **2**, 243–252 (2009).

36. Zhang, Y., Wei, G., Yu, J., Birch, D. J. S. & Chen, Y. Surface plasmon enhanced

energy transfer between gold nanorods and fluorophores: application to endocytosis study and RNA detection. *Faraday Discuss.* **178**, 383–394 (2015).

37. Racknor, C., Singh, M. R., Zhang, Y., Birch, D. J. S. & Chen, Y. Energy transfer between a biological labelling dye and gold nanorods. *Methods Appl. Fluoresc.* **2**, 015002 (2013).

38. Wei, G. *et al.* Hairpin DNA-functionalized gold nanorods for mRNA detection in homogenous solution. *J. Biomed. Opt.* **21**, 097001 (2016).

39. Yun, C. S. *et al.* Nanometal Surface Energy Transfer in Optical Rulers, Breaking the FRET Barrier. *J. Am. Chem. Soc.* **127**, 3115–3119 (2005).

40. Ray, P. C., Fortner, A. & Darbha, G. K. Gold Nanoparticle Based FRET Asssay for the Detection of DNA Cleavage. *J. Phys. Chem. B* **110**, 20745–20748 (2006).

41. Griffin, J. *et al.* Size- and Distance-Dependent Nanoparticle Surface-Energy Transfer (NSET) Method for Selective Sensing of Hepatitis C Virus RNA. *Chem. - A Eur. J.* **15**, 342–351 (2009).

42. Aslan, K., Lakowicz, J. R. & Geddes, C. D. Plasmon light scattering in biology and medicine: new sensing approaches, visions and perspectives. *Curr. Opin. Chem. Biol.* **9**, 538–544 (2005).

43. Fu, Y., Zhang, J. & Lakowicz, J. R. Plasmon-Enhanced Fluorescence from Single Fluorophores End-Linked to Gold Nanorods. *J. Am. Chem. Soc.* **132**, 5540–5541 (2010).

44. Fu, Y., Zhang, J. & Lakowicz, J. R. Large enhancement of single molecule fluorescence by coupling to hollow silver nanoshells. *Chem. Commun.* **48**, 9726 (2012).

45. Sarid, D. Long-Range Surface-Plasma Waves on Very Thin Metal Films. *Phys. Rev. Lett.* **47**, 1927–1930 (1981).

46. Chen, Y., Munechika, K. & Ginger, D. S. Dependence of fluorescence intensity on the spectral overlap between fluorophores and plasmon resonant single silver nanoparticles. *Nano Lett.* **7**, 690–696 (2007).

47. Anger, P., Bharadwaj, P. & Novotny, L. Enhancement and quenching of single-

molecule fluorescence. *Phys. Rev. Lett.* **96**, 3–6 (2006).

48. Bharadwaj, P. & Novotny, L. Spectral dependence of single molecule fluorescence enhancement. *Opt. Express* **15**, 14266 (2007).

49. Zhang, W. *et al.* Giant and uniform fluorescence enhancement over large areas using plasmonic nanodots in 3D resonant cavity nanoantenna by nanoimprinting. *Nanotechnology* **23**, 225301 (2012).

50. Abadeer, N. S., Brennan, M. R., Wilson, W. L. & Murphy, C. J. Distance and Plasmon Wavelength Dependent Fluorescence of Molecules Bound to Silica-Coated Gold Nanorods. *ACS Nano* **8**, 8392–8406 (2014).

51. Khatua, S. *et al.* Resonant plasmonic enhancement of single-molecule fluorescence by individual gold nanorods. *ACS Nano* **8**, 4440–4449 (2014).

52. Kinkhabwala, A. *et al.* Large single-molecule fluorescence enhancements produced by a bowtie nanoantenna. *Nat. Photonics* **3**, 654–657 (2009).

53. Reineck, P. *et al.* Distance and wavelength dependent quenching of molecular fluorescence by Au@SiO2core-shell nanoparticles. *ACS Nano* **7**, 6636–6648 (2013).

54. Bardhan, R., Grady, N. K. & Halas, N. J. Nanoscale Control of Near-Infrared Fluorescence Enhancement Using Au Nanoshells. *Small* **4**, 1716–1722 (2008).

55. Cui, Q., He, F., Li, L. & Möhwald, H. Controllable metal-enhanced fluorescence in organized films and colloidal system. *Adv. Colloid Interface Sci.* **207**, 164–177 (2014).

56. Myroshnychenko, V. *et al.* Modelling the optical response of gold nanoparticles. *Chem. Soc. Rev.* **37**, 1792 (2008).

57. Near, R. D., Hayden, S. C., Hunter, R. E., Thackston, D. & El-Sayed, M. A. Rapid and efficient prediction of optical extinction coefficients for gold nanospheres and gold nanorods. *J. Phys. Chem. C* **117**, 23950–23955 (2013).

58. Ming, T. *et al.* Strong Polarization Dependence of Plasmon-Enhanced Fluorescence on Single Gold Nanorods. *Nano Lett.* **9**, 3896–3903 (2009).

59. Khan, N. U., Lin, J., Younas, M. R., Liu, X. & Shen, L. Synthesis of gold

nanorods and their performance in the field of cancer cell imaging and photothermal therapy. *Cancer Nanotechnol.* **12**, 1–33 (2021).

60. Nejati, K., Dadashpour, M., Gharibi, T., Mellatyar, H. & Akbarzadeh, A. Biomedical Applications of Functionalized Gold Nanoparticles: A Review. *J. Clust. Sci.* **33**, 1–16 (2022).

61. Davidson, M. *et al.* Hybrid Mesoporous Silica/Noble-Metal Nanoparticle Materials—Synthesis and Catalytic Applications. *ACS Appl. Nano Mater.* **1**, 4386–4400 (2018).

62. Tham, H. P. *et al.* Photosensitizer anchored gold nanorods for targeted combinational photothermal and photodynamic therapy. *Chem. Commun.* **52**, 8854–8857 (2016).

63. Mbalaha, Z. S., Edwards, P. R., Birch, D. J. S. & Chen, Y. Synthesis of Small Gold Nanorods and Their Subsequent Functionalization with Hairpin Single Stranded DNA. *ACS Omega* **4**, 13740–13746 (2019).

64. Alkilany, A. M., Thompson, L. B., Boulos, S. P., Sisco, P. N. & Murphy, C. J. Gold nanorods: Their potential for photothermal therapeutics and drug delivery, tempered by the complexity of their biological interactions. *Adv. Drug Deliv. Rev.* **64**, 190–199 (2012).

65. Zhang, Y., Qian, J., Wang, D., Wang, Y. & He, S. Multifunctional Gold Nanorods with Ultrahigh Stability and Tunability for In Vivo Fluorescence Imaging, SERS Detection, and Photodynamic Therapy. *Angew. Chemie Int. Ed.* **52**, 1148–1151 (2013).

66. Ortiz, N., Hong, S. J., Fonseca, F., Liu, Y. & Wang, G. Anisotropic Overgrowth of Palladium on Gold Nanorods in the Presence of Salicylic Acid Family Additives. *J. Phys. Chem. C* **121**, 1876–1883 (2017).

67. Wang, F., Cheng, S., Bao, Z. & Wang, J. Anisotropic overgrowth of metal heterostructures induced by a site-selective silica coating. *Angew. Chemie - Int. Ed.* **52**, 10344–10348 (2013).

68. Grzelczak, M., Pérez-Juste, J., García de Abajo, F. J. & Liz-Marzán, L. M. Optical Properties of Platinum-Coated Gold Nanorods. *J. Phys. Chem. C* **111**,

6183–6188 (2007).

69. Wu, B. *et al.* Anisotropic Growth of TiO2 onto Gold Nanorods for Plasmon-Enhanced Hydrogen Production from Water Reduction. *J. Am. Chem. Soc.* **138**, 1114–7 (2016).

70. Wang, H. *et al.* Efficient Plasmonic Au/CdSe Nanodumbbell for Photoelectrochemical Hydrogen Generation beyond Visible Region. *Adv. Energy Mater.* **9**, 1803889 (2019).

71. Adelt, M., MacLaren, D. A., Birch, D. J. S. & Chen, Y. Morphological Changes of Silica Shells Deposited on Gold Nanorods: Implications for Nanoscale Photocatalysts. *ACS Appl. Nano Mater.* **4**, 7730–7738 (2021).

72. Szychowski, B., Leng, H., Pelton, M. & Daniel, M. C. Controlled etching and tapering of Au nanorods using cysteamine. *Nanoscale* **10**, 16830–16838 (2018).

73. Dreaden, E. C., Alkilany, A. M., Huang, X., Murphy, C. J. & El-Sayed, M. A. The golden age: gold nanoparticles for biomedicine. *Chem. Soc. Rev.* **41**, 2740–2779 (2012).

74. Li, W. & Chen, X. Gold nanoparticles for photoacoustic imaging. *Nanomedicine* **10**, 299–320 (2015).

75. Smith, A. M., Mancini, M. C. & Nie, S. Bioimaging: Second window for in vivo imaging. *Nat. Nanotechnol.* **4**, 710–711 (2009).

76. Zhang, Y., Yu, J., Birch, D. J. S. & Chen, Y. Gold nanorods for fluorescence lifetime imaging in biology. *J. Biomed. Opt.* **15**, 020504 (2010).

77. Kuo, T. R. *et al.* Multiple release kinetics of targeted drug from gold nanorod embedded polyelectrolyte conjugates induced by near-infrared laser irradiation. *J. Am. Chem. Soc.* **132**, 14163–14171 (2010).

78. Ke, X. *et al.* Co-enhancement of fluorescence and singlet oxygen generation by silica-coated gold nanorods core-shell nanoparticle. *Nanoscale Res. Lett.* **9**, 666 (2014).

79. Gérard, D. & Gray, S. K. Aluminium plasmonics. *J. Phys. D. Appl. Phys.* **48**, 184001 (2015).

80. Kittler, S., Greulich, C., Diendorf, J., Köller, M. & Epple, M. Toxicity of silver nanoparticles increases during storage because of slow dissolution under release of silver ions. *Chem. Mater.* **22**, 4548–4554 (2010).

81. Li, W., Ren, K. & Zhou, J. Aluminum-based localized surface plasmon resonance for biosensing. *TrAC - Trends Anal. Chem.* **80**, 486–494 (2016).

82. Zhang, J., Fu, Y., Chowdhury, M. H. & Lakowicz, J. R. Metal-Enhanced Single-Molecule Fluorescence on Silver Particle Monomer and Dimer: Coupling Effect between Metal Particles. *Nano Lett.* **7**, 2101–2107 (2007).

83. Shao, L. *et al.* Angle- and Energy-Resolved Plasmon Couplings in Gold Nanorod Dimers. *ACS Nano* **3053**, 3062 (2010).

84. Pramod, P. & Thomas, K. G. Plasmon Coupling in Dimers of Au Nanorods. *Adv. Mater.* **20**, 4300–4305 (2008).

85. Jain, P. K. & El-Sayed, M. A. Plasmonic coupling in noble metal nanostructures. *Chem. Phys. Lett.* **487**, 153–164 (2010).

86. Zhang, T., Gao, N., Li, S., Lang, M. J. & Xu, Q. H. Single-particle spectroscopic study on fluorescence enhancement by plasmon coupled gold nanorod dimers assembled on DNA Origami. *J. Phys. Chem. Lett.* **6**, 2043–2049 (2015).

87. Haidar, I. *et al.* Highly stable silica-coated gold nanorods dimers for solution-based SERS. *Phys. Chem. Chem. Phys.* **18**, 32272–32280 (2016).

88. Ray, K., Chowdhury, M. H. & Lakowicz, J. R. Aluminum nanostructured films as substrates for enhanced fluorescence in the ultraviolet-blue spectral region. *Anal. Chem.* **79**, 6480–6487 (2007).

89. Hsu, L. Y. *et al.* Large-Scale Inhomogeneous Fluorescence Plasmonic Silver Chips: Origin and Mechanism. *Chem* **6**, 3396–3408 (2020).

90. Funari, R., Miranda, B., Chu, K. Y., Maffettone, P. L. & Shen, A. Q. Metal-enhanced fluorescence immunosensor based on plasmonic arrays of gold nanoislands on an etched glass substrate. *ACS Appl. Nano Mater.* **3**, 10470–10478 (2020).

91. Ray, K., Szmacinski, H. & Lakowicz, J. R. Enhanced Fluorescence of Proteins

and Label-Free Bioassays Using Aluminum Nanostructures. *Anal. Chem.* **81**, 6049–6054 (2009).

92. Kasani, S., Curtin, K. & Wu, N. A review of 2D and 3D plasmonic nanostructure array patterns: fabrication, light management and sensing applications. *Nanophotonics* **8**, 2065–2089 (2019).

93. Hao, Q. *et al.* Facile design of ultra-thin anodic aluminum oxide membranes for the fabrication of plasmonic nanoarrays. *Nanotechnology* **28**, 105301 (2017).

94. Auguié, B., Bendaña, X. M., Barnes, W. L. & García De Abajo, F. J. Diffractive arrays of gold nanoparticles near an interface: Critical role of the substrate. *Phys. Rev. B - Condens. Matter Mater. Phys.* **82**, 1–7 (2010).

95. Lamprecht, B. *et al.* Metal Nanoparticle Gratings: Influence of Dipolar Particle Interaction on the Plasmon Resonance. *Phys. Rev. Lett.* **84**, 4721–4724 (2000).

96. Sugawa, K. *et al.* Metal-enhanced fluorescence platforms based on plasmonic ordered copper arrays: Wavelength dependence of quenching and enhancement effects. *ACS Nano* **7**, 9997–10010 (2013).

97. Sugawa, K. *et al.* Performance Improvement of Triplet–Triplet Annihilation-Based Upconversion Solid Films through Plasmon-Induced Backward Scattering of Periodic Arrays of Ag and Al. *Langmuir* **37**, 11508–11519 (2021).

98. Fayyaz, S., Tabatabaei, M., Hou, R. & Lagugné-Labarthet, F. Surface-enhanced fluorescence: Mapping individual hot spots in silica-protected 2D gold nanotriangle arrays. *J. Phys. Chem. C* **116**, 11665–11670 (2012).

99. Pang, J. *et al.* Gold nanodisc arrays as near infrared metal-enhanced fluorescence platforms with tuneable enhancement factors. *J. Mater. Chem. C* **5**, 917–925 (2017).

100. Cui, X., Tawa, K., Kintaka, K. & Nishii, J. Enhanced fluorescence microscopic imaging by plasmonic nanostructures: from a 1d grating to a 2d nanohole array. *Adv. Funct. Mater.* **20**, 945–950 (2010).

101. Kelf, T. A. *et al.* Localized and delocalized plasmons in metallic nanovoids. *Phys. Rev. B - Condens. Matter Mater. Phys.* **74**, 1–12 (2006).

102. Cui, X., Tawa, K., Hori, H. & Nishii, J. Tailored plasmonic gratings for enhanced fluorescence detection and microscopic imaging. *Adv. Funct. Mater.* **20**, 546–553 (2010).

103. Jose, B. *et al.* Emission enhancement within gold spherical nanocavity arrays. *Phys. Chem. Chem. Phys.* **11**, 10923–10933 (2009).

104. Dong, J., Zhang, Z., Zheng, H. & Sun, M. Recent Progress on Plasmon-Enhanced Fluorescence. *Nanophotonics* **4**, 472–490 (2015).

105. Zhang, Q. *et al.* Surface plasmon-enhanced fluorescence on Au nanohole array for prostate-specific antigen detection. *Int. J. Nanomedicine* **12**, 2307–2314 (2017).

106. Seo, S., Ameen, A. & Liu, G. L. Colorimetric Effect of Gold Nanocup Arrays on Fluorescence Amplification. *J. Phys. Chem. C* **119**, 18518–18526 (2015).

107. Wi, J.-S., Son, J. G., Han, S. W. & Lee, T. G. Nanoparticles inside nanodishes for plasmon excitations. *Appl. Phys. Lett.* **107**, 203102 (2015).

108. Wi, J.-S., Son, J. G. & Lee, T. G. Lithographically-prepared gold nanobowls to detect mesoscale target analytes. *Opt. Mater. Express* **10**, 3185 (2020).

109. Zuo, Z. *et al.* Effective plasmon coupling in conical cavities for sensitive surface enhanced Raman scattering with quantitative analysis ability. *Nanoscale* **11**, 17913–17919 (2019).

110. Sierra-Martin, B. & Fernandez-Barbero, A. Particles and nanovoids for plasmonics. *Adv. Colloid Interface Sci.* **290**, 102394 (2021).

111. Cole, R. M. *et al.* Understanding Plasmons in Nanoscale Voids. *Nano Lett.* **7**, 2094–2100 (2007).

112. Wang, W. *et al.* Heterostructured TiO 2 Nanorod@Nanobowl Arrays for Efficient Photoelectrochemical Water Splitting. *Small* **12**, 1469–1478 (2016).

113. Bartlett, P. N., Baumberg, J. J., Coyle, S. & Abdelsalam, M. E. Optical properties of nanostructured metal films. *Faraday Discuss.* **125**, 117–132 (2004).

114. Deng, F. *et al.* Dynamic and Reversible Tuning of Particle-in-Bowl Shaped Plasmonic Resonators for Switchable Surface Enhanced Raman Scattering. *Adv.*

Mater. Interfaces **9**, 2101837 (2022).

115. Xu, J. *et al.* Facilely Flexible Imprinted Hemispherical Cavity Array for Effective Plasmonic Coupling as SERS Substrate. *Nanomaterials* **11**, 3196 (2021).

116. Lee, T. *et al.* Highly robust, uniform and ultra-sensitive surface-enhanced Raman scattering substrates for microRNA detection fabricated by using silver nanostructures grown in gold nanobowls. *Nanoscale* **10**, 3680–3687 (2018).

117. Qiu, T. *et al.* Tailoring light emission properties of organic emitter by coupling to resonance-tuned silver nanoantenna arrays. *Appl. Phys. Lett.* **95**, 1–4 (2009).

118. Qiu, T. *et al.* High-sensitivity and stable cellular fluorescence imaging by patterned silver nanocap arrays. *ACS Appl. Mater. Interfaces* **2**, 2465–2470 (2010).

119. Volpati, D. *et al.* Exploring copper nanostructures as highly uniform and reproducible substrates for plasmon-enhanced fluorescence. *Analyst* **140**, 476–482 (2015).

120. Spada, E. R. *et al.* Copper spherical cavity arrays: Fluorescence enhancement in PFO films. *Appl. Surf. Sci.* **392**, 1181–1186 (2017).

121. Lordan, F., Rice, J. H., Jose, B., Forster, R. J. & Keyes, T. E. Effect of cavity architecture on the surface-enhanced emission from site-selective nanostructured cavity arrays. *J. Phys. Chem. C* **116**, 1784–1788 (2012).

122. Gimenez, A. V., Kho, K. W. & Keyes, T. E. Nano-substructured plasmonic pore arrays: a robust, low cost route to reproducible hierarchical structures extended across macroscopic dimensions. *Nanoscale Adv.* **2**, 4740–4756 (2020).

123. Jose, B., Mallon, C. T., Forster, R. J. & Keyes, T. E. Regio-selective decoration of nanocavity metal arrays: Contributions from localized and delocalized plasmons to surface enhanced Raman spectroscopy. *Phys. Chem. Chem. Phys.* **13**, 14705–14714 (2011).

124. Sai, H., Fujiwara, H., Kondo, M. & Kanamori, Y. Enhancement of light trapping in thin-film hydrogenated microcrystalline Si solar cells using back reflectors with self-ordered dimple pattern. *Appl. Phys. Lett.* **93**, 1–4 (2008).

125. Hao, Q. *et al.* Tunable fluorescence from patterned silver nano-island arrays for sensitive sub-cell imaging. *J. Phys. D. Appl. Phys.* **46**, 495302 (2013).

126. Lee, M. H. *et al.* Roll-to-roll anodization and etching of aluminum foils for high-throughput surface nanotexturing. *Nano Lett.* **11**, 3425–3430 (2011).

127. Ikeda, H. *et al.* Nanostructural characterization of ordered gold particle arrays fabricated via aluminum anodizing, sputter coating, and dewetting. *Appl. Surf. Sci.* **465**, 747–753 (2019).

128. Mao, P. *et al.* Broadband single molecule SERS detection designed by warped optical spaces. *Nat. Commun.* **9**, 5428 (2018).

129. Haiss, W., Thanh, N. T. K., Aveyard, J. & Fernig, D. G. Determination of Size and Concentration of Gold Nanoparticles from UV−Vis Spectra. *Anal. Chem.* **79**, 4215–4221 (2007).

130. Perkin-Elmer. Lambda 2 UV/VIS Spectrometer Operator’s Manual. (1992).

131. Fluorolog-3 Spectrofluorometer. *Operation Manual, v3.2* (2008).

132. Wahl, M. Time-Correlated Single Photon Counting. PicoQuant, Technical note. *J. Lumin.* **44**, 161–165 (1989).

133. Yip, P. Nanometrology using Time-Resolved Fluorescence Techniques. *PhD Thesis* (University of Strathclyde, 2016).

134. Edinburgh Photonics. Why use TCSPC for fluorescence lifetime measurements? Technical note. 1–2 (2013).

135. Hirvonen, L. M. & Suhling, K. Wide-field TCSPC: Methods and applications. *Meas. Sci. Technol.* **28**, (2017).

136. Suhling, K., McLoskey, D. & Birch, D. J. S. Multiplexed single-photon counting. II. The statistical theory of time-correlated measurements. *Rev. Sci. Instrum.* **67**, 2238–2246 (1996).

137. HORIBA. DataStation v2.4, Software for single photon counting data acquisition. **49**, 1–155

138. Becker, W. *The Bh TCSPC Handbook.* (2019).

139. HORIBA. Time-resolved fluorescence anisotropy, technical note TRFT-2.

140. Horiba Scientific. DAS6 Operating manual. 89–100 (2017).

141. Egerton, R. F. *Physical Principles of Electron Microscopy*. (Springer US, 2005).

142. Vernon-Parry, K. D. Scanning electron microscopy: an introduction. *III-Vs Rev.* **13**, 40–44 (2000).

143. Krumeich, F. *Introduction into Transmission and Scanning Transmission Electron Microscopy*. (ETH Zürich, 2018).

144. Zhou, W. & Lin, Z. *Scanning Microscopy for Nanotechnology - Techniques and Applications*. (Springer New York, 2007).

145. Chen, Y., Preece, J. A. & Palmer, R. E. Processing and characterization of gold nanoparticles for use in plasmon probe spectroscopy and microscopy of biosystems. *Ann. N. Y. Acad. Sci.* **1130**, 201–206 (2008).

146. Chen, Y., Palmer, R. E. & Wilcoxon, J. P. Sintering of Passivated Gold Nanoparticles under the Electron Beam. *Langmuir* **22**, 2851–2855 (2006).

147. Zhang, Y., Birch, D. J. S. & Chen, Y. Two-photon excited surface plasmon enhanced energy transfer between DAPI and gold nanoparticles: Opportunities in intra-cellular imaging and sensing. *Appl. Phys. Lett.* **99**, (2011).

148. Barnard, A. S. & Chen, Y. Kinetic modelling of the shape-dependent evolution of faceted gold nanoparticles. *J. Mater. Chem.* **21**, 12239 (2011).

149. Lim, Z.-Z. J., Li, J.-E. J., Ng, C.-T., Yung, L.-Y. L. & Bay, B.-H. Gold nanoparticles in cancer therapy. *Acta Pharmacol. Sin.* **32**, 983–990 (2011).

150. Gu, P., Birch, D. J. S. & Chen, Y. Dye-doped polystyrene-coated gold nanorods: towards wavelength tuneable SPASER. *Methods Appl. Fluoresc.* **2**, 024004 (2014).

151. Wei, G. *et al.* Revealing the photophysics of gold-nanobeacons via time-resolved fluorescence spectroscopy. *Opt. Lett.* **40**, 5738 (2015).

152. Murphy, C. J. *et al.* Chemical sensing and imaging with metallic nanorods. *Chem. Commun.* 544–557 (2008).

153. Xu, J., Gu, P., Birch, D. J. S. & Chen, Y. Plasmon-Promoted Electrochemical Oxygen Evolution Catalysis from Gold Decorated MnO2 Nanosheets under Green Light. *Adv. Funct. Mater.* **28**, 1801573 (2018).

154. Ming, T., Chen, H., Jiang, R., Li, Q. & Wang, J. Plasmon-controlled fluorescence: Beyond the intensity enhancement. *J. Phys. Chem. Lett.* **3**, 191–202 (2012).

155. Wu, W. & Tracy, J. B. Large-Scale Silica Overcoating of Gold Nanorods with Tunable Shell Thicknesses. *Chem. Mater.* **27**, 2888–2894 (2015).

156. Fang, L., Wang, W., Liu, Y., Xie, Z. & Chen, L. Janus nanostructures formed by mesoporous silica coating Au nanorods for near-infrared chemo–photothermal therapy. *J. Mater. Chem. B* **5**, 8833–8838 (2017).

157. Liberman, A., Mendez, N., Trogler, W. C. & Kummel, A. C. Synthesis and surface functionalization of silica nanoparticles for nanomedicine. *Surf. Sci. Rep.* **69**, 132–158 (2014).

158. Nikoobakht, B. & El-Sayed, M. A. Preparation and Growth Mechanism of Gold Nanorods (NRs) Using Seed-Mediated Growth Method. *Chem. Mater.* **15**, 1957–1962 (2003).

159. Burrows, N. D. *et al.* Surface Chemistry of Gold Nanorods. *Langmuir* **32**, 9905–9921 (2016).

160. Gorelikov, I. & Matsuura, N. Single-Step Coating of Mesoporous Silica on Cetyltrimethyl Ammonium Bromide-Capped Nanoparticles. *Nano Lett.* **8**, 369–373 (2008).

161. Rowe, L. R., Chapman, B. S. & Tracy, J. B. Understanding and Controlling the Morphology of Silica Shells on Gold Nanorods. *Chem. Mater.* **30**, 6249–6258 (2018).

162. Hinman, J. G. *et al.* Oxidation State of Capping Agent Affects Spatial Reactivity on Gold Nanorods. *J. Am. Chem. Soc.* **139**, 9851–9854 (2017).

163. Huang, C., Chung, M., Souris, J. S. & Lo, L.-W. Controlled epitaxial growth of mesoporous silica/gold nanorod nanolollipops and nanodumb-bells. *APL Mater.*

2, 113312 (2014).

164. Wang, M., Hoff, A., Doebler, J. E., Emory, S. R. & Bao, Y. Dumbbell-Like Silica Coated Gold Nanorods and Their Plasmonic Properties. *Langmuir* **35**, 16886–16892 (2019).

165. Zhu, X. *et al.* Selective Pd Deposition on Au Nanobipyramids and Pd Site-Dependent Plasmonic Photocatalytic Activity. *Adv. Funct. Mater.* **27**, 1700016 (2017).

166. Yin, J. *et al.* Tumor-targeted nanoprobes for enhanced multimodal imaging and synergistic photothermal therapy: core–shell and dumbbell Gd-tailored gold nanorods. *Nanoscale* **9**, 16661–16673 (2017).

167. Li, J. Gold nanorod surface functionalization: construction of dynamic surfaces and heterogeneous silica coating. (University of Illinois, 2016).

168. Baliś, A. & Zapotoczny, S. Tailored Synthesis of Core-Shell Mesoporous Silica Particles—Optimization of Dye Sorption Properties. *Nanomaterials* **8**, 230 (2018).

169. Manojlovic, J. The Krafft temperature of surfactant solutions. *Therm. Sci.* **16**, 631–640 (2012).

170. Orendorff, C. J. & Murphy, C. J. Quantitation of metal content in the silver-assisted growth of gold nanorods. *J. Phys. Chem. B* **110**, 3990–3994 (2006).

171. Ye, X., Zheng, C., Chen, J., Gao, Y. & Murray, C. B. Using binary surfactant mixtures to simultaneously improve the dimensional tunability and monodispersity in the seeded growth of gold nanorods. *Nano Lett.* **13**, 765–771 (2013).

172. Huang, X., Neretina, S. & El-Sayed, M. A. Gold Nanorods: From Synthesis and Properties to Biological and Biomedical Applications. *Adv. Mater.* **21**, 4880–4910 (2009).

173. Grzelczak, M., Pérez-Juste, J., Mulvaney, P. & Liz-Marzán, L. M. Shape control in gold nanoparticle synthesis. *Chem. Soc. Rev.* **37**, 1783 (2008).

174. Sajanlal, P. R., Sreeprasad, T. S., Samal, A. K. & Pradeep, T. Anisotropic

nanomaterials: structure, growth, assembly, and functions. *Nano Rev.* **2**, 5883 (2011).

175. Liu, M. & Guyot-Sionnest, P. Mechanism of silver(I)-assisted growth of gold nanorods and bipyramids. *J. Phys. Chem. B* **109**, 22192–22200 (2005).

176. Song, J. T., Zhang, X. S., Qin, M. Y. & Zhao, Y. Di. One-pot two-step synthesis of core-shell mesoporous silica-coated gold nanoparticles. *Dalt. Trans.* **44**, 7752–7756 (2015).

177. Jana, N. R., Gearheart, L. & Murphy, C. J. Seed-mediated growth approach for shape-controlled synthesis of spheroidal and rod-like gold nanoparticles using a surfactant template. *Adv. Mater.* **13**, 1389–1393 (2001).

178. Hubert, F., Testard, F. & Spalla, O. Cetyltrimethylammonium bromide silver bromide complex as the capping agent of gold nanorods. *Langmuir* **24**, 9219–9222 (2008).

179. Almora-Barrios, N., Novell-Leruth, G., Whiting, P., Liz-Marzán, L. M. & López, N. Theoretical description of the role of halides, silver, and surfactants on the structure of gold nanorods. *Nano Lett.* **14**, 871–875 (2014).

180. Singh, L. P. *et al.* Sol-Gel processing of silica nanoparticles and their applications. *Adv. Colloid Interface Sci.* **214**, 17–37 (2014).

181. Belton, D. J., Deschaume, O. & Perry, C. C. An overview of the fundamentals of the chemistry of silica with relevance to biosilicification and technological advances. *FEBS J.* **279**, 1710–1720 (2012).

182. Tang, X. *et al.* Ultrathin and Highly Passivating Silica Shells for Luminescent and Water-Soluble CdSe/CdS Nanorods. *Langmuir* **33**, 5253–5260 (2017).

183. Stöber, W., Fink, A. & Bohn, E. Controlled growth of monodisperse silica spheres in the micron size range. *J. Colloid Interface Sci.* **26**, 62–69 (1968).

184. Nooney, R. I., Thirunavukkarasu, D., Yimei, C., Josephs, R. & Ostafin, A. E. Synthesis of nanoscale mesoporous silica spheres with controlled particle size. *Chem. Mater.* **14**, 4721–4728 (2002).

185. Nooney, R. I., Thirunavukkarasu, D., Chen, Y., Josephs, R. & Ostafin, A. E.

Self-Assembly of Mesoporous Nanoscale Silica/Gold Composites. *Langmuir* **19**, 7628–7637 (2003).

186. Wu, S.-H., Mou, C.-Y. & Lin, H.-P. Synthesis of mesoporous silica nanoparticles. *Chem. Soc. Rev.* **42**, 3862 (2013).

187. Jain, P. K., Eustis, S. & El-Sayed, M. A. Plasmon coupling in nanorod assemblies: Optical absorption, discrete dipole approximation simulation, and exciton-coupling model. *J. Phys. Chem. B* **110**, 18243–18253 (2006).

188. Nikoobakht, B., Wang, Z. L. & El-Sayed, M. A. Self-Assembly of Gold Nanorods. *J. Phys. Chem. B* **104**, 8635–8640 (2002).

189. Ahmad, I. *et al.* Self-assembly and wetting properties of gold nanorod–CTAB molecules on HOPG. *Beilstein J. Nanotechnol.* **10**, 696–705 (2019).

190. Venkataraman, N. V. & Vasudevan, S. Hydrocarbon chain conformation in an intercalated surfactant monolayer and bilayer. *J. Chem. Sci.* **113**, 539–558 (2001).

191. Fothergill, S. M., Joyce, C. & Xie, F. Metal enhanced fluorescence biosensing: from ultra-violet towards second near-infrared window. *Nanoscale* **10**, 20914–20929 (2018).

192. Chowdhury, M. H., Ray, K., Gray, S. K., Pond, J. & Lakowicz, J. R. Aluminum Nanoparticles as Substrates for Metal-Enhanced Fluorescence in the Ultraviolet for the Label-Free Detection of Biomolecules. *Anal. Chem.* **81**, 1397–1403 (2009).

193. Tian, S. *et al.* Aluminum nanocrystals: A sustainable substrate for quantitative SERS-Based DNA Detection. *Nano Lett.* **17**, 5071–5077 (2017).

194. Martin, J. & Plain, J. Fabrication of aluminium nanostructures for plasmonics. *J. Phys. D. Appl. Phys.* **48**, 184002 (2015).

195. Sharma, B. *et al.* Aluminum Film-Over-Nanosphere Substrates for Deep-UV Surface-Enhanced Resonance Raman Spectroscopy. *Nano Lett.* **16**, 7968–7973 (2016).

196. Sultangaziyev, A. *et al.* Aluminum foil as a substrate for metal enhanced

fluorescence of bacteria labelled with quantum dots, shows very large enhancement and high contrast. *Sens. Bio-Sensing Res.* **28**, 100332 (2020).

197. Bukasov, R. *et al.* High Contrast Surface Enhanced Fluorescence of Carbon Dot Labeled Bacteria Cells on Aluminum Foil. *J. Fluoresc.* **30**, 1477–1482 (2020).

198. Solanki, R., Rostamabadi, H., Patel, S. & Jafari, S. M. Anticancer nano-delivery systems based on bovine serum albumin nanoparticles: A critical review. *Int. J. Biol. Macromol.* **193**, 528–540 (2021).

199. Buddanavar, A. T. & Nandibewoor, S. T. Multi-spectroscopic characterization of bovine serum albumin upon interaction with atomoxetine. *J. Pharm. Anal.* **7**, 148–155 (2017).

200. Tao, C., Chuah, Y. J., Xu, C. & Wang, D.-A. Albumin conjugates and assemblies as versatile bio-functional additives and carriers for biomedical applications. *J. Mater. Chem. B* **7**, 357–367 (2019).

201. Ferrer, M. L., Duchowicz, R., Carrasco, B., De La Torre, J. G. & Acuña, A. U. The conformation of serum albumin in solution: A combined phosphorescence depolarization-hydrodynamic modeling study. *Biophys. J.* **80**, 2422–2430 (2001).

202. Russell, B. A., Kubiak-Ossowska, K., Mulheran, P. A., Birch, D. J. S. & Chen, Y. Locating the nucleation sites for protein encapsulated gold nanoclusters: a molecular dynamics and fluorescence study. *Phys. Chem. Chem. Phys.* **17**, 21935–21941 (2015).

203. Russell, B. A. Protein Encapsulated Gold Nanoclusters for Biological Applications, Doctoral thesis. (University of Strathclyde, Glasgow, 2017).

204. Kluz, M. *et al.* Revisiting the conformational state of albumin conjugated to gold nanoclusters: A self-assembly pathway to giant superstructures unraveled. *PLoS One* **14**, e0218975 (2019).

205. Qu, X. *et al.* Fluorescent Gold Nanoclusters: Synthesis and Recent Biological Application. *J. Nanomater.* **2015**, 1–23 (2015).

206. Xie, J., Zheng, Y. & Ying, J. Y. Protein-Directed Synthesis of Highly Fluorescent Gold Nanoclusters. *J. Am. Chem. Soc.* **131**, 888–889 (2009).

207. Qian, H., Zhu, M., Wu, Z. & Jin, R. Quantum Sized Gold Nanoclusters with Atomic Precision. *Acc. Chem. Res.* **45**, 1470–1479 (2012).

208. Kaur, N., Aditya, R. N., Singh, A. & Kuo, T.-R. Biomedical Applications for Gold Nanoclusters: Recent Developments and Future Perspectives. *Nanoscale Res. Lett.* **13**, 302 (2018).

209. Kang, X. & Zhu, M. Tailoring the photoluminescence of atomically precise nanoclusters. *Chem. Soc. Rev.* **48**, 2422–2457 (2019).

210. Chen, L. Y., Wang, C. W., Yuan, Z. & Chang, H. T. Fluorescent gold nanoclusters: Recent advances in sensing and imaging. *Anal. Chem.* **87**, 216–229 (2015).

211. Wu, Z. & Jin, R. On the ligand's role in the fluorescence of gold nanoclusters. *Nano Lett.* **10**, 2568–2573 (2010).

212. Xu, Y. *et al.* The role of protein characteristics in the formation and fluorescence of Au nanoclusters. *Nanoscale* **6**, 1515–1524 (2014).

213. Raut, S. *et al.* Evidence of energy transfer from tryptophan to BSA/HSA protected gold nanoclusters. *Methods Appl. Fluoresc.* **2**, 035004 (2014).

214. Wen, X., Yu, P., Toh, Y. R. & Tang, J. Structure-correlated dual fluorescent bands in BSA-protected Au 25 nanoclusters. *J. Phys. Chem. C* **116**, 11830–11836 (2012).

215. Wen, X. *et al.* Fluorescence Dynamics in BSA-Protected Au 25 Nanoclusters. *J. Phys. Chem. C* **116**, 19032–19038 (2012).

216. Wang, X. Y., Del Guerzo, A. & Schmehl, R. H. Photophysical behavior of transition metal complexes having interacting ligand localized and metal-to-ligand charge transfer states. *J. Photochem. Photobiol. C Photochem. Rev.* **5**, 55–77 (2004).

217. Zheng, Y., Lai, L., Liu, W., Jiang, H. & Wang, X. Recent advances in biomedical applications of fluorescent gold nanoclusters. *Adv. Colloid Interface Sci.* **242**, 1–16 (2017).

218. Krishna Kumar, A. S. & Tseng, W. L. Perspective on recent developments of

near infrared-emitting gold nanoclusters: Applications in sensing and bio-imaging. *Anal. Methods* **12**, 1809–1826 (2020).

219. Xie, J., Zheng, Y. & Ying, J. Y. Highly selective and ultrasensitive detection of Hg2+ based on fluorescence quenching of Au nanoclusters by Hg2+–Au+ interactions. *Chem. Commun.* **46**, 961–963 (2010).

220. Durgadas, C. V., Sharma, C. P. & Sreenivasan, K. Fluorescent gold clusters as nanosensors for copper ions in live cells. *Analyst* **136**, 933–940 (2011).

221. Tao, Y., Lin, Y., Ren, J. & Qu, X. A dual fluorometric and colorimetric sensor for dopamine based on BSA-stabilized Au nanoclusters. *Biosens. Bioelectron.* **42**, 41–46 (2013).

222. Wu, X. *et al.* Ultrasmall near-infrared gold nanoclusters for tumor fluorescence imaging in vivo. *Nanoscale* **2**, 2244–2249 (2010).

223. HORIBA. A practical guide to time-resolved luminescence lifetime determination using dedicated Time-Correlated Single-Photon Counting systems. 1–31

224. Chib, R. *et al.* Effect of quencher, denaturants, temperature and pH on the fluorescent properties of BSA protected gold nanoclusters. *J. Lumin.* **168**, 62–68 (2015).

225. Alkudaisi, N. A. Lysozyme Encapsulated Gold Nanocluster for Studying Protein Denaturation A Thesis submitted to the University of Strathclyde for the degree of Doctor of Philosophy By. (University of Strathclyde, Glasgow, 2020).

226. Efstratiou, M., Christy, J., Bonn, D. & Sefiane, K. The Effect of Substrate Temperature on the Evaporative Behaviour and Desiccation Patterns of Foetal Bovine Serum Drops. *Colloids and Interfaces* **5**, 43 (2021).

227. Pozzobon, V., Levasseur, W., Do, K.-V., Palpant, B. & Perré, P. Household aluminum foil matte and bright side reflectivity measurements: Application to a photobioreactor light concentrator design. *Biotechnol. Reports* **25**, e00399 (2020).

228. Asselin, J., Legros, P., Grégoire, A. & Boudreau, D. Correlating Metal-Enhanced

Fluorescence and Structural Properties in Ag@SiO2 Core-Shell Nanoparticles. *Plasmonics* **11**, 1369–1376 (2016).

229. Lu, M. *et al.* Plasmonic enhancement of cyanine dyes for near-infrared light-triggered photodynamic/photothermal therapy and fluorescent imaging. *Nanotechnology* **28**, 445710 (2017).

230. Handschuh-Wang, S. *et al.* Detailed study of BSA adsorption on micro- and nanocrystalline diamond/β-SiC composite gradient films by time-resolved fluorescence microscopy. *Langmuir* **33**, 802–813 (2017).

231. Wang, H.-D., Niu, C. H., Yang, Q. & Badea, I. Study on protein conformation and adsorption behaviors in nanodiamond particle–protein complexes. *Nanotechnology* **22**, 145703 (2011).

232. Norde, W. & Giacomelli, C. E. BSA structural changes during homomolecular exchange between the adsorbed and the dissolved states. *J. Biotechnol.* **79**, 259–268 (2000).

233. Roach, P., Farrar, D. & Perry, C. C. Interpretation of protein adsorption: Surface-induced conformational changes. *J. Am. Chem. Soc.* **127**, 8168–8173 (2005).

234. Vilhena, J. G., Rubio-Pereda, P., Vellosillo, P., Serena, P. A. & Pérez, R. Albumin (BSA) Adsorption over Graphene in Aqueous Environment: Influence of Orientation, Adsorption Protocol, and Solvent Treatment. *Langmuir* **32**, 1742–1755 (2016).

235. Kubiak-Ossowska, K., Tokarczyk, K., Jachimska, B. & Mulheran, P. A. Bovine Serum Albumin Adsorption at a Silica Surface Explored by Simulation and Experiment. *J. Phys. Chem. B* **121**, 3975–3986 (2017).

236. Tokarczyk, K., Kubiak-Ossowska, K., Jachimska, B. & Mulheran, P. A. Energy Landscape of Negatively Charged BSA Adsorbed on a Negatively Charged Silica Surface. *J. Phys. Chem. B* **122**, 3744–3753 (2018).

237. Beykal, B., Herzberg, M., Oren, Y. & Mauter, M. S. Influence of surface charge on the rate, extent, and structure of adsorbed Bovine Serum Albumin to gold electrodes. *J. Colloid Interface Sci.* **460**, 321–328 (2015).

238. Ma, G. J., Ferhan, A. R., Jackman, J. A. & Cho, N.-J. Conformational flexibility of fatty acid-free bovine serum albumin proteins enables superior antifouling coatings. *Commun. Mater.* **1**, 45 (2020).

239. Hlady, V. & Andrade, J. D. Fluorescence emission from adsorbed bovine serum albumin and albumin-bound 1-anilinonaphthalene-8-sulfonate studied by TIRF. *Colloids and Surfaces* **32**, 359–369 (1988).

240. Rainbow, M. R., Atherton, S. & Eberhart, R. C. Fluorescence lifetime measurements using total internal reflection fluorimetry: Evidence for a conformational change in albumin adsorbed to quartz. *J. Biomed. Mater. Res.* **21**, 539–555 (1987).

241. Russell, B. A., Jachimska, B. & Chen, Y. Polyallylamine hydrochloride coating enhances the fluorescence emission of Human Serum Albumin encapsulated gold nanoclusters. *J. Photochem. Photobiol. B Biol.* **187**, 131–135 (2018).

242. Silin, V., Weetall, H. & Vanderah, D. J. SPR studies of the nonspecific adsorption kinetics of human IgG and BSA on gold surfaces modified by self-assembled monolayers (SAMs). *J. Colloid Interface Sci.* **185**, 94–103 (1997).

243. Kim, J. & Somorjai, G. A. Molecular packing of lysozyme, fibrinogen, and bovine serum albumin on hydrophilic and hydrophobic surfaces studied by infrared-visible sum frequency generation and fluorescence microscopy. *J. Am. Chem. Soc.* **125**, 3150–3158 (2003).

244. Singh, P. & Chowdhury, P. K. Crowding-induced quenching of intrinsic tryptophans of serum albumins: A residue-level investigation of different conformations. *J. Phys. Chem. Lett.* **4**, 2610–2617 (2013).

245. Gupta, M. & Chowdhury, P. K. Protein dynamics as a sensor for macromolecular crowding: Insights into mixed crowding. *J. Mol. Liq.* **347**, 117969 (2022).

246. Ota, C. & Takano, K. Behavior of Bovine Serum Albumin Molecules in Molecular Crowding Environments Investigated by Raman Spectroscopy. *Langmuir* **32**, 7372–7382 (2016).

247. Sogami, M., Itoh, K. B. & Nemoto, Y. Fluorescence polarization studies on the conformational transition of bovine plasma albumin in acidic solutions. *Biochim.*

Biophys. Acta - Protein Struct. **393**, 446–459 (1975).

248. Moreira, C. *et al.* Approaches for deep-ultraviolet surface plasmon resonance sensors. *Opt. Lett.* **45**, 4642 (2020).

249. Le Guével, X., Hötzer, B., Jung, G. & Schneider, M. NIR-emitting fluorescent gold nanoclusters doped in silica nanoparticles. *J. Mater. Chem.* **21**, 2974–2981 (2011).

250. Alkudaisi, N., Russell, B. A., Jachimska, B., Birch, D. J. S. & Chen, Y. Detecting lysozyme unfolding via the fluorescence of lysozyme encapsulated gold nanoclusters. *J. Mater. Chem. B* **7**, 1167–1175 (2019).

251. Alkudaisi, N., Russell, B. A., Birch, D. J. S. & Chen, Y. Lysozyme encapsulated gold nanoclusters for probing the early stage of lysozyme aggregation under acidic conditions. *J. Photochem. Photobiol. B Biol.* **197**, 111540 (2019).

252. Pyo, K. *et al.* Ultrabright Luminescence from Gold Nanoclusters: Rigidifying the Au(I)–Thiolate Shell. *J. Am. Chem. Soc.* **137**, 8244–8250 (2015).

253. Andrews, D. L. & Bittner, A. M. Energy transfer in a static electric field. *J. Lumin.* **55**, 231–242 (1993).

254. Es-Souni, M. & Habouti, S. Ordered Nanomaterial Thin Films via Supported Anodized Alumina Templates. *Front. Mater.* **1**, 1–9 (2014).

255. Tsao, Y.-C. *et al.* Pore size dependence of diffuse light scattering from anodized aluminum solar cell backside reflectors. *Opt. Express* **21**, A84 (2013).

256. Hao, Q. *et al.* Aluminum plasmonic photocatalysis. *Sci. Rep.* **5**, 15288 (2015).

257. Colson, P., Henrist, C. & Cloots, R. Nanosphere Lithography: A Powerful Method for the Controlled Manufacturing of Nanomaterials. *J. Nanomater.* **2013**, 1–19 (2013).

258. Kahraman, M., Daggumati, P., Kurtulus, O., Seker, E. & Wachsmann-Hogiu, S. Fabrication and Characterization of Flexible and Tunable Plasmonic Nanostructures. *Sci. Rep.* **3**, 3396 (2013).

259. Focsan, M. *et al.* Flexible and Tunable 3D Gold Nanocups Platform as Plasmonic Biosensor for Specific Dual LSPR-SERS Immuno-Detection. *Sci. Rep.* **7**, 1–11

(2017).

260. Fan, X., Hao, Q. & Qiu, T. *Reviews in Plasmonics 2015*. **2015**, (Springer International Publishing Switzerland, 2016).

261. Fan, X. *et al.* Assembly of gold nanoparticles into aluminum nanobowl array. *Sci. Rep.* **7**, 1–7 (2017).

262. Kikuchi, T., Nakajima, D., Nishinaga, O., Natsui, S. & Suzuki, R. O. Porous Aluminum Oxide Formed by Anodizing in Various Electrolyte Species. *Curr. Nanosci.* **11**, 12 (2015).

263. Lee, W. The anodization of aluminum for nanotechnology applications. *JOM* **62**, 57–63 (2010).

264. Jagminas, A. & Vrublevsky, I. Anodizing of aluminum under the burning conditions. in *Nanostructured Anodic Metal Oxides* 89–122 (Elsevier, 2020).

265. Ma, Y. *et al.* Fabrication of self-ordered alumina films with large interpore distance by janus anodization in citric acid. *Sci. Rep.* **6**, 6–13 (2016).

266. Masuda, H., Yada, K. & Osaka, A. Self-ordering of cell configuration of anodic porous alumina with large-size pores in phosphoric acid solution. *Japanese J. Appl. Physics, Part 2 Lett.* **37**, 9–12 (1998).

267. Assaud, L., Bochmann, S., Christiansen, S. & Bachmann, J. A large electrochemical setup for the anodization of aluminum towards highly ordered arrays of cylindrical nanopores. *Rev. Sci. Instrum.* **86**, 073902 (2015).

268. Lide, D. R. & Haynes, W. M. *CRC Handbook of Chemistry and Physics: A Ready-Reference Book of Chemical and Physical Data*. (CRC Press: Boca Raton, 2009).

269. Johnson, P. B. & Christy, R. W. Optical Constants of the Noble Metals. *Phys. Rev. B* **6**, 4370–4379 (1972).

270. Qiu, T. *et al.* Controlled Assembly of Highly Raman-Enhancing Silver Nanocap Arrays Templated by Porous Anodic Alumina Membranes. *Small* **5**, 2333–2337 (2009).

271. Ilango, M. S., Mutalikdesai, A. & Ramasesha, S. K. Anodization of Aluminium

using a fast two-step process. *J. Chem. Sci.* **128**, 153–158 (2016).

272. Ehrenreich, H., Philipp, H. R. & Segall, B. Optical Properties of Aluminum. *Phys. Rev.* **132**, 1918–1928 (1963).

273. Cheng, L. *et al.* UV Plasmonic Resonance of Aluminum Shallow Pit Arrays. *J. Phys. Chem. C* **119**, 14304–14311 (2015).

274. Huang, G. S., Wu, X. L., Mei, Y. F., Shao, X. F. & Siu, G. G. Strong blue emission from anodic alumina membranes with ordered nanopore array. *J. Appl. Phys.* **93**, 582–585 (2003).

275. Gao, T., Meng, G. W. & Zhang, L. De. Origin of the blue luminescence in porous anodic alumina films formed in oxalic acid solutions. *Chinese Phys. Lett.* **20**, 713–716 (2003).

276. Stojadinovic, S. *et al.* Photoluminescent properties of barrier anodic oxide films on aluminum. *Thin Solid Films* **519**, 3516–3521 (2011).

277. Xu, Q. *et al.* Preparation and growth mechanism of a gold-coloured Ag@AAO composite film with no angular dependence. *Appl. Surf. Sci.* **553**, 149592 (2021).

278. Axelevitch, A., Gorenstein, B. & Golan, G. Investigation of Optical Transmission in Thin Metal Films. *Phys. Procedia* **32**, 1–13 (2012).

279. Coyle, S. *et al.* Confined plasmons in metallic nanocavities. *Phys. Rev. Lett.* **87**, 15–18 (2001).

280. Kelf, T. A., Sugawara, Y., Baumberg, J. J., Abdelsalam, M. & Bartlett, P. N. Plasmonic band Gaps and trapped plasmons on nanostructured metal surfaces. *Phys. Rev. Lett.* **95**, 1–4 (2005).

281. Wallace, G. Q., Foy, H. C., Rosendahl, S. M. & Lagugné-Labarthet, F. Dendritic Plasmonics for Mid-Infrared Spectroscopy. *J. Phys. Chem. C* **121**, 9497–9507 (2017).

282. Lang, X. *et al.* Silver nanovoid arrays for surface-enhanced raman scattering. *Langmuir* **28**, 8799–8803 (2012).

283. Yang, S. *et al.* Large-Scale Fabrication of Three-Dimensional Surface Patterns Using Template-Defined Electrochemical Deposition. *Adv. Funct. Mater.* **23**,

720–730 (2013).

284. Lordan, F., Rice, J. H., Jose, B., Forster, R. J. & Keyes, T. E. Surface enhanced resonance Raman and luminescence on plasmon active nanostructured cavities. *Appl. Phys. Lett.* **97**, 10–13 (2010).

285. Live, L. S., Murray-Méthot, M. P. & Masson, J. F. Localized and propagating surface plasmons in gold particles of near-micron size. *J. Phys. Chem. C* **113**, 40–44 (2009).

286. Lordan, F. *et al.* The Effect of Ag Nanoparticles on Surface-Enhanced Luminescence from Au Nanovoid Arrays. *Plasmonics* **8**, 1567–1575 (2013).

287. Kong, F. *et al.* Band-gap-dependent emissions from conjugated polymers coupled silver nanocap array. *Appl. Phys. Lett.* **99**, 233112 (2011).

288. Nagy, P. *et al.* Processing and characterization of a multibeam sputtered nanocrystalline CoCrFeNi high-entropy alloy film. *Surf. Coatings Technol.* **386**, 125465 (2020).

289. Ivleva, E. A. *et al.* Albumin-stabilized fluorescent metal nanoclusters: fabrication, physico-chemical properties and cytotoxicity. *Mater. Des.* **192**, 108771 (2020).

290. Sarkar, S., Sengupta, A., Hazra, P. & Mandal, P. Blue Emission in Proteins. arXiv preprint arXiv:1404.6859. (2014).

291. Chavez, J. *et al.* Direct excitation of tryptophan phosphorescence. A new method for triplet states investigation. *Methods Appl. Fluoresc.* **10**, 025001 (2022).

292. Niyangoda, C., Miti, T., Breydo, L., Uversky, V. & Muschol, M. Carbonyl-based blue autofluorescence of proteins and amino acids. *PLoS One* **12**, e0176983 (2017).

293. Jia, H. *et al.* Synthesis of Absorption-Dominant Small Gold Nanorods and Their Plasmonic Properties. *Langmuir* **31**, 7418–7426 (2015).

294. Huang, C. *et al.* Hybrid breath figure method: A new insight in Petri dishes for cell culture. *J. Colloid Interface Sci.* **541**, 114–122 (2019).

295. Roach, L., Coletta, P. L., Critchley, K. & Evans, S. D. Controlling the Optical

Properties of Gold Nanorods in One-Pot Syntheses. *J. Phys. Chem. C* **126**, 3235–3243 (2022).

296. Wijaya, A. & Hamad-Schifferli, K. Ligand customization and DNA functionalization of gold nanorods via round-trip phase transfer ligand exchange. *Langmuir* **24**, 9966–9969 (2008).

297. Abadias, G. *et al.* Review Article: Stress in thin films and coatings: Current status, challenges, and prospects. *J. Vac. Sci. Technol. A Vacuum, Surfaces, Film.* **36**, 020801 (2018).

Appendix

A. Impact of the Oxide Breakdown on the Quality of AlNB Surfaces

As stated, the application of high voltage during phosphoric acid anodizing is accompanied by a growth in current density and a rapid generation of heat which may result in overheating and burning of the porous oxide if it is not compensated for (Figure 71). Burning can produce severe surface deformations formed through a rapid uncontrolled growth.[262,264] The high voltage and high current densities create random high-temperature current hot spots where electron avalanching occurs.[264] The surface develops micro cracks and vertical protrusions at these regions as a result of induced expansionary forces and mechanical stress (Figure 71a,b).[264] An appropriate temperature of the electrolyte and a rapid stirring are therefore prerequisites for the efficient heat removal and mitigation of overheating.

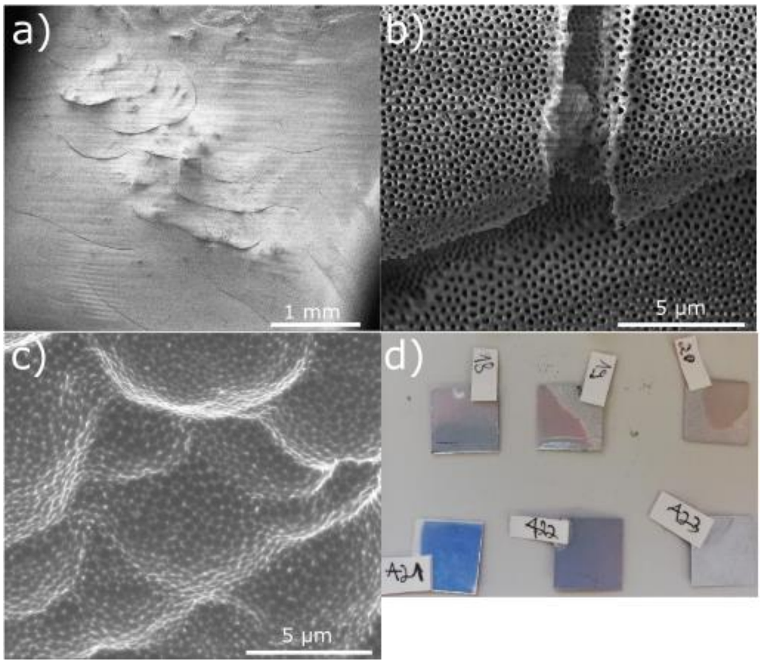

Figure 71: Burnt aluminium oxide produced at 195 V in phosphoric acid due to overheating. SEM images of a) surface deformations on the aluminium oxide, b) cracked porous aluminium oxide layer, c) deformed Al surface after etching, and d) a photograph of anodized Al sheets showing signs of partially and completely burnt surfaces. The rapid growth induces defects such as cracking of the surface but does not interrupt the growth of the porous layer. Selective etching of the porous oxide uncovers additional deformations of the Al surface beneath.

Despite surface defects, the porosity of the oxide layer is preserved. However, etching can reveal that the uncontrolled growth affects the Al surface and the NB pattern beneath as well (Figure 71c). This surface morphology makes further use NBs problematic and any uniform functionalization would be difficult to achieve. The burnt oxide also gives surfaces the characteristic appearance of rough white spots on the anodized surface (Figure 71d).

In this study, the severe heating also presented a technical issue due to burning and melting of components of sample holders designed for low-voltage anodizing (Figure 72). Various sample configurations were employed to produce good-quality aluminium oxide films and the configuration that provided the best results is shown in Figure 41.

Figure 72: Photograph of a sample holder for anodizing with a copper tape for connecting Al samples.

B. Fluorescence Study of BSA-AuNCs on AuNBs in the Presence of GNRs

Sample Preparation

After carrying out fluorescence measurements of BSA-AuNCs on AuNBs, small GNRs (26.1 ± 4.4 nm/7.4 ± 1.4 nm) were added onto immobilized BSA-AuNCs and the measurements were repeated with same parameters. GNRs were produced by a modified seed-mediated growth method described by Jia et. al. (courtesy of Zinuo Li).[63,293] Apart from mixing of the seed and the growth solutions, the synthesis includes an addition of hydrochloric acid (HCl) to decelerate the reaction kinetics and slow down the growth of

GNRs, while allowing more homogeneous growth of GNRs.[295] The seed solution was prepared by mixing 9.75 mL of 0.1 M CTAB solution with 0.25 mL of 0.01 M $HAuCl_4$ and 0.6 mL of 0.01 M $NaBH_4$. The growth solution was made by mixing 0.5 mL of 0.01 M $HAuCl_4$, 8.8 mL of 0.1 M CTAB, 0.045 mL of 0.01M $AgNO_3$, 0.08 mL of ascorbic acid and 0.4 mL of 1 M HCl. To prevent chemical decomposition of BSA due to the presence of cytotoxic CTAB, a ligand exchange was carried out on CTAB-coated GNRs using a capping agent mercaptohexanoic acid (MHA).[296] Purified GNRs were resuspended in TBE (Tris/Borate/EDTA) buffer and further diluted with distilled water to the final working concentration. The concentration of GNRs (~0.32 nM) was tuned to approximately 1:1 ratio of AuNBs@1:GNRs and the same concentration was also used for large AuNB@2. Characterization of GNRs was done via STEM using parameters listed earlier in this work for the imaging of silica-coated GNRs. Dimensions of GNRs were obtained by measuring one hundred GNRs in the image processing software ImageJ.

Fluorescence characterization

Fluorescence spectra of BSA-AuNCs in the presence of GNRs were collected using same parameters that were used for fluorescence spectroscopy of BSA-AuNCs on AuNBs. 3D Excitation emission matrices (EEMs) were collected at the range of excitation and emission wavelengths in order to record the full emission of BSA-AuNCs. EEMs were corrected for the 1st and the 2nd order of Rayleigh scattering. The bandwidth resolution was set to 10 nm.

Results

Absorption spectra of GNRs (26.1 ± 4.4 nm/7.4 ± 1.4 nm) and AuNCs exhibited showed a longitudinal SPR band at ~710 nm which strongly overlaps with the AuNC emission spectrum (Figure 73).

Figure 74 shows that adding GNRs to BSA-AuNCs in resulted in a minor increase in fluorescence emission intensity of tryptophan (Figure 74a). Under 8 ° excitation, an enhancement of the AuNC fluorescence was also observed (Figure 74b,c). However, at angles of incidence above 8 °, the effect of GNRs on the AuNC emission was inconsistent, causing various changes in fluorescence intensities. Emission spectra of AuNCs excited at 30 ° remained relatively unchanged but decreased on both substrates when excited at 45 °. The excitation at 60 ° again led to varying response on both substrates. It can be speculated that the decrease in fluorescence intensities of AuNCs was caused by SET at longer wavelengths due to the spectral overlap between absorption spectra of GNRs and AuNCs (Figure 73).

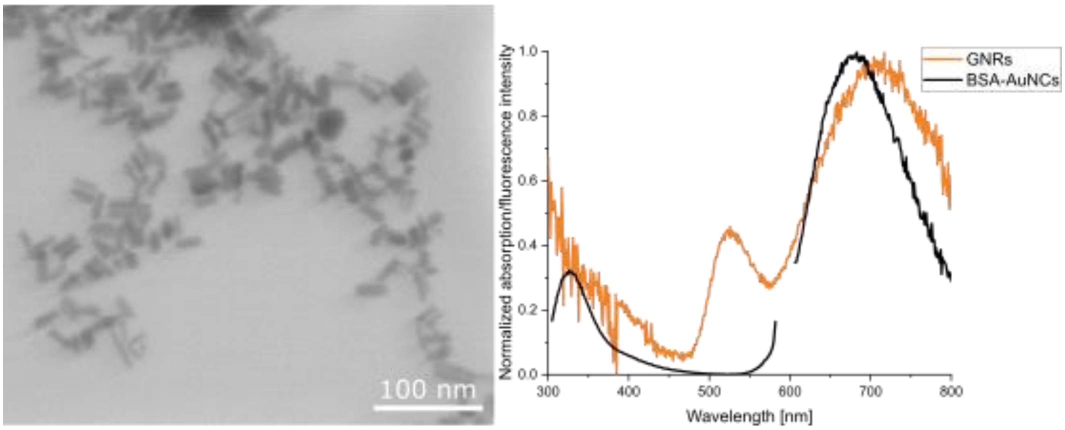

Figure 73: STEM image of GNRs and absorption and fluorescence spectra of GNRs and the BSA-AuNC solution (~0.38 µM), respectively.

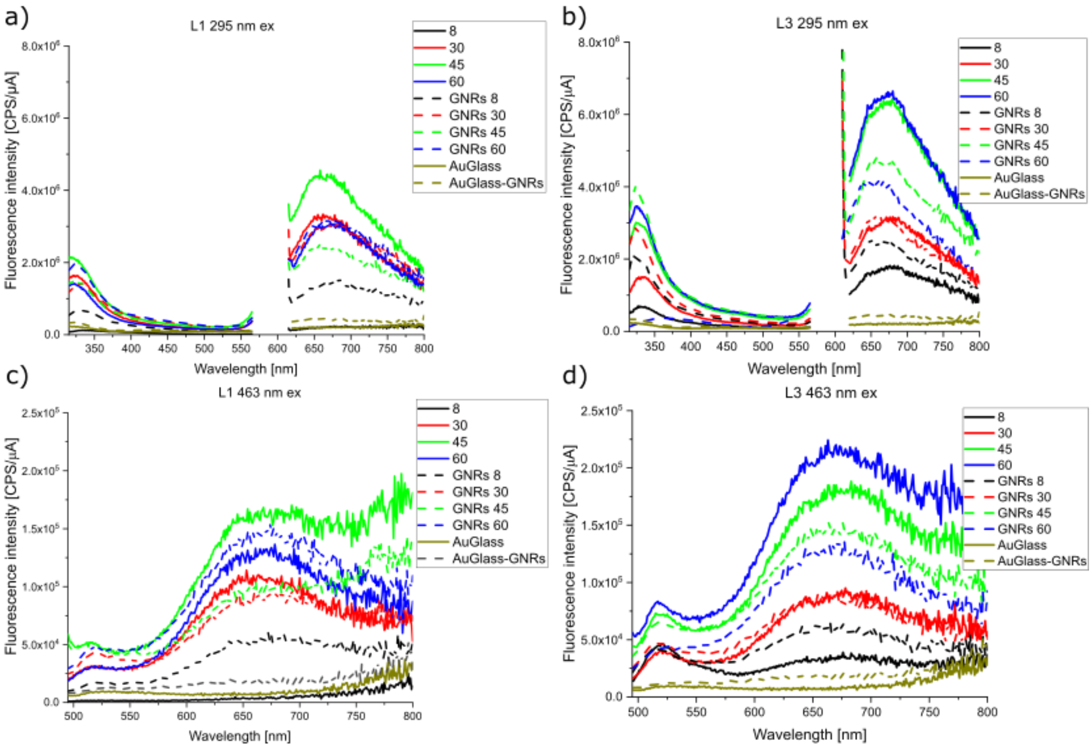

Figure 74: Fluorescence spectra of BSA-AuNC on AuNBs L1 (a, c) and L3 (b, d) under 295 and 463 excitations in the absence/presence of GNRs.

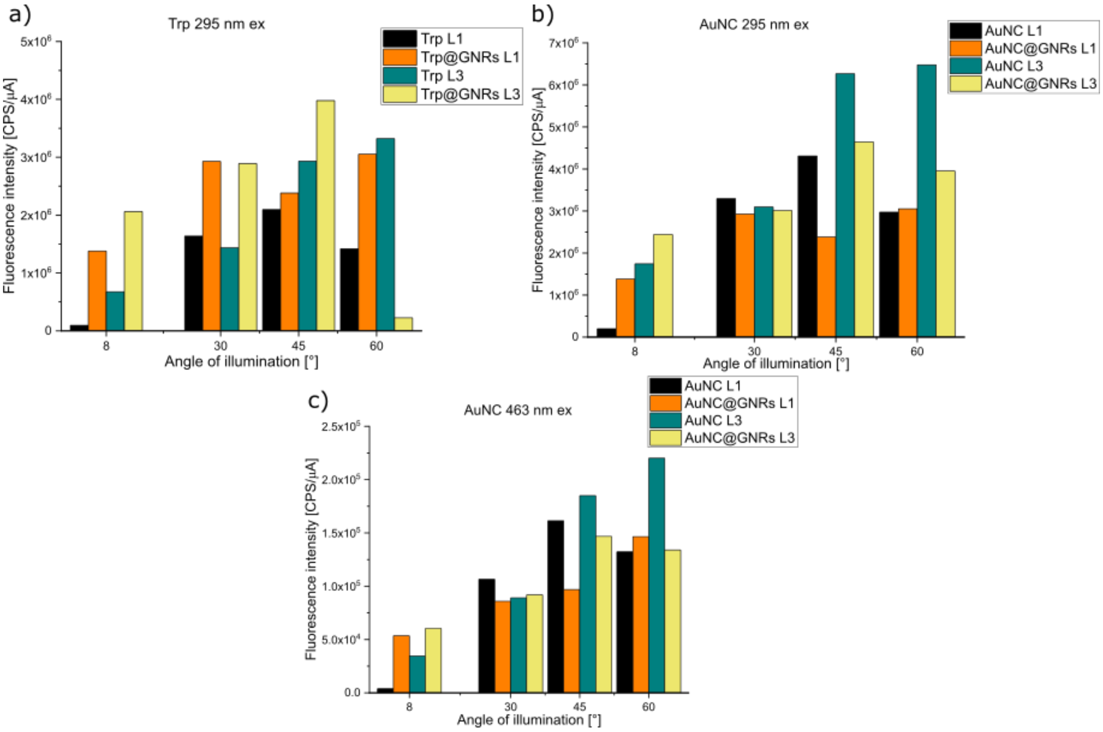

Figure 75: Comparison of maximum fluorescence intensities of BSA-AuNC on L1 and L3 in the absence/presence of GNRs.

Figure 76 shows 3D excitation emission matrices (EEMs) of BSA-AuNCs. In Figure 76b, an additional hot spot with increased fluorescence intensity at around 400 nm that is related to the blue emission of BSA was observed in the presence of GNRs. Similar feature was observed also in EEMs collected from S3.

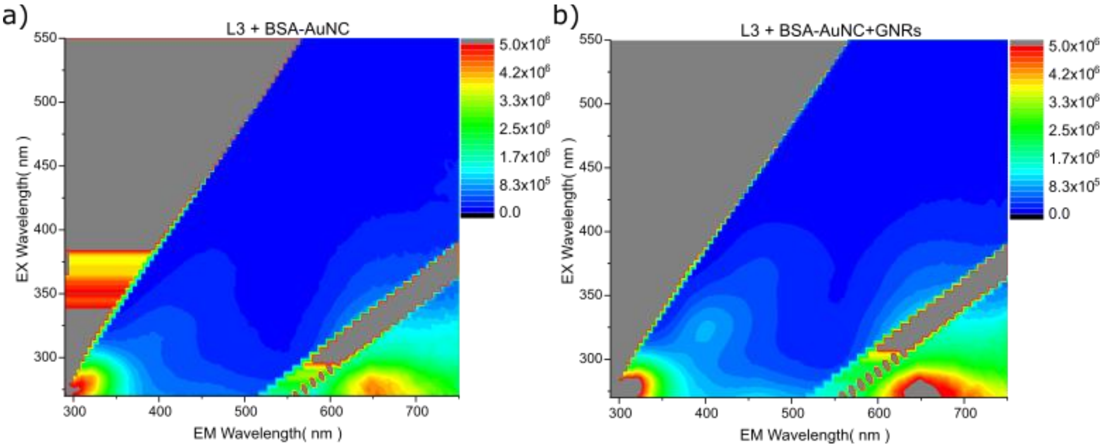

Figure 76: 3D EEMs of BSA-AuNC on AuNBs L3 without (left) and with (right) GNRs. Strong Ryleigh scattering first- and second-order maxima are visible in top left and bottom right corners of EEMs (step-like pattern) and represent artifacts that do not belong to the samples.

The presence of GNRs had little effect on the emission of BSA-AuNCs on S1 (Figure 77, Figure 78), causing only small changes in fluorescence intensities of both tryptophan and AuNCs.

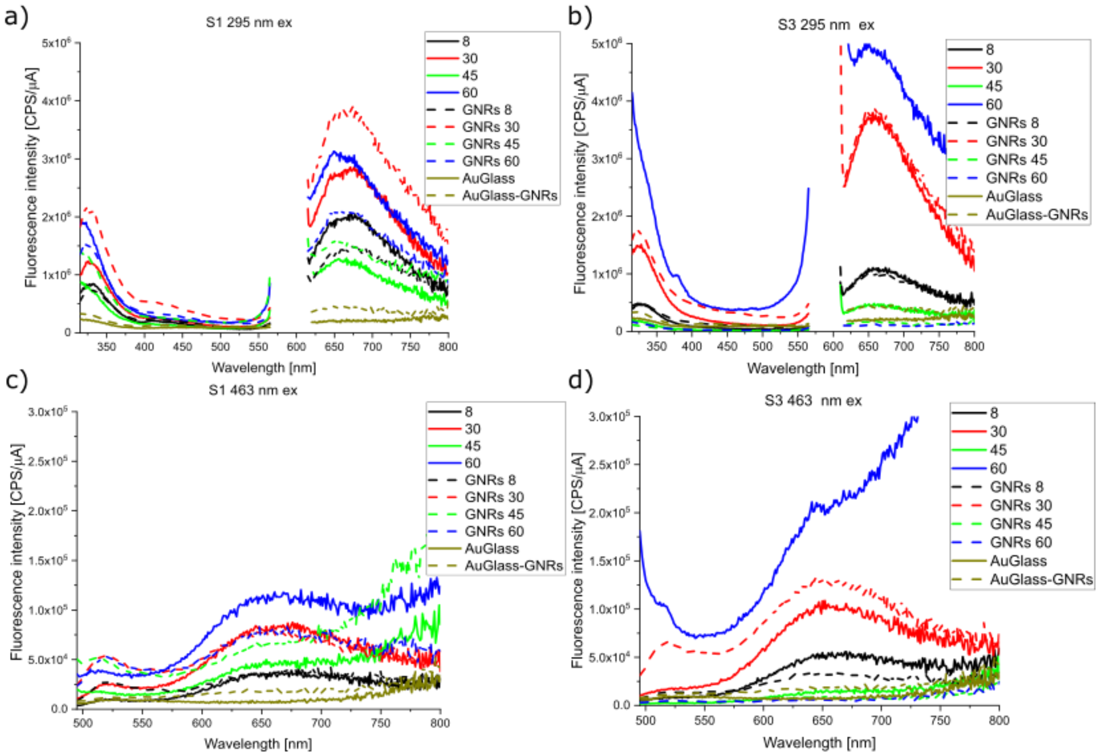

Figure 77: Fluorescence spectra of BSA-AuNC on AuNBs S1 (a, c) and S3 (b, d) under 295 and 463 excitations in the absence/presence of GNRs.

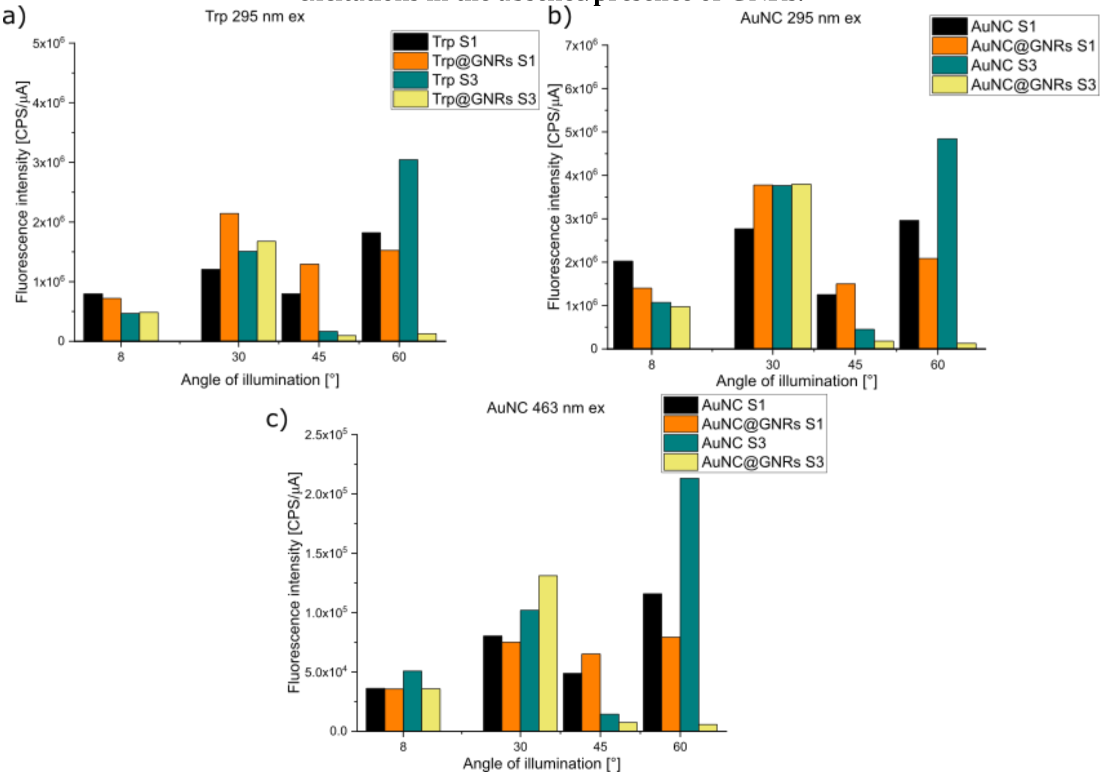

Figure 78: Comparison of maximum fluorescence intensities of tryptophan and BSA-AuNC on S1 and S3 substrates in the absence/presence of GNRs.

The presence of GNRs also led to the enhancement of the blue BSA emission (Figure 79) which is again highlighted by the hot spot at around 400 nm (Figure 79).

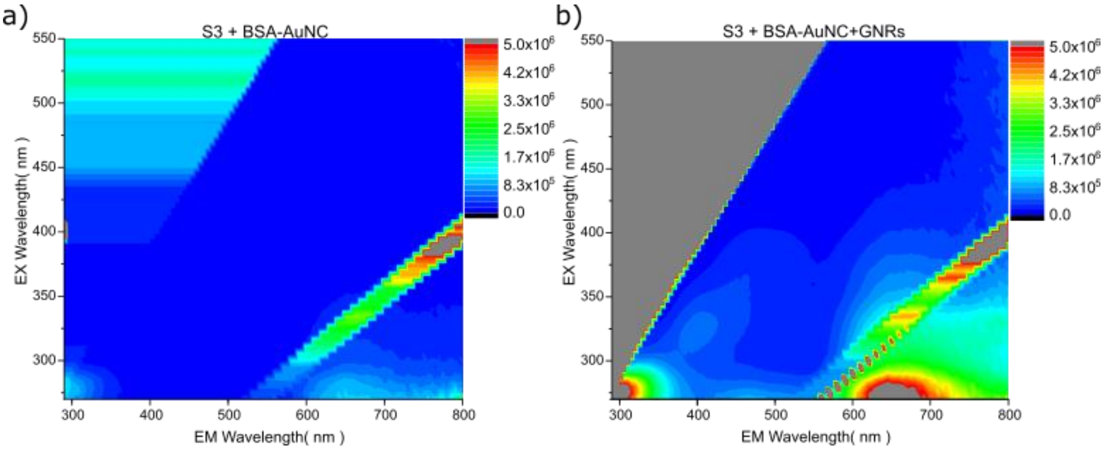

Figure 79: 3D EEMs of BSA-AuNC on AuNBs S3 without (left) and with (right) GNRs. Strong Ryleigh scattering first- and second-order maxima are visible in top left and bottom right corners of EEMs (step-like pattern) and represent artifacts that do not belong to the samples.

C. Mechanical Stability of the AuNB Surface

The state of the surface after two cycles of solvent evaporation was investigated via SEM. Examination of SEM images revealed localized damage of the surface (Figure 80). Cracks in the gold film had not been observed after the Au deposition and should be the result of drying of BSA-AuNC and GNR solutions. It is not uncommon to observe cracking of thin metallic coatings due to the surface tension at the metal-substrate interface, particularly in cases when substrates include surface features with complex geometries.[297] Another factor to consider is the surface unevenness of AlNB substrates that can be subsequently transferred to deposited Au films, causing inhomogeneous distribution of tensile stress at the Au surface. It can be assumed that due to the combination of these factors and drying of solutions, a critical tension at the interface can be reached and cause local rupturing of the Au surface at weakened points. Only a few such defects were observed across all AuNB substrates, and they are expected to not have a significant impact on performed fluorescence measurements with GNRs.

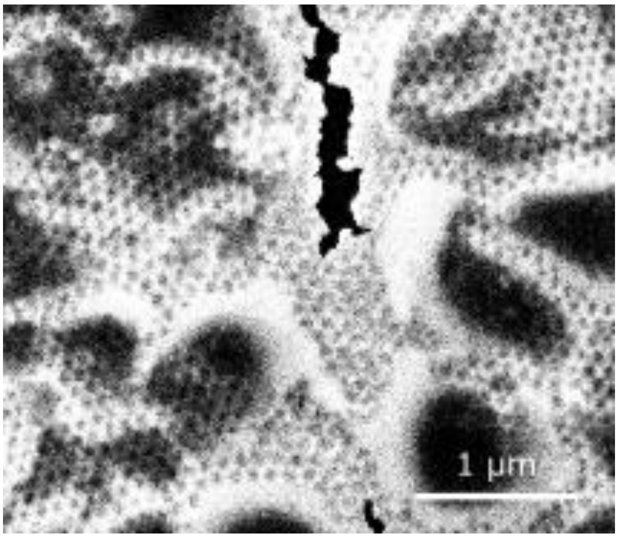

Figure 80: SEM image of an AuNB substrate after two drying cycles of BSA-AuNC and GNR solution.

In the case of a repeated use AuNB substrates or an application of multiple liquids, the stability of the Au surface should be experimentally tested as defects may spread and eventually cause an extensive damage to the NB pattern. This can present a technical issue for dry measurements in spectrofluorometers and similar “inside the box” instrumentation which require vertical positioning of samples. Drying may not be an issue for microscope-based setups where the solvent evaporation is not a necessary step and liquid samples can be sealed on a substrate with conventional cover slips to preserve the liquid and slow down the evaporation.